
**Structural and biophysical studies on
integral membrane proteins (IMPs) in a
native-like lipid environment**

DISSERTATION

*zur Erlangung des Doktorgrades der Naturwissenschaften (Dr. rer. nat.)
an der Fakultät für Mathematik, Informatik und Naturwissenschaften
der Universität Hamburg, Fachbereich Chemie*

vorgelegt von

Julius Nitsche

Hamburg, August 2019

Die vorliegende Arbeit wurde im Zeitraum von Juni 2014 bis Dezember 2018 in der Arbeitsgruppe von Prof. Dr. H. Tidow am Institut für Biochemie und Molekularbiologie des Fachbereichs Chemie der Universität Hamburg durchgeführt.

1. Gutachter: Prof. Dr. Henning Tidow

2. Gutachter: Prof. Dr. Christian Betzel

Datum der Disputation: 25.10.2019

Datum der Druckfreigabe: 19.10.2020

Table of Contents

	Page
Abstract	iii
Zusammenfassung	v
Publication associated with this thesis	vii
List of Figures	ix
List of Tables	xii
List of Abbreviations	xiii
I Introductory Preface	1
1 Membrane proteins	3
1.1 Overview of model membrane systems for the study of membrane proteins	3
1.1.1 Detergents	3
1.1.2 Bicelles	4
1.1.3 Lipid vesicles	5
1.1.4 Nanolipoprotein particles	5
2 Structural studies of membrane proteins using small-angle scattering techniques	9
2.1 Basic concept of small-angle scattering	9
2.1.1 Model free size parameter	11
2.1.1.1 Pair-distance distribution function	11
2.1.1.2 Size determination	11
2.1.2 SANS contrast variation	12
2.2 Small-angle scattering of membrane proteins	13
2.2.1 Stealth-carrier nanodiscs for small-angle scattering experiments	14
Aim of the thesis	17

II Biochemical and biophysical studies on integral membrane proteins in lipidic carrier systems	19
3 Comparison of lipidic carrier systems	21
3.1 Introduction	21
3.2 Material and methods	23
3.2.1 Expression and purification of MSP1D1	23
3.2.2 Expression and purification of SapA	23
3.2.3 Preparation of nanodiscs and saposin nanoparticles	24
3.2.4 Differential scanning fluorimetry using Prometheus	24
3.2.5 Small-angle X-ray scattering (SAXS)	25
3.3 Results and discussion	26
3.3.1 Reconstitution of MSP1D1 nanodiscs and SapA nanoparticles	26
3.3.2 Biophysical properties of nanodiscs and SapA nanoparticles	28
3.3.2.1 Long-term stability	28
3.3.2.2 Thermal stability	31
3.3.3 Structural effects of different lipids on nanodiscs and SapA-nanoparticles	32
3.3.3.1 SAXS-analysis	32
3.4 Conclusion	35
4 Studies on the activation of plasma-membrane Ca²⁺-ATPase ACA8	37
4.1 Introduction	37
4.1.1 Calcium as a second messenger	37
4.1.2 P-type ATPases	38
4.1.3 Plasma-membrane Ca ²⁺ -ATPases	39
4.2 Material and methods	41
4.2.1 Cloning of ACA8 constructs	41
4.2.2 Small-scale expression screening of ACA8	42
4.2.3 Fluorescence-detection size exclusion chromatography	42
4.2.4 Expression of full-length ACA8, ACA8core and ACA8RD	43
4.2.5 Purification of full-length ACA8, ACA8core and ACA8RD	44
4.2.6 Expression and purification of CaM7	45
4.2.7 Differential scanning fluorimetry using Prometheus	45
4.2.8 Reconstitution of ACA8 into MSP nanodiscs	47
4.2.9 Native mass spectrometry	47
4.2.10 Activity measurements	48
4.2.11 Fluorescence anisotropy titration	49
4.2.12 Small-angle X-ray scattering (SAXS)	50
4.3 Results and discussion	52
4.3.1 Optimization of expression and purification of ACA8	52

4.3.1.1	GFP-based expression screening of ACA8	52
4.3.1.2	Optimization of purification of ACA8	56
4.3.2	Reconstitution of ACA8 into nanodiscs	65
4.3.3	Biochemical characterization of the activation process	69
4.3.3.1	Native mass spectrometry confirms a bimodular mechanism	69
4.3.3.2	Activity measurements	71
4.3.4	Biophysical characterization of the activation process	73
4.3.4.1	Fluorescence anisotropy titration	73
4.3.4.2	Small-angle X-ray scattering analysis	76
4.4	Conclusion	79

III Stealth carrier nanodiscs 81

5 Stealth carrier nanodiscs for structural investigation of membrane proteins in a lipid environment using small-angle neutron scattering – MsbA as a case study 83

5.1	Introduction	83
5.2	Material and methods	86
5.2.1	Expression and purification of deuterated MSP1D1	86
5.2.2	Expression and purification of MsbA	86
5.2.3	Expression and purification of deuterated phosphatidylcholine lipids	87
5.2.4	Reconstitution of MsbA into stealth carrier nanodiscs	87
5.2.5	Activity measurements	88
5.2.6	Small-angle X-ray scattering (SAXS)	88
5.2.7	Small-angle neutron scattering (SANS)	89
5.2.8	Model calculation from SANS data	90
5.3	Results and discussion	91
5.3.1	Reconstitution of MsbA into stealth nanodiscs	91
5.3.2	Structural characterization of MsbA by combined SAXS / SANS	93
5.3.3	Structural modelling of MsbA in nucleotide-free state	99
5.4	Conclusion	101

6 Small-angle neutron scattering of ACA8 in stealth nanodiscs – modelling of the CaM-activated state 103

6.1	Introduction	103
6.2	Material and methods	105
6.2.1	Expression and purification of deuterated CaM	105
6.2.2	Reconstitution of ACA8 into stealth carrier nanodisc	105

6.2.3	Small-angle neutron scattering (SANS)	106
6.2.4	Model calculation from SANS Data	106
6.3	Results and discussion	108
6.3.1	Reconstitution of ACA8 into stealth nanodiscs (sND)	108
6.3.2	Structural characterization of ACA8 by SANS	109
6.3.3	Structural modelling of ACA8 in its activated state	111
6.4	Conclusion	115
References		117
IV Appendix		139
A Supplementary Data		141
A.1	Supplementary Figures	141
A.1.1	Native mass spectrometry of CaM7	141
A.1.2	Incorporation of flACA8 into nanodisc composed of various lipids	142
A.1.3	SAXS analysis of ACA8 and its complex with CaM	143
A.1.4	SANS analysis of ACA8 in stealth carrier nanodisc	144
A.1.5	SANS analysis of MsbA in stealth carrier nanodisc	145
A.1.6	Incorporation of MsbA in lipid carrier with different lipids	147
A.2	Supplementary Tables	148
A.2.1	Sequences of Proteins used in this Study	148
A.2.2	Masses of ACA8-CaM complexes measured by NMS	150
A.2.3	SAXS/SANS parameters	151
A.3	Scripts	153
B General Sample Preparation Techniques		157
C Instrumentation and Chemicals		163
C.1	Instrumentation	163
C.2	Chemicals used (GHS Classification)	166
C.3	GHS Hazard Statements	176
C.4	GHS Precautionary Statements	177
C.5	Disposal	179
Acknowledgements		181
Eidesstattliche Erklärung		183

Abstract

Membrane proteins (IMPs) are embedded into a complex lipid environment. For the majority of biophysical studies it is necessary to extract them from the natural lipid bilayer by solubilisation using detergents. The surrounding detergent micelle, however, is a bad mimic of the lipid bilayer, which often lead to protein instability and reduced activity. Nano-lipoprotein complexes have become a valuable tool for biophysical studies in a native-like lipid environment. These discoidal protein-lipid complexes consist of a lipid bilayer surrounded by an amphipathic protein, yielding a membrane protein incorporated in a lipid environment with a defined size that is soluble in aqueous solution. This carrier systems has been successfully used for functional studies of a variety of different membrane proteins. In the framework of this thesis structural and functional studies on two membrane proteins were carried out using these protein-lipid complexes.

In a first project, a comparative study of two nano-lipoprotein particles showed that both systems are equally stable and stabilization effects of incorporated membrane proteins are comparable.

In a second project, the activation process of plasma-membrane Ca^{2+} ATPases (PMCA) was analysed in great detail. PMCA are key regulators of the Ca^{2+} homeostasis in eukaryotic cells. They export calcium ions (Ca_{2+}) from the cytosol to the extracellular milieu and are tightly regulated. Calmodulin (CaM), as its main activator, binds to a unique regulatory domain which releases the autoinhibition and activates the pump. In this thesis, the PMCA from *A. thalina*, ACA8, was characterized. The results revealed that two CaM molecules can bind to the full-length enzyme, which is in good agreement with previous studies on the isolated regulatory domain. Activity assays of ACA8 in nanodiscs further supported the bimodular activation model and showed that negatively charged lipid headgroups are able to stabilize the activated state.

In a third project, the recently developed "stealth carrier" nanodiscs (sND) were applied to membrane proteins for the first time. Fractionally deuterium labelled nanodisc components lead to discs that are effectively invisible to small-angle neutron scattering (SANS), which enables low-resolution structural characterization of membrane proteins in a native-like lipid environment without the contribution of the nanodiscs to the scattering signal. Small-angle neutron scattering data of the bacterial ATP-binding cassette (ABC) transporter incorporated into sND revealed a distinct conformational state in the nucleotide free form, which could not be seen in small-angle X-ray scattering experiments. In addition, subtle conformational differences upon nucleotide binding could be detected reliably from the SANS data.

The stealth nanodisc technique was used to characterize the activation process of the plasma-membrane Ca^{2+} ATPase ACA8. The data revealed large conformational

changes and flexible regulatory domain upon CaM binding. A model of the CaM-activated ACA8 could be generated from the SANS data, which, together with the functional data, revealed the structural basis for the activation of PMCAs.

Zusammenfassung

Membranproteine (IMPs) sind von einer komplexen Lipidschicht umgeben. Für die meisten biophysikalischen Studien ist es jedoch notwendig, sie mittels Detergenzien aus der natürlichen Lipiddoppelschicht zu extrahieren. Durch die Verwendung von Detergenzien ist die Proteinstabilität und häufig auch die Aktivität herabgesetzt. Die Entwicklung von Nano-Lipoprotein-Komplexen hat sich für biophysikalische Studien in einer nativen Lipidumgebung als wertvolles Werkzeug herausgestellt. Diese Protein-Lipid-Komplexe bestehen aus einer Lipiddoppelschicht, die von einem amphipatischen Protein umgeben ist und stabilisiert wird. In diesen Komplexen können Membranproteine eingebaut werden und sind so von einer Lipiddoppelschicht umgeben die eine definierte Größe besitzt und Membranproteine in wässriger Lösung stabilisiert. Diese Technik wurde erfolgreich für funktionelle Studien einer Vielzahl von verschiedenen Membranproteinen eingesetzt. Im Rahmen dieser Arbeit wurden strukturelle und funktionelle Untersuchungen an zwei verschiedenen Membranproteinen mit Hilfe dieser Protein-Lipid-Komplexen durchgeführt.

Im ersten Teil der Arbeit wurden die beiden gängigsten Nano-Lipoprotein Systeme systematisch miteinander verglichen. Es konnte gezeigt werden, dass beide Systeme gleich stabile Komplexe bilden und in einem ähnlichen Umfang die eingebauten Membranproteine stabilisieren.

In einem zweiten Projekt wurde der Aktivierungsprozess von Plasmamembran Ca^{2+} -ATPasen (PMCA) detailliert analysiert. PMCA's nehmen eine Schlüsselrolle in der Ca^{2+} -Homöostase in eukaryotischen Zellen ein. Sie transportieren Calciumionen (Ca^{2+}) aus dem Cytosol in das extrazelluläre Milieu. Zudem ist ihre Aktivität streng reguliert. Durch die Bindung von Calmodulin (CaM) an die regulatorische Domäne, wird die Inhibierung durch die regulatorische Domäne aufgelöst und die Pumpe aktiviert. In dieser Arbeit wurde die PMCA aus *A. Thalina*, ACA8, untersucht und es konnte gezeigt werden, dass zwei CaM-Moleküle an das Volllängenzym binden, welches ein zuvor postulierten bimodularen Aktivierungsmechanismus bestätigt. Diese Ergebnisse konnten durch Aktivitätsstudien in Nanodiscs weiter untersucht werden und es wurde gezeigt, dass negativ geladene Kopfgruppen der Lipide die Konformation des aktivierten Zustandes stabilisieren und dadurch die Aktivität weiter moduliert wird.

Im dritten Projekt wurden die kürzlich entwickelten "Stealth Carrier" -Nanodiscs (sND) erstmals mit eingebauten Membranproteinen angewendet. Die deuterierten Nanodiscbestandteile bewirken das die Nanodiscs im SANS-Experiment nicht zum Streusignal beitragen. Dies ermöglichte eine niedrigauflösende strukturelle Analyse von Membranproteinen in einer nativen Lipidumgebung, ohne das die Nanodiscs in die Analyse mit einbezogen werden müssen. SANS-Daten vom bakteriellen ABC Transporter MsbA, welcher in "Stealth Nanodiscs" eingebaut wurde, ergaben einen deutlichen konformationellen Unterschied zu publizierten Kristallstrukturen ohne

gebundene Nukleotide. Des Weiteren konnten feine konformationelle Unterschiede durch die Bindung von Nukleotide detektiert werden.

Die "Stealth Carrier" -Nanodiscs (sND) wurden aurdem verwendet um den Aktivierungsprozess der Plasmamembran Ca^{2+} ATPase ACA8 zu charakterisieren. Die Daten zeigten, dass durch die Bindung von Calmodulin große Konformationsänderungen ausgelöst werden. Des Weiteren konnte gezeigt werden, dass die regulatorische Domäne flexibler wird. Zusammen mit der funktionellen Charakterisierung konnten weitere Informationen über den Aktivierungsmechanismus von PMCAs gewonnen werden.

Publication associated with this thesis

Parts of this thesis were published in

Chapter 3

Dominique-Maurice Kehlenbeck, Inokentijis Josts, **Julius Nitsche**, Sebastian Busch, V. Trevor Forsyth, Henning Tidow, *Comparison of lipidic carrier systems for integral membrane proteins – MsbA as case study*, Biological Chemistry (2019)

Chapter 4 + 6

Julius Nitsche, Inokentijis Josts, Johannes Heidemann, Haydyn D. Mertens, Selma Maric, Martine Moulin, Michael Haertlein, Sebastian Busch, V. Trevor Forsyth, Dmitri I. Svergun, Charlotte Uetrecht, Henning Tidow, *Structural basis for activation of plasma-membrane calcium ATPase by calmodulin*, Communications Biology (2018) 1, 206

Chapter 5

Inokentijis Josts, **Julius Nitsche**, Selma Maric, Haydyn D. Mertens, Martine Moulin, Michael Haertlein, Sylvain Prevost, Dmitri I. Svergun, Sebastian Busch, V. Trevor Forsyth, Henning Tidow, *Conformational States of ABC Transporter MsbA in a Lipid Environment Investigated by Small-Angle Scattering Using Stealth Carrier Nanodiscs*, Structure (2018), 26(8), 1072-1079

List of Figures

Figure 1.1	Schematic representation different model membranes.	4
Figure 1.2	Schematic representation of the assembly process of nanodiscs.	7
Figure 2.1	Schematic representation of a small-angle scattering experimental set up.	10
Figure 2.2	Schematic representation of SANS studies of a membrane protein in stealth nanodisc.	16
Figure 3.1	Optimization of ratios for nanodisc and SapNP assembly.	27
Figure 3.2	Structures of lipids used for comparative studies.	28
Figure 3.3	Long-term stability of empty MSP1D1 nanodiscs and saposin nanoparticles (SapNP).	29
Figure 3.4	nDSF measurements to investigate the thermal stability of MsbA incorporate in different lipid carrier systems.	32
Figure 3.5	Analysis of SEC fractions of empty nanodiscs and SapNPs by small-angle X-ray scattering.	34
Figure 4.1	Comparison of SERCA structures showing key states of of the reaction cycle.	39
Figure 4.2	Proposed model of PMCA activation by Tidow <i>et al.</i> [67].	41
Figure 4.3	In-cell expression screening of ACA8.	54
Figure 4.4	In-gel fluorescence showing the expression of ACA8	56
Figure 4.5	Solubilization efficiency of ACA8-GFP	57
Figure 4.6	Fluorescence detection size-exclusion (FSEC) profiles of ACA8-GFP in various detergents.	58
Figure 4.7	Size-exclusion chromatography (SEC) of ACA8 in DDM.	59
Figure 4.8	Thermal stability analysis of ACA8 by nDSF to optimize detergent and additive conditions.	61
Figure 4.9	Thermal stability analysis of ACA8 by nDSF to optimize buffer pH conditions.	62
Figure 4.10	Size-exclusion chromatography (SEC)of ACA8 in maltoside neopentyl glycol detergents.	63
Figure 4.11	Size-exclusion chromatography of assembly of ACA8 into MSP1E3 nanodiscs.	66

Figure 4.12	Size-exclusion chromatography of assembly of ACA8 into MSP1D1 nanodiscs.	67
Figure 4.13	Stability of ACA8-MSP1D1 nanodiscs.	68
Figure 4.14	Native mass spectrometry experiments of ACA8-CaM complex.	69
Figure 4.15	Full m/z ratio of native mass spectrum of DDM-purified ACA8-CaM.	71
Figure 4.16	ATPase activity of ACA8 in MSP1D1 nanodiscs.	72
Figure 4.17	Fluorescence anisotropy to characterize binding affinities within ACA8-CaM complex.	75
Figure 4.18	Small-angle X-ray scattering (SAXS) analysis of nanodisc-incorporated ACA8 and its complex with CaM.	77
Figure 4.19	Flexibility analysis of the ACA8-CaM complex using scattering intensity decay power laws.	79
Figure 5.1	Models of MsbA in different states.	84
Figure 5.2	Reconstitution of MsbA into MSP1D1 nanodiscs without endogenous lipids.	92
Figure 5.3	Stability and activity of MsbA in stealth nanodisc.	93
Figure 5.4	Small-angle neutron scattering of MsbA incorporated into stealth nanodisc.	93
Figure 5.5	Comparison of X-ray and neutron scattering data from MsbA-sND.	94
Figure 5.6	Conformational analysis of MsbA-sND.	97
Figure 5.7	Differences in SANS profiles of MsbA-sND in different conformational changes.	98
Figure 5.8	Ab initio modelling of apo MSbA.	100
Figure 5.9	Modelling of MsbA in its nucleotide free state.	101
Figure 6.1	Cartoon illustration of used stealth nanodisc technique to study activation process of ACA8.	104
Figure 6.2	Reconstitution of ACA8 in stealth nanodiscs.	109
Figure 6.3	Small-angle neutron scattering of ACA8 incorporated into stealth nanodiscs.	110
Figure 6.4	Analysis of SANS scattering of ACA8-sND.	111
Figure 6.5	Ensemble optimized method to model the activated state of ACA8.	112
Figure 6.6	Ensemble optimized method to model the activated state of ACA8 – selected models.	114
Figure A.1	Native mass spectrometry of CaM7.	141
Figure A.2	SEC chromatogram of ACA8 in nanodisc with different lipids.	142

Figure A.3	SAXS analysis of ACA8-ND at different concentrations.	143
Figure A.4	SAXS of ACA8 in nanodisc with anionic lipids.	143
Figure A.5	Comparison of SANS curves of empty sND with ACA8-sND.	144
Figure A.6	Rg distribution of ACA8-sND in apo conformation.	144
Figure A.7	Kratky analysis of MsbA in stealth carrier nanodisc.	145
Figure A.8	Cryson fits of MsbA ind different conformation.	145
Figure A.9	Cluster analysis of ab initio models derived from sND/SANS experiments.	146
Figure A.10	SEC profiles of MsbA incorporated into MSP1D1 nanodiscs and SapNP composed of different lipids.	147

List of Tables

Table 2.1	Neutron scattering lengths of the most abundant elements found in proteins and lipids.	12
Table 3.1	Overall structural parameter of empty MSP1D1 nanodiscs and saposin nanoparticles.	33
Table 4.1	Prometheus screen	46
Table 4.2	Purification specification of different ACA8 constructs	64
Table A.1	Aminoacid sequences of proteins used in this study.	148
Table A.2	Comparison of theoretical and experimental M_r of ACA8 CaM7.150	
Table A.3	SAXS parameters – ACA8-ND	151
Table A.4	SANS parameters – ACA8-sND	152
Table A.5	SAXS/SANS parameters – MsbA-sND	156
Table B.1	Yeast growth media.	157
Table B.2	<i>E. coli</i> growth media.	158
Table B.3	Properties of proteins used in this study.	159
Table B.4	Bacterial and yeast strains.	160
Table C.1	Instrumentation (listed alphabetically)	163
Table C.2	Chemicals (listed alphabetically)	166

List of Abbreviations

α	Alpha
Å	Angstrom
ABC	ATP binding cassette
ACA8	Calcium-transporting ATPase 8
Amp	Ampicillin
AMPPCP	Adenosine-5'-[(β , γ)-methylene] triphosphate (β , γ non-hydrolyzable ATP)
APS	Ammonium persulfate
ATP	Adenosine triphosphate
β	Beta
C	Celsius
CaM	Calmodulin
CD	Circular dichroism
CHAPS	3-[(3-Cholamidopropyl)dimethylammonio]-1-propanesulfonate
Chlor	Chloramphenicol
CHS	Cholesterol hemisuccinate
CMC	Critical micelle concentration
cryo-EM	cryo electron microscopy
Da	Dalton
DDM	n-Dodecyl- β -D-maltopyranoside
dH ₂ O	Distilled water
DLS	Dynamic light scattering
DM	n-Decyl- β -D-maltopyranoside
DMNG	Decyl maltose neopentyl glycol (2,2-dioctylpropane-1,3-bis- β -D-maltopyranoside)
DMPC	1,2-dimyristoyl-sn-glycero-3-phosphocholine
DNA	Deoxyribonucleic acid
DOPC	1,2- dioleoyl-sn-glycero-3-phosphocholine
DTT	Dithiothreitol
EDTA	Ethylenediaminetetraacetic acid
EGTA	Ethylene glycol-bis(β -aminoethyl ether)-N,N,N',N'-tetraacetic acid
EOM	Ensemble optimisation method
FSEC	Fluorescent size exclusion chromatography
γ	Gamma
g	Gram
h	Hour
HEPES	4-(2-hydroxyethyl)-1-piperazineethanesulfonic acid
IMAC	Immobilised metal affinity chromatography
IPTG	Isopropyl- β -D-thiogalactopyranosid
ITC	Isothermal titration calorimetry
k	Kilo

K	Kelvin
Kan	Kanamycin
K_d	Equilibrium dissociation constant
l	Liter
LB	Lysogenic Broth
LMNG	Lauryl maltose neopentyl glycol (2,2-didecylpropane-1,3-bis- β -D-maltopyranoside)
LPS	Lipopolysaccharide
M	Molar
min	Minute
mm	Millimeter
M_r	Molecular mass
μ	Micro
Mes	2-(N-morpholino)-ethanesulfonic acid
MsbA	Lipid A export ATP-binding/permease protein
MSP	Membrane scaffold protein
Ni-NTA	Nickel-Nitrilotriacetic acid
nm	Nanometer
OD ₆₀₀	Optical density at 600 nm
PC	Phosphatidylcholine
PCR	Polymerase chain reaction
PDB	Protein Data Bank
PEG	Polyethylene glycol
pI	Isoelectric point
PMSF	Phenylmethylsulfonylfluoride
POPC	1-palmitoyl-2-oleoyl-glycero-3-phosphocholine
POPG	1-palmitoyl-2-oleoyl-sn-glycero-3-phospho(1'-rac-glycerol)
R_g	Radius of gyration
rpm	Rounds per minute
s	Second
SANS	Small-angle neutron scattering
SapA	Saposin A
SAXS	Small-angle X-ray scattering
SDS	Sodium dodecyl sulphate
SDS-PAGE	Sodium dodecyl sulphate-polyacrylamide gel electrophoresis
SEC	Size exclusion chromatography
soyPI	L- α -phosphatidylinositol (soy)
TB	Terrific Broth
TEV	Tobacco etch virus
Tris	tris-(hydroxymethyl)-aminomethane
UV	Ultraviolet
V/V	Volume per volume
WT	Wild-type
w/v	Weight per volume
yeGFP	yeast-enhanced green fluorescent protein

Part I

Introductory Preface

Chapter 1

Membrane proteins

1.1 Overview of model membrane systems for the study of membrane proteins

Integral membrane proteins (IMPs) are embedded in different types of cellular membranes of the cell. Integrated into the membrane, IMPs are of major physiological relevance in diverse cellular processes, such as, e.g. cell-cell communication, signal transduction, ion and nutrient transport, mechanosensation and energy metabolism [1–6]. Around 30 % of all open reading frames (ORF) in eukaryotic cells encode for IMPs [7] with nearly 50 % of them represents potential targets for pharmacological drugs [8, 9], illustrating the importance of this class of macromolecules. Membrane proteins have evolved to be located in the hydrophobic environment of the mosaic lipid bilayer, which is a complex and dynamic system and, hence, detergents have to be used to extract those proteins and keep them soluble in aqueous solution. This limits the use of many biophysical techniques to characterize the structure and function, like X-ray crystallography, circular dichroism, ligand-binding studies and kinetic characterization, as most of them are difficult to perform in the native membrane. For this reason, it is important to stabilize the hydrophobic transmembrane domain and mimic the lipidic environment, in order to perform *in vitro* studies on IMPs outside their native environment. Several systems have been developed with the most common systems being detergent micelles, bicelles, liposomes and nanolipoprotein particles (Fig. 1.1). Their structural and functional properties are summarized in the following sections.

1.1.1 Detergents

Detergents are amphipathic molecules consisting of a polar head group and a hydrophobic tail. The overall geometry of detergents are conic and due to the hydrophobic effect, they self-assemble into spherical micelles in aqueous solution with the head groups facing the hydrophilic solvent (Fig. 1.1 b). Although the hydrophobic effect drives the aggregation process into micelles, detergents also exist as

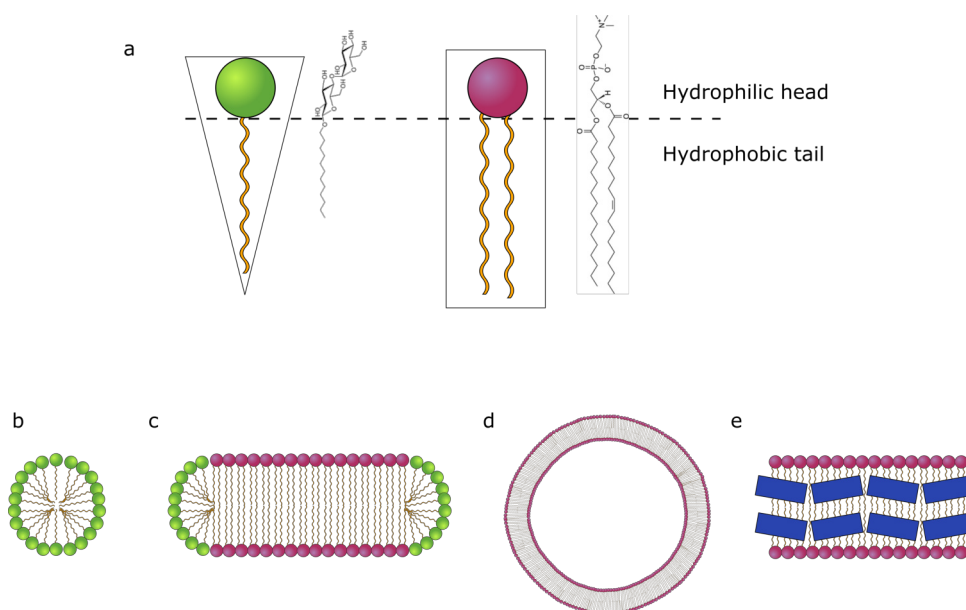


Figure 1.1: Schematic representation different model membranes. (a) Detergents and lipids reveal a different geometrical structure. As detergent show a conical structure they form spherical micelles in solution (b). In contrast, Lipids have a cylindrical structure and assemble to a bilayer (a). Lipids in a complex with detergents like cholate forms bicelles (c). Without detergents lipids they might assemble into large vesicles (d). (a) The lipid bilayer encircled with amphipathic proteins, such as MSP or SapA form discoidal nanolipoprotein complexes.

monomers in solution. The formation of aggregates only begins once the monomer concentration reaches a certain concentration, known as the critical micelle concentration (CMC). The cmc varies between the different detergents and depends on the length of the hydrophobic chain as well as the chemical nature of the headgroup. Detergents can be classified, according to the nature of their headgroup, into ionic, non-ionic, zwitterionic and bile acid salt detergents. Besides the different headgroups many different chain length exists as well, increasing the diversity of detergents. Nevertheless, due to their conic structure detergents form micelles, which do not properly represent the overall geometry of a lipidic bilayer. Thus, many IMPs show reduced activity and stability in detergents [10].

1.1.2 Bicelles

Bilayered micelles, often referred to as bicelles, are a versatile class of model membranes that resemble the natural lipid bilayer more closely than detergents. In this system, a bilayer composed of long-chain lipids is formed which is edge-stabilized by either detergents or short chain lipids [11] (Fig. 1.1 c). Lipids contain two hydrophobic chains and the overall geometry is cylindrical. Therefore, they form a bilayer structure, which is surrounded by micelle forming detergents or short chain

lipids. This discoidal lipid-detergent assembly represent an intermediate morphology between lipid vesicles (liposomes) and detergent micelles [11]. Incorporated into bicelles membrane proteins are surrounded by a bilayer which more closely resembles the the natural membrane environment. It could be shown that the diacylglycerol kinase (DAGK) is more active in bicelles than in detergents alone [12], emphasizing the importance of a lipid environment for the functionality of membrane proteins. Bicelles were originally developed for solid state NMR [13] but were successfully used for crystallization of membrane proteins in a more native-like environment [14, 15].

1.1.3 Lipid vesicles

Lipid vesicles are large spherical structures formed by lipid bilayer. This structure results in a hydrophilic inner compartment which is separated from the outer aqueous solution by the surrounding bilayer (Fig. 1.1 d). Vesicles offer a native-like environment as well as compartmentalization which is a powerful tool for transport studies through the membrane performed by, for example ion pumps or channels [16, 17]. The size of vesicles can be easily controlled and reconstitution of membrane proteins into these systems are well established [18], making it a versatile tool for functional studies of membrane proteins.

1.1.4 Nanolipoprotein particles

Another model membrane system are nanolipoprotein particles which are composed of a lipid bilayer which is stabilized by a surrounding amphipatic protein (i. e. membrane scaffold protein or saposinA) (Fig. 1.1 e) [19, 20].

Phospholipid bilayer nanodiscs were developed in the past decade and are a promising new platform for the studies of IMPs. Originally, the scaffold protein used in this technique derived from the apolipoprotein A (apo-A1) which is known to form high-density lipoproteins (HDL) particles in the cells [21, 22]. Further biological engineering of the apo-A1 protein of members of the Sligar lab resulted in the formation discoidal homogenous lipoprotein particles [23]. The optimized apo-A1 is usually referred to "membrane scaffold protein" (MSP1D1) in the literature. Apo-A1 contains a globular domain at the N-terminus followed by ten amphipatic helices which are crucial for lipid binding. The globular domain together with the first 11 amino acids of helix 1 were removed from the apo-A1 [23]. Instead, a His-tag tag with a tobacco etch virus (TEV) protease cleavage site was introduced to facilitate the purification of the protein. Assembled MSP1D1 nanodiscs consist of a lipid bilayer and two MSP1D1 molecules bind to the hydrophobic part of the lipids in order to stabilize the complex and keep the whole complex soluble. Usually an assembled MSP1D1 nanodiscs consists of about 90 -120 phospholipids [23]. This number might

vary with different types of lipids[23, 24]. The size of the formed nanodiscs can be adjusted by repeating several helices of the MSP1D1, which extends the size of the MSP molecule and, therefore, the size of the nanodiscs. The nanodisc system was successfully used to reconstitute a variety of membrane proteins and perform functional studies in a native-like environment under defined experimental conditions [25–28]. Since the size of the nanodiscs can be precisely controlled by varying the length of MSP it is possible to selectively reconstitute either monomers or oligomers of the target IMP [23, 29].

1.1. Overview of model membrane systems for the study of membrane proteins

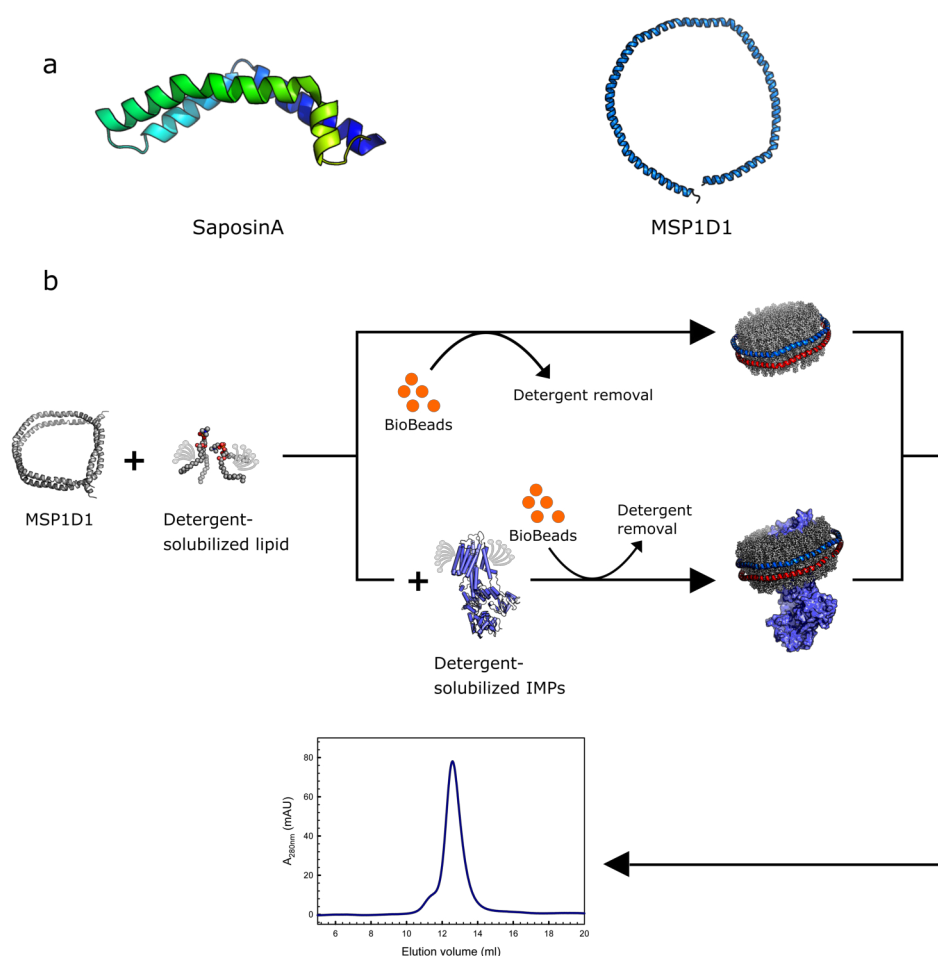


Figure 1.2: Schematic representation of the assembly process of nanodiscs. (a) Cartoon representation of saposinA (pdb: 4ddj) compared to MSP1D1 (pdb: 6clz) showing the size differences. (b) Representation of the nanodiscs assembly process. Detergent-solubilized lipids and MSP molecules are mixed together. Nanodiscs are formed in a self-assembly process once detergents are removed. To incorporate membrane proteins into nanodiscs, they were added to the lipid-MSP mixture before detergent removal. If the IMP:MSP:lipid ratio is right, stable monodisperse nanodiscs are formed and can be purified on a size-exclusion column using buffer without detergents.

The assembly of nanodiscs follows a so called direct-self-assembly process [24], which is a two-step process. First, the phospholipids are solubilized in detergents to form a mixed lipid-detergent micelles. Second, the lipids are transformed into a lipid bilayer by detergent removal. The transition of the detergent from a spherical to a planar bilayer geometry is driven by the hydrophobic effect and the formed bilayer is subsequently stabilized by the surrounding MSP molecules [30]. At an optimized molar MSP:lipid ratio, the MSP molecules covers the whole hydrophobic area of the bilayer and thus stable nanodiscs can form (Fig. 1.2 b).

Recently, another lipid carrier has been developed, the saposin nanoparticles (Sap-NPs) [19]. Similar to MSP nanodiscs, SapNP form disc shaped lipid bilayers, surrounded by saposinA (SapA), an amphipathic lipid binding protein [19, 31, 32]. SapA is further stabilized by a disulfide bond, forming a rigid lipid-binding molecule. Due to the smaller size of SapA (8 kDa) compared to MSP1D1 (22 kDa) (Fig. 1.2 a), several saposin molecules are needed to form a disc shaped nanoparticle. Similar to MSP nanodiscs membrane proteins can be stabilized in a lipid bilayer and it is likely that the assembly follows a comparable mechanism [19]. In contrast to MSP nanodiscs, saposin nanoparticle are formed by several saposinA molecules, which increase the degree of freedom during the assembly process. This in turn enables the SapNP to form different sizes of particles without the need of changing the size of the saposin construct. Therefore, the SapNP can easily adapt to different size of integral membrane proteins.

Chapter 2

Structural studies of membrane proteins using small-angle scattering techniques

2.1 Basic concept of small-angle scattering

Probing conformational changes of biological macromolecules, complexes and assemblies in different environments has become an important aspect in modern systems structural biology. Methods for high-resolution structure determination like X-ray crystallography, NMR spectroscopy and cryo electron microscopy (cryo-EM) provide atomic details of biological macromolecules. However, structural analysis of large conformational changes and complex formation or oligomerization becomes increasingly difficult to analyse using these techniques. Small-angle scattering techniques (SAS) have become a powerful alternative to study dynamic processes in proteins [33–35]. The method analyses macromolecular samples directly in solution and can be applied to a vast array of different sample environments [36–39]. The particles are randomly distributed in solution and the rotational averaging of the molecules limits the resolution of SAS but it enables the dynamical structural characterization. Moreover, global structural parameters like the radius of gyration (R_g), the maximal particle dimension (D_{max}) and the distribution of distances within a particle can be extracted directly from the experimental data [40].

In the following chapters, small-angle scattering using either X-ray photons (SAXS) or neutrons (SANS) were applied to study membrane proteins incorporated into nanodiscs. Even though, the interaction of X-rays or neutrons with matter is rather different, the theory and the interpretation of the data is essentially similar. Therefore, the theory described below applies to both, SAXS and SANS.

Figure 2.1 shows a typically setup for a small-angle scattering (SAS) experiment of biological macromolecules. After the collimation section the beam illuminates the macromolecule in solution, which is usually placed in a quartz capillary (SAXS) or quartz cuvette (SANS). When the X-ray photons or the neutrons pass the sample a small portion will be scattered by the sample. The scattered particles are recorded on a 2D position sensitive detector. In an X-ray scattering experiment the X-ray photons are scattered by electrons, whereas in neutron scattering, neutrons are primarily

scattered by the atomic nuclei of the sample. Since macromolecules in solution are randomly oriented, the resulting scattering pattern is centrosymmetric and the intensities at each angle can be radially averaged. The yielding a scattering intensity can be plotted as a function of the scattering angle 2θ . The wavelength dependent scattering angle 2θ can be converted into the wavelength independent scattering vector

$$q = \frac{4\pi\sin\theta}{\lambda} \quad (2.1)$$

where 2θ is the angle between the scattered beam and the incident beam (Fig. 2.1), and λ is the wavelength of the incident radiation [41].

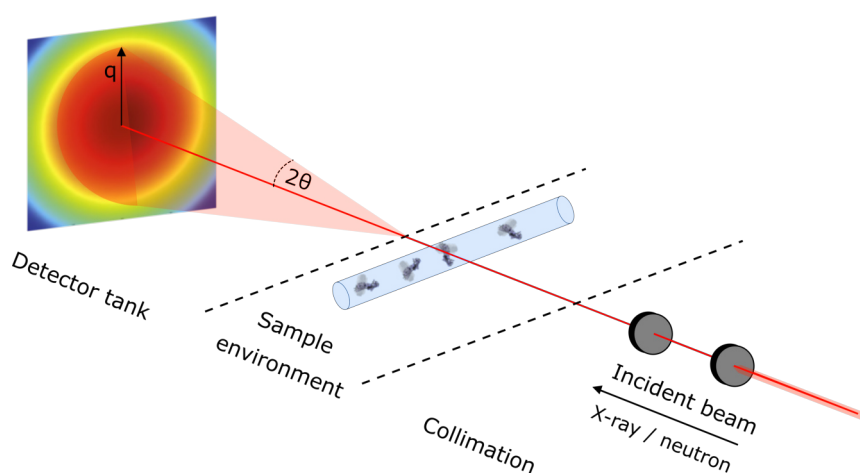


Figure 2.1: Schematic representation of a small-angle scattering experimental set up. A highly collimated X-ray or neutron beam illuminates the macromolecule in solution and the scattered radiation is detected on a 2D detector.

The main objective of SAS experiments is the low-resolution structural analysis of macromolecules in solution. For coherent scattering the resulting scattering pattern is related to the size and the shape of the investigated sample. If a sample contains n randomly oriented particles the relationship of the angular-dependent scattering intensity I to the structure of the macromolecule in solution can be expressed as follows:

$$I(q) = S(q) \sum_i^n [(\Delta p_i V_i)^2 P_i(q)] \quad (2.2)$$

where $I(q)$ is the scattering intensity at certain angle (q), $S(q)$ is the structure factor, $P_i(q)$ is the form factor, Δp_i is the contrast and V_i is the volume of each particle. Equation 2.2 shows that the scattering intensity is a sum of the scattering of each individual particle, i , in the measured sample and is proportional to aforementioned factors.

The measured scattering intensity consists of scattering from the molecule of interest and the surrounding solvent. By subtracting the scattering intensity of the solvent from that of the sample, the resulting scattering intensity derives only from the

molecule of interest. These differences in scattering-length density (SLD) between the molecule of interest and the solvent is defined as the contrast, $\Delta\rho$. In a SAXS experiment the contrast depends on the difference between the averaged electron density of the particle of interest and that of the solvent. The X-ray scattering length is proportional to the number electrons in the atom and the measured scattering intensity is therefore a difference in electron density. The contrast in a neutron scattering experiment is discussed in detail in section 2.1.2.

The structure factor ($S(q)$) encodes information which are related to interparticle distances. In an ideal, stable, homogeneous and diluted sample the contribution from interparticle interactions become negligible and $S(q) = 1$. In this case, equation 2.2 can be simplified to

$$I(q) = N(\Delta\rho V)^2 P(q) \quad (2.3)$$

with N describing the number density of homogeneous particles in the sample. This means, that under non-interacting conditions the magnitude of $I(q)$ only depends on the particle concentration, the volume (V), the contrast ($\Delta\rho$) and the form factor ($P(q)$). The form factor ($P(q)$) describes the overall structural information of the particles and is, therefore the most interesting to the structural biologist. Since all atoms in the measured solution contribute to the scattering signal, the solvent scattering contributions needs to be accurately subtracted from the sample scattering in order to calculate a reliable $P(q)$ from the macromolecule.

2.1.1 Model free size parameter

2.1.1.1 Pair-distance distribution function

The scattering intensity profile contains the overall structural information in the reciprocal space. This information is related to the probable real-space distance distribution ($p(r)$) within a molecule by a Fourier transform. The $p(r)$ function describes the probable frequency of intraparticle distances and defines the maximal particle dimension (D_{\max}). Hence, this function provides information about the shape of the molecule as well as its the volume [42].

Since $I(q)$ can only be measured over a finite q -range, the $p(r)$ function is calculated by an indirect Fourier transform method [43]. This method depends on several assumptions: (i) $p(r)$ is zero at $r = 0$ and at the maximal particle dimension (D_{\max}) and (ii) the proposed $p(r)$ function should be smooth.

2.1.1.2 Size determination

Two parameters can be directly determined from the experimental scattering data; the radius of gyration (R_g) and the forward scattering intensity at zero angle ($I(0)$). The R_g is the radial distance (root-mean squared distance) from the center of mass

of the macromolecule. For particles with homogenous contrast the R_g provides information on the size and mass distribution within a particle. For example, objects that have the same volume but differ in shape have different R_g values [44].

The scattering intensity at an angle of zero ($\theta = 0$), $I(0)$, represents the sum of all correlated distances weighted by the contrast squared. The $I(0)$ is proportional to the squared volume of the macromolecule, the number of scattering particles (N) and the contrast ($\Delta\rho$) and can be expressed as follows:

$$I(0) = N(\Delta\rho V)^2 \quad (2.4)$$

Due to technical restrictions the $I(0)$ cannot be measured directly but it is determined by extrapolation to zero angles [45]. The $I(0)$ can be related to the molecular weight of the particle by normalizing it to $I(0)$ values of molecules with defined size and concentration. Both values, the R_g and $I(0)$ can be calculated from the Guinier approximation

$$I(q) = I(0)e^{-\frac{q^2 R_g^2}{3}} \quad (2.5)$$

A plot of $\ln I(q)$ versus q^2 yields a linear fit in the low- q range and the slope of the fit yields the R_g , whereas the $I(0)$ is calculated from the y-intercept [46].

2.1.2 SANS contrast variation

X-ray scattering derives from the interaction of X-rays with electrons, while neutrons interact with the nuclei of an atom. The X-ray scattering length is, therefore, dependent on the number of electrons of an atom. In contrast, the neutron scattering length varies non-systematically and, is isotope dependent [47]. Examples of neutron scattering lengths of elements frequently found in proteins and lipids are shown in Table 2.1.

Table 2.1: Neutron scattering lengths of the most abundant elements found in proteins and lipids.

Element	Scattering length ($(\sum b / 10^{-5} \text{ \AA})$)
Hydrogen	-3.74
Deuterium	6.671
Carbon	6.646
Nitrogen	9.36
Oxygen	5.803
Phosphorus	5.13
Sulfur	2.847

Notably, the values of the scattering length can be either positive or negative. By definition, isotopes have a positive neutron scattering if the scattered neutrons show

a phase inversion proportionally to the incident beam [48–50]. Together with deuterium (^2H), the most commonly occurring biological isotopes have a positive scattering length density. In contrast, in the case for hydrogens (^1H) this phase inversion does not occur, resulting in a negative neutron scattering length. In a solution containing both isotopes, ^1H and ^2H , neutrons scattered from ^1H are 180° out of phase with scattered neutrons from ^2H [50].

The contrast ($\Delta\rho$) in a neutron scattering experiment is defined as the difference between the summed coherent scattering length of a macromolecule (per unit volume) compared with that of the solvent. Due to the vast different neutron scattering length of ^1H and ^2H the contrast ($\Delta\rho$) can be manipulated by varying the $^1\text{H} : ^2\text{H}$ ratio of the solvent (by substitution with ^2H) [50]. At a certain ratio of $^1\text{H}_2\text{O} : ^2\text{H}_2\text{O}$ in the solvent the neutron scattering length density of the macromolecule equals that of the solvent. After buffer subtraction the contrast would be zero ($\Delta\rho = 0$) and effectively no net coherent scattering will be obtained from the macromolecule. At this point, the macromolecule does not contribute to the scattering signal and is rendered "neutron invisible". This point is defined as the "contrast match point" [51]. The match point of a particular macromolecule depends on the averaged ^1H concentration within the molecule. Consequently, each class of macromolecules have a match point at a different percentage of ^2H in the solvent. This effect is exploited in studies on macromolecular complexes composed of molecules of different classes, typically protein-DNA or protein-lipid complexes [51]. In these experiments, individual components can be matched out and the conformation of the other components can be characterized separately. This can greatly simplify data analysis of small-angle scattering data on complex systems [51].

2.2 Small-angle scattering of membrane proteins

The improvement of synchrotron radiation and neutron sources have been reduced the required amounts of samples to about 10-20 μl in a range of few mg/ml protein concentration for SAXS and to 100-300 μl at the similar protein concentration for SANS [45, 52]. This low sample consumption enables the analysis of membrane proteins by small-angle scattering, since the yield of IMPs during purification lie in the range of the required amount for data collection [53, 54].

Detergents are the most common approach for stabilizing membrane proteins during the purification process [10, 55]. However, the analysis of detergent-solubilized membrane proteins using small-angle scattering can be difficult. Most membrane proteins are purified in detergent close or above the critical micelle concentration, which results in a mixed population containing membrane protein / detergent micelles as well as pure detergent micelles. The concentration of pure detergent micelles co-purified with the IMPs are difficult to estimate. This makes it difficult to

provide an optimal buffer match for SAS measurements. Therefore, the resulting scattering signal will contain information about membrane protein/ detergent micelle complex and the pure detergent micelles. Both of these populations have to be taken into account during structural analysis. Amphipols are amphipatic polymers which can be used to stabilize membrane proteins in solution. Due to their much lower CMC, the amount of free amphipols are greatly reduced. This property is beneficial for background subtraction as no or only minor amounts of amphipols in the buffer are present. Nevertheless, in some cases the amphipol environment can significantly reduce the activity of IMPs [56, 57].

To overcome this effect, IMPs can be reconstituted into liposomes. In this native-like environment, the functional activity of the IMP can be restored. However, the molecular mass of the liposomes are much higher compared to the membrane protein. Consequently, the scattering signal originating from the liposomes will be much stronger than that derived from the IMP, making structural analysis challenging. Bicelles might be a compromise between detergent micelles and liposomes, as they are much smaller. This produces disc shaped lipid bilayer with the long chain lipids in the center surrounded by the short chain lipids. Membrane proteins have been incorporated into bicelles and successfully used for structure determination of IMPs [11, 14, 15]. However, due to the large structural dispersity of bicelles, analysis of SAS data of an IMP can be challenging.

The negative effect of the size dispersity can be overcome by using Nanolipoprotein particles (NLP). NLPs form disc shaped particles like bicelles. Due to the surrounding amphipatic protein molecules (MSP or Saposin) the diameter of the discs can be precisely controlled. As shown in section 3, assembly of these lipid carrier systems yield a highly homogenous sample, which are well suited for structural studies using SAS. The controlled disc size enables the control of the oligomeric states of the membrane proteins as well. The membrane proteins incorporated into these lipid carriers generally show an increased activity, indicating the importance for a more native-like lipid environment [58, 59]. The lipid environment together with the homogenous disc make the nano lipidprotein particles an ideal candidate for SAS studies of membrane proteins in solution.

2.2.1 Stealth-carrier nanodiscs for small-angle scattering experiments

The major advantage of SANS in the study of biological macromolecules is the possibility to alter the contrast by changing the solvent from ^1H to ^2H . This makes it possible to reach the match point at which the scattering length of the molecule matches that of the solvent background, making it "neutron invisible". The required ^2H concentration to reach the match point depends on the ^1H concentration within the macromolecule and, therefore, depends on the chemical background of the molecule. Nanodiscs are a promising tool for studying membrane proteins in native-like lipid

environment using small-angle scattering. However, the large signal contribution of the nanodiscs makes data analysis and structural characterization of the incorporated IMP extremely challenging [60]. The use of contrast variation in a SANS experiment makes it possible to match out different parts of the nanodiscs. However, the lipid carrier consists of a phospholipid bilayer which is encircled by two membrane scaffold proteins and both components are of different chemical nature with different match points, making it impossible to match out both components at the same ^2H concentration. By altering the ^1H concentration within a molecule, the scattering length density of the specific molecule can be modified, which in turn changes the match point of the molecule. By perdeuteration of both components the match point of both molecules can be specifically adjusted to become neutron invisible at the same ^2H concentration in the solvent. Maric *et al.* described the production of selectively deuterated nanodiscs which are effectively neutron invisible at 100 % ^2H [61]. In order to produce perdeuterated phosphatidylcholine lipids with a matchpoint at 100 % ^2H , a genetically modified *E. coli* strain was employed to yield a deuteration level of 78 % in the headgroup and 92 % in the acyl chain of the phospholipids [62]. The matchpoint of MSP was adjusted by introducing ^2H into 70 % of the non-exchangeable hydrogen positions during the recombinant expression in *E. coli* by using deuterated growth media [61].

Due to the large incoherent neutron scattering cross-section of ^1H , the use of $^1\text{H}_2\text{O}$ in biological SANS experiments increases the background signal resulting in the decrease of the coherent scattering signal of the sample. In order to increase the signal-to-noise ratio SANS experiments are typically performed in 100 % D_2O . Selective deuteration of the nanodisc components are, therefore, designed to obtain a match point at 100 % D_2O . In a first SANS study, Maric *et al.* showed that both deuterated nanodisc components are effectively matched out at 100 % $^2\text{H}_2\text{O}$, resulting in a minimal SANS scattering [61]. The use of this "stealth carrier nanodiscs" enables the structural characterization of IMPs embedded in native-like environment without the contribution of the lipid carrier to the scattering signal (Fig. 2.2).

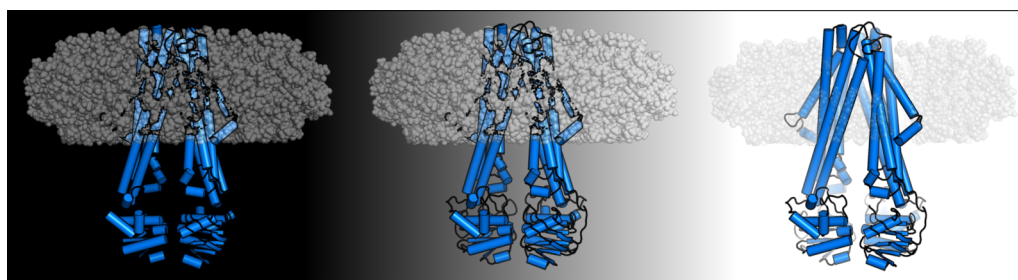


Figure 2.2: Schematic representation of SANS studies of a membrane protein in stealth nanodisc. A membrane protein incorporated into stealth nanodisc in buffer solution with increasing $^2\text{H}_2\text{O}$ (decreasing greyscale). Deuterated nanodisc components (shown in grey) do not contribute to the scattering signal at $100\ ^2\text{H}_2\text{O}$ (right structure) and only the membrane protein (blue cartoon model) can be "seen" in the point of view of neutrons. Figure adapted from Maric et al. [61].

Aim of the thesis

The aim of this study focusses on the characterization of different intergral membrane proteins in a native-like lipid environment. The surrounding lipidic bilayer can be crucial for the function and dynamics of membrane proteins [10, 63]. Hence, the need for lipid carrier for *in vitro* studies on membrane proteins has raised. Nanodiscs provide a lipid bilayer of a defined size which is able to stabilize IMPs in aqueous solutions and is, therefore, well suited for functional studies. Since the size of the nanodisc is well defined, this carrier system enables structural characterization of IMPs using small-angle scattering (SAS), which is a powerful technique to analyse large conformational changes.

The results of this thesis are subdivided into two parts (II + III). In the first chapter of Part II the differences between the two main lipid carrier should be explored. Both carriers provide a lipid bilayer, which is either surrounded by a membrane scaffold protein (MSP, nanodiscs) or the lipid-binding protein SapA (Saposin nanoparticles, SapNP). These two proteins bind differently to the lipid bilayer [64, 65]. MSP contains 11 amphipathic α -helices which wrap around one bilayer leaflet in a belt-like shape. In contrast, SapA is a much smaller protein containing only two amphipathic α -helices, which are stabilized by a disulfid bond, forming a very rigid molecule [66]. Several SapA monomers are needed in order to form a saposin nanoparticle (SapNP). Due to the structural differences of both carrier systems, the first part intended to systematically compare both lipid carriers in terms of long-term-stability and homogeneity, as these two parameters are crucial for studies on membrane proteins incorporated into one of these systems.

The second chapter of the first part focusses on the activation mechanism of the plasma-membrane Ca^{2+} -ATPase (PMCA), ACA8. PMCAs are located in the plasma-membrane and extrude calcium ions (Ca^{2+}) from the cytosol. They are of major physiological relevance and are, therefore, tightly regulated. At low Ca^{2+} concentrations in the cytosol, these pumps are autoinhibited, which is facilitated by an intrinsical domain, the regulatory domain (RD). The ubiquitous Ca^{2+} sensor protein calmodulin (CaM) is one of the major activators of PMCAs and the binding of CaM to the regulatory domain activates the pump. Previous studies on the regulatory domain suggested a more complex bimodular activation mechanism [67]. However, the structural basis of this activation process remains to be investigated. In order to characterize the activation process the different binding events during the activation

of ACA8 are investigated by using fluorescence polarization and native mass spectrometry. Moreover, the effect of lipids on the activation and overall activity should be characterized by incorporation of ACA8 into nanodiscs. The nanodiscs enabled to vary the lipid content in a controlled manner. Due to the defined size of the nanodiscs it should be able to analyse the structural changes using small-angle X-ray scattering (SAXS).

The second part of this thesis aims to investigate conformational changes of membrane proteins in nanodiscs using small-angle neutron scattering (SANS). The main advantage of using SANS is the possibility of specifically varying the contrast of different components within a macromolecular complex. The recently described stealth carrier nanodiscs (sND) are composed of selectively deuterated MSP molecules and phosphatidylcholine lipids, which does not contribute to the SANS scattering signal. The use of these discs enables the investigation of membrane proteins in a lipidic environment, without taking the discs components into account. In a first experiment the suitability of the stealth nanodiscs should be probed on a test case. The bacterial ABC-transporter MsbA is a well expressed and very stable membrane protein. The structure of MsbA is well characterized in different conformational states. These differences are expected to be big enough to be detected by SANS. In a second experiments the stealth carrier nanodiscs/ SANS method should be applied to ACA8 in order to further characterize the activation process. Due to the lack of structural models of full-length PMCAs in the activated state this result might provide important information on the structural basis of the activation process of this pump.

Part II

Biochemical and biophysical studies on integral membrane proteins in lipidic carrier systems

Chapter 3

Comparison of lipidic carrier systems

Results of comparative studies shown in this chapter were mainly obtained during a master thesis from Dominique-Maurice Kehlenbeck under my supervision.

3.1 Introduction

The most common approach for studying integral membrane proteins in solution is the use of detergent micelles [68]. Detergents are amphipatic molecules consisting of a polar headgroup and a hydrophobic chain. Above the cmc they spontaneously form spherical micellar structures in aqueous solutions. The hydrophobic chains of detergents are capable of binding to the transmembrane part of membrane proteins and thereby mimic the hydrophobic environment of the lipid bilayer [69–71]. Nevertheless, they often show adverse effects on the stability, activity and function of IMPs [10, 71–73]. IMPs often require specific lipids for their activity [74]. Due to the dissociation properties of detergents important lipids might be washed off from the membrane protein in a process called delipidation [75], which in turn might lead to a decreased activity.

To overcome the problems associated with the use of detergents several nanolipoprotein particles (NLP) have been evolved. Nanodiscs, as one of the developed NLPs, are discoidal protein-lipid complexes that consist of two "membrane scaffold proteins" (MSPs), which encircle a lipid bilayer due to their amphipatic nature (see Chapter 1.1.4) [20, 76]. Due to the length of the MSP molecule the size of the nanodisc is precisely defined and the lipids inside the formed complex are stable and soluble in aqueous solutions. Membrane proteins can be incorporated into nanodiscs, which offers the possibility to render a membrane protein soluble in a detergent free aqueous solution, whilst incorporated into a lipidic environment. Using these particles diverse structural studies of integral membrane proteins in a native-like lipid environment are possible, like in cryo-electron microscopy [77], NMR [78] or X-ray and neutron scattering [79, 80]. It has been shown that many membrane proteins incorporated into nanodiscs possess a higher activity [63], suggesting the importance of surrounding lipids for their function.

Recently, a new lipid carrier system has been described, which uses of the lipid binding protein saposin (SapA) [19, 81]. In the presence of lipids these saposin molecules form disc-shaped particles (saposin-like nanoparticles, SapNPs) comparable to nanodiscs, which have been successfully used to incorporate membrane proteins [81, 82]. In contrast to nanodisc, SapNPs can be formed with varied numbers of saposin molecules to adjust the size of the assembled disc, which enables the incorporation of membrane protein assemblies of various sizes. Flayhan *et al.* [82] have characterized the SapNPs and demonstrated their advantage over IMPs in detergent. In this chapter both lipid carrier systems were systematically compared with respect to long-term stability, thermal stability and homogeneity.

3.2 Material and methods

3.2.1 Expression and purification of MSP1D1

For expression of MSP1D1 a pET28a plasmid harbouring the gene for MSP1D1 was transformed in *E. coli* BL21 (DE3) cells and incubated on LB plates supplemented with kanamycin ((25 µg/ml)). A single colony was used to inoculate 10 ml preculture with terrific broth (TB) media, which was grown for approx. 16 h at 37 °C. The expression culture (TB media) was inoculated with an OD₆₀₀ of 0.05 and grown at 37 °C. At an OD₆₀₀ of 1.5 the protein expression was induced by adding 1 mM IPTG and cells were further grown for 4 h at 37 °C. Cell paste was collected by centrifugation at 3000 x g for 25 min.

Protein purification was carried out according to a modified protocol established by Sligar and co-workers [83]. Cells were resuspended in lysis buffer containing 50 mM Tris pH 8.0, 500 mM NaCl, which was supplemented with 1 % (v/v) Triton X-100, 0.5 ml Lysozyme (100 mg/ml) (*Gallus gallus*, Sigma-Aldrich) and DNase (1 mg/ml) and broken using sonication. The lysate was cleared by centrifugation at 40,000 x g for 45 min and the supernatant containing MSP1D1 was loaded on a HisTrap column. Subsequently the column with bound MSP1D1 was washed with ten column volumes (cv) of lysis buffer each containing 1 % Triton X-100 and 50 mM cholate, respectively, to wash off bound endogenous lipids. Unspecifically bound proteins were eluted with lysis buffer containing 25 mM imidazol and MSP1D1 was eluted with 500 mM imidazol. Fractions containing MSP1D1 were pooled and incubated with TEV protease overnight to cleave off the His₆-tag. During the incubation with TEV protease the buffer was exchanged to 30 mM Tris pH 8.0 and 150 mM NaCl. To remove the protease and the cleaved His₆-tag a second IMAC chromatography step was applied. MSP1D1 without His₆-tag was concentrated up to 400 µM and stored at -80 °C until further use.

3.2.2 Expression and purification of SapA

Sapoin A (SapA) was expressed with an N-terminal His₆-tag and a TEV protease cleavage site. For expression SapA in pNIC28-Bsa4 vector was transformed into *E. coli* Rosetta-gami 2 cells. Freshly transformed cells were used to inoculate 10 ml preculture with TB media. Subsequently, the preculture was used to inoculate the expression culture (as well in TB media) and cells were grown at 37 °C until an OD₆₀₀ of 1 - 1.5. By adding 0.1 mM IPTG (final concentration) the expression of SapA was induced and cells were grown at 20 °C overnight (approx. 16 h). Cells were harvested by centrifugation at 3000 x g for 25 min and resuspended in lysis buffer (20 mM Na-phosphate, 300 mM NaCl, 15 mM imidazole, 5 % (v/v) glycerol). The

lysate was supplemented with 0.5 ml lysozyme (100 mg/ml) (*Gallus gallus*, Sigma-Aldrich) and DNase (1 mg/ml) and cells were broken by sonication. Subsequently, lysate was incubated at 70 °C for 20 min, which leads to an enrichment of the thermostable SapA. The lysate was cleared by centrifugation at 16,000 x g for 20 min and SapA in the supernatant was bound to an IMAC column. After washing the column with 10 column volume of lysis buffer with 30 mM imidazole SapA was eluted with 400 mM imidazole. Elution fractions containing SapA were pooled and incubated with TEV protease over night. A second IMAC column was applied to remove the His₆-tag and the TEV protease. Pure SapA was further purified on a Superdex75 size exclusion column and the fractions corresponding to monomeric SapA were pooled and concentrated. The pure SapA sample were stored at -80 °C in buffer containing 20 mM phosphate pH 7.4, 300 mM NaCl, 5% glycerol and 2 mM DTT

3.2.3 Preparation of nanodiscs and saposin nanoparticles

In order to compare the effect of different headgroups as well as different chain length following lipids were tested: (1) POPC, (2) POPG, (3) DOPC and (4) DMPC. Lipid powder was resuspended in buffer containing 30 mM Tris pH 7.5, 150 mM NaCl, 1 mM β -mercaptoethanol and 100 mM cholate to a final lipid concentration of 50 mM. Lipid suspension was solubilised using freeze-thaw cycles until the solution became clear. For the assembly of "empty" nanodiscs MSP1D1 were mixed with lipids in a molar ratio of 1:30 (protein:lipid) and for assembly of "empty" SapNPs SapA was mixed with lipids in a molar ratio of 1:12. To reconstitute MsbA into MSP nanodisc DDM-purified MsbA was mixed with MSP1D1 and corresponding lipids in a ratio of 1:1:25 (MsbA:MSP1D1:lipid). For reconstitution of MsbA into SapNPs MsbA (in DDM), SapA and lipids in a ratio of 1:4:20 were mixed. All assembly mixes were supplemented with cholate to ensure a final cholate concentration of 20 mM. After a pre-incubation time of 45 min the assembly reaction was initiated by adding 0.8 g/ml biobeads to the solution. Reactions were incubated overnight (approx. 16 h) at 4 °C under constant agitation. Assembly reactions were further purified on a Superdex200 column (GE Healthcare) in a buffer containing 30 mM Tris pH 7.5, 150 mM NaCl and 1 mM β -mercaptoethanol. Fractions containing either empty nanodiscs/SapNPs or nanodiscs/SapNP- embedded MsbA were pooled and concentrated up to 3-8 mg/ml.

3.2.4 Differential scanning fluorimetry using Prometheus

The thermal stability of MsbA in either MSP1D1 nanodiscs or SapNPs was measured using the nDSF differential scanning fluorimeter (Prometheus, NanoTemper Technologies, Munich). The emission spectra as well as the emission intensity of the intrinsic fluorescence of tryptophan residues changes with differences in the

surrounding environment (see Chapter 4.2.7). Once MsbA unfolds intrinsic tryptophanes within MsbA gets solvent exposed and the change in fluorescence was measured, which is an indirect measure of MsbA unfolding. Tryptophanes were excited at 280 nm and fluorescence emission were measured at 330 nm and 350 nm. The first derivative of F350/330 was used to calculate the transition midpoint (T_m), which in turn was used to characterize and compare the thermal stability of MsbA in different lipid carrier systems. 12 μ l of each sample were loaded in a capillary and the fluorescence was measured at a heating rate of 1 $^{\circ}$ C/min. To reduce temperature-dependent pH changes in the buffer, all different MsbA samples were dialysed against buffer containing 20 mM HEPES pH 7.5 and 150 mM NaCl. All experiments were performed as triplicates.

3.2.5 Small-angle X-ray scattering (SAXS)

Homogeneity of both lipid carrier systems was analysed by using small-angle X-ray scattering. All data were acquired using the Bio-SAXS instrument P12 on the storage ring Petra III (DESY, Hamburg, Germany). Assembled "empty" MSP1D1 nanodiscs and saposin nanoparticles (SapNPs) were purified on a Superdex200 column (10/300) using buffer containing 30 mM Tris pH 7.5 and 150 mM NaCl. All peak fractions were concentrated, dialysed and measured individually. SAXS measurements were carried out at 10 $^{\circ}$ C in 30 mM Tris (pH 7.5), 150 mM NaCl, and 0.5 mM TCEP at protein concentrations ranging from 0.5 - 3 mg/ml. The scattering intensity of each fraction was recorded as a function of the scattering vector q with

$$|q| = \frac{4\pi \sin\Theta}{\lambda} \quad (3.1)$$

using a wavelength (λ) of 0.124 nm. The total exposure time was 1s, measured in 20frames each with an exposure time of 50 ms. All samples were normalized, background subtracted. Subsequently, corresponding buffer were subtracted from the normalized scattering intensity using automatic procedures on the beamline [84]. Scattering intensities were calibrated into absolute units (cm^{-1}) using the forward scattering intensity of bovine serum albumin at known concentrations. All data processing was performed using PRIMUS [84]. Different peak fractions were compared using difference plots. Fractions from a size-exclusion run were scaled and subtracted from each other and plotted.

3.3 Results and discussion

3.3.1 Reconstitution of MSP1D1 nanodiscs and SapA nanoparticles

Lipid carrier nanoparticles, such as MSP1D1- based or saposin- based, are formed in a direct self-assembly process [24]. This is a two-step process where the lipids are first dissolved by detergent to form a mixed detergent-lipid micelle and afterwards transformed into a lipid bilayer. The bilayer is stabilized either by the amphipatic MSP1D1 or the lipid-binding protein saposin A. The self-assembly process is started by detergent removal using biobeads. If the lipid to MSP1D1/SapA ratio is correct the majority of formed particles will be stable nanoparticles.

Since, the assembly efficiency of lipid carrier systems is ratio dependent, the optimal MSP1D1/SapA to lipid ratios were screened and analysed on a size-exclusion column (Superde200, 5/150 (for MSP1D1 nanodiscs), 10/300 (for SapA nanoparticles)) (Fig. 3.1). The phosphatidylcholine lipid POPC was used for screening for both lipid carrier systems. POPC has a phase transition temperature of -2 °C and assemblies in the cold at 4 °C, which results in a liquid crystalline phase of the lipids, that is required to successfully assemble nanoparticles. At a MSP1D1 to POPC ratio of 1:30 or 1:50 the chromatogram showed a single peak at around 2.1 ml, which corresponds to stable assembled nanodiscs (Fig. 3.1 a). By increasing the lipid concentration to 1:80 and 1:100 the peak shifts towards lower elution volume, indicating an increase in the hydrodynamic radius. As the lipid concentration is increased more lipids might pack in a nanodisc which results at some point in a partly opening of the MSP1D1 belt around the bilayer, which in turn increases the overall size. The open MSP1D1 belt cannot fully shield the hydrophobic chains which therefore destabilizes the overall nanodisc conformation. This effect is seen in MSP1D1:lipid ratios with even higher POPC concentrations. At a ratio of 1:100 or 1:150 more peaks with a much bigger hydrodynamic radius start to appear and at a ratio of 1:200 most of the MSP1D1 protein elutes at the void volume, indicating that much larger particles are assembled. These results show that a ratio of 1:30 to 1:50 leads to stable and homogenous nanodiscs. This ratio is in good agreement with the published data [85]. Monomeric SapA (ratio 1:0) showed a single peak with an elution volume at 17.6 ml (Fig. 3.1 b). At a ratio of 1:6 (SapA:POPC) the peak intensity at 17.6 ml is significantly decreased and a second peak at 14.7 ml appeared, indicating that saposin nanoparticles (SapNP) started to form. By increasing the SapA:POPC ratio to 1:12 the peak at 14.7 ml shifted further to an elution volume of 14.2 ml. This peak corresponds to SapNP with bigger hydrodynamic radius. Since, no peak at 17.6 ml was visible the result suggests that the assembly efficiency was higher compared to the 1:6 ratio. Increasing the SapA:lipid ratio even further (1:15 or 1:25) resulted in a peakshift, showing that the size of the assembled nanodiscs further increase. Moreover the shape of the peak gets broader, which indicates that the saposin nanoparticles get

more heterogenous with the elution of several sub-populations. Based on the elution profiles the results show that at a SapA:POPC ratio of 1:12 homogenous saposin nanoparticles are formed.

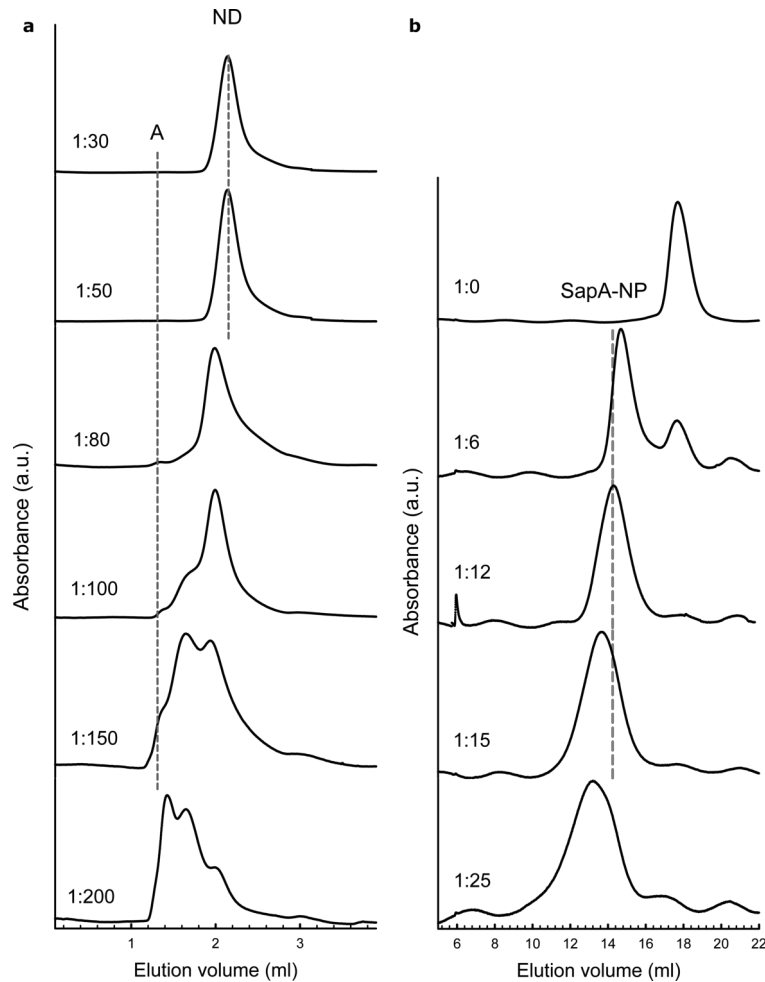


Figure 3.1: Optimization of ratios for nanodisc and SapNP assembly. (a) Size-exclusion chromatography (SEC) profiles of MSP1D1 nanodiscs assemblies at different MSP1D1 to lipid ratios. Samples were analysed on a S200 5/150 column. (b) SEC profiles (Superdex200, 10/300 column) of saposin nanoparticles assembled at different SapA:lipid ratios.

3.3.2 Biophysical properties of nanodiscs and SapA nanoparticles

3.3.2.1 Long-term stability

Lipid carrier systems (MSP nanodiscs or saposin nanoparticles, hereafter denoted as ND or SapNP) are designed to stabilize integral membrane proteins (IMPs) in a native-like lipid environment, as they are surrounded by lipid bilayer [86]. In order to stabilize the incorporated IMP the "empty" NDs or SapNPs need to form a stable complex on their own. In this context, "empty" describes lipid carrier without any IMPs incorporated. However, they are filled with lipids. If these empty NDs or SapNPs are not stable they are not suited to stabilize incorporated IMPs. Therefore, long-term stability tests with both lipid carrier systems have been carried out. The effect of different lipid chain length (14C/16C/18C), saturation state and headgroups (choline and glycerol) were screened by using following lipids: DMPC, DOPC, POPC, POPG (Fig. 3.2) [86].

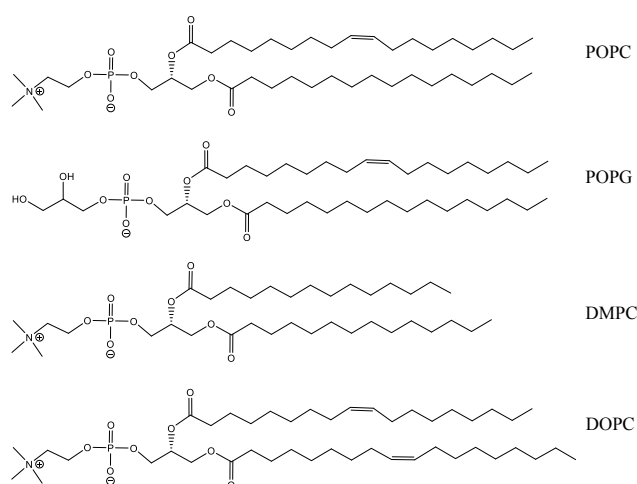


Figure 3.2: Structures of lipids used for studies.

NDs or SapNPs were assembled with the different lipids, purified on a size exclusion column (Superdex200, 10/300) and incubated for up to 70 days at 4 °C. Following ratios were used, which showed the best results in the optimization (see Chapter 3.3.1): (1) 1:30 for MSP1D1 nanodiscs and (2) 1:12 for SapNPs. All samples were analysed after 1 day, 14 days, 36 days and 70 days by loading them on an analytical size-exclusion chromatography column (Superdex200, 10/300). Based on the chromatogram the size, shape and position of the main elution peak were monitored over the time (Fig. 3.3). These parameters were used as indicators for the sample dimension, homogeneity and aggregation state, which in turn gave information about

the general stability of each carrier system in the corresponding lipids [86].

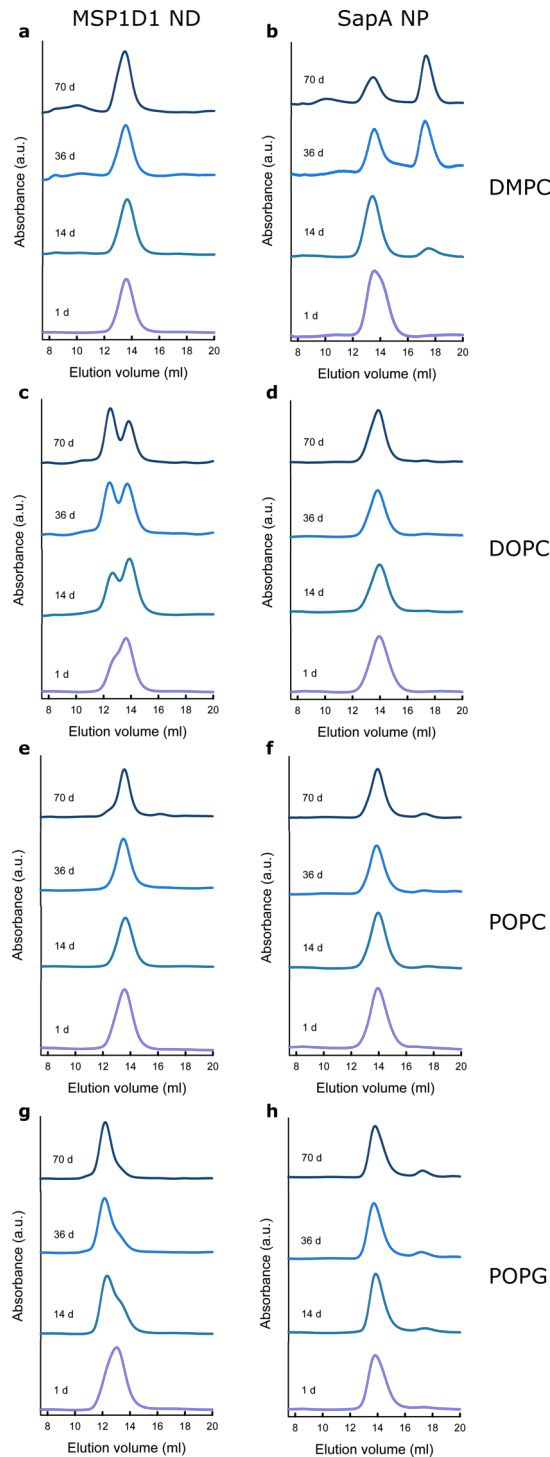


Figure 3.3: Long-term stability of empty MSP1D1 nanodiscs and saposin nanoparticles (SapNP). MSP1D1 nanodiscs (**a, c, e, g**) and saposin nanoparticles (**b, d, f, h**) were assembled in different lipids (DMPC, DOPC, POPC, POPG) and long-term stability was analysed on a Superdex200 (10/300) size-exclusion column after 1d, 14d, 36d, 70d. [86]

MSP1D1 nanodiscs assembled with DMPC, a saturated short-chain (14C) phosphatidylcholine lipid, showed a single peak at 13.8 ml. This elution volume was unchanged over the time course of the 70 days (Fig. 3.3 a). However, the peak intensity was significantly reduced after 70 days (data not shown) [86]. Since, no void peak was visible, the nanodisc is likely aggregated and spun down before loading on the size-exclusion column. SapNP:DMPC particles showed a single peak at 14.2 ml after 1 day, but this peak intensity is significantly reduced over time (Fig. 3.3 b). At the same time a second peak started to appear after 14 days, which corresponds to monomeric SapA, showing that the nanoparticles fall apart. After 70 days most SapA eluted as a monomer and only small amounts still formed nanoparticles. These results showed that both lipid carrier systems did not form stable nanoparticles with DMPC as the lipid [86].

Nanodiscs prepared with the double unsaturated DOPC lipid show already a shoulder in the elution peak after one day. After 14 days the shoulder gets more pronounced and two peaks were clearly visible (Fig. 3.3 c). In contrast, SapNPs formed with DOPC show one peak, which stays unchanged throughout the time course of the experiments (Fig. 3.3 d). Both lipid carrier systems form a very stable complex with POPC, with neither a change in the elution volume nor the shape of the peak (Fig. 3.3 e-f). Nanodisc containing POPG showed a shift in the peak position (Fig. 3.3 g). This might be due to dimerization of the discs caused by a slight opening of the belt protein. In contrast, saposin nanoparticles containing POPG showed no peak shift but after 14 days a small peak at 18 ml appeared (Fig. 3.3 h). This result indicates that small amounts of the formed complex fell apart and, therefore, monomeric SapA appears in the chromatogram [86].

In summary, these results indicated that saposin nanoparticles seem to be more flexible with respect to lipids compared to nanodiscs. SapNPs often tended to dissociate rather than aggregate. In contrast, MSP1D1 nanodiscs often showed more sample heterogeneity as well as aggregation over the time course of these experiments. The differences in the organization of both carrier systems might explain these effects. Several saposin monomers are bound around the lipid bilayer, which increases the degree of freedom making the whole complex more flexible to adapt to different lipid packing. In contrast, two MSP1D1 molecules need to wrap around the bilayer completely in order to form a stable complex. Differences in lipid packing, therefore, need a more precise optimization of the ratios during the assembly. Notably, in all cases where shifts in peak elution volumes appeared the chromatogram after one day already showed indications for sample heterogeneity, suggesting that already the initial assembly did not form a stable complex [86].

3.3.2.2 Thermal stability

In order to test the ability of both lipid carrier systems to stabilize incorporated membrane proteins, the thermal stability of the complex was analysed by differential scanning fluorimetry (nDSF). This method measures changes in the emission spectra of intrinsic tryptophanes once they get solvent exposed due to unfolding of the proteins. Veith *et al.* [87] successfully applied this method to membrane proteins. As a test case the bacterial ABC transporter MsbA was incorporated into both lipid carrier systems containing different lipids (DMPC, DOPC, POPC, POPG). MsbA over-expresses well, is stable and homogenous in DDM micelles and could be successfully incorporated into both carriers (Supplementary Fig. A.10), making it a good test case for comparative studies .

For all tested MsbA-carrier combinations, the nDSF traces showed a clear minimum in first derivative plots of the ratio $F_{350\text{nm}}/F_{330\text{nm}}$, allowing unambiguous assignment of a transition mid-point (T_m) (Fig. 3.4 a). A representative nDSF measurement of MsbA incorporated in POPC-based carrier systems is shown in Figure 3.4a. The T_m of MsbA in MSP1D1 nanodiscs is slightly higher (increase by around 4 °C) compared to MsbA in SapNPs. A comparison of T_m values of MsbA in either nanodiscs or SapNPs containing DOPC and POPG showed a similar trend, with a slightly increased T_m of MsbA in MSP1D1 nanodiscs (Fig. 3.4). In contrast, tests with MsbA in DMPC-SapNP showed a slightly higher T_m compared to MSP1D1 nanodiscs with the same lipid. Empty carrier systems were measured as a control and both showed a significant increase in T_m compared to samples with incorporated MsbA. This result indicates that the measured transition derived from MsbA, due to more tryptophanes in the MsbA sequence. Therefore, the obtained differences in T_m values of MsbA in different lipids derived from the differences in the stability of the lipid carrier systems. Two MSP1D1 molecules are wrapped around the bilayer in belt-shaped manner. In contrast, several saposin monomers are organized around the lipid bilayer, allowing a higher degree of freedom and therefore more flexibility to adapt the size of the nanoparticles. This higher flexibility might result in a lower thermal stability. However, the differences between both carrier are relatively small and whether the structural differences of both carrier systems lead to these differences in thermal stability remains to be investigated. Nevertheless, MsbA was significantly more stable in both carrier systems compared to MsbA in amphipols, which highlights the importance of surrounding lipids for the stability of membrane proteins [86].

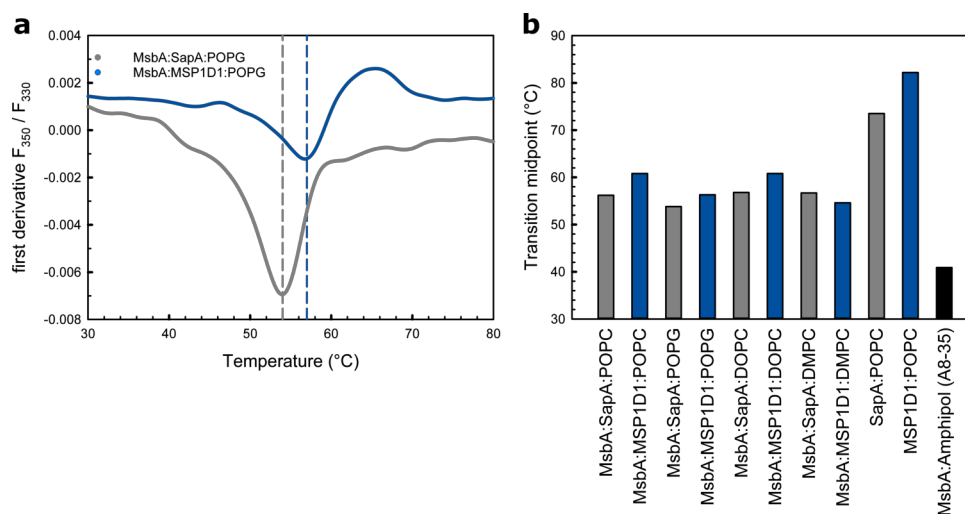


Figure 3.4: nDSF measurements to investigate the thermal stability of MsbA incorporated in different lipid carrier systems. (a) First derivative analysis of MsbA incorporated in MSP1D1 nanodiscs and saposin nanoparticles. The minimum represents the transition temperature (T_m). (b) Bar plot showing melting temperatures (T_m) of MsbA in nanodiscs (blue) and SapNPs (grey) with different lipid as well as T_m values of empty NDs and SapNPs as comparison.

3.3.3 Structural effects of different lipids on nanodiscs and SapA-nanoparticles

3.3.3.1 SAXS-analysis

Previous studies suggested that the small-angle scattering profiles of nanodiscs change with different lipids as well as throughout a size-exclusion peak, indicating structural heterogeneity of the discs [64]. In this chapter, small-angle X-ray scattering (SAXS) was used to characterize the conformational heterogeneity of empty lipid carrier systems, like nanodiscs and saposin nanoparticles. Therefore, MSP1D1 nanodiscs and saposin nanoparticles were assembled with either DOPC, POPC or POPG and purified on a size-exclusion chromatography column (Superdex200, 10/300). Subsequently, each individual fraction was concentrated and analysed individually by SAXS. Small-angle X-ray scattering (SAXS) does not provide high-resolution information but it is a suitable technique to determine flexibility as well as overall conformational changes.

Comparison of overall structural parameters of both carrier systems showed that MSP1D1-based nanodiscs had a significant larger radii of gyration (R_g between 3.9 nm and 4.9 nm) compared to saposin-based nanoparticles (R_g of 3.4 nm for all different lipids) (Table 3.1). The same trend is visible in the maximum particle dimension (D_{max}).

The SAXS profiles of individual fractions (fraction 17 - 21) of MSP1D1:POPC nanodiscs showed a minimum in the mid- q range which is gradually shifted between 0.6 nm^{-1} - 0.8 nm^{-1} throughout the individual peak fractions (Fig. 3.5 a). A similar trend was visible for SapA:POPC nanoparticles, showing a minimal shift between 0.7 nm^{-1}

Table 3.1: Overall structural parameter of empty MSP1D1 nanodiscs and saposin nanoparticles.

	R_g [nm]	D_{max} [nm]
MSP1D1:POPC	4.6	10
MSP1D1:POPG	3.9	9.5
MSP1D1:DOPC	4.9	12
SapA:POPC	3.4	8.4
SapA:POPG	3.4	8.4
SapA:DOPC	3.4	8.5

- 1 nm⁻¹ (Fig. 3.5 b). To visualize and analyse the differences, different plots were calculated for each carrier-lipid combination. For all MSP1D1 nanodiscs a minimum at around 0.4 nm⁻¹ and a maxima at around 0.8 nm⁻¹ was visible (Fig. 3.5 c e, g). In all different SapA nanoparticles the minimum was around 0.6 nm⁻¹ and the maxima at around 1.2 nm⁻¹ (Fig. 3.5 d, g, h). These differences get more pronounced with higher fraction numbers, showing increasing structural differences within the peak fractions. Notably, the intensities of the difference plots were higher for all tested saposin nanoparticles compared to MSP1D1 nanodiscs, indicating that the structural heterogeneity might be more pronounced in SapNPs. Since, saposin nanoparticles are composed of several individual SapA monomers the degree of freedom might be slightly increased. This increase in flexibility might lead to a higher heterogeneity.

Comparing the different plots of MSP1D1 nanodiscs and SapA nanoparticles containing different lipids showed that the differences in scattering profiles are much more pronounced in carrier systems containing POPG. This effect is visible for both carrier systems indicating that the negative net charge of POPG's headgroup might affect the homogeneity of both carrier systems.

In summary, these results illustrate the structural heterogeneity of both lipid carrier systems. This effect is slightly more pronounced in saposin nanoparticles, most likely due to the different organization of the complex of SapA and lipids. Moreover, the structural flexibility makes analysis and modelling of both lipid carrier systems extremely challenging [88].

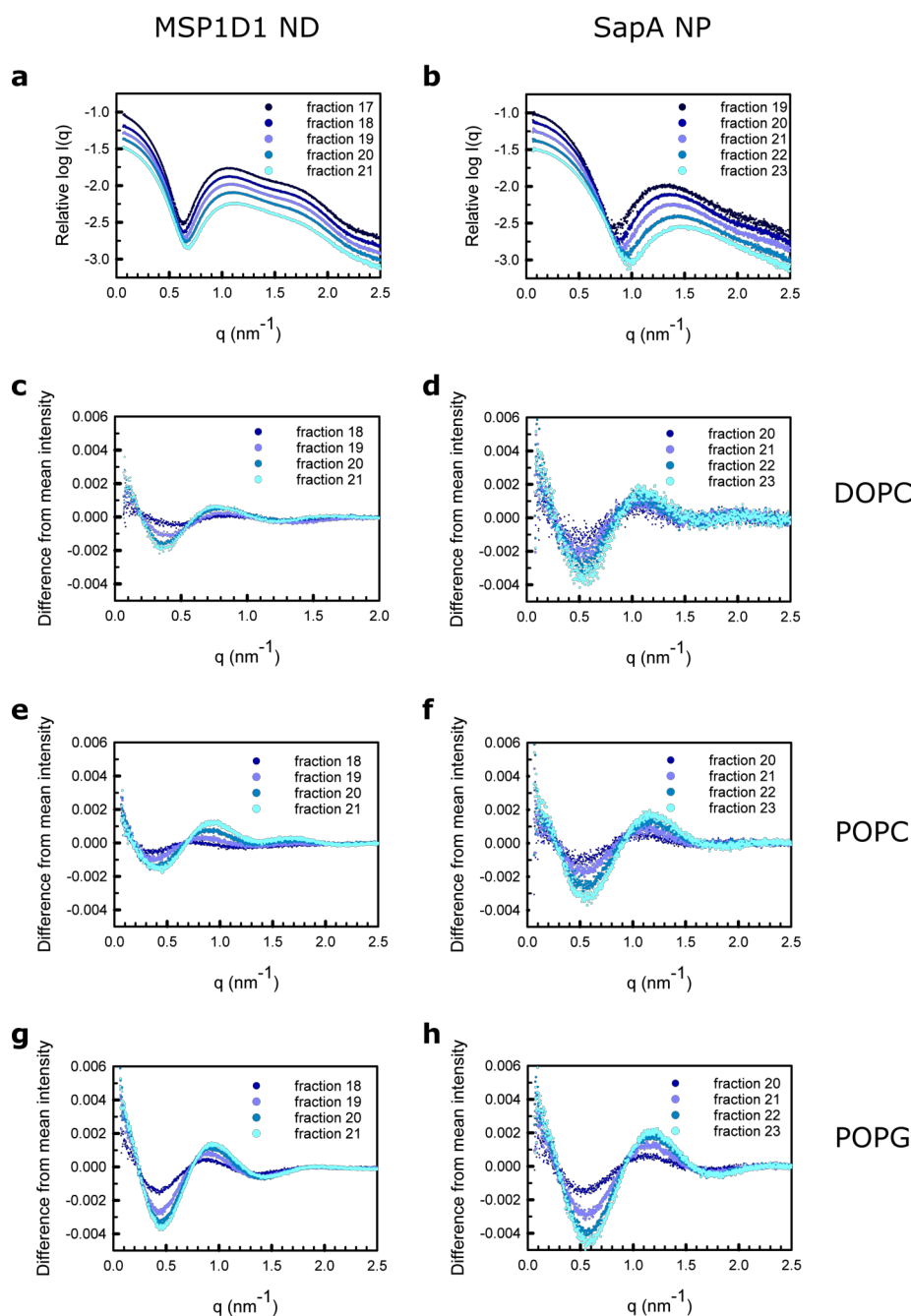


Figure 3.5: Analysis of SEC fractions of empty nanodiscs and SapNPs by small-angle X-ray scattering. Empty MSP1D1 nanodiscs and SapNPs were assembled with DOPC, POPC, POPG and purified on a Superdex200 column (10/300). Fractions of each carrier system - lipid combination were analysed individually by SAXS. (a-b) Semi-log plot showing differences in scattering profiles of MSP1D1:POPC nanodiscs (a) and SapA:POPC nanoparticles (b) throughout the peak fractions. (c-g) Difference plots were calculated for each chromatogram of each lipid carrier system - lipid combination.

3.4 Conclusion

It has been shown that integral membrane proteins (IMPs) often show a reduced activity in detergent compared to those in lipid bilayer [10, 58, 63], which illustrates the need of a lipid carrier system for *in vitro* functional studies of IMPs. MSP- and saposin-based carriers both encircle a lipid bilayer of defined size to keep it soluble in aqueous solution. In MSP nanodiscs the amphipatic membrane scaffold protein wraps around the hydrophobic part of the lipid bilayer, forming a rather rigid scaffold system with defined size. In contrast, several of the much smaller saposinA molecules are needed to form the saposin-based nanoparticles, which provides a larger flexibility to adopt different sizes. Comparison of both systems in a long-term stability assay showed that MSP1D1 nanodiscs are slightly more sensitive to the lipid composition. The different packing parameters, which are influenced by the length and the saturation state of the hydrophobic chain of the lipids, might be better compensated by the more flexible structure of SapNPs, whereas the ratio needs to be adjusted in MSP nanodiscs. In contrast, the more rigid nanodisc complex seems to be slightly more stable as seen in the nDSF experiments. All effects are in good agreement with the SAXS studies, showing that the saposin nanoparticles are structurally more flexible compared to the nanodiscs. Nevertheless, both carrier systems showed structural heterogeneity throughout the size-exclusion chromatography peak. In general, both lipid carrier systems seem to be equally well suited to analyse IMPs in a native-like lipid environment.

Chapter 4

Studies on the activation of plasma-membrane Ca^{2+} -ATPase ACA8

Native mass spectrometry data presented in this chapter has been performed in collaboration with Dr. Johannes Heidemann (Utrecht lab, Heinrich-Pette-Institute, Hamburg, Germany).

4.1 Introduction

4.1.1 Calcium as a second messenger

Calcium ions (Ca^{2+}) are a ubiquitous intracellular signal, which affects numerous cellular processes (reviewed in [89, 90]). The basic principle of calcium signaling relies in the establishment of a steep concentration gradient of Ca^{2+} between the cytosol and the extracellular space and/or intracellular stores. Cells in a resting state have a very low Ca^{2+} concentration in the cytosol (~ 100 nM) compared to the extracellular space with Ca^{2+} concentrations of around 1-2 mM [90, 91]. Internal calcium stores like the endoplasmic reticulum (ER) or Golgi apparatus contain a luminal Ca^{2+} concentration of around 60-800 μM [92, 93], which is still above that of the cytosol. However, the ER is considered the main Ca^{2+} pool inside the cell. Upon activation, the cytosolic Ca^{2+} concentration transiently rises up to 1000 nM [90]. Ca^{2+} can enter the cytosol either from the extracellular space, through channels located in the plasma-membrane, or from intracellular Ca^{2+} stores [94, 95].

The calcium signalling process can be divided into three functional phases: (1) a stimulus generating various Ca^{2+} mobilizing signals, (2) the "ON mechanism" leading to the real Ca^{2+} influx into the cytosol and (3) the "OFF mechanism" including exporters, which pumps Ca^{2+} out of the cell or back into internal Ca^{2+} storage [90]. The Ca^{2+} mobilizing signals are generated by stimulated cell-surface receptors. These generated signals include inositol-1,4,5-triphosphate (IP3), cyclic ADP ribose (cADPR) and nicotinic acid dinucleotide phosphate (NAADP), which in turn leads to Ca^{2+} influx into the cytosol from internal and external sources by various channels, including IP3-receptors, ryanodine receptors, voltage-operated channels

and receptor operated channels. The Ca^{2+} release into the cytoplasm activates various Ca^{2+} -sensitive processes which translate this signal into a cellular response [94, 95]. In order to maintain the low Ca^{2+} concentration in the cytosol various pumps and exchangers are expressed, which rapidly remove Ca^{2+} . The plasma membrane Ca^{2+} -ATPase (PMCA) and the $\text{Na}^+/\text{Ca}^{2+}$ exchanger are located in the plasma-membrane and extrude Ca^{2+} to the extracellular environment. In contrast, the sarco-endoplasmic reticulum ATPase (SERCA) transports Ca^{2+} into the internal stores [95].

4.1.2 P-type ATPases

P-type ATPases constitute an important family among actively transporting ATPases which covers a wide range of cationic and lipid substrates. Based on their substrates they are grouped into five subfamilies, P_I to P_V [96–98]. All P-type ATPases share a common overall domain architecture of the main catalytic subunits. They are composed of 4 domains: the transmembrane domain and three soluble domains called the N-domain (nucleotide binding), P-domain (phosphorylation) and A-domain (actuator) (Fig. 4.1).

One of the best-studied P-type ATPase is the sarcoplasmic endoplasmic reticulum Ca^{2+} ATPase (SERCA), which belongs to the P_{IIa} subfamily. They are important for restoring the low Ca^{2+} levels in the cytoplasm of activated cells (see chapter 4.1.1) and are particularly important for Ca^{2+} -mediated signalling [99–101]. Crystal structures of SERCA in many different states revealed the catalytic pumping mechanism of P-type ATPases [102, 103]. The P-domain contains a highly conserved Asp residue, which gets phosphorylated during the reaction cycle, forming a phosphoenzyme intermediate state (4.1). The nucleotide binding domain (N-domain) performs the ATP binding and phosphorylates the P-domain. The A-domain performs the dephosphorylation and functions as a built-in phosphatase. The transmembrane domain accomplishes the ion transport through the membrane. In the transport processes the TMD alternates between two main conformational states, denoted E1 and E2. In the E1 conformation, the ion binding site has a high affinity to the substrate. In contrast, in the E2 conformation, the same sites have low-affinity for the substrate ion [1, 104–106], which releases the cations on the other side of the membrane. The vectorial transport of the cations is coupled to intermediate phosphorylation of the enzyme by the soluble domains. This phosphorylation as well as the conformational changes are split between the soluble domains (Fig. 4.1) [103].

Despite a low sequence homology between the P-type ATPases of the different subgroups crystal structures of representative pumps from different groups have shown a similar overall domain architecture, suggesting a comparable reaction cycle among all P-type ATPases [1].

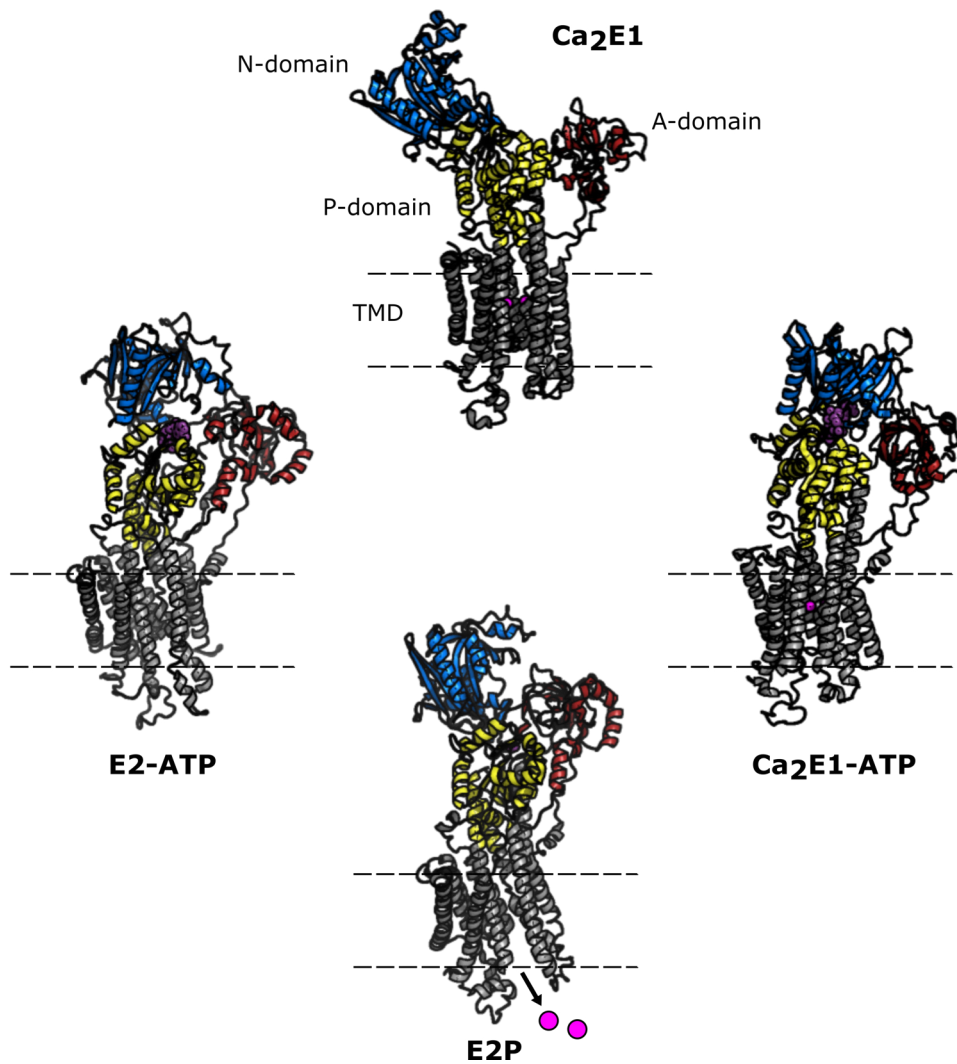


Figure 4.1: Comparison of SERCA structures showing key states of the reaction cycle. Cartoon representation of SERCA structures in different representative states throughout the pump cycle. The transmembrane domain (TMD) is shown in grey, the A domain in red, the N domain in blue and the P domain in yellow. Bound Ca^{2+} is shown as magenta spheres and ATP as pink spheres. Figure adapted from Bublitz *et al.* [103]

4.1.3 Plasma-membrane Ca^{2+} -ATPases

Plasma-membrane Ca^{2+} -ATPases (PMCA) belong to the P_{IB} subfamily of P-type ATPases [96]. They are located in the plasma membrane and export Ca^{2+} from the cytosol to the extracellular environment of eukaryotic cells [107–109]. Together with SERCA and the $\text{Na}^+/\text{Ca}^{2+}$ exchangers (NCX), PMCAs are the major plasma membrane transport system. They are of major physiological importance for the regulation of the low Ca^{2+} concentration of the intracellular resting state [109]. It has been shown that they are essential for sperm motility, pre- and post-synaptic Ca^{2+} regulation in neurons and feedback signalling in the heart [107]. PMCAs share the common

domain architecture with other P-type primary ion transport ATPases, including a transmembrane domain, and three soluble domain (P-, N-, A-domain), which are essential for the pumping cycle (see section 4.1.2). In addition PMCAs contain an autoinhibitory or regulatory domain, which is located either at the N-terminus (in plants) [110] or the C-terminus (in mammals) [111]. This regulatory domain (RD) contains a calmodulin (CaM) binding site and once calcium-loaded CaM binds to the RD both the Ca^{2+} -affinity and the pump rate is substantially increased. Based on these findings it has been proposed that binding of CaM to the regulatory domain induces conformational changes that displaces the RD from the pump core structure [112–114].

PMCAs are expressed in several isoforms to functionally adapt to the physiological needs of particular cell types. Alternative splicing further increase the functional variety. Two main locations in plasma-membrane Ca^{2+} -ATPases are affected by alternative splicing, including the regulatory domain and the first intracellular loop, which forms the A-domain. It has been recently suggested that the diversity of PMCA isoforms and splice variants are able to regulate the basic Ca^{2+} homeostasis (in the 100 nM range) and the high Ca^{2+} concentration during cell stimulation (in the μM range) [67, 115]. The crystal structure of the regulatory domain of ACA8, a plasma-membrane Ca^{2+} -ATPase from *A. thaliana*, revealed two calmodulin binding sites (CaMBS) with different affinities suggesting a more complex activation mechanism [67], which enables a precisely tuning of the activity of PMCAs to cover a broad range calcium concentrations in the cytoplasm (see Fig. 4.2). Combining both alternative splicing, generating different length of the regulatory domain, with the two calmodulin binding sites shows that the precise regulation of PMCAs are of major physiological importance. However, the structural changes leading to the activation of PMCAs are not well understood. A recent published cryo-electron microscopy structure of the human PMCA1 revealed the structural homology to the family of P-type ATPases, but could not resolve the regulatory domain [116]. Studies using a photoactivatable phosphatidylcholine analogue showed major conformational changes in the transmembrane domain during the activation of PMCAs by calmodulin [117–119], however, structural data about the full-length enzyme remain to be elusive. In order to investigate the structural basis for the activation of PMCAs by CaM this chapter aimed to characterized the different binding events by a combination of biochemical and biophysical methods. To further analyse the bimodular mechanism the *A. thaliana* ACA8 was used. Since Bonza and Luoni [111] showed that plant and mammalian PMCAs share a common autoinhibitory mechanism findings on the activation mechanism should apply for both PMCAs.

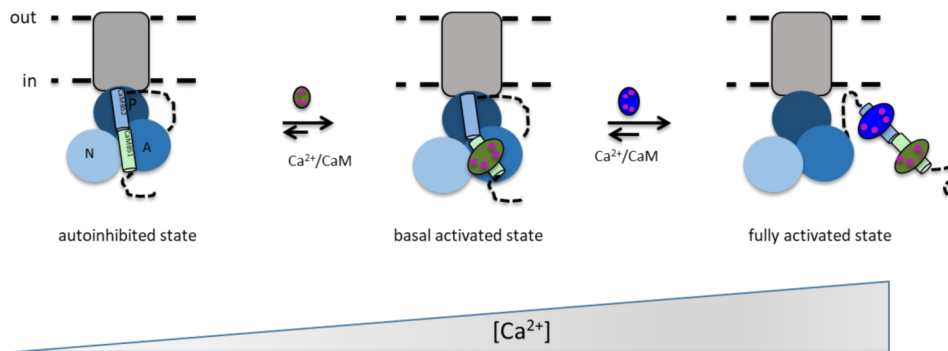


Figure 4.2: Proposed model of PMCA activation by Tidow et al. [67]. At low Ca^{2+} calcium-loaded calmodulin (CaM) bind first to the high affinity site of the regulatory domain. With increasing Ca^{2+} CaM binds to the low affinity binding site which completely replaces the regulatory domain leading to maximal pumping rate. Figure adapted from Tidow et al. [67].

4.2 Material and methods

4.2.1 Cloning of ACA8 constructs

Full-length ACA8 was cloned with an N-terminal His₆-tag in the pYES2 vector by Dr. Henning Tidow and was modified in this study. The His₆-tag was elongated by additional two histidine residues. In addition, a TEV protease cleavage site was introduced between the His-tag and the ACA8 gene via site-directed mutagenesis. ACA8 gene was cloned in a pDDGFP-LEU2d vector [120], which was a gift from Simon Newstead (Addgene plasmid # 58352), by homologous recombination as described in [121], which creates an ACA8-yEGFP fusion construct. The pDDGFP-LEU2d vector consists of a sequence for yEGFP [122] with a C-terminal octa-His tag and a TEV protease site upstream of GFP-His₈. Moreover, the vector contains two marker genes and allows for dual selection using either the URA3 or LEU2D marker. The LEU2D promoter was shortened and therefore weaker, which induces, growing in leucine-depleted medium, an additional selective pressure which in turn leads to a higher plasmid copy number in the cell and sometimes to an increase in the protein expression level [120]. An ACA8 construct with a C-terminal His₈-tag was obtained by removing the yEGFP sequence from the pDDGFP-LEU2d-ACA8 construct via site-directed mutagenesis resulting in a pDD-LEU2d-ACA8 construct. The ACA8core, a construct which lacks residues 1-138 of ACA8 (which contain the regulatory domain) were obtained from the pDD-LEU2d-ACA8 construct by site-directed mutagenesis. The regulatory domain of ACA8 (aa 1-130) (ACA8RD) contains fusion at the N-terminus composed of His₆-lipoamyl-TEV-tag. The fusion construct was cloned into pET28a vector by Dr. Henning Tidow [123]. In this study a cysteine was introduced N-terminal of the regulatory domain via site-directed mutagenesis to allow site specific labeling with thiol-reactive probes.

4.2.2 Small-scale expression screening of ACA8

Expression conditions of ACA8 were screened by whole-cell fluorescence analysis. ACA8-yEGFP construct was transformed (see B) into *S. cerevisiae* strains K616, InvSc1 and BJ5460 (see B) [124] and grown on either uracil- or leucine-depleted SC-plates (-URA or -LEU) for 72 h at 30 °C. Colonies from transformed BJ5460, InvSc1 and K616 cells were inoculated in 10 ml SC-media with 2% glucose (see B) (-URA or -LEU) and incubated overnight in an orbital shaker at 30 °C with 220 rpm. The following day the starter culture was used to inoculate 10 ml expression culture with SC-media with 0.1 % glucose (either -URA or -LEU) to an OD₆₀₀ of 0.12, and incubated at 30 °C with 220 rpm. At an OD₆₀₀ of 0.6 (after approx. 6-7 h) expression was induced by adding 20 % (w/v) galactose to a final concentration of 2 % (w/v), again incubated at 30 °C with 220 rpm. 22 hours post-induction the cells were harvested by centrifugation at 3,000 × g and resuspended in 300 µl buffer containing 50 mM TrisHCl pH 7.6, 5 mM EDTA, 10% glycerol. GFP fluorescence of the cell suspension was measured on a Tecan Infinite[®] 200 microplate reader at $\lambda_{\text{excitation}} = 488 \text{ nm}$, $\lambda_{\text{emission}} = 512 \text{ nm}$. In order to compare the expression level per cell all cell suspensions were adjusted to the same OD₆₀₀. To estimate background fluorescence transformed cells were grown in the presence of 2 % glucose (instead of 2 % galactose) from all different expression tests and used as negative control samples. In-cell concentration of expressed yeGFP (in mg/ml) were calculated as described in [121] using following equation:

$$[yEGFP]_{\text{expressed}} = \left([yEGFP] * \frac{F(+GAL) - F(+GLU)}{F(yEGFP)} \right) * DF^{-1} \quad (4.1)$$

where $F(+GAL)$ is the fluorescence of cells grown in 2 % galactose, $F(+GLU)$ the fluorescence of cell grown in 2 % glucose, $F(yeGFP)$ the fluorescence of purified yEGFP with a known concentration ($[yeGFP]$) and DF the dilution factor. The calculated value for the amount of expressed yEGFP was used to calculate the amount of expressed ACA8 as followed:

$$[ACA8]_{\text{expressed}} = [yeGFP]_{\text{expressed}} * \frac{MW_{ACA8}(kDa)}{MW_{yeGFP}(kDa)} \quad (4.2)$$

For further improvements each media and strain combination was tested with or without additional dimethylsulfoxide (DMSO) as a chemical chaperone at a final concentration of 0.04 % (w/v).

4.2.3 Fluorescence-detection size exclusion chromatography

Fluorescence-detection size exclusion chromatography (FSEC) was used for a first detergent screening. The method uses a construct with GFP fused to the membrane

protein of interest. The membrane fraction is solubilised with different detergents and the soluble fraction of detergent-solubilised membranes are analysed on a size exclusion column. The GFP fluorescence can be easily detected and the quality of the tested detergent can be judged by analyzing the shape of the chromatogram.

Yeast-enhanced GFP (yEGFP) was fused to full-length ACA8 to perform FSEC analysis (see 4.2.1). Membrane fractions from 2 L expression culture were used, resuspended in TBS buffer (50 mM Tris pH 7.6, 150 mM NaCl) and adjusted to 3.5 mg/ml total protein concentration. For each detergent tested, 100 μ l freshly prepared detergent solution was added to 900 μ l membrane suspension (final 3 mg/ml) and incubated for 1 h at 4 °C with constant agitation. The final detergent concentration was adjusted to 1 % unless otherwise stated. Subsequently, non-solubilized material were pelleted by ultracentrifugation at 100,000 \times g for 45 min. GFP fluorescence was measured from samples before and after the ultracentrifugation and used to calculate the detergent solubilization efficiency. 500 μ l of cleared detergent solubilized sample were injected on a Superdex 200 10/300 GL (GE Healthcare) column, pre-equilibrated in buffer containing 30 mM Tris pH 7.6, 150 mM NaCl, 0.03 % DDM and 100 μ l sized fractions were collected throughout the run. GFP fluorescence were measured for each fractions ($\lambda_{\text{excitation}} = 488$ nm, $\lambda_{\text{emission}} = 512$ nm) on a Tecan Infinite[®] 200 microplate reader and plotted against the corresponding elution volume.

4.2.4 Expression of full-length ACA8, ACA8core and ACA8RD

Full-length ACA8 with an N-terminal His₈-tag (in pYES2) or with an C-terminal His₈-tag (in pDD-LEU2D) as well as ACA8core (in pDD-LEU2d) were transformed in BJ5460 *S. cerevisiae* cells [124] and grown on SC-agar plates (-URA). 10 ml SC media with 2 % glucose (-URA) starter culture was inoculated with freshly transformed BJ5460 cells and incubated in an orbital shaker for 24 h at 30 °C and 220 rpm. The starter culture were diluted into 100 ml SC media with 2 % glucose (-URA) and incubated for 8-10 h at 30 °C and 220 rpm and diluted afterwards again into 500 ml SC media with 2 % glucose (-URA). After approx. 16 h the 500 ml pre-culture were used to inoculate 12 \times 900 ml SC media with 0.1 % glucose (-URA) to an OD₆₀₀ of 0.12 and incubated in an orbital shaker at 30 °C and 220 rpm (approx. 6-8 h). At an OD₆₀₀ of 0.7 the expression was induced by adding 20 % galactose to a final concentration of 2 % and incubated for 20 h at 30 °C and 220 rpm. The cells were harvested by centrifugation at 3,000 \times g for 10 min and were resuspended in 30 mM Tris pH 8.0, 300 mM NaCl, 20 % (v/v) glycerol, 3 mM β -mercaptoethanol, 20 mM EDTA.

ACA8RD (in pET28a) was cotransformed together with CaM7 (in pET42a) in *E. coli* strain C41 [125]. Cells harbouring the both plasmids were used to inoculate 20 ml preculture with LB-medium containing ampicillin and kanamycin and grown for 16 h at 37 °C at 180 rpm. The expression culture (6 L 2 \times TY media) were inoculated using

the preculture to an OD₆₀₀ of 0.1 and cells were grown at 37 °C and 180 rpm to an OD₆₀₀ of 1.0. Subsequently, the temperature was shifted to 20 °C and the expression was induced by adding 0.1 mM IPTG and grown for approx. 16 h. The cells were harvested by centrifugation at 4,000 x g for 30 min and the pellet was resuspended in lysis buffer (30 mM Tris pH 7.5, 300 mM NaCl, 10 % glycerol, 2 mM CaCl₂, 1 mM Tris-(2-carboxyethyl)-phosphin (TCEP)).

4.2.5 Purification of full-length ACA8, ACA8core and ACA8RD

For purification of full-length ACA8 and ACA8core the resuspended cell pellet was supplemented with 1 mM PMSF. The Cells were broken with 0.5 mm sized glass-beads in a BeadBeater for 6 x 30 s. In a first low speed centrifugation step at 10,000 x g all cell debris were spun down. Membrane fractions were isolated with an ultracentrifugation step at 180,000 x g for 100 min and the pellet was resuspended in buffer containing 30 mM Tris pH 8.0, 300 mM NaCl, 10 % (v/v) glycerol, 1 mM CaCl₂, 2 mM β-mercaptoethanol. The membranes were solubilized in either 1 % lauryl maltose neopentylglycol (LMNG) or 1 % dodecyl-β-D-maltopyranoside (DDM) for 1.5 h with gentle stirring, depending on the experiments afterwards. To remove insoluble material the solubilized membranes were centrifuged at 100,000 x g for 45 min. Ni-affinity chromatography using a Ni-NTA column was applied. The cleared solubilized membrane fraction were incubated with Ni²⁺ affinity resin for 1 h at 4 °C with gentle stirring. The resin was pre-equilibrated with buffer containing 30 mM Tris pH 8.0, 300 mM NaCl, 2 mM CaCl₂, 1 mM β-mercaptoethanol, 0.005% LMNG (buffer A). In a first step the column was washed with 10 column volume (cv) of buffer A. Subsequently, unspecific bound proteins were gradually eluted with 10 mM and 40 mM imidazole ACA8 was eluted with 150 mM imidazole. The purity of ACA8 was judged by SDS-PAGE and suitable fractions were combined. The combined fraction were either used directly to incorporate ACA8 into nanodiscs (see 4.2.8) or a second purification step using size exclusion chromatography (SEC) was applied. For SEC, combined elution fraction were concentrated to a suitable volume and loaded on Superdex 200 (10/300) column (GE Healthcare) which was pre-equilibrated with buffer containing 30 mM Tris pH 8.0, 150 mM NaCl, 1 mM CaCl₂ 0.5 mM TCEP, 0.003 % LMNG [126].

For purification of ACA8RD the resuspended pellet of co-expressed ACARD and CaM7 was supplemented with 0.5 ml Lysozyme (100 mg/ml) (*Gallus gallus*, Sigma-Aldrich) and DNase (1 mg/ml) and incubated for 30 min under gentle agitation at 4 °C. The cells were lysed using a high-pressure homogenizer (EmulsiFlex-C3, Avestin) and lysate was cleared by centrifugation at 40,000 x g for 45 min. A metal ion affinity chromatography step using HisTrap column (GE Healthcare) was applied as a first purification step in buffer containing 30 mM Tris pH 7.5, 300 mM NaCl, 10 % glycerol, 2 mM CaCl₂, 1 mM TCEP. Unspecifically bound proteins were eluted with

20 mM imidazole before the ACA8RD-CaM complex was eluted with 200 mM imidazole. The combined elution fractions were dialyzed against imidazole free elution buffer at 4 °C and incubated with TEV protease overnight. A second nickel affinity chromatography step was applied to remove the His-lipoamyl-TEV tag [123] and the flow-through containing the ACA8RD-CaM complex was analysed on a SDS-PAGE and concentrated to a suitable volume before fluorescence labeling (see 4.2.11) [126].

4.2.6 Expression and purification of CaM7

CaM7 was cloned in pET42a vector with an N-terminal fusion consisting of His₆-tag and a TEV protease cleavage site by Dr. Henning Tidow and provided for this study. The plasmid containing CaM7 was transformed into *E.coli* BL21 Gold (DE3). A single colony was used to inoculate 10 ml preculture with LB-medium containing kanamycin (25 µg/ml), which was incubated for approx. 16h at 37 °C and 180 rpm. The preculture was used to inoculate the expression culture in LB-medium to an OD₆₀₀ of 0.05. Expression were induced with 0.5 mM IPTG at an OD₆₀₀ of 0.6 and grown for another 16 h at 20 °C. Cells were harvested by centrifugation for 30 min at 3000 x g.

For purification cell pellet was resuspended in 30 mM Tris pH 7.5, 50 mM NaCl, 1 mM ME, 2 mM CaCl₂, supplemented with 0.5 ml Lysozyme (100 mg/ml) (*Gallus gallus*, Sigma-Aldrich) and DNase (1 mg/ml) and incubated for 30 min under gentle agitation at 4 °C. The cells were broken using three cycles at a high-pressure homogenizer (EmulsiFlex-C3, Avestin). The lysate was cleared by centrifugation for 45 min at 40,000 x g and the supernatant was bound to HiTrap Phenyl HP column, pre-equilibrated with buffer containing 30 mM Tris pH 7.5, 50 mM NaCl, 1 mM ME, 2 mM CaCl₂. CaM7 was eluted with 5 mM EDTA and purity of the sample was judged on a SDS-PAGE. Fractions containing pure CaM7 were pooled, concentrated to 10 mg/ml and stored at -80 C until further use.

4.2.7 Differential scanning fluorimetry using Prometheus

In order to optimize buffer conditions and screen for detergents with stabilizing effects, thermal unfolding behavior of ACA8 was investigated using a nanoDSF differential scanning fluorimeter (Prometheus, NanoTemper Technologies). This method monitors the protein's intrinsic fluorescence upon temperature induced denaturation. The fluorescence emission of tryptophan residues in a protein is solvatochromic and therefore strongly depends on the environment. Upon unfolding the tryptophan becomes solvent exposed and changes its fluorescence intensity. In addition, the emission peak usually shifts from 330 nm to 350 nm (red shift). The change of intrinsic fluorescence of tryptophan residues at 330 nm and 350 nm after excitation at 280 nm was measured and the ratio of F₃₃₀/350 was plotted against the temperature. The melting temperature (T_m) was determined by first derivative

analysis. The T_m is defined as the temperature at which 50 % of the protein is already unfolded. This value was used as a measure to characterize the protein stability in different buffer conditions.

For additive screening ACA8 was purified in dodecyl- β -D-maltopyranoside (DDM) (see 4.2.5) in a buffer containing 20 mM HEPES pH 7.5, 150 mM NaCl, 0.017 % DDM (2x CMC) and for buffer screening was purified in the same buffer but containing 0.01% lauryl maltose neopentylglycol (LMNG) instead of DDM. Size exclusion fractions containing pure ACA8 were concentrated to $2.5 \text{ mg}\cdot\text{ml}^{-1}$ and subsequently diluted to $0.5 \text{ mg}\cdot\text{ml}^{-1}$ in new buffer (buffer screening) or the same buffer with different detergents (detergent screening) prior to analysis. $10 \mu\text{l}$ ACA8 was loaded in a capillary and the unfolding was measured at a heating rate of $1 \text{ }^\circ\text{C}/\text{min}$ from $20 \text{ }^\circ\text{C}$ to $90 \text{ }^\circ\text{C}$. The tested additives and buffer conditions are listed below in Table 4.1.

Table 4.1: *Prometheus screen*

additive screen		buffer screen	
additive	conc.	buffer	conc.
MgCl ₂	5 mM	acetate pH 4.5	119 mM
CaCl ₂	5 mM	Mes pH 6.0	119 mM
EDTA	10 mM	K-phosphate pH 6.0	119 mM
Mg-AMP	1 mM	citrate pH 6.0	119 mM
Mg-ADP	1 mM	Bis-Tris pH 6.5	119 mM
Mg-ATP	1 mM	Mes pH 6.5	119 mM
Mg-AMPPCP	1 mM	Na ₂ -phosphate pH 7.0	119 mM
POPC	5 mM	K-phosphate pH 7.0	119 mM
POPG	5 mM	Hepes pH 7.0	119 mM
soyPC	5 mM	Ammonium-actetate	119 mM
		pH 7.3	
UDM	1 mM	Tris-HCl pH 7.5	119 mM
ω -UDM	1 mM	Na ₂ -phosphate pH 7.5	119 mM
DTM	1 mM	Imidazol pH 7.5	119 mM
LMNG	1 mM	Hepes pH 8.0	119 mM
DMNG	1 mM	Tris-HCl pH 8.0	119 mM
OGNG	1 mM	Tricine pH 8.0	119 mM
CHS	1 mM	Bicine pH 8.0	119 mM
GDN	1 mM	Bicine pH 8.5	119 mM
C12E8	1 mM	Tris-HCl pH 8.5	119 mM
Cymal-5	1 mM	Ches pH 9.0	119 mM
Cymal-6	1 mM		

4.2.8 Reconstitution of ACA8 into MSP nanodiscs

In order to characterize the activation process in a native-like lipid environment ACA8 and ACA8core were reconstituted into nanodisc. The size of the nanodisc was controlled by the use of different membrane scaffold protein (MSP) constructs. In this study MSP1D1 as well as MSP1E3 were used. To analyse the effect of different lipid-headgroups on the activity, 1-palmitoyl-2-oleoyl-sn-glycero-3-phosphocholine (POPC), 1-palmitoyl-2-oleoyl-sn-glycero-3-phospho-(1'-rac-glycerol) (POPG) or L- α -phosphatidylinositol (soy-PI) (Avanti Polar Lipids) were used for the assembly. Lipid mixtures contained 70% POPC and 30% POPG or 70% POPC and 30% soy-PI, respectively [126].

Lipid powder was resuspended in storage buffer (30 mM Tris pH 8.0, 150 mM NaCl, 100 mM cholate) to a final concentration of 50 mM and solubilised using freeze-thaw cycles until the solution became clear. ACA8 or ACA8core were purified in LMNG (Lauryl maltose neopentyl glycol) and used directly after affinity chromatography (see 4.2.5). For reconstitution of ACA8 or ACA8core into nanodiscs, ACA8, the membrane scaffold protein (MSP1D1 or MSP1E3) and the lipids were mixed in a molar ratio of 1:5:150 (for MSP1D1 nanodisc) or 1:5:400 (for MSP1E3 nanodisc) in 30 mM Tris pH 8.0, 150 mM NaCl, 2 mM CaCl₂, 1 mM β -mercaptoethanol and incubated for 1 h at 4 °C. The cholate concentration within the mixture was adjusted to 20 mM and it was important to keep the LMNG concentration in the mix below 1 x CMC (< 0.001 %). Nanodisc assembly was initiated by adding detergent removal beads (Thermo Fischer Scientific) in a 1:1 (v/v) ratio. The assembly mix was incubated overnight (approx. 12 h) at 4 °C under constant agitation. Detergent removal beads were removed by centrifugation (1,000 x g, 2 min) and subsequently aggregates were spun down at 20,000 x g for 10 min. ACA8 or ACA8core containing nanodisc were separated from 'empty' nanodisc (nanodisc containing only lipids and MSP) on a Superdex200 column (GE Healthcare) in a buffer containing 20 mM Tris pH 8.0, 150 mM NaCl, 1 mM CaCl₂, 1 mM β -mercaptoethanol. The purity of the sample was judged on a SDS-PAGE and fractions containing ACA8 in nanodiscs were pooled, concentrated and stored at 4 °C until further use [126].

4.2.9 Native mass spectrometry

Native mass spectrometry was performed by Dr. Johannes Heidemann (Utrecht Lab, HPI, Germany). ACA8 was solubilized and purified in Dodecyl- β -D-maltopyranoside (DDM). After affinity chromatography and size exclusion chromatography (SEC) (see 4.2.5) fractions containing pure ACA8 were pooled and concentrated to 1 mg/ml and mixed with five-fold excess of purified CaM (see 4.2.6). Subsequently, the buffer of purified ACA8-CaM complex as well as ACA8 alone was exchanged to 200 mM ammonium acetate pH 8.3, 0.018% DDM (2xCMC) using centrifugal filter

units (Vivaspin 500, 10,000 MWCO, Sartorius) at 4 °C and 15,000 × g [126].

Nano electrospray ionization (ESI) capillaries were prepared by Dr. Johannes Heine-mann (Utrecht lab) and subsequently gold-coated using a sputter coater (Q150R; Quorum Technologies Laughton, UK, 40 mA, 200 s, tooling factor 2.3, end bleed vacuum 8×10^{-2} mbar argon) [127].

Native MS experiments were performed with a nanoESI source in positive ion mode on a QToF2 (Waters and MS Vision) mass spectrometer that was modified for the analysis of high-mass ions [127, 128]. Capillary and sample cone voltage were used at 1700 V and 190 V, respectively. 7 mbar source pressure and 1.7×10^{-2} mbar argon as collision gas were used. Capillary and cone voltages were set to 1.7 kV and 190 V, respectively. The collision energy was gradually ramped to 400 V to release protein complexes from detergent micelles. Gas pressures were 10 mbar in the source region and 1.7-2 mbar argon in the collision cell. Illustrated spectra were recorded at 200 V [126, 127].

CsI (25 mg/ml) spectra were acquired and used to calibrate raw data using MassLynx software (Waters). Data was analyzed using MassLynx and Massign [129]. Average measured masses of protein complexes, standard deviations of replicate measurements and average full width at half maximum (FWHM) values as a measure of the mass resolution are listed in Table A.2 [126, 127].

4.2.10 Activity measurements

ACA8 activity was assessed by measuring the ATPase activity using the Baginsky assay [130, 131]. The method measures the production of inorganic phosphate, a result of ATP hydrolysis. The produced inorganic phosphate forms a complex with ammonium heptamolybdate, which can be quantified colorimetrically.

Activity was measured from purified ACA8 or ACA8core (ACA8 construct lacking the regulatory domain), either in LMNG or nanodiscs composed of different lipids (see 4.2.5 & 4.2.8). Mixed lipids contained 70% POPC and 30% POPG or 70% POPC and 30% soy-PI, respectively. All measurements were performed in the presence or absence of the major PMCA activator CaM7 to ensure full functionality. ATPase activity was analysed in either a CaM-dependent or ATP-dependent manner. The CaM concentration was varied between 5 nM and 10 μ M and ATP concentration between 50 μ M and 4 mM. The enzyme concentration as well as the incubation time with ATP was adapted to perform all measurements under initial velocity conditions. In general, reactions were performed in buffer containing 30 mM Tris-HCl (pH 7.4 at 25 °C), 150 mM NaCl, 2 mM MgCl₂, 1.95 mM EGTA, and 2 mM CaCl₂, in order to get 50 μ M final free Ca²⁺ concentration. 3 μ g of purified ACA8 in LMNG and 2 μ g ACA8-nanodiscs complex were used. The reaction volume was 50 μ l. The ATPase reaction was started by adding the corresponding ATP concentration and

incubated for 10 min at 25 °C. The reaction was stopped by adding 50 µl ascorbic acid solution (140 mM ascorbic acid, 0.5 M HCl, 0.1% SDS, 5 mM ammonium heptamolybdate). After 10 min the addition of 75 µl containing 75 mM sodium citrate, 2% (w/v) sodium metaarsenite and 2% (v/v) acetic acid stopped the colorimetric reaction and the absorbance at 860 nm was read on a Tecan Infinite® 200 microplate reader after 30 min. The spontaneous and non-enzymatic hydrolysis of ATP just in buffer was subtracted from the measurements with ACA8. A calibration curve using sodium phosphate in a concentration range from 0.01 mM to 0.6 mM was used for determining the concentration of released phosphate [126]. In ATP titration and CaM titration experiments all measured activities were normalized to the protein concentration and incubation time with ATP to get the specific activity ($[\text{hydrolysed ATP}] \cdot \text{min}^{-1} \cdot \text{mgACA8}^{-1}$), which was plotted against the ATP concentration. In ATP titration experiments reactions were assumed to follow the Michealis-Menten kinetics and the data was fitted using following equation:

$$v = \frac{v_{\max} * [S]}{K_m + [S]} \quad (4.3)$$

where $[S]$ is the ATP concentration, K_m is the the Michaelis constant. K_m defines the substrate concentration at which the reaction rate is half maximum, which in turn describes the substrate's affinity to the enzyme. V_{\max} is the maximum reaction rate. All reactions were measured as triplicates [126].

4.2.11 Fluorescence anisotropy titration

Fluorescence anisotropy was used to characterize the binding of CaM to the regulatory domain of ACA8 (ACA8RD), as well as the binding of ACA8RD to ACA8core (ACA8 construct lacking the regulatory domain). For titration experiments Alexa Fluor™488 C5 maleimide (Thermo Fischer Scientific, USA) was used to label CaM or the regulatory domain from ACA8 (ACA8RD), respectively. The maleimide enables the thiol-specific labeling of proteins. Wildtype CaM7 contains only one cysteine at position 27, which was used to introduce the fluorescent dye at a specific position. For ACA8RD a cysteine was introduced between the TEV cleavage site and the regulatory domain.

For fluorescence labeling Alexa Fluor™488 maleimide was added to 40 µM purified ACA8RD-(CaM7)₂ (see 4.2.5) or 40 µM purified CaM (see 4.2.6), respectively, in a molar ratio of 10:1 and incubated overnight (approx. 16h) at 4 °C. The reaction was stopped by adding 5 mM β-mercaptoethanol. Free fluorescein isothiocyanate (FITC) was separated with a PD10 column. Afterwards the ACA8RD-(CaM)₂ complex was dissociated by adding 10 mM EDTA followed by binding of ACA8RD to a cation exchange chromatography column to further purify FITC-ACA8RD. Fractions containing FITC-ACA8RD were pooled, concentrated and flash frozen in liquid nitrogen

until further use. FITC-labeled CaM was used directly after PD10 column [126]. Measurements were performed on an Agilent Cary Eclipse fluorescence spectrophotometer. Fluorescence anisotropy was measured with excitation at 480 nm and emission at 520 nm and slit width of 10 nm. Each measurement was integrated over 5 sec and the photomultiplier voltage was set to 700 V [126].

The fluorescence anisotropy r was calculated from fluorescence intensities that were measured with a vertically oriented excitation polarizer and vertically (I_{vv}) or horizontally (I_{vh}) oriented emission polarizer [reviewed 132, chapter 10] from the following equation:

$$r = \frac{I_{vv} - G * I_{vh}}{I_{vv} + 2 * G * I_{vh}} \quad (4.4)$$

The G-factor (G) is a correction for the instrument sensitivity towards vertically and horizontally polarized light. It is defined as

$$G = \frac{I_{hv}}{I_{hh}} \quad (4.5)$$

and was measured for each sample immediately before the experiment using the same sample and instrument settings as used for the experiment [126].

All Reactions were carried out at 20 °C in buffer containing 30 mM Tris pH 8.0, 150 mM NaCl, 2 mM CaCl₂, 0.5 mM TCEP. In the binding experiments, 25 μM ACA8core (in POPC nanodiscs)(see 4.2.8) were titrated into 50 nM fluorescein-labeled ACA8RD or full-length ACA8 (in POPC nanodiscs)(see 4.2.8) was titrated into 15 nM FITC-labeled CaM. In the competition binding assay ACA8core (in POPC nanodiscs) were titrated into labeled ACA8RD until r did'nt further increase and subsequently 50 nM CaM was titrated into the preformed complex. After each titration the solution was stirred for 30 s before horizontally and vertically emmission were measured. Dissociation constants were obtained by fitting anisotropy data to the equation corresponding to a one-site binding model with

$$r_{obs} = r_0 + \frac{\Delta r * [P]}{K_d + [P]} \quad (4.6)$$

where r_0 is the initial anisotropy value of the unbound labeled CaM or ACA8RD, Δr is the change in anisotropy upon binding of full-length ACA8 (fACA8) or CaM (to the complex of labeled ACA8RD and ACA8core), $[P]$ is the concentration of the titrant and the dissociation K equals P_{50} [126].

4.2.12 Small-angle X-ray scattering (SAXS)

Small-angle X-ray scattering (SAXS) was used to characterize the activation process of ACA8. All data was aquired on the Bio-SAXS instrument P12 on the storage ring

Petra III (DESY, Hamburg, Germany) [133]. All SAXS measurements were carried out at 10 °C in 30 mM Tris pH 7.5, 150 mM NaCl, 2 mM CaCl₂, 2 mM MgCl₂ and 0.5 mM TCEP at protein concentrations ranging from 1-8 mg/ml [126]. ACA8 was reconstituted into nanodisc to reduce negative side-effects from buffer mismatch due to empty detergent micelles. Different membrane scaffold protein constructs were used to control and optimize the size of the nanodisc. In the present study MSP1D1 (nanodisc diameter of 9.7 nm) and MSP1E3D1 (nanodisc diameter of 12.7 nm) were used (see 4.2.8). ACA8 was reconstituted in nanodiscs composed of different lipid composition as described in 4.2.8. ACA8-CaM complex were formed by mixing ACA8-ND with excess of CaM which was subsequently purified from excess of CaM on a Superdex200 (10/300) column (GE Healthcare, USA) and concentrated before measurements.

The scattered intensity was recorded as a function of the scattering vector q with

$$|q| = \frac{4\pi \sin\theta}{\lambda} \quad (4.7)$$

using a wavelength (λ) of 0.124 nm. The scattering from the corresponding buffer was collected before and after each protein sample. A total of 20 frames, each with an exposure time of 50 ms, were collected for each buffer and samples exposure. The average of the data was normalized and background subtracted using automatic procedures on the beamline [84]. An average of buffer scattering was subtracted from the samples scattering. Inter-particle interference was inspected by analysing the Guinier region of each scattering curve in the concentration series. If needed, low-angle scattering data obtained for the lowest concentration of the protein was merged with high-angle data obtained from the highest concentration of the same protein to reduce the contribution of inter-particle effects to R_g determination. Calibration of the scattering intensity into absolute units of cm⁻¹ was performed using the forward scattering intensity of bovine serum albumin [126].

All data processing was performed using PRIMUS [84]. The distance distribution function, $p(r)$, was obtained by indirect Fourier transform (FT) of the scattering intensity using GNOM [43], which provides the maximal particle dimension, D_{max} , and the radius of gyration (R_g). The radius of gyration was also evaluated from the experimental SAXS pattern using the Guinier approximation ($\ln I(q)$ vs q^2). The Guinier-derived R_g was compared with the R_g determined by the indirect FT over the whole scattering range in order to make sure no aggregation was present in the sample [126].

4.3 Results and discussion

4.3.1 Optimization of expression and purification of ACA8

4.3.1.1 GFP-based expression screening of ACA8

The natural abundance of membrane proteins is generally too low to obtain sufficient amounts from natural sources for biochemical and biophysical studies [134, 135]. Therefore, membrane proteins often need to be overexpressed to yield milligram amounts of pure and functional protein for downstream analysis. One of the most abundantly used expression hosts for the overexpression of membrane proteins is *Escherichia coli*, an organism which can be handled and genetically modified with ease [136]. For that reason, *E. coli* was tested as a first expression system to produce ACA8. The corresponding gene were cloned into the pNEK vector to create a fusion construct with an N-terminal His₈-tag. ACA8 expression was screened by varying *E. coli* strains, the expression temperature (37 °C or 20 °C) and the IPTG concentration (ranging from 0.05 mM to 1mM). Tested *E. coli* strains included BL21, C43 [125], Lemo [137] and Rosetta-Gami2 cells. The selected *E. coli* strains, like C43, Lemo or Rosetta-Gami2, provide different advantages for recombinant expression of challenging proteins and were therefore chosen to screen a broad range of properties. For example, proliferation of intracellular membranes in the C43 strain helped improving the expression of subunit b of the F₁F₀ATP synthase [138] which make this strain a suitable candidate for membrane protein overexpression. In some cases the overexpression of membrane proteins can be toxic to *E. coli* cells. The Lemo strain enables the precise control of T7 RNA polymerase activity, which in turn prevents the SEC translocon from a overload and therefore helps reducing the toxicity of overexpression. The Rosetta-gami2 strain are designed for overexpression of eukaryotic proteins, as it able to express tRNAs from codons rarely used in *E. coli*. Moreover due to a less reducing cytoplams disulfide bonds are able to form, which are often important for eukaryotic proteins [139].

For each strain and growth-condition combination, 50 ml expression culture was grown and a pulldown experiment was undertaken. For this, corresponding membrane fractions were purified and solubilised in DDM, bound to Ni²⁺- affinity chromatography resin and the elution fraction were analysed on a SDS-PAGE. None of the tested combination showed a significant expression level of ACA8, indicating that no protein was properly expressed and inserted into the membrane to yield a functional protein. All selected strains are engineered to optimize either the expression of membrane proteins or eukaryotic proteins but did not show any expression of ACA8. The lipid structure of *E. coli* membranes as well as the composition differs significantly from eukaryotic cells. The recombinant expression of membrane

proteins requires a proper membrane environment [140]. However, as a prokaryotic expression system, *E. coli* may lack essential lipids, molecular chaperons, and post-translational modifications that are required for the correct membrane insertion, folding, and function of eukaryotic IMPs, such as ACA8 [136, 141].

Eukaryotic membrane proteins has been successfully expressed in *S. cerevisiae* [121]. Yeasts are simple eukaryotes that combine the ease and cost effectiveness of *E. coli* but come with the added benefit of eukaryotic folding pathways [142]. Therefore three different *S. cerevisiae* strains were used to screen for the overexpression of ACA8 in a eukaryotic expression system. Tested yeast strains included the K616, InvSc1 and BJ5460. The K616 strain lacks the endogenous active Ca^{2+} transport systems [143] and is widely used for functional studies of Ca^{2+} ATPases. Yeast strain BJ5460 is a protease deficient strain and showed reasonable high expression levels when expressing eukaryotic membrane proteins [142]. The gene encoding full length ACA8 was cloned into the pDDGFP-LEU2D vector through which the proteins are expressed with a C-terminal TEV-cleavage site, GFP-tag and a His₈-tag. GFP fusion has several advantages; the C-terminal GFP folds and thus becomes fluorescent only if the fused membrane protein is properly folded and integrated into the membrane. Thus, the resulting fluorescence can be used as a fast and accurate measure of membrane-integrated expression level [144–146] as it is easily detected in liquid culture, standard SDS-gels and detergent-solubilized membranes. Additionally, the vector harbours two metabolic markers which enables the growth in either uracil or leucine depleted medium. The leucine marker, LEU2D, is under the control of a truncated promotor, which leads to a higher plasmid copy number in the cell and was demonstrated to increase the expression level of several membrane proteins [142].

To identify potential expression conditions for large-scale expression, a small-scale expression test in 50 ml media was carried out using either uracil or leucine depleted medium or full medium (YPG). For each type of media the effect of DMSO as a chemical chaperone were tested as well. The in-cell fluorescence of ACA8-GFP for each strain and media combination were measured as described in 4.2.2 and the amount of expressed ACA8-GFP was calculated. In general, the BJ5460 strain showed the highest expression level over all different conditions, whereas the K616 strain expressed much less ACA8-GFP (see Fig. 4.3 a+b).

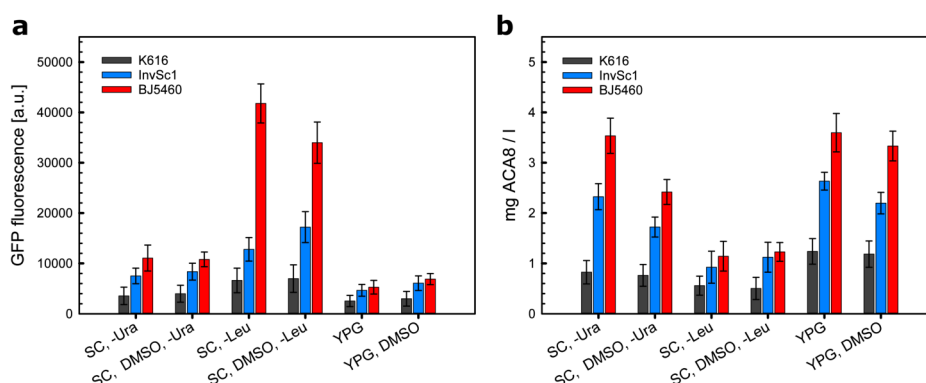


Figure 4.3: In-cell expression screening of ACA8. ACA8-GFP was expressed in either K616 (grey), InvSc1 (blue) or BJ5460 (red) *S. cerevisiae* cells under different conditions. Cells were grown in either full-media (YPG) or selective media (either -URA or -LEU). Each cell and media combination were tested with addition of 0.04% DMSO as chemical chaperone. (a) In-cell fluorescence intensities normalized by OD_{600} given the expression rate per cell. (b) Amount of expressed ACA8-GFP per liter expression medium.

As the endogenous active Ca^{2+} transport systems are altered in the K616 strain the calcium signalling might be disturbed, which in turn might have a negative effect on the expression rate. In contrast, in BJ5460 three endogenous proteases are deleted, which might have a positive effect on the lifetime of overexpressed proteins and therefore on the expression level of ACA8. In leucine-depleted media the expression level per cell is four times higher in BJ5460 cells compared to expression condition under uracil depleted media (Fig. 4.3 a). This indicates that the additional selective pressure, due to the truncated LEU2D promoter, indeed leads to a higher plasmid copy number and in turn to a much higher expression level in the cell. Interestingly, this effect is much less pronounced in the tested K616 or InvSc1 strains, where the expression rate in leucine-depleted media is almost the same as in uracil-depleted media. However, the cells grew significantly slower in leucine-depleted media, as already described in [142], and therefore the amount of expressed ACA8-GFP per liter expression medium was only 30% of that in uracil-depleted medium (Fig. 4.3 b). In contrast, the expression level per cell in YPG medium is the lowest which is compensated by a much higher OD_{600} , which leads to almost the same amount of expressed ACA8 per liter expression medium as in uracil depleted medium. It seems that, due to the loss in selective pressure in YPG media, the plasmid copy number in the cell is significantly reduced, which explains the low expression rate per cell. The addition of DMSO showed no positive effect in none of the tested expression condition.

Overall, the BJ5460 strain in uracil-depleted as well as in YPG media expressed the highest amount of ACA8-GFP, but in uracil-depleted media the concentration of ACA8 in the cell is significantly increased. More biomass can have negative side

effects in downstream processes. Therefore large-scale expression of ACA8 was carried out in BJ4560 strains in uracil-depleted media.

4.3.1.2 Optimization of purification of ACA8

GFP-based detergent screening

The GFP moiety in the ACA8-GFP fusion enables a fast screening of different detergents. In order to screen for solubilization efficiency, ACA8-GFP was expressed in 2L uracil-depleted selective media as described above in 4.3.1.1 and membrane fraction were purified by differential centrifugation (see 4.2.5). In-gel fluorescence analysis of all membrane purification steps showed a single fluorescent band at 150 kDa in the membrane fraction sample (lane 4), which correspond to the ACA8-GFP fusion (Fig. 4.4) and no degradation is visible.

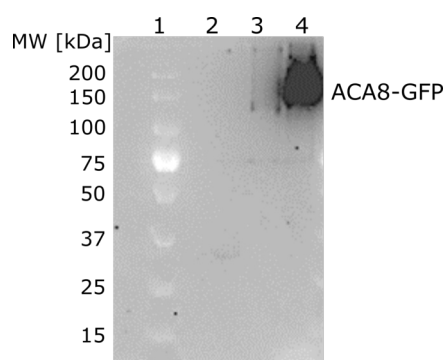


Figure 4.4: In-gel fluorescence showing the expression of ACA8 ACA8-GFP was expressed in BJ5460 cells, membrane fractions were isolated and all samples were loaded on a 15% SDS-PAGE. Fluorescent bands were detected by a CCD camera system. Bands; 1 = molecular weight marker, 2 = non-induced cells, 3 = cell debris after centrifugation at 10,000 x g, 4 = membrane fraction

Purified membrane fractions were solubilized with 1% final detergent concentration for 1h and cleared with an ultracentrifugation step afterwards. Solubilization efficiency was calculated by measuring the GFP fluorescence of samples before and after the centrifugation step. Figure 4.5 shows the solubilization efficiency of all screened detergents. This screen included different classes of detergent, where the charge state and the nature of the head group as well as the length of the hydrophobic chain were varied. The dodecyl- β -D-maltopyranoside (DDM) clearly showed the best solubilization efficiency with 90-97 % solubilized ACA8-GFP.

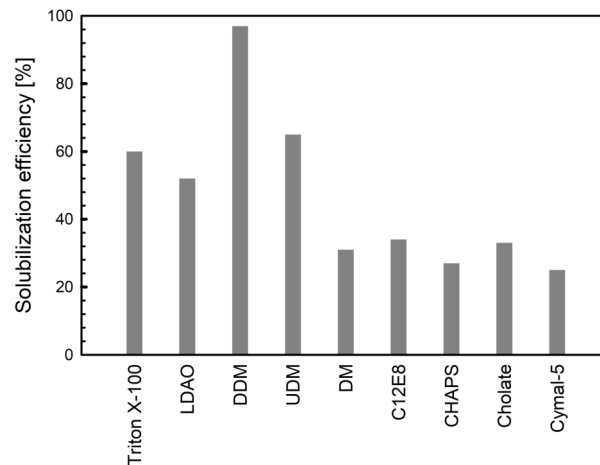


Figure 4.5: Solubilization efficiency of ACA8-GFP ACA8-GFP were expressed in BJ5460 cells and membrane fractions were isolated. For solubilization 1 % detergent (final concentration) was added to the membrane fraction and cleared by ultracentrifugation after 1h. GFP fluorescence was measured before and after the centrifugation step to calculate the solubilization efficiency.

The ability of detergents to stabilize the native conformation of IMPs is even more important than the solubilization efficiency. To determine the stability of ACA8-GFP in different detergents, fluorescence-detection size-exclusion chromatography (FSEC) was performed. SEC is one of the most useful tool for monitoring the monodispersity and stability of the target protein [147, 148]. In an FSEC experiment the GFP fluorescence, and therefore the protein of interests which is fused to GFP, can be followed easily on a gel filtration chromatography column. Based on the shape of the chromatogram the protein behavior can be evaluated to judge the ability of the detergent to stabilize the IMP [149]. Membrane fractions of expressed ACA8-GFP were solubilized in 1 % detergent and the soluble portion were separated from the non-solubilised protein by ultracentrifugation. FSEC experiments were performed by loading the supernatant of the cleared membrane fraction onto a size exclusion column (Superdex 200 10/300) and following the fluorescence of GFP over time. Figure 4.6 shows chromatograms of ACA8-GFP in all tested detergents. Chromatograms of ACA8-GFP solubilized in either DDM or C12E8 both showed only minor peaks at the void volume and a major peak between 11.5 ml and 11.7 ml, which might correspond to monomeric ACA8-GFP (4.6 a + b). Whereas, in chromatograms of UDM, a maltoside with shorter hydrophobic chains than DDM, the main peak is shifted towards lower elution volumes, indicating an increase in hydrodynamic radius, probably due to aggregation/unfolding (4.6 c). This effect is more pronounced in DM a detergent which has even shorter hydrophobic chain than UDM. The chromatogram shows a second peak at even lower elution volumes (4.6 e). All other tested detergents could not stabilize ACA8-GFP more than DDM or C12E8 did. The void peak was higher or the main peak was shifted towards lower elution volumes in all other

chromatograms (4.6 d + f-i). Since, DDM shows the highest solubilisation efficiency as well as gave a rather homogenous sample in the FSEC experiment, large-scale purification of ACA8 was performed in DDM.

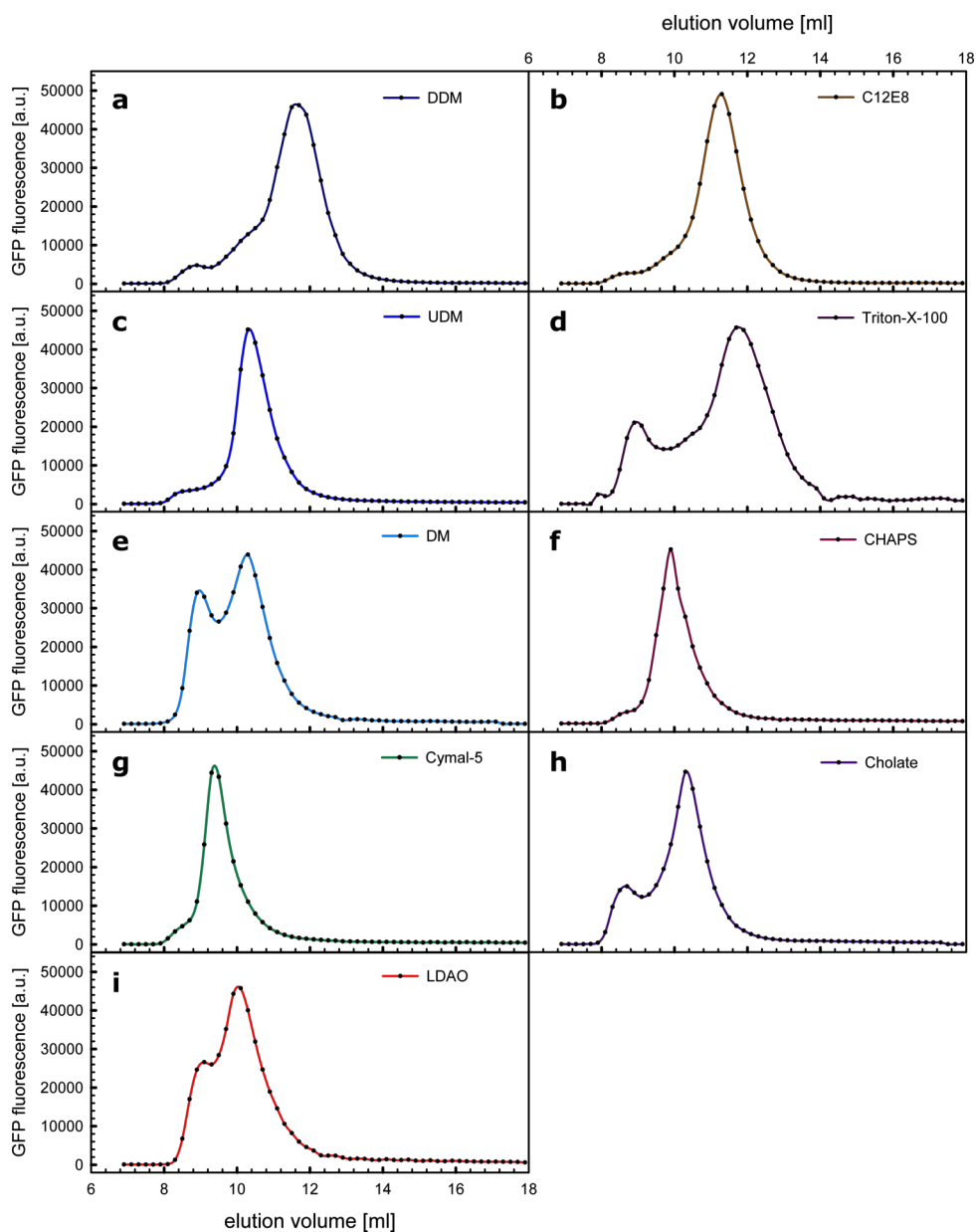


Figure 4.6: Fluorescence detection size-exclusion (FSEC) profiles of ACA8-GFP in various detergents. (a-i) Membrane fractions of ACA8-GFP were solubilized in 1% of corresponding detergent and cleared solubilized membranes were loaded on a S200 (10/300) column, the GFP fluorescence of each fraction was measured and plotted against the elution volume.

Purification of ACA8 in DDM

Based on the results from pre-screening of detergents of ACA8-GFP, large-scale purification was carried out in DDM. Briefly, membrane fractions of expressed ACA8-GFP were purified and solubilized in DDM. After solubilisation non-solubilised proteins were removed via ultracentrifugation and further purified over a Ni-NTA column. Elution fractions containing ACA8-GFP were pooled and the GFP/His-tag was cleaved off through TEV-cleavage overnight. A second His-trap column was applied to bind the His-GFP and TEV protease to the column whereas the ACA8 did not. Purified ACA8 was loaded on a gel filtration column (S200 10/300) to judge the stability and homogeneity.

The proteins showed similar and reproducible solubilisation efficiency in DDM ranging from 80 % to 95 %. Similar observations could be made for their binding efficiency to the Ni-NTA resin (60-80 %). After the second His-Trap column only minor contaminants were present in the sample, which were further purified by size-exclusion chromatography (Fig. 4.7 b). However, the size-exclusion profile revealed a concentration dependent aggregation (Fig. 4.7 a). At low concentration (1 mg/ml) the chromatogram showed two main peaks, one at the void volume (8.5 ml) and one at 12 ml, which corresponds to monomeric ACA8. Increasing the concentration up to 2.5 mg/ml, the 12 ml peak is nearly vanished and nearly all ACA8 was aggregated and eluted in the void peak (Fig. 4.7 a).

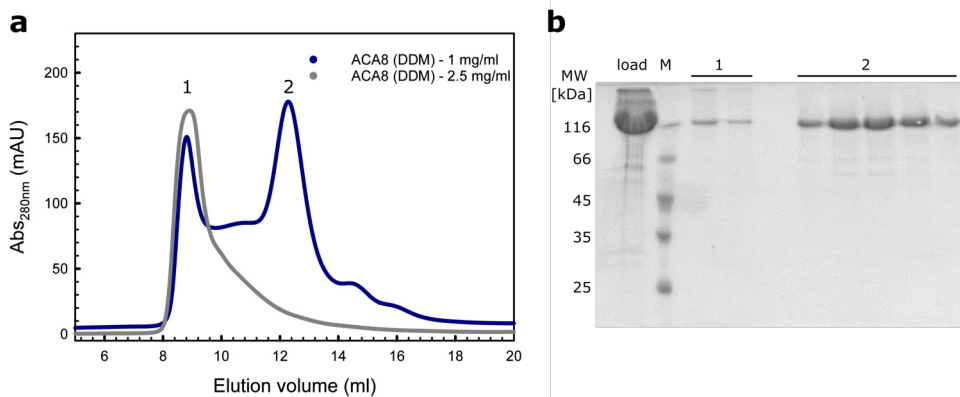


Figure 4.7: Size-exclusion chromatography (SEC) of ACA8 in DDM. (a) ACA8 were purified in DDM and concentrated to either 1 mg/ml (blue) or 2.5 mg/ml (grey) and loaded on a S200 (10/300) column to analyse the stability. (b) SDS-PAGE analysis of SEC chromatogram of ACA8 (DDM) - 1 mg/ml. Bands; load = Ni-NTA elution fraction, M = molecular weight marker, 1 = void volume, 2 = elution fraction of second peak

The results are contradictory to the FSEC experiments indicating that major changes in the ACA8 sample occurred. The concentration of ACA8 in the membrane fraction was certainly below 1 mg/ml and therefore much lower in the FSEC experiments

than for the experiments with purified ACA8. As Fig 4.7 shows higher protein concentration clearly drives the aggregation/unfolding process. Concentration dependent aggregation is often seen in cases where the detergent does not fully cover the transmembrane part of the protein and therefore badly mimics the membrane environment. During the FSEC experiments the cleared membrane fraction was loaded onto the column. It is likely that ACA8 contained much more bound lipids in the membrane fraction than in purified fractions. Lipids can be crucial for stabilizing the native conformation of a membrane protein. As it seems that DDM is not able to cover the whole transmembrane part of ACA8 completely, lipids become more important. With each purification process more and more lipids get washed off and the lack in surrounding lipids might further destabilize ACA8. Many parameters changed from FSEC experiments to full purification experiments. These results show, although the screening of the homogeneity of IMPs in crude lysates using FSEC is a cheap and time saving method, it is a relatively poor mimic of preparative purification and was not suitable for ACA8. Moreover, these results clearly show that DDM is not a suitable detergent for ACA8 and further screening was necessary.

Buffer and detergent optimization using differential scanning fluorimetry

One of the major factors that can influence the stability and homogeneity of a membrane protein is the detergent it is solubilised and purified in [150–153]. A bad coverage of the hydrophobic part of an IMP by the detergent micelle can contribute to increased sample heterogeneity and a dramatically reduced thermodynamic stability [154, 155]. A widely used method to assess the thermal stability of a protein is differential scanning fluorimetry [156, 157]. This method often uses fluorescent dyes such as 7-diethylamino-3-(4-maleimidyl-phenyl)-4-methylcoumarin (CPM) and SYPRO Orange, which can be problematic with IMPs [157–159]. Therefore, thermal unfolding was measured by monitoring changes in intrinsic fluorescence of the aromatic residues upon heat unfolding by using the Prometheus NT.48 (see section 4.2.7), a method, which has been successfully applied to membrane proteins [87, 160]. By using the intrinsic fluorescence the transition midpoint (T_m) values can be determined without the need for additional dyes [87, 157, 161]. In contrast to the performed FSEC experiments, detergent screening using DSF was carried out with purified ACA8, which better mimics preparative purification conditions and therefore greatly accelerates the transition from analytical results to large-scale purification.

In order to optimize the buffer condition as well as the detergent micelle around the hydrophobic transmembrane part of ACA8, a high-throughput additive and detergent screen was designed. To reduce side effects coming from the fused GFP molecule ACA8 was expressed with a C-terminal His₈-tag but without GFP (see

4.2.1) and purified in DDM with a concentration close to the cmc. Subsequently, concentrated ACA8 was diluted fivefold in buffer containing the new detergent and incubated for 1 h before the measurements. A broad range of detergents was screened including the detergents already used in the FSEC experiments. In addition, more recently developed detergents such as the neopentylglycol based detergents (LMNG, DMNG, OGNG) as well as steroid based detergents like CHS or GDN were screened [162, 163]. For all of the investigated detergents, the DSF traces allowed unambiguous assignment of a transition mid-point (T_m).

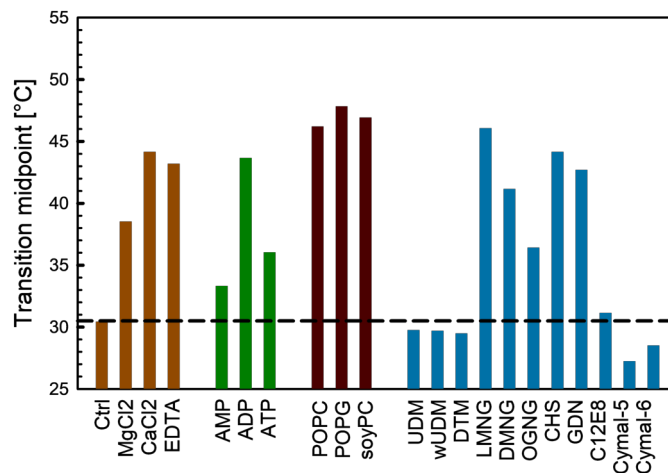


Figure 4.8: Thermal stability analysis of ACA8 by nDSF to optimize detergent and additive conditions. Overview of melting temperatures (T_m) of ACA8 in buffer containing different additives as well as different detergents/lipids. ACA8 was purified in DDM and concentrated to 2.5 mg/ml. Concentrated ACA8 was diluted in buffer containing new additives or detergents (as listed in Table 4.1).

The thermal stability of purified ACA8 in DDM is very low with a T_m of 30 °C. The neopentylglycol (NG)-based detergents LMNG and DMNG increased the thermal stability by 16 °C or 11 °C, respectively (Fig. 4.8). On the other hand, the stabilizing effect of OGNG, a NG-based detergent with a shorter hydrophobic chain than LMNG, was much less pronounced. Sterol-based detergents such as CHS and GDN are well known to be important for stabilizing eukaryotic membrane proteins [164]. The stabilizing effect of these two detergents was slightly weaker than for LMNG ($\Delta T_m = 14^\circ\text{C}$, $\Delta T_m = 12^\circ\text{C}$) but significantly increased the thermal stability of ACA8 as well. Whereas, the addition of maltoside based detergent did not show any stabilizing effect. Previous experiments already suggested the importance of surrounding lipids in order to stabilize ACA8. Therefore, different lipids with negatively charged headgroups as well as zwitterionic lipids were screened. All tested lipids significantly increased the thermal stability ($\Delta T_m = 15^\circ\text{C}$) but no major differences between the head groups were visible.

Approximately 50 % of ACA8 are cytoplasmic domains. These soluble domains are

not stabilized by the detergent micelle but might have an impact on the overall thermal stability of ACA8. The domains are involved in nucleotide binding and hydrolysis. Therefore, different nucleotides as well as divalent ions were screened for their ability to stabilize the soluble domains. All nucleotides showed stabilizing effects with ADP showing the highest T_m of 43 °C amongst them. The addition of divalent ions (Mg^{2+} or Ca^{2+}) leads to an increased thermal stability ($\Delta T_m = 8^\circ C$ or $\Delta T_m = 14^\circ C$). Almost the same effect is visible after the addition of EDTA ($\Delta T_m = 13^\circ C$), which binds all co-purified divalents. Whether the stabilizing effect of divalent ions to ACA8 is significant is therefore not clear. Overall, the screen found different detergent as well as additives, which all on their own are able to significantly increase the thermal stability in contrast to DDM alone.

The detergent micelle is a critical parameter for optimizing the stability of ACA8s

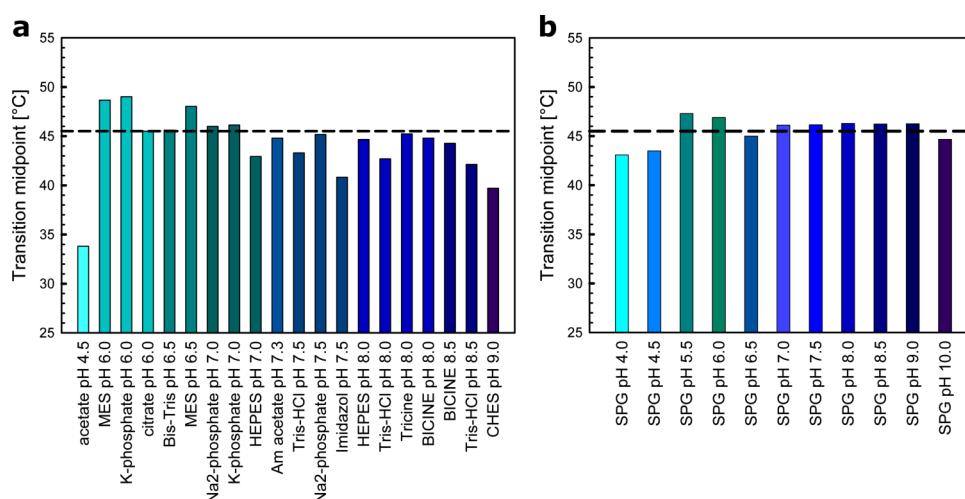


Figure 4.9: Thermal stability analysis of ACA8 by nDSF to optimize buffer pH conditions. Overview of melting Temperatures (T_m) of ACA8 in buffer with different pH values. Standard buffer components (a) or complex buffer (b) in a pH range from 4.0 - 9.0 were used. ACA8 were purified in LMNG and concentrated to 5 mg/ml. Concentrated ACA8 were diluted in buffer containing new buffers (as listed in Table 4.1).

transmembrane domain. As around 50 % of ACA8s mass are soluble domains the buffer pH might be a critical parameter for the stability and homogeneity as well. For that reason, a pH screen, based on the developed RUBIC thermofluor screen [165] was used to further optimize the buffer. ACA8 was purified in LMNG (see 4.2.5) and a buffer pH ranging from pH 4.5 - pH 9.0 was screened. Figure 4.9 a shows the results from the screen with standard buffer components. The transition midpoints above pH 4.5 and below pH 8.5 scatter around the reference line (T_m of ACA8 in LMNG). None of the condition showed a significant stabilizing effect. To ensure that the T_m values are not affected by the components itself rather than the pH, the same pH range was screened with complex buffer systems. The combination of succinic acid, sodium phosphate monobasic monohydrate and glycine (SPG)

covers a large pH range and enables to screen for optimal buffer pH without seeing buffer effects. SPG buffer revealed similar results, showing that a change in the buffer pH does not increase the thermal stability.

Purification of ACA8 in LMNG

ACA8 showed the highest thermal stability in LMNG, a neopentyl glycol - based detergent. This relatively new class of amphiphiles binds much stronger to the protein as the CMC is an order of magnitude lower than that of DDM. It has been shown that they are able to extract IMPs from native membranes as well as stabilizing a variety of different eukaryotic membrane proteins [162]. As DDM greatly destabilized ACA8, LMNG was kept throughout the whole purification, including solubilization. After solubilisation non-solubilised proteins were removed via ultracentrifugation and further purified over a Ni-NTA column. Elution fractions containing ACA8 were pooled and purified ACA8 was loaded on a gel filtration column (S200 10/300) to judge the stability and homogeneity. LMNG was added to the SEC buffer

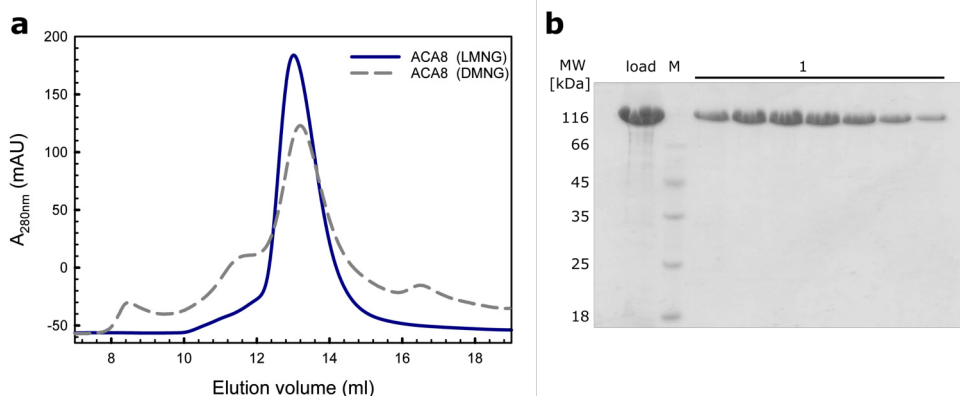


Figure 4.10: Size-exclusion chromatography (SEC) of ACA8 in maltoside neopentyl glycol detergents. (a) ACA8 was solubilized with LMNG (blue, solid line) and either kept for further purification or changed during Ni-NTA purification to DMNG (grey, dashed line). Affinity-purified ACA8 was concentrated to 5 mg/ml and loaded on a S200 (10/300) column to analyse the stability. (b) SDS-PAGE analysis of SEC chromatogram of ACA8 (LMNG). Bands; load = Ni-NTA elution fraction, M = molecular weight marker, 1 = elution fraction of SEC peak

(30 mM Tris pH 8.0, 150 mM NaCl, 1 mM CaCl₂ 0.5 mM TCEP) to a final concentration of 0.003 % - 0.01 % (3 - 10 × cmc). The chromatogram of ACA8 in LMNG showed a single, highly symmetrical peak with an elution volume of around 13 ml, suggesting that the molecule behaves as a monodisperse species (Fig. 4.10 a). In contrast, the chromatogram of ACA8 in DMNG shows three peaks; one small void peak, a main peak at 13.2 ml and a third one at around 11.5 ml. This indicates that changing the detergent to DMNG ACA8 starts to unfold, which yields a slightly more polydisperse solution. It is likely that the slightly shorter hydrophobic chain

does not fully cover the transmembrane domain and therefore induced the unfolding process. SDS-PAGE shows minor impurities in the affinity elution fraction and a highly pure sample after SEC with 95-98 % pure sample (Fig. 4.10 b).

Three different constructs were tested to further improve the yield of purified and stable ACA8. In addition to the already described ACA8-GFP-His₈ construct, the GFP was deleted which produced ACA8 with a C-terminal His₈-tag. Moreover, a construct with N-terminal His₈-tag was tested as well. The solubilization efficiency was almost the same for all constructs but ACA8 with N-terminal His₈-tag binds more efficiently to the Ni-NTA resin, suggesting that the N-terminal region is more accessible. The higher binding efficiency leads to the highest yield of 0.5 mg ACA8 per 1 l SC medium, whereas the ACA8-His₈ construct yield 0.3 mg ACA8 per 1 l SC medium. Due to the lower binding efficiency as well as the general loss during TEV-cleavage the ACA8-GFP-His₈ yield the lowest amount of purified ACA8 (0.1 mg ACA8 per 1 l SC medium). Combining all results, expressing ACA8 with N-terminal His₈-tag in BJ5460 cell in uracil depleted selective media (SC media) and solubilizing as well as purifying in LMNG yields the highest amount of pure ACA8.

Table 4.2: Purification specification of different ACA8 constructs

Construct	Solubilisation efficiency [%]	Binding efficiency to resin [%]	ACA8 from 1 L SC media [mg]
ACA8-GFP-His ₈	80 - 90	60-70	0.1
ACA8-His ₈	80 - 95	60-70	0.3
His ₈ -ACA8	80 - 95	70-80	0.5

4.3.2 Reconstitution of ACA8 into nanodiscs

Detergents do not mimic the natural lipid environment and often result in reduced activity of IMPs and may also lower membrane protein stability [10, 86, 166, 167]. Moreover, the presence of specific lipids is often essential for the activity of IMPs, and due to their dissociating properties, detergents can strip off structurally and functionally important lipids [168]. It has been previously demonstrated that phospholipids, both the hydrophobic chain as well as the head group are important for human PMCA activity and also stability [169, 170]. Phospholipid bilayer nanodiscs, developed in the last decade, have proven a promising new platform for studies of membrane anchored and integral membrane proteins under defined experimental conditions [76]. Several types of nanodiscs, like MSP-based and saposin-based ones, have been established in order to perform structural studies of integral membrane protein in a native-like lipid environment. Systematic comparison of both systems showed that they perform equally well in terms of stability and activity (see Chapter 3) and are both suited for structural and functional studies of IMPs in solution. The use of nanodiscs has enabled investigations of lipid dynamics, molecular relationships between lipids and proteins and other small molecules [17, 82, 171] and is therefore well suited to study the activation process of ACA8 in a native-like lipid environment.

The goal was to incorporate ACA8 into MSP-based nanodiscs, as they showed slightly higher thermal stability (see chapter 3.3.2.2). Assembly of membrane proteins into nanodiscs follows the rules for empty nanodiscs. Additional parameters to consider are the choice of detergent to initially solubilize the IMP from its membrane, choice of nanodisc size, and the lipid to MSP to membrane protein ratio. Since, it is usually not known how many lipids a particular protein will displace in the fully assembled nanodisc, a titration at various target:MSP:lipid ratios is usually needed [24, 172]. Importantly, a critical number of phospholipids associated with the nanodisc-protein complex may be necessary for the successful assembly [29]. For that reason ACA8 was first incorporated into the bigger nanodiscs based on MSP1E3 protein to ensure enough lipids are surrounded. The used ACA8:MSP1E3 ratio was high (1:10), as the excess of MSP molecules keeps the MSP1E3:lipid ratio almost unaffected from that of empty nanodiscs (nanodiscs without IMP), which reduces the parameters that need to be screened. ACA8 was affinity-purified in LMNG and elution fractions were pooled and used directly for assembly. The zwitterionic lipid POPC was used as a starting point as its phase transition temperature enables the assembly in the cold (at 4 °C).

SEC chromatograms of all tested ratios showed the presence of several peaks (Fig. 4.11). The leading peak at 8.5 ml corresponds to high molecular weight aggregates, which is followed by a broad peak at around 11 ml and two at 11.9 ml to 14 ml. ACA8 co-elutes together with MSP1E3 between 9.5 ml to 13 ml, whereas in the last

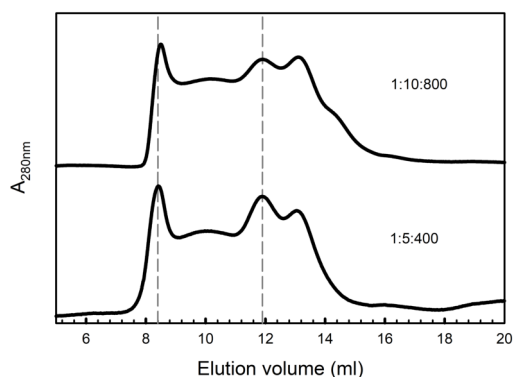


Figure 4.11: Size-exclusion chromatography of assembly of ACA8 into MSP1E3 nanodiscs. ACA8 was affinity purified in LMNG and mixed with MSP1E3 and POPC in a molar ratio of either 1:10:800 or 1:5:400 (ACA8:MSP1E3:POPC). Samples were loaded after biobead incubation on a S200 10/300 column to analyse the assembly rate. Reference line (dotted gray line) marks peaks corresponding to either the void volume (8.5 ml) or ACA8 monomer in MSP1E3 nanodiscs.

peak only MSP1E3 is visible, which corresponds to empty MSP1E3 nanodiscs. The peaks at 10 ml and 11.9 ml might correspond to assembled nanodiscs with either monomeric (peak at 11.9 ml) or dimeric (peak at 10 ml) species of ACA8 but could also correspond to partly assembled discs with partly aggregated ACA8. Previous studies on human PMCAs showed potential dimeric species after unfolding of individual functional domains, which illustrates the ability of PMCAs to form dimers [173]. Whether the peak at 10 ml corresponds to a fully assembled and stable nanodisc with an ACA8 dimer or to partly aggregated species cannot be distinguished based on the chromatogram. However, the overall shape of the chromatogram does not change significantly by varying the ACA8:MSP:lipid ratio, especially the peak intensity at 10 ml. Only minor changes in the peaks at 11.9 ml and 13 ml are visible, indicating that MSP1E3 nanodisc might enable the incorporation of a significant proportion of ACA8 dimers. For that reason the size of the nanodisc was changed from 12 nm to 9.7 nm by varying the size of the MSP molecule from MSP1E3 to MSP1D1 to selectively incorporate monomeric ACA8.

To optimize the incorporation of ACA8 into MSP1D1 nanodisc a broad range of different ratios was screened. The optimal MSP1D1:POPC ratio for the assembly of empty nanodiscs is 1:30 (see chapter 3). This ratio was kept in high ACA8:MSP1D1 ratios and was gradually reduced together with lower ACA8:MSP1D1 ratios. Detergents were removed with BioBeads to start the assembly reaction. All SEC chromatograms showed two main peaks at 8.5 ml and 13.8 ml, respectively (Fig. 4.12 a). In the peak at the void volume mostly aggregated ACA8 eluted and the peak intensity increased with lower ACA8:MSP1D1 ratios. The second peak at 13.8 ml corresponds to empty nanodisc. With lower ACA8:MSP1D1 and therefore lower

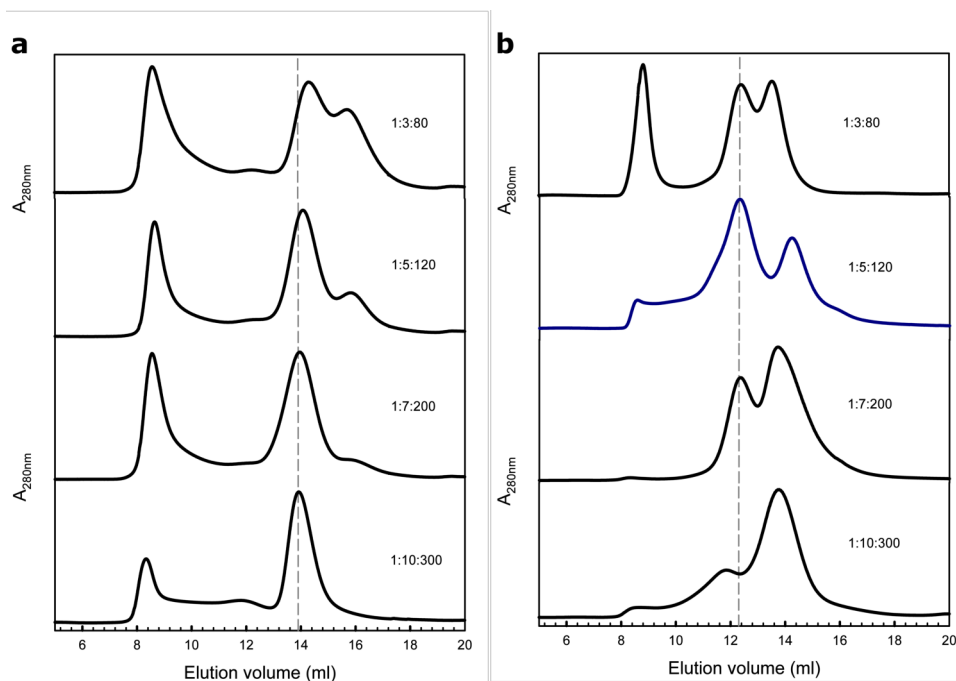


Figure 4.12: Size-exclusion chromatography of assembly of ACA8 into MSP1D1 nanodiscs. ACA8 were affinity purified in LMNG and mixed with MSP1D1 and POPC in different molar ratios. Detergents were removed with either BioBeads (a) or cyclodextrin (b). Samples were loaded afterwards on a S200 10/300 column to analyse the assembly rate. Reference line (dotted gray line) marks elution volume where peaks corresponding to either ACA8 monomer in MSP1D1 nanodisc (b) or empty nanodiscs elutes (a).

MSP:lipid ratios a third peak at 16 ml appeared, which corresponds most likely to MSP1D1 molecules alone. However, in none of the tested ratios a peak which corresponds to assembled ACA8-MSP1D1 nanodiscs was visible, indicating that given conditions are not sufficient to efficiently incorporate ACA8 into MSP1D1 nanodiscs. Detergent removal is one of the driving forces during the assembly of nanodiscs and incorporation of IMPs in the aforementioned. The lipids were always solubilized in cholate, a detergent with a high CMC, which binds rather weakly and is easy to remove. In contrast to that, ACA8 was purified in LMNG which has a very low cmc and binds much stronger to ACA8 and hence is more difficult to remove. During the assembly it is likely that cholate is much faster removed than LMNG, which in turn favors the assembly of empty nanodiscs rather than the assembly of ACA8-MSP1D1 nanodiscs. For that reason, in another screen detergents were removed with cyclodextrin instead of BioBeads. Cyclodextrin is composed of a sugar ring with a hydrophobic core inside which has a higher affinity for detergents and is applicable to a wide range of detergents [174]. Bigger cyclodextrin rings (like γ -cyclodextrin) are able to bind more voluminous detergents such as LMNG, which is likely to improve the assembly kinetics of LMNG-purified ACA8 into nanodiscs.

Detergent removal with cyclodextrin reduced the intensity of the void peak significantly, indicating an improved incorporation rate of ACA8 into MSP1D1 nanodiscs. SEC chromatograms of all tested ratios showed a peak at 12.2 ml, which corresponds to monomeric ACA8 incorporated into MSP1D1 nanodiscs (Fig. 4.12 b). The peak intensity at 13.8 ml gradually decreased with lowering the ACA8:MSP1D1 ratio, whereas the peak intensity at 12.2 ml increases at the same time. A molar ratio of 1:5:120 (ACA8:MSP1D1:POPC) showed the best result with almost no void peak and a major peak at 12.2 ml (ACA8-MSP1D1 nanodiscs). Reducing the ACA8:MSP ratio further void peak significantly increased, which indicates that more ACA8 started to aggregate as the ratio is slightly off. These results show that detergent removal of LMNG is much more efficient using cyclodextrin, which in turn enables a sufficient incorporation of monomeric ACA8 into MSP1D1 nanodiscs. Size-exclusion chromatography of ACA8-MSP1D1 nanodiscs after 5 days showed a single symmetrical peak at 12.2 ml, indicating that stable nanodiscs were formed. Moreover, the native-like lipid environment further stabilizes ACA8, giving a thermal stability of almost 60 °C (Fig. 4.13).

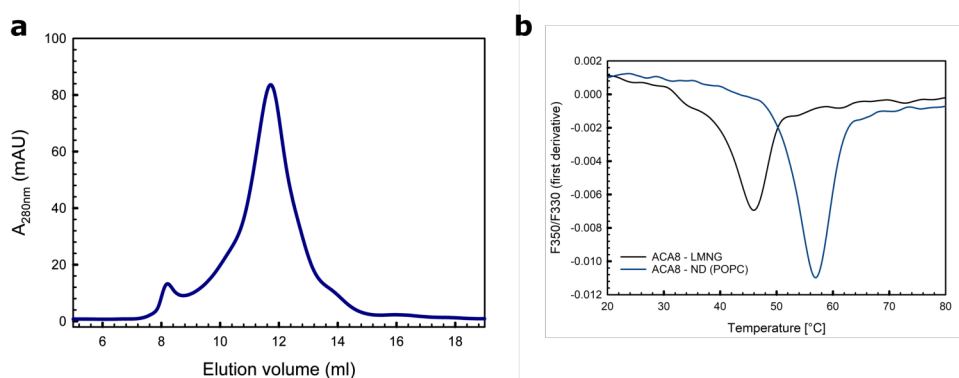


Figure 4.13: Stability of ACA8-MSP1D1 nanodiscs. ACA8 was incorporated into MSP1D1 nanodiscs and corresponding size-exclusion fractions were loaded on a S200 10/300 column after 5d (a). Stability of ACA8 in nanodiscs was measured using nDSF techniques and the transition midpoint (T_m) were calculated from first derivative analysis (b).

4.3.3 Biochemical characterization of the activation process of ACA8 by CaM

4.3.3.1 Native mass spectrometry confirms a bimodular mechanism

Previous crystallization studies on ACA8's regulatory domain showed two calmodulin binding sites with different affinities suggesting a two-step activation mechanism of ACA8 [67]. Native mass spectrometry is able to determine protein stoichiometries in soluble and membrane protein complexes [126, 175]. Therefore, native mass spectrometry experiments were carried out in order to investigate the stoichiometry of bound calmodulin during the activation process of ACA8, in the context of the full-length protein. Full-length ACA8 was solubilized in DDM, and further purified (see 4.2.5 4.3.1.2). The complex was formed by mixing purified ACA8 with excess of CaM/ right before the buffer exchange to ammonium acetate (see 4.2.9). The resulting spectra revealed masses of ions that correspond to apo ACA8 (without bound CaM), as well as ACA8 with one (ACA8-CaM) or two bound CaM molecules (ACA8-CaM₂) (see Fig. 4.14, theoretical and measured masses in Table A.2) [126, 127].

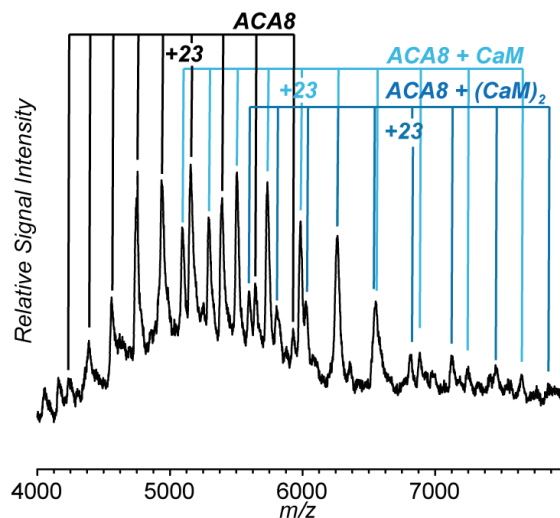


Figure 4.14: Native mass spectrometry experiments of ACA8-CaM complex. DDM-purified ACA8-CaM complex was analysed by native mass spectrometry. Spectrum shows masses that correspond to apo-ACA8 (black), ACA8 + CaM (light blue) and ACA8 + 2CaM (dark blue). Reprinted from Nitsche et al. [126, 127]

Notably, the ratios of apo-ACA8 and the different ACA8-CaM complexes, indicated by the signal intensities does not reflect the distribution of the aforementioned species in solution. The detergent micelle around the transmembrane part was released for MS analysis. This release required high collision energies during the measurements, meaning that analyte ions were accelerated and collided with argon molecules in the

collision cell. By such high energy, protein-protein interactions can be disrupted as a negative side effect, causing collision-induced dissociation. In the full m/z range spectrum clear signs of CaM dissociation from ACA8 are visible (Fig. 4.15) [126, 127]. In the spectrum all species were identified. Free CaM can be found in the low m/z -range. Based on the charge state of CaM and ACA8 it was possible to judge whether they were dissociation products or never formed a complex. The expected charge number of dissociated CaM was higher compared to "unbound" CaM (CaM that did not dissociate) [126, 127, 176]. Therefore, CaM was analysed separately to analyse the charge state of unbound CaM and it carried either +6 or +8 charges (Supplementary A.1). In the analysis of the ACA8-CaM complex charge states ranging from +5 to +12 were observed (Fig. 4.15). This indicates that detected CaM molecules derives from a dissociation event. Due to the charge partitioning effect [176] ACA8 was expected to carry less charges after a dissociation event. In the spectrum only low-charged masses corresponding to ACA8 with one bound CaM was found. This indicates that the maximum of two CaM molecules are able to bind to ACA8 [126, 127]. This data is in good agreement with the proposed bimodular activation mechanism of PMCA8 [67].

DDM proved to be a suboptimal detergent which significantly destabilizes ACA8 and certainly made data acquisition more challenging. Native mass spectrometry experiments with ACA8 purified in LMNG, a more stabilizing detergent, did not yield applicable data. The critical micelle concentration (cmc) from LMNG is almost an order of magnitude lower than those for DDM, which results in a stronger interaction with ACA8's transmembrane part. Native mass spectrometry experiments with ACA8 purified in LMNG were not successful as the release of detergent micelles needed even higher activation energies, which in turn increased the collision induced dissociation events.

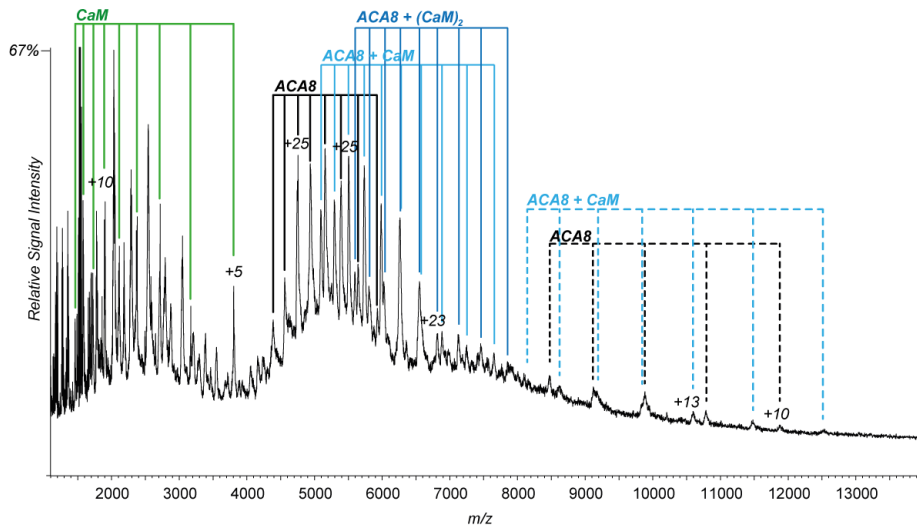


Figure 4.15: Full m/z ratio of native mass spectrum of DDM-purified ACA8-CaM. In addition to the identified masses for apo-ACA8 (black, solid line), ACA8 + CaM (light blue, solid line) and ACA8 + 2CaM (dark blue, solid line), ACA8 in a low charged state (black, dotted line) and low-charged ACA8 + CaM (light blue dotted line) were found. CaM (green, solid line) can be found in the low m/z -range. Reprinted from Nitsche et al. [126, 127]

4.3.3.2 Activity measurements

In order to gain functional insights into the activation process of ACA8 ATPase activity measurements were carried out using the Baginsky assay [130]. The method measures the production of inorganic phosphate, a result of ATP hydrolysis, which is correlated to ACA8's pump rate. For functional studies ATPase activity was measured in the presence or absence of CaM, its major activator. The ACA8-CaM complex in LMNG showed a two-fold higher ATPase activity compared to the activity in the absence of CaM (basal activity) (Fig. 4.16 a), indicating the functionality of the pump in LMNG [126].

Since previous studies showed that lipids affect the pump stability as well as the activity [169, 170], ATPase activity assays were carried out in ACA8 reconstituted in nanodiscs containing 1-palmitoyl-2-oleoyl-sn-glycero-3-phosphocholine (POPC) as lipid, which enables the controlled variation of the lipidic environment surrounding the pump. ATP hydrolysis assays of ACA8 in POPC-nanodiscs showed a much higher activity in the presence of CaM compared to the activity in detergents (Fig. 4.16 a). This result shows the importance of a lipidic environment for the activation process of ACA8 [126] as previously demonstrated for human PMCA [170, 177].

Previous studies on human PMCA suggested that acidic phospholipids increase the enzymes apparent affinity for Ca^{2+} and its turnover whereas neutral phospholipids

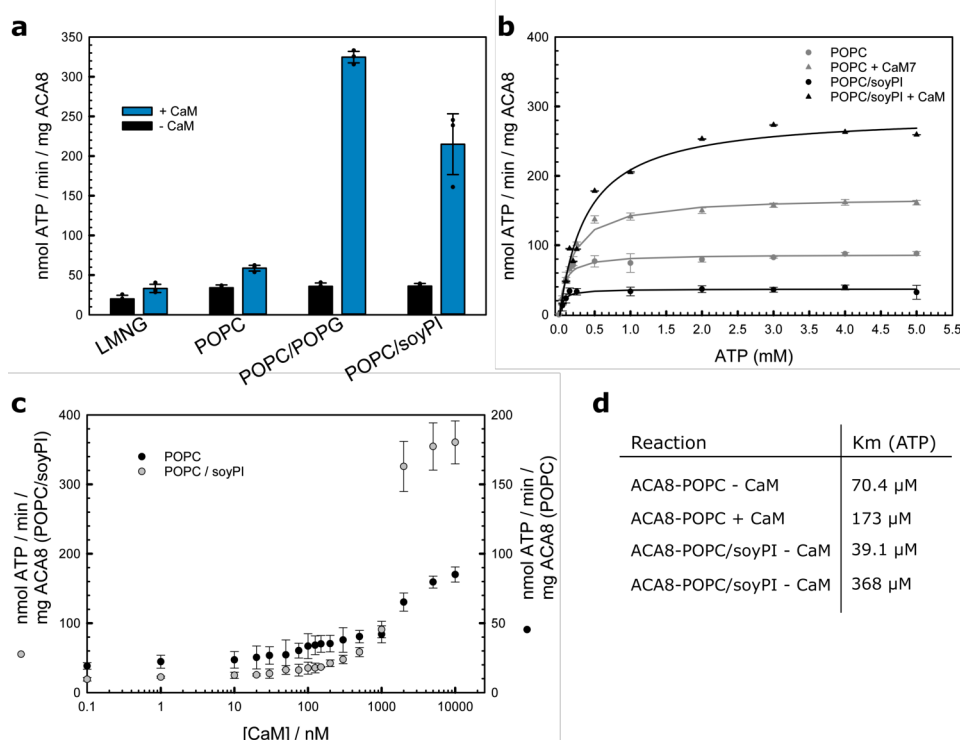


Figure 4.16: ATPase activity of ACA8 in MSP1D1 nanodiscs. (a) ATPase activity assay of ACA8 in detergent micelles (LMNG) and nanodiscs containing different lipids (POPC, POPG, soyPI) with (blue bars) or without (black bars) calmodulin. (b) ATP-titration activity measurements of ACA8 in nanodiscs containing either POPC (grey) or POPC/soyPI mix (black). ATP titrations were performed in the presence and absence of CaM and resulting Km values are listed in d. (c) CaM titration activity assay of ACA8 incorporated in nanodiscs containing POPC (black) or POPC/soyPI (grey).

(PL) like PC and PE were without effect [177–179]. In order to analyse the effect of anionic lipids, ACA8 was reconstituted in MSP1D1 nanodiscs (ND) using lipid mixtures containing POPC with either POPG or soyPI. All different ACA8-nanodisc complexes showed similar profiles on a size-exclusion chromatography profiles, indicating no major structural changes due to the different lipids leading to different hydrodynamic radius (Supplementary Fig. A.2) [126]. Reconstitution of ACA8 into nanodiscs containing 30 % POPG or 30 % soyPI showed a drastic increase in ATPase activity (3-5 fold) compared to ACA8 POPC-nanodiscs (Fig. 4.16 a). These results suggest that the negatively charged head groups are able to further increase the ATPase activity, and most likely the pump rate [126]. The specific activities of CaM-activated ACA8 in this study are in good agreement with previous published activities in microsome preparations [111, 180–182]. Notably, the tested composition with acidic PLs does not show any stimulating effect in the absence of CaM, showing that these lipids are not able to activate the pump independently.

The role of acidic PLs in ACA8 activation by CaM were further analysed by performing a CaM-titration to the apo-ACA8 in POPC and POPC/soy-PI NDs. Both curves show a CaM-dependent increase in the ATPase activity rate. In addition, two transition were observed for both curves, whereas the first transition is much less pronounced compared to the second one. Nevertheless, these results further supports the bimodular activation mechanism [67, 126]. Moreover, above CaM concentrations of 500 nM (second transition) a significant differences in ATPase activity between ACA8 in POPC-nanodiscs and POPC/soyPI-nanodiscs is shown. In the presence of soyPI in the nanodiscs the ATPase activity was much higer (above 500 nM CaM). This results indicates that once two CaM molecules are bound, the head group of soyPI is able to further stimulate the activity [126]. Studies on PMCAs with a photo-activatable phosphatidylcholine analog showed that CaM and phosphatic acid (PA) have both independently effects the enzyme activity as well as transmembrane conformation [117]. These findings are in good agreement with the results presented in this study [126].

Acidic PLs have no significant effect on the affinity of Ca^{2+} for sarcoplasmic/ endoplasmatic reticulum Ca^{2+} ATPase (SERCA), but do reduce the level of ATP binding, thereby inhibiting the enzyme activity [183]. The effect of acidic phospholipids on ATP affinities on ACA8 was investigated. Therefore, ATP was titrated to apo-ACA8 in POPC and POPC/soyPI NDs in the presence and absence of CaM. Enzyme activity increased with [ATP] along a hyperbolic curve and reached saturation between 2 mM and 3 mM ATP. The presence of CaM increased the V_{max} , which is further increased by soyPI. In general, neither the presence of CaM nor acidic PLs affect the apparent affinity of ATP.

Altogether, these results support the bimodular activation mechanism and further show the importance of diverse surrounding lipids for the activation process [126]. Although acidic PLs are not able to independently activate ACA8, it is likely that the negative head groups interacts with the regulatory domain (RD) after it is replaced from the core enzyme by CaM. This interaction may stabilize the activated conformation and, thus, increase the maximal velocity (V_{max}) of the pump.

4.3.4 Biophysical characterization of the activation process of ACA8 by CaM

4.3.4.1 Fluorescence anisotropy titration

In order to investigate the structural changes leading to the activation of ACA8 by CaM, the different binding events were analysed by fluorescence polarization spectroscopy [126]. Fluorescence polarization (FP) measurements provide information on molecular orientation and molecular mass. Fluorescent molecules, which are excited with linearly polarized light, will emit polarized light as well. The polarization

state is proportional to the molecular volume and therefore to the mass, when the viscosity and temperature are kept constant [132, 184]. Small fluorescent molecules tumble rapidly in solution resulting in depolarized emitted light. Upon binding of a larger molecule the tumbling speed of the fluorescent molecules significantly decreases (if the size difference is big enough), which increase the amount of polarized light (increase in FP). The sensitivity of the fluorescent dye makes FP a sensitive and powerful technique in protein-protein interaction studies of membrane proteins, as they are generally overexpressed to much less extent [185, 186].

Activation of ACA8 by CaM has been proposed to occur by binding of CaM to the regulatory domain (RD), which is then displaced from the core enzyme (ACA8core), removing the self-inhibition of the enzyme and thereby enables full conformational changes during the pump cycle [180, 187–190]. Previously, the activation of PM-CAs has been characterized only indirectly by detection of enzyme activity in the presence or absence of CaM [191]. Here, by fluorescence labeling of either RD or CaM it was possible to carefully dissect the different binding affinities of the various protein-protein interactions during activation [126].

Titration experiments

All experiments were performed using ACA8 constructs reconstituted in POPC-nanodiscs (see chapter 4.3.2) to ensure the mass differences in the different binding events are big enough to be detected by FP [126]. In a first experiment full-length ACA8 (flACA8) was titrated into fluorescein-labelled CaM (FITC-CaM) (Fig. 4.17 a). Thiol-specific fluorescein label was used to label CaM. As CaM harbors only one cysteine, the label was site-specifically introduced in a position which is neither involved in RD nor in Ca^{2+} binding. Titration of flACA8 into labeled CaM lead to an increase in the steady state anisotropy of FITC-CaM, as it is bound to larger flACA8 (measured fluorescence polarization values was converted into anisotropy values, which will be used in throughout the following section). Dissociation constants (K_d) were obtained by fitting the data to the equation corresponding to a one-site binding model, revealing a tight binding with an apparent K_d of 18 nM (Fig. 4.17 a).

In Tidow et al., 2012 [67] two independent CaM binding sites with different affinities to CaM were described. In this setup, only the binding of CaM to the high-affinity CaM binding site (CaMBS) is detected as the mass differences after binding of a second CaM molecule are too small. The obtained dissociation constants are in good agreement with previously published affinities determined for the isolated RD [67, 126]. To characterize the structural changes of the regulatory domain (RD) during the activation process, the regulatory domain of ACA8 (ACA8RD, residues 1-130) was expressed and purified in *E. coli*. To ensure fluorescence labeling a cysteine was

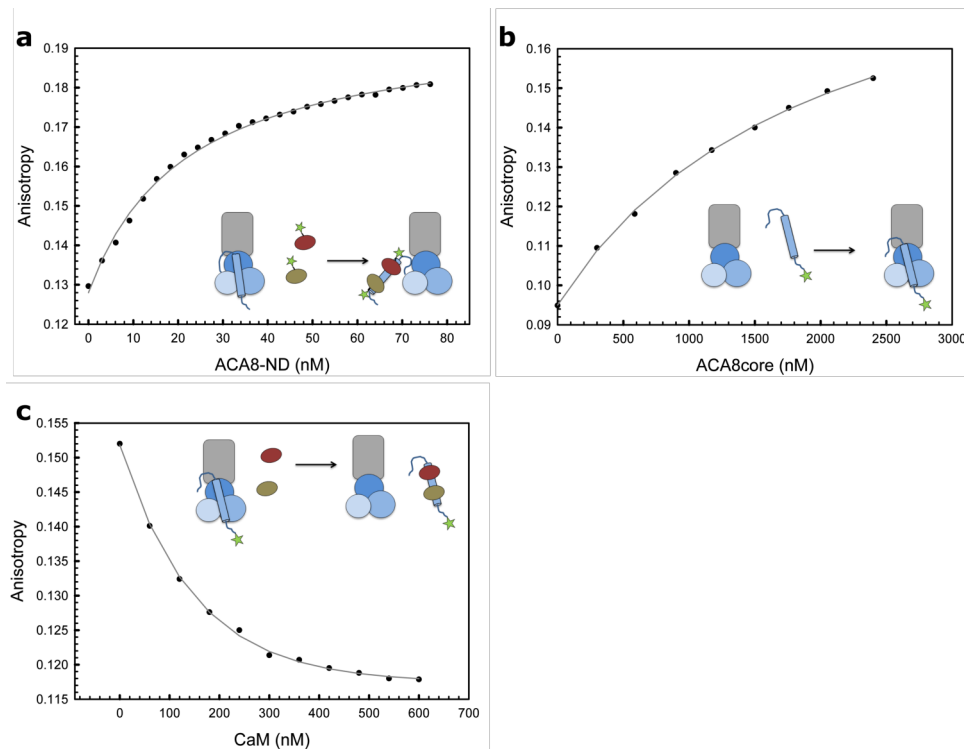


Figure 4.17: Fluorescence anisotropy to characterize binding affinities within ACA8-CaM complex. (a) Titration of of fluorescein-labeled CaM to full-length ACA8. Increase in FP indicate a binding with an K_d of 18 nM. (b) ACA8core was titrated into fluorescein-labeled RD. Binding curve shows a much weaker bining ($K_d = 1.7 \mu\text{M}$). (c) Competition assay. Complex composed of ACA8core fluorescein-labeled RD were formed as described in (b) and CaM were titrated to the complex. Decrease in anisotropy indicates displacement of RD from ACA8core through CaM-binding to RD. All experiments were performed using protein re-constituted in nanodiscs. Reprinted from Nitsche et al. [126]

introduced at the N-terminus of the ACA8RD sequence. Titration of the fluorescein-labelled ACA8RD to the core of ACA8 (residues 131-1074, a construct lacking the regulatory domain) yielded a dissociation constant (K_d) of 1.7 μM (Fig. 4.17 b), indicating a much weaker affinity of ACA8RD to the core of the pump [126]. In a competition experiment unlabeled CaM were titrated to the preformed complex, resulting in a decrease in steady state anisotropy ($K_{0.5}$ approx. 120 nM). This shows that ACA8RD forms a much smaller complex after titration of CaM, which is most likely due to the displacement of the RD from the core. This curve further shows that the displacement of ACA8RD from the core of ACA8 is dependent on CaM-binding to ACA8RD (Fig. 4.17 c) [126]. The displacement setup described in Fig. 4.17 c and the calculated $K_{0.5}$ shows indirectly binding a affinity of the low affinity CaMBS, as ACA8RD is only displaced once two CaM molecules are bound. This is in good agreement with the previously described bimodular mechanism [67, 126]. Overall, these binding experiments indicate that the regulatory domain binds weakly to the core of the ACA8 pump. CaMBS in the regulatory domain or regions in proximity

to those also binds to the core enzyme of ACA8. The binding of CaM to the regulatory domain results in the displacement of the RD from the core enzyme [180]. The regulatory domain has a lower affinity to the core enzyme than to Ca^{2+} -loaded CaM, suggesting that the availability of CaM is one of the dominant factors in the regulation of the activity of ACA8 [126].

4.3.4.2 Small-angle X-ray scattering analysis

Previous experiments showed that binding of CaM replaces the regulatory domain from the core enzyme rearranging the overall conformation of ACA8 (see Chapter 4.3.4.1). These conformational changes can be observed by size-exclusion chromatography (SEC) as well. The chromatogram of the ACA8-CaM complex showed a shift in the elution volume by almost 1 ml on a Superdex200, 10/300 column (11.1 ml for complex vs. 11.9 ml for ACA8 alone) (Fig. 4.18 a). This significant increase in the hydrodynamic radius upon CaM binding cannot be explained by the binding of two CaM molecules. However, this shift suggest a drastic change in hydrodynamic radius due to large conformational changes [126]. (Fig. 4.18 a). Studying such large conformational changes by X-ray crystallography are complicated, whereas small-angle X-ray scattering (SAXS) can easily provide low resolution structural information. Therefore, SAXS was used to study the activation process of ACA8 by CaM.

SAXS measurements were carried out using ACA8 alone as well as in complex with CaM. ACA8 was incorporated into nanodiscs composed of the zwitterionic lipid POPC to perform measurements in a native-like lipid environment. Each sample was measured with varying protein concentration (1-8 mg/ml) and no inter-particle interference was observed (see Supplementary Fig. A.3). Therefore, the dataset which corresponded to the most concentrated sample was chosen for further analysis (Fig. 4.18 b-d). Inspection of the Guinier region showed a linear line, indicating that the sample was free of aggregates. Binding of CaM lead to an increase in radius of gyration (R_g) from 5.3 nm for the apo ACA8 to 5.88 nm for the CaM-activated state and a slight increase in maximum diameter (D_{max}) (20 nm / 22 nm) once CaM is bound (Fig. 4.18 b-d) [126]. The measured $I(0)$ gave an estimate of M_r of 259 kDa for apo-ACA8 which is close to the theoretical M_r of 256.2 kDa calculated from a complex composed of 1xACA8 + 2x MSP1D1 +124xPOPC molecules (Table A.3). This assumption is based on a homology model of ACA8 incorporated into MSP1D1-POPC nanodisc using the CHARMM GUI web server [192]. The good agreement of both M_r values implied that the sample was monodisperse and ACA8 was incorporated into nanodiscs as a monomer.

In order to study the effect of anionic lipids on the activation process of ACA8 SAXS

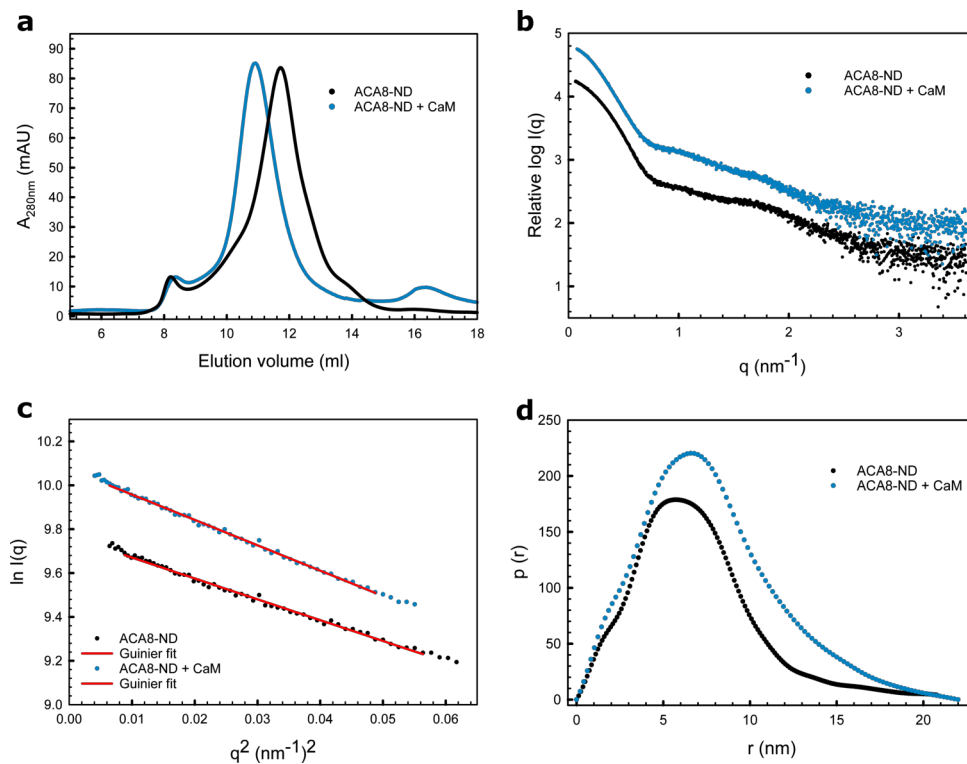


Figure 4.18: Small-angle X-ray scattering (SAXS) analysis of nanodisc-incorporated ACA8 and its complex with CaM. (a) Size-exclusion chromatography profile of ACA8 in nanodiscs (black line) and in complex with CaM (blue line) showed an expansion once CaM is bound (b) Scattering curve obtained for ACA8 in nanodiscs in apo conformation (black) as well as in complex with CaM (blue). (c) Guinier fit to the scattering data in the Guinier region of the data shown in (a) showed that the R_g is increased from 5.3 nm to 5.88 nm when CaM is bound. Linearity of the data points indicated the absence of inter particle interference. (d) Distance distribution plot of ACA8 in MSP1D1 nanodiscs in apo conformation (black) and in complex with CaM (blue) indicating that D_{max} increased once CaM is bound. [126]

measurements were carried out using ACA8 incorporated into MSP1D1 nanodiscs containing either POPG or soyPI. The R_g values of these samples were comparable to those obtained from apo-ACA8 in POPC-nanodiscs (Supplementary Fig. A.4). Upon binding of CaM leads to an increase in R_g values, indicating that the anionic lipids cannot activate the pump without the binding of CaM to the regulatory domain. However, combining these data with the results from the activity assays suggest that anionic lipids might function in later stages of CaM activation. Therefore it is likely that anionic lipids might stabilize an intermediate conformation that can readily be activated by CaM-binding leading to high activity gain (see Chapter 4.3.3.2) [126].

Experimental data from fluorescence polarization as well as from SAXS experiments suggest that the regulatory domain is displaced from the core enzyme during activation by CaM leading to major structural changes. Secondary structure analysis of the

regulator domain alone (ACA8RD, residues 1-130) were performed using far-UV circular dichroism spectroscopy. These experiments indicated that this domain consists partly of random coil segments with some degree of α -helicity, presumably spanning residues 4095 as observed in the ACA8RD-(CaM)₂ crystal structure [67] (pdb:4aqr) (Fig. 4.19 b) [126]. Due to the random coil region in ACA8RD it is likely that the regulatory domain becomes flexible in the activated state. Since SAXS provides structural information about the macromolecular flexibility and conformational heterogeneity of a molecule, the molecular flexibility of ACA8 in its CaM-activated state was inspected [193]. The Kratky plot reflects the global overall particle flexibility and is related to the particle volume as well as the scattering contrast between the protein and the buffer components. When the particle is flexible, the scattering contrast becomes poor and the scattering at high angles increases. Inspection of the dimensionless Kratky plot ($(qR_g)^2 I(q)/I(0)$ vs qR_g) revealed that both the apo state as well as the activated state showed increased scattering at high angles. Due to the multiple contrast situation in the nanodisc alone, empty nanodisc showed increased scattering at high angles as well, making analysis of flexibility using Kratky plots more complicated. Nevertheless, the dimensionless Kratky plot showed an additional peak in the mid q -range where usually domain movements are visible, indicating conformational rearrangement. Combining both, Fluorescence polarization studies with SAXS measurements, these conformational changes are most likely due to the displacement of the regulatory domain upon CaM binding (Fig. 4.19 a) [126].

Since the multiple contrast of empty nanodisc makes flexibility analysis of ACA8 more complicated, the flexibility of the regulatory domain in the activated state was analysed using the Porod-Debye plot ($q^4 I(q)$ vs. q^4) [126]. This plot depicts the decay of scattering intensity with the fourth power of q (the momentum transfer). Typically, for a compact molecule a hyperbolic curve with a plateau is observed. A significantly decreased particle contrast, due to flexibility, will result in a loss of the plateau. A clear plateau is visible for ACA8 in its autoinhibited state (Fig. 4.19 c). In contrast, the ACA8-CaM complex does not show a plateau in the low q -range of the Porod-Debye plot ($q^4 < 0.1 \text{ nm}^{-4}$), indicative of a more diffuse contrast that is consistent with a flexible conformation. For flexible particles a plateau would be reached under a different (usually smaller) power law that reflects a more rapid scattering decay [194]. The Kratky-Debye plot ($q^2 I(q)$ vs. q^2) showed the expected plateau for ACA8-CaM complex, confirming the presence of the flexible molecule (Fig. 4.19 d). Altogether, the analysis of the scattering intensity decay showed that the activated state of ACA8 exists as a flexible molecule in solution, most likely due to the flexible nature of the displaced regulatory domain [126].

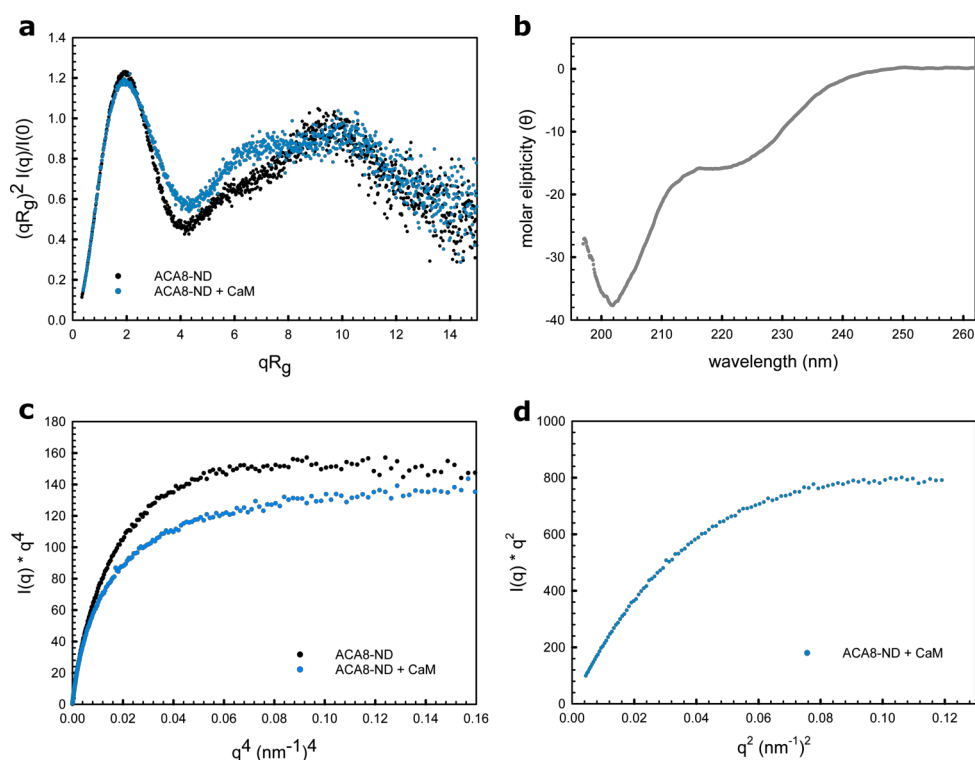


Figure 4.19: Flexibility analysis of the ACA8-CaM complex using scattering intensity decay power laws. (a) Dimensionless Kratky plot of the apo state and the activated state, highlighting the conformational change of the regulatory domain upon CaM binding to ACA8. (b) Far-UV CD spectrum of ACA8 regulatory domain (residues 1-130). (c) Porod-Debye-Plot plot without plateau for the ACA8-CaM complex indicating a decrease in the overall contrast due to a more flexible conformation. (d) The Kratky-Debye plot showed that the hyperbolic character of the scattering intensity decay is achieved much later (power of 2) than in compact, more rigid molecules

4.4 Conclusion

Plasma-membrane Ca^{2+} ATPases (PMCA) are key regulators of the calcium homeostasis in the cell and need to be tightly regulated. One major activator is CaM, which binds to the regulatory domain and thereby activates the pump. In Tidow *et al.*, 2012 [67], a study on the isolated regulatory domain, a more complex activation mechanism was proposed as two independent CaM binding sites (CaMBS) were found. In this chapter, a comprehensive analysis of the activated state of full length ACA8, a PMCA from *A. thaliana*, is presented. The results show that ACA8 can be expressed in yeast and purified to homogeneity in LMNG. The proposed bimodular mechanism was confirmed by native mass spectrometry showing that the maximum of two CaM can bind to the full-length ACA8. Consistent with these results, activity assays showed that two CaM are required to fully activate the pump. These results are in good agreement with fluorescence polarization studies showing a replacement of the regulatory domain (RD) from the core enzyme with an apparent dissociation

constant, which is consistent with the previously published affinities for the low affinity binding site [67]. Moreover, fluorescence polarization studies carefully dissected the different binding events of the regulatory domain during activation and showed that calcium-loaded CaM binds to the RD with higher affinity than the RD to the core enzyme, indicating that the concentration of calcium-loaded CaM is the major driving force for the activation of ACA8.

ACA8 was successfully incorporated into MSP1D1 nanodiscs, which enabled analysis of the activated state in a more native-like lipid environment. The overall activity was significantly higher in nanodiscs compared to detergent micelles, illustrating the importance of lipids for the activity. Nevertheless, ACA8 activity is further modulated by the presence of anionic lipids. They are able to increase the maximal velocity of the enzyme once CaM is bound, but are not able to activate the pump on their own. The results suggest that anionic lipids further stimulate the pump rate of CaM-activated ACA8 by stabilizing an intermediate state of the activated conformation. At the N-terminus of the RD of ACA8 a stretch of positively charged residues supports the theory and might be crucial for this interaction. Interestingly, in different isoforms of PMCAs the length of the aforementioned region varies [107, 114, 195], which might lead to different sensitivities to surrounding acidic PLs, which in turn leads to varying V_{\max} . The activated state was further analysed by small-angle X-ray scattering (SAXS), showing large conformational changes upon CaM binding, due to the rearrangement of the regulatory domain. Moreover, the SAXS data suggested that ACA8 becomes more flexible in the activated state, which is in good agreement with CD spectroscopy data of the isolated RD, showing significant portions of unstructured regions. The results add further structural insights to the previously proposed bimodular activation mechanism [67] showing that binding of two CaM molecules leads to full activation of this Ca^{2+} pump via displacement of the regulatory domain and characterized the activated state [126].

Part III

Stealth carrier nanodiscs

Chapter 5

Stealth carrier nanodiscs for structural investigation of membrane proteins in a lipid environment using small-angle neutron scattering – MsbA as a case study

Experiments reported in this chapter were designed and performed together with Dr. Inokentij Josts (Tidow lab). Deuteration of PC lipids and MSP1D1 were accomplished in collaboration with Dr. Selma Maric (ESS MAXIV, Sweden) and the Deuteration Laboratory at ILL (Grenoble, France).

5.1 Introduction

ATP-binding cassette (ABC) transporters are integral membrane proteins that actively transport a wide range of chemically diverse molecules across the lipid bilayers of cellular membranes [196–199]. In general, movements of lipids are energetically unfavorable and often require active transport by specific flippases [200–202]. The bacterial ABC transporter MsbA transports lipid A, glycolipids and lipopolysaccharides (LPS) from the inner to the outer leaflet [203].

All ABC transporters share a common architecture. They are composed of two transmembrane domains (TMDs) that are spanning the lipid bilayer and two water-exposed nucleotide binding domains (NBDs), which are located in the cytoplasm. MsbA forms a homodimer with each monomer, where each monomer consists of one transmembrane domain and one nucleotide-binding domain. The two TMDs form the LPS translocation pathway and the two NBDs perform the hydrolysis of ATP. Previous studies suggested an alternating-access mechanism with MsbA, alternating between inward-facing and an outward facing conformation [204–206]. Highly conserved residues among the NBDs suggest that ABC transporters share a common transport mechanism. During the transport cycle NBDs have shown to transiently form a sandwich dimer in a head-to tail fashion, trapping two ATP molecules at their interface [207, 208]. This closed conformation can also be stabilized by

vanadate-induced ADP trapping. Previously published 3D structures and electron paramagnetic resonance (EPR) spectroscopy experiments suggest that large conformational changes occur during the catalytic cycle, with the transporter oscillating between the apo, open and closed conformation (Fig. 5.1 a-c) [205, 209, 210]. The conformational heterogeneity of the protein as well as transitions between conformational states of MsbA have, however, remained elusive [60].

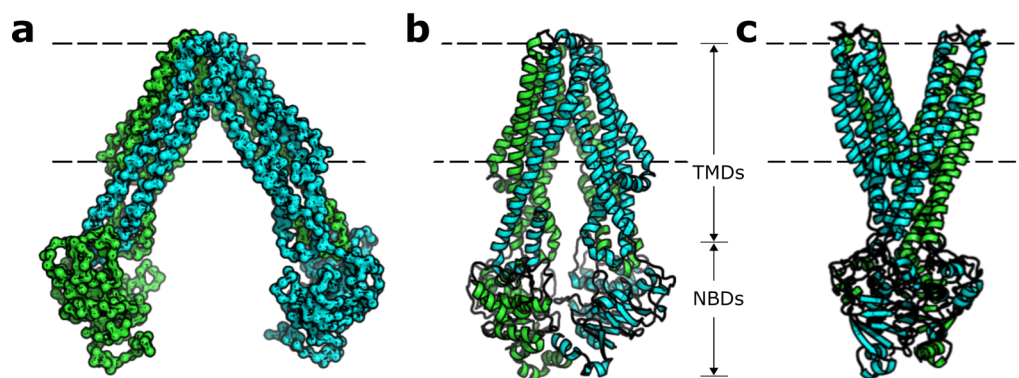


Figure 5.1: Models of MsbA in different states. Structure of MsbA in three different conformations. (a) V-shapes open (inward facing) (pdb: 3b5w) (b) apo MsbA (pdb: 4q4h) (c) closed state (outward facing) (pdb: 3b6o). Each monomer is coloured either in green or blue. Each nucleotide-binding domain (NBD) binds one ATP. Binding of ATP to the NBDs leads to dimerization of the NBDs and hydrolysis of ATP leads to conformational changes in the transmembrane domain (TMD) via a power stroke mechanism.

Kawei et al., 2011 have shown that ATPase activity of MsbA is significantly increased in lipid bilayer compared to the activity in detergent, indicating the importance of surrounding lipids [63]. Due to the improved background subtraction of nanodiscs, these lipid bilayer scaffolds became an important tool for SAS studies of IMPs in a native-like lipid environment. The MSP molecule forms a belt-like structure and surrounds the hydrophobic part of the lipid bilayer. These protein-lipid complexes yield a discoidal lipid bilayer that is soluble in aqueous solution [20, 76]. However, nanodiscs have shown to be structurally heterogeneous (see Chapter 3.3.3.1) [211], which makes structural analysis and modelling of SAS data extremely challenging. While, shortening of helix 5 of MSP1D1 resulted in a more homogeneous nanodisc [85], the complex multi-contrast scattering contribution of the scaffold disc still makes data analysis and structural analysis of the incorporated IMP difficult [60]. Maric *et al.* published recently an elegant nanodisc system that renders the discs effectively invisible to neutron scattering, called stealth-carrier nanodiscs (sND). A combination of deuterated MSPs and selectively deuterated phosphatidylcholine results in a negligible SANS signal when measured in 100% D₂O solvent (see Chapter 2.2.1) [60, 61].

Data in this chapter present the successful incorporation of a first membrane protein into stealth carrier nanodisc. The ATP-binding cassette (ABC) transporter protein MsbA has been already assembled into nanodiscs of various sizes [63] showing that MsbA-nanodiscs form a stable complex. Moreover, MsbA undergoes large conformational changes during the transport cycle with distinct conformational states, which can be detected by small-angle neutron scattering. This made MsbA a very promising test sample to probe the stealth carrier nanodisc system. Therefore, the goal was to incorporate MsbA into stealth nanodisc and investigate different conformational states in 100% D₂O using small-angle neutron scattering (SANS) (Fig. ??).

5.2 Material and methods

5.2.1 Expression and purification of deuterated MSP1D1

Matchout-labeled MSP1D1 (d-MSP1D1) was overexpressed in *E. coli* strain BL21 (DE3) in minimal medium as described in Chapter [61, 212]. In order to remove all hydrogens, hydrogenated metal salts were dissolved in D₂O, dried in a rotary evaporator and dissolved in minimal media. The cells were adapted to growth in minimal media using a stepwise process in which cells were inoculated into minimal media, grown for 36 h and then transferred into fresh minimal media. This was repeated until a sufficient growth rate was obtained [213]. After adaption of the strain to minimal deuterated medium [214] cultures were grown in flasks in 85% deuterated minimal medium with glycerol as a carbon source [215]. The culture was induced with 1 mM IPTG at an OD₆₀₀ of 0.8-1 and incubated overnight at 30 °C [61].

The protein was purified according to a modified protocol established by Sligar and co-workers [83]. Briefly, cells were harvested by centrifugation at 3000 × g, resuspended in lysis buffer (50mM Tris pH 8.0, 500mM NaCl) with 1% Triton X-100 and broken using sonication. The cleared lysate was loaded onto a HisTrap column and washed with lysis buffer containing 1 % Triton X-100 and 50mM cholate, respectively. Impurities were washed off the beads with lysis buffer containing 25 mM imidazole before MSP1D1 was eluted with 500mM imidazole. Fractions containing pure protein were pooled and incubated with TEV protease overnight. Subsequently, the protease and cleaved His-tag were separated by applying a second IMAC chromatography step and MSP1D1 without His-tag was concentrated up to 300µM and stored at 80°C until further use [60].

5.2.2 Expression and purification of MsbA

A pNEK vector containing the gene for *E. coli* MsbA was transformed into *E. coli* strain C43 (DE3). Cells were grown in 2xTY medium at 37 °C until an OD₆₀₀ of 1.0 was reached. Expression was induced by adding 0.25 mM isopropyl β-D-1-thiogalactopyranoside (IPTG) at 20 °C and cells were harvested 6 h postinduction by centrifugation at 4,000 × g for 20 min. Cell paste was resuspended in 30 mM Tris (pH 7.5), 300 mM NaCl, 1 mM β-mercaptoethanol (buffer A) and disrupted in 3 cycles in a high-pressure homogenizer (EmulsiFlex-C3, Avestin), followed by centrifugation at 20,000 g for 25 min. The membrane fractions were isolated by centrifugation at 100,000 g for 1.5 h. Membranes were solubilized in 1% DDM for 1.5 h with gentle stirring and incubated with Ni-NTA resin for 1.5 h. The resin was washed with 10 column volumes of buffer A containing 1% DDM to wash off all endogenous lipids. Subsequently, impurities were eluted by washing the Ni-NTA resin with 20-30 column volumes of buffer A + 30 mM imidazole and 0.03% DDM. MsbA was eluted

with buffer A supplemented with 0.03% DDM and 200 mM imidazole. Purity was judged by SDS-PAGE and fractions containing MsbA were pooled together and concentrated to 2-5 mg/ml before reconstitution into nanodiscs [60].

5.2.3 Expression and purification of deuterated phosphatidylcholine lipids

In order to match out all nanodisc components at 100% D₂O, PC lipids with a scattering length density that matches those for the buffer need to be produced. Therefore, selectively deuterated PC lipids were expressed with 78% deuteration in the head group and 93% in the fatty acyl chain. Expression of selectively deuterated PC (dPC) has been performed in collaboration with the D-lab in Grenoble. Purification of dPC was carried out in collaboration with Dr. Selma Maric, Sweden. Selectively deuterated mixed acyl phosphatidylcholine, d-PC, was produced in the *E. coli* strain AL95 carrying the plasmid pAC-PCSlp-Sp-Gm which allows for the expression of PC synthase [216]. Cells were adapted to growth in minimal media according to established protocols (see Chapter 5.2.1) [214]. Expression of selectively deuterated match-out labeled PC was achieved by amplifying the adapted starter culture in minimal 100% deuterated medium supplemented with 5 % deuterated glycerol (1,1,2,3,3-d₅, 99%; Eurisotop) and 2 mM partially deuterated choline chloride (trimethyl- d₉, 98%; Eurisotop) as previously described [62]. After incubation at 37 °C for 24 h cells were harvested by centrifugation and washed with MiliQ water. Total phospholipids were extracted using the method of Bligh and Dyer [217]. Subsequently, lipid extracts were separated into individual phospholipids using silica-gel chromatography with varying ratios of chloroform and methanol [9:1 (0.2 l), 4:1 (0.2 l), 1:1 (0.2 l), 1:4 (0.2 l) and 100 % methanol (0.3 l)] to purify phosphatidyl choline lipids [62].

5.2.4 Reconstitution of MsbA into stealth carrier nanodiscs

Purified match-out deuterated PC-lipids were resuspended from a dry lipid film in 30 mM Tris (pH 7.5), 150 mM NaCl, 1mM β -mercaptoethanol and 100 mM cholate buffer to yield a 50 mM stock solution. Solution was solubilized using freeze-thaw cycles until the solution became clear. DDM-purified MsbA, deuterated MSP1D1 and deuterated lipids were mixed in a molar ratio of 1:1:25 to reconstitute MsbA into stealth carrier nanodiscs and the assembly mixture was pre-incubated for 1h at 4 °C. Additional cholate was added to keep the final concentration above 20 mM. The nanodisc formation was initiated by adding 0.8 g/ml biobeads to the reaction and the assembly was incubated overnight at 4 °C under constant agitation. Reconstituted MsbA was separated from aggregates on a Superdex200 column (GE Healthcare) in a buffer containing 30 mM Tris (pH 7.5), 150 mM NaCl and 1 mM β -mercaptoethanol and fractions containing nanodisc-embedded MsbA were concentrated up to 3-6 mg/ml. All buffer during the assembly contains H₂O and prior

to the SANS measurements the H₂O containing buffer used during nanodisc preparation was exchanged by a D₂O-based buffer solution using dialysis with a 50 kDa cutoff membrane for at least 20 h to ensure full replacement. For samples in the ADP and ADP+vanadate state, MsbA-sND was dialyzed in the presence of 1 mM Mg-ADP and 1 mM vanadate [60].

5.2.5 Activity measurements

MsbA activity was measured either in DDM or stealth carrier nanodiscs using the Baginski assay [130, 131]. The method measures the production of inorganic phosphate due to ATP hydrolysis, which was used as measure for the overall activity of MsbA. 2 µg of purified MsbA in DDM and 1 µg MsbA in stealth carrier nanodiscs were incubated in 50 l 30 mM Tris (pH 7.5), 150 mM NaCl, 2 mM MgCl₂, 1 mM β-mercaptoethanol. By adding 1 mM ATP to the sample the reaction was started and incubated for 10 min at 25 °C (room temperature) before the reaction was stopped by adding 50 µl ascorbic acid solution (140 mM ascorbic acid, 0.5 M HCl, 0.1% SDS, 5 mM ammonium heptamolybdate). The addition of 75 µl 75 mM sodium citrate, 2% (w/v) sodium metaarsenite and 2% (v/v) acetic acid stopped the calorimetric reaction and absorbance at 860 nm was detected using a Tecan Infinite200 microplate reader after 30 min [60, 86]. A calibration curve using sodium phosphate in a concentration range from 0.01 mM to 0.6 mM was used to determine the concentration of released phosphate during the ATPase reaction. The non-enzymatic hydrolysis of ATP in buffer was subtracted from the measurements with MsbA. All experiments were performed as triplicates.

5.2.6 Small-angle X-ray scattering (SAXS)

MsbA incorporated in stealth nanodiscs (sND) were characterized in a combined SAXS/SANS experiment. Small-angle X-ray scattering (SAXS) data were acquired using the Bio-SAXS instrument P12 on the storage ring Petra III (DESY, Hamburg, Germany) or the beamline BM29 at the European Synchrotron Radiation Facility (ESRF, Grenoble), respectively. All SAXS measurements were carried out at 10 °C in 30 mM Tris (pH 7.5), 150 mM NaCl, and 0.5 mM TCEP at protein concentrations ranging from 1-6 mg/ml. Samples were purified on a Superdex200 (10/300) column to separate the aggregates, concentrated and subsequently dialysed for 24 h before measurements were carried out. The scattered intensity was recorded as a function of the scattering vector q with

$$|q| = \frac{4\pi \sin\Theta}{\lambda} \quad (5.1)$$

using a wavelength (λ) of 0.124 nm. The scattering from corresponding buffer was collected before and after each protein sample and the average of the data was normalized and background subtracted using automatic procedures on the beamline

[84]. The total exposure time of 1 s was measured in 20 frames each with an exposure time of 50 ms. Calibration of the scattering intensity into absolute units of cm^{-1} was performed using the forward scattering intensity of bovine serum albumin. All data processing was performed using PRIMUS [84]. The radius of gyration (R_g) was evaluated from the experimental SAXS pattern using the Guinier approximation ($\ln I(q)$ vs q^2) and as well from the entire scattering curve using the program GNOM (Svergun, 1992). The latter also provided the distance distribution function, $P(r)$, and maximal particle dimension, D_{max} [60].

5.2.7 Small-angle neutron scattering (SANS)

Different conformations of MsbA incorporated into stealth carrier nanodisc (sND) were analysed by small-angle neutron scattering (SANS). Apo-MsbA was measured in the absence of substrates and nucleotides. Additionally, MsbA was analysed in the presence of ADP and ADP-vanadate to mimic the post-hydrolysis states. MsbA was incorporated into sND as described above (see Chapter 5.2.4) and dialysed in 100% D_2O buffer (30 mM Tris pH 7.5, 150 mM NaCl) with corresponding additives for at least 20 h. Empty sND (nanodisc composed of MSP and lipids) were assembled and dialysed in the same buffer and measured as a control. All samples were measured in concentrations ranging from 1-6 mg/ml to optimize the signal-to-noise ratio as well as to exclude inter-particle effects. All measurements were carried out at 10 °C [60].

SANS data from empty sND, apo MsbA-sND and MsbA-sND (ADP) were collected using the small-angle scattering instrument D11 at the Institut Laue - Langevin (ILL, Grenoble, France), while data from ADP and ADP-vanadate bound MsbA-sND were collected at the SANS-1 instrument at Heinz Maier-Leibnitz Zentrum (MLZ) in Munich [218]. All reported measurements from D11 at ILL were performed at a fixed neutron wavelength (λ) of 4.6 Å. A combination of two different configurations of 1.5 m / 1.5 m and 8 m / 8 m (collimation length / sample-detector distances) were used to cover a sufficiently wide q -range ($0.03 < q < 0.58 \text{Å}^{-1}$). Measurements at SANS-1 were performed at 5 Å with a sample-detector distance of 5.5 m and 20 m ($0.01 < q < 0.58 \text{Å}^{-1}$) and the detector was moved by 400 mm perpendicular to the beam in both detector distances. Water reference sample ($\text{H}_2\text{O} + \text{D}_2\text{O}$), buffers, empty cell, the direct beam and the total absorber boron-cadmium were measured to perform data reduction [60]. Radial averaging, background subtraction and absolute scale calibration to convert the data into scattering intensities $I(q)$ in units of cm^{-1} as a function of momentum transfer with

$$|q| = \frac{4\pi \sin\theta}{\lambda} \quad (5.2)$$

where θ is the half scattering angle and λ is the wavelength of the incoming beam, were carried out using the GRASP software (D11) or BerSANS (SANS-1). The data reduction has been performed in collaboration with Dr. Sylvain Prevost (D11) or Dr. Sebastian Busch (SANS-1). Scattering curves of all samples were buffer subtracted using the software PRIMUS [84] and the radii of gyration (R_g) extracted by the Guinier approximation. The R_g and scattering intensities were back-calculated from the atomic models of MsbA using the program CRYSON [219] and scored in a χ^2 fit against the respective experimental SANS data. Molecular masses (M_r) from data at 100% D₂O were calculated from the forward scattering ($I(0)$). The contrast as well as the partial specific volume was determined for the solution components and protein sequences using the MULCH server (<http://smb-research.smb.usyd.edu.au/NCVWeb/>).

All SANS and SAXS scattering parameters are listed in Supplementary Table A.5 [220].

5.2.8 Model calculation from SANS data

Model calculation has been performed in collaboration with Dr. Inokentij Josts. Based on the SANS scattering data of apo-MsbA-snD a low resolution *ab initio* models were generated with the program DAMMIF [221]. Dammif applies simulated annealing to dummy atoms in order to generate models that fit the data. P2 symmetry constraints were applied to DAMMIF. 10 independent DAMMIF models were generated and aligned using SUPCOMB [222]. After alignment using DAMAVER the generated models were filtered for the highest consistency using DAMFILT [222–224].

The mixed elastic network modelling program PATH-ENM [225] was used to model a theoretical conformational transition starting from the V-shaped open conformation to the closed apo conformation. R_g values from generated models were derived using CRYSON [219] and compared with the experimentally derived R_g values of apo-MsbA-sND sample.

Rigid-body modelling was applied using SASREF [226] to further improve the apo-MsbA model. Several constraints were applied, including P2 symmetry between the monomeric MsbA model as well as several spacial restraints to ensure that both transmembrane domains (TMD) keep in close proximity. Therefore, Residues 51 and 55 of monomer #1 and residues 251 and 255 of monomer #2 were selected to stay within a 7 Å distance from each other. All the models were fitted against the experimental data using the program CRYSON [219] and the χ^2 was used to judge the quality of the generated model [60].

5.3 Results and discussion

5.3.1 Reconstitution of MsbA into stealth nanodiscs

In stealth carrier nanodiscs (sND) the scattering length densities (SLD) of all nanodisc components are optimized to become "invisible" to neutrons in 100% D₂O based buffer due to selective deuteration [61, 62]. This makes structural analysis of membrane proteins much easier, as the contribution of the complex multi-phase nanodisc to the SANS scattering signal can be neglected. The ABC transporter MsbA was overexpressed to sufficient milligram amounts and purification in DDM yielded a stable, monodispersible sample, well suited for incorporation into nanodisc (see Chapter 3), making this a good test sample for the stealth carrier nanodisc system.

It is important to minimize the concentration of non-deuterated endogenous lipids during the assembly, to exclude scattering signals coming from non-deuterated lipids. Therefore, the amount of co-purified lipids in the MsbA sample, was examined before incorporation of MsbA into stealth carrier nanodiscs. To test this, MsbA was mixed with MSP1D1 without addition of external lipids and assembly was initiated by detergent removal. Subsequent analysis on a Superdex200 (10/300) size-exclusion column showed two major peaks at 8.5 ml and 12.2 ml (dashed grey line), where the latter corresponded to assembled nanodiscs with incorporated MsbA (Fig. 5.2, lower chromatogram). This elution volume is in good agreement with previous assemblies, indicating that stable fully assembled nanodiscs are formed. The results showed that during MsbA purification enough endogenous lipids are co-purified to fully assemble into stable nanodiscs.

In order to wash off residual co-purified lipids in the MsbA sample an additional washing step with 1% DDM during Ni-NTA affinity column was introduced. Afterwards the assembly without external lipids was repeated and analysed on the Superdex200 column. The peak intensity at 12.2 ml was greatly reduced, showing that concentration of co-purified endogenous lipids in the MsbA sample is not sufficient to assemble stable nanodiscs (Fig. 5.2, middle chromatogram). The fact that the void peak at 8.5 ml is much bigger showed that the majority of MsbA is aggregated during detergent removal due to the lack of surrounding lipids.

MsbA was incorporated into stealth carrier nanodisc (composed of d-PC and d-MSP1D1) after washing the sample with 1% DDM and purified on the size-exclusion column (S200, 10/300). The chromatogram shows two peaks, with a main peak at 12.2 ml and a smaller peak at 8.5 ml (Fig. 5.2, upper chromatogram). MsbA eluted in both peaks, but deuterated MSP1D1 (d-MSP1D1) only eluted in the second peak indicating the assembly was incomplete. Perdeuteration is known to affect the phase transition temperature of phospholipids [227, 228] as well as high resolution structural composition of lipid systems [229, 230]. Moreover, the deuterated PC lipids used for the assembly are composed of a mixture of different acyl chain length,

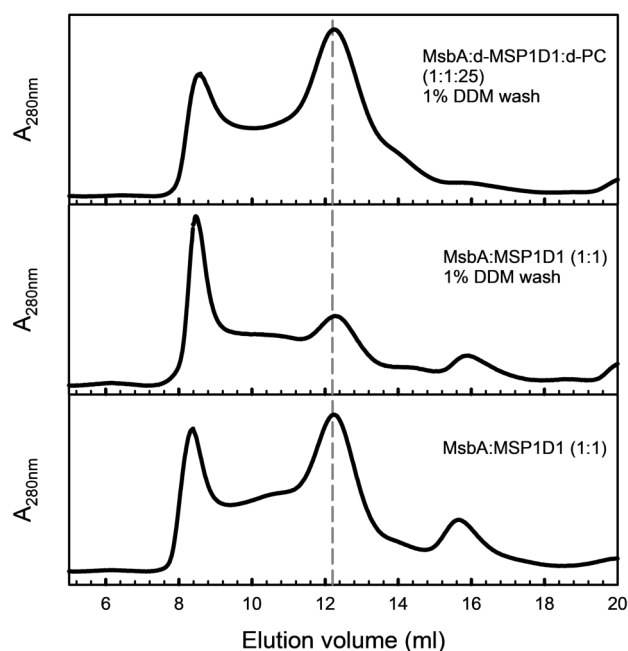


Figure 5.2: Reconstitution of MsbA into MSP1D1 nanodiscs without endogenous lipids. Size-exclusion profiles of MsbA reconstituted into MSP1D1 nanodisc under various conditions. Additional washing step with 1% DDM reduces the concentration of co-purified endogenous lipids to optimize MsbA sample quality for incorporation into stealth carrier nanodiscs.

which might affect the transition temperature as well. The altered phase transition temperatures might have an effect on the lipid packing, which in turn might affect the optimal MSP:lipid ratio. Nevertheless, based on the profile of the chromatogram the incorporation rate was sufficient enough to yield milligram amounts of MsbA-SND sample.

To investigate the stability of the formed complex, the peak fraction containing MsbA incorporated into stealth nanodiscs were pooled and reloaded onto the size-exclusion column after several days. The chromatogram showed one major peak with nearly no void peak, indicating that the assembly yielded in a stable and monodisperse sample suitable for SAXS and SANS experiments. To investigate whether the deuterated disc components affect the functional properties of MsbA, ATPase activity assays were performed. MsbA displays much higher activity when incorporated in stealth nanodisc compared to its activity in DDM (17 fold increase), illustrating the need for lipidic environment for MsbA function. MsbA incorporated into non-deuterated nanodiscs showed almost the same activity, which demonstrates that the protein activity is not affected by the deuterated disc constituents [60].

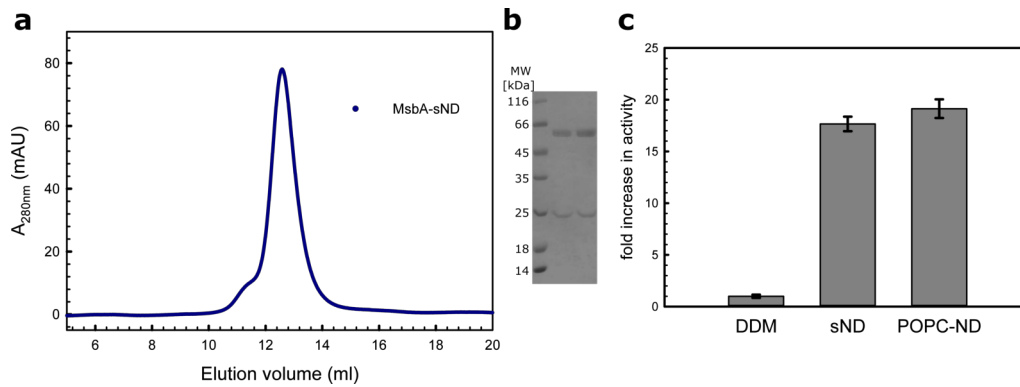


Figure 5.3: Stability and activity of MsbA in stealth nanodisc. (a) Size-exclusion chromatography (S200) profile of reloaded MsbA-sND complex. (b) SDS-PAGE gel electrophoresis of peak fraction, containing MsbA (60 kDa) and deuterated MSP1D1 (22 kDa). (c) ATPase activity assay of MsbA in DDM or reconstituted in either POPC nanodisc or stealth nanodisc. MsbA reveals much higher activity in lipid environment compared to detergent. [60]

5.3.2 Structural characterization of MsbA by combined SAXS / SANS

Small-angle neutron scattering was carried out in 100% D_2O -based buffer to fully match out the selectively deuterated disc components. The residual scattering intensity of stealth nanodiscs (sND) alone was determined by measuring empty sND (containing only deuterated MSP1D1 and deuterated PC). These data were compared to scattering intensities of MsbA in sNDs (Fig. 5.4 a).

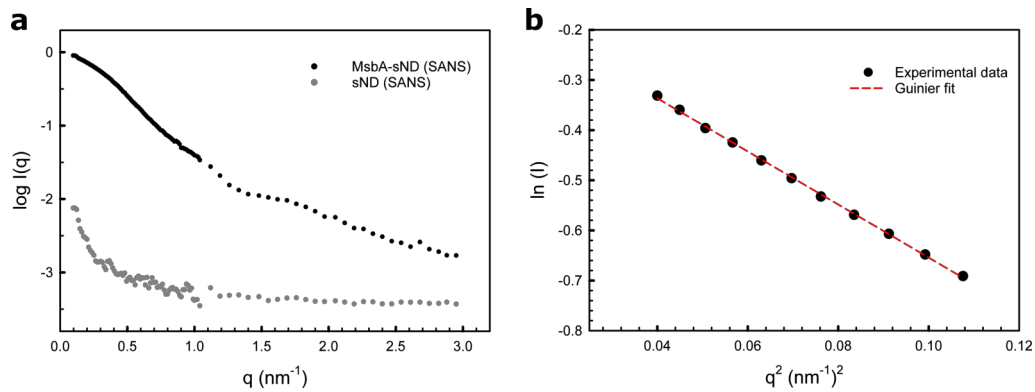


Figure 5.4: Small-angle neutron scattering of MsbA incorporated into stealth nanodisc. (a) SANS scattering curves of empty stealth nanodiscs (containing deuterated lipids and deuterated MSP1D1 only) (grey squares) as well as from MsbA incorporated into sND (black dots). The scattering intensity from MsbA-sND is much stronger than that from empty stealth nanodiscs indicating that contribution from sND constituents to the scattering signal can be neglected. (b) Guinier fit to the raw scattering data in the Guinier region determines an R_g of 40.11 Å. Linearity of the residuals indicates the absence of inter-particle interference. [60]

Scattering profiles of empty sNDs show an almost flat line with only minor scattering signals in the low q -range (0.01 - 0.5 nm^{-1}), which is comparable to previously

published SANS data of empty sND [61]. The residual signal is likely to derive from the statistical fluctuations in the deuteration level of the lipids and MSP1D1. Nevertheless, the scattering intensity in the low q -region is only slightly above that of the experimental background, showing that the stealth nanodiscs are effectively matched out. In contrast to that, the scattering signal from MsbA-sND shows a typical profile for biological macromolecules and the intensity is more than two orders of magnitude stronger than that from empty stealth nanodiscs (Fig. 5.4 a) [60]. The experimentally derived radius of gyration (R_g) using the Guinier approximation is 40.0 \AA , which is smaller than those obtained for the MsbA-sND complex by SAXS (R_g of 47.7 \AA) further showing the minimal scattering contribution of the nanodiscs to the SANS data (all parameters listed in Supplementary Table A.5). This data suggests that measured scattering intensities only derive from MsbA and the contribution of sND components to the scattering signal is neglectable, which enables data analysis as well as structural modelling without the need to consider complex multi-phase and contrast effects from the nanodisc [60, 231].

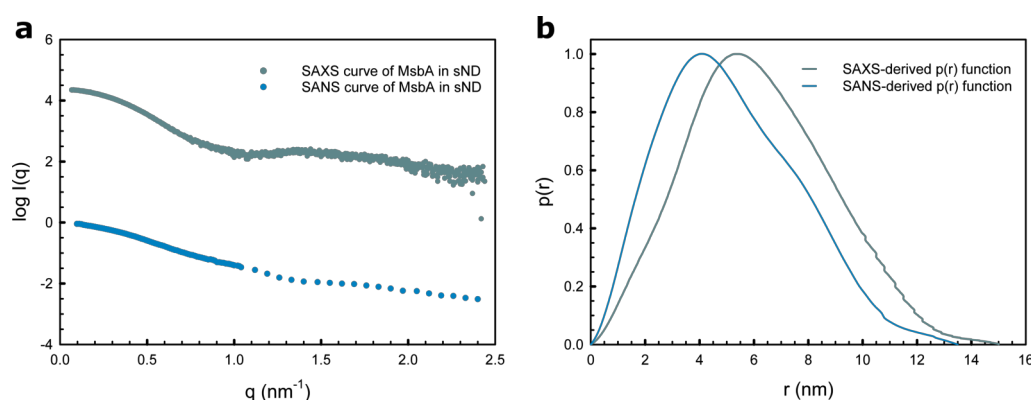


Figure 5.5: Comparison of X-ray and neutron scattering data from MsbA-sND. (a) Semi-log plot of identical MsbA-sND sample investigated by SAXS (grey) and SANS (light blue). (b) Distance distribution plots ($p(r)$) of data shown in (a).

Small-angle X-ray scattering was performed on the identical sample of MsbA-sND and compared to the measured SANS data (Fig. 5.5). The SAXS profile shows typical feature in the mid q -range of around 0.9 nm^{-1} which derives from the nanodisc, and is not present in the SANS curve (Fig. 5.5 a). The radius of gyration was 47.5 \AA and significantly bigger than that derived from the SANS data. Besides a bigger R_g the maximal particle dimension is increased as well (Supplementary Table A.5). The maximal particle dimension is 160 \AA in SAXS measurements and 130 \AA in the SANS data. The pair distance distribution function ($p(r)$) derived from the SANS data has a bilobed shape with two peaks at 3.5 nm and 7.5 nm , which is consistent with a multi-domain particle, seen in the crystal structures (Fig. 5.5 b) [204, 232]. In the $p(r)$ -function derived from the SAXS data the main peak at 3.5 nm is shifted

towards larger distances and the second peak is much less pronounced. Due to the significant contribution of the disc constituents to the SAXS data, the overall size parameters are much larger than those from the same sample as obtained by SANS in "stealth conditions" (100% D₂O). Moreover, scattering signals derived from MsbA are less pronounced in the SAXS data. This shows that contribution of nanodisc to the SAXS scattering signal overlay those derived from MsbA, making structural characterization much more difficult [60].

Conformational states of MsbA in solution

The R_g derived from the indirect Fourier transform of the entire SANS curve is 40.11 Å and in good agreement with the value calculated from the Guinier approximation, showing a high quality of the SANS data of MsbA-sND [60]. The Kratky plot shows one major peak in the low- q -range and no increase in scattering in the high- q -range which indicates a compact domain structure (Supplementary Fig. A.7). High-resolution structures of MsbA in the open as well as in the closed conformation were used to calculate theoretical radii of gyration. The calculated R_g of the closed crystal structure from *Vibrio cholerae* [204] is 38.0 Å and is in good agreement with the recently determined cryo-EM structure POPG containing nanodisc [232] (calculated R_g 37.7 Å). In contrast to that, the calculated R_g from the V-shaped open apo structure from *E. coli* [204] is significantly higher (calculated R_g 45.9 Å). The comparison of the calculated R_g values with that from the SANS data reveals that MsbA conformation in solution resemble those of the closed structures [60].

To ascertain the fit between the SANS data and the aforementioned MsbA structures, theoretical scattering curves were computed using CRYSON [219] and plotted against the SANS data of apo MsbA-sND (Fig. 5.6 a). These data showed a similar trend. The open apo state produces a very poor fit with a χ^2 of 280.3, ruling out this conformational state. A much better fit is obtained for the closed model of MsbA from *Vibrio cholera* [204] with a χ^2 of 2.99. The curve fits the entire q -range well, suggesting that our conformation of MsbA in the disc resembles this closed state. However, the curve of the closed model shows local discrepancies in the mid- q -range, and the experimental R_g of MsbA in stealth nanodisc is larger than that of the closed model. Due to both mentioned discrepancies, a distinct structural state of MsbA is likely to be present in solution [60]. This is further supported by recent cryo-EM studies as well as previous EPR and MS studies, showing structural flexibility in the nucleotide binding domains of MsbA [205, 233, 234].

The same analysis was carried out of identical MsbA-sND samples from the SAXS data. Theoretical scattering intensities of high-resolution structures of MsbA in the open and closed conformation were computed using CRY SOL [219] and plotted against SAXS data of MsbA-sND (Fig. 5.6 b). Since sND contributes to the scattering signal, nanodisc were included in the calculations. Therefore, models of MsbA were theoretically assembled into MSP1D1 nanodisc using the CHARMM-GUI web server [192]. Different models in the open state as well as in the closed state were generated based on published structures (pdb (apo open): 3b5w, pdb (closed): 3b6o) [204, 232]. The model of apo MsbA in its open conformation, with a χ^2 of 75.1 can be clearly distinguished from the closed conformation (χ^2 of 4.8). The model of the closed conformation fits well in the low- q -range, showing that the overall conformation of the model fits the SAXS data. Nevertheless, the fit shows large inconsistencies

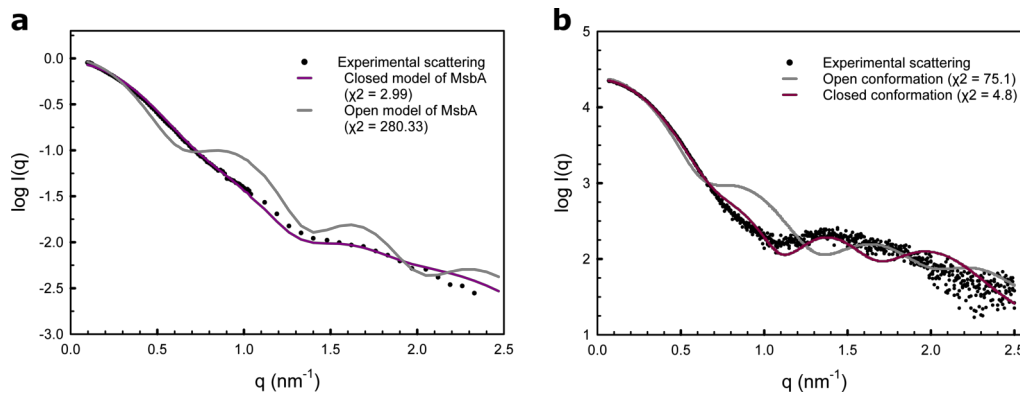


Figure 5.6: Conformational analysis of MsbA-sND. Scattering intensities were back-calculated from high-resolution structures of MsbA in different conformations and plotted against the SANS data (a) or SAXS data (b). Fits could be used to discriminate between the open (grey) or closed (purple) conformation. The closed apo model (red) produces a better fit to the experimental data (black dots) than the open apo model (grey). [60]

in the mid- q -range. Structural heterogeneity arising from the nanodisc (see Chapter 3.3.3) could lead to differences of the scattering intensities in the mid- q -range as well as a distinct conformation of MsbA in solution. Significant contributions of the stealth nanodisc to the scattering signal makes it difficult to confidently differentiate whether the differences arise from distinct conformational changes in MsbA or are due to structural heterogeneity coming from the nanodiscs. Moreover, the different nanodiscs components possess different electron densities, which changes the contrast ($\Delta\rho$) making the nanodiscs a multi-phase scattering system in a SAXS experiment

citeJosts2018. Since, the deuterated nanodisc components are "neutron invisible" in 100% D_2O , SANS analysis enabled to unambiguously determine conformational changes from the membrane protein of interest more precisely [60].

Conformational changes of MsbA upon ATP hydrolysis

MsbA is a member of the lipid flippase ABC exporters and changes its conformation upon ATP binding, hydrolysis and ADP release. Thereby, the conformational changes of the nucleotide binding domains (NBD) during the ATP hydrolysis cycle are tightly coupled to the transmembrane domains (TMD) from inward- to outward facing conformation by a "power stroke mechanism [235]. In previous published structures of MsbA in complex with ADP and the phosphate mimetic vanadate, as well as the structure of the multidrug ABC transporter Sav1866 with the non-hydrolysable ATP analogue AMP-PNP bound show similar conformations of transporters with an outward open TMD and a closed inward-facing NBD dimer [204, 236]. The studies suggested this conformation as post-hydrolysis intermediate state in the reaction cycle [235]. Since, small-angle scattering of MsbA in stealth

carrier nanodisc is able to detect conformational changes more precisely than SAXS can, it was tested whether it is possible to determine conformational changes in the post-hydrolysis state. Therefore, MsbA SANS data were acquired of MsbA in complex with ADP + vanadate and scattering profiles were compared with the apo state [60].

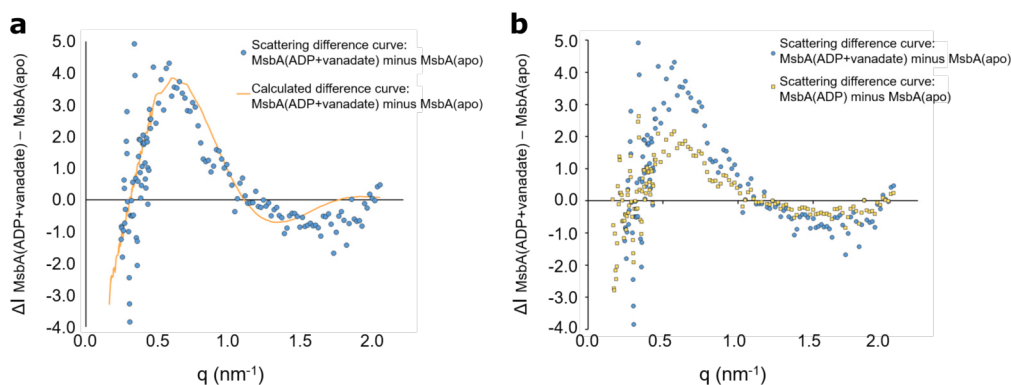


Figure 5.7: Differences in SANS profiles of MsbA-sND in different conformational changes. (a) Difference curve of SANS-derived scattering data of MsbA(ADP+vanadate) minus MsbA(apo) (blue points) compared to of a calculated difference curve based on existing structures (orange line). SANS data of MsbA were acquired with MsbA incorporated into sND. (b) Scattering data from either MsbA(ADP+vanadate) (blue points) or MsbA(ADP) (yellow points) were subtracted from MsbA(apo) to yield the corresponding difference curves. ADP leads to structural changes, but to much lower extent. Figure reprinted from Josts et al. [60]

To clarify changes in the scattering profile, scattering curves from the apo state of MsbA were subtracted from the MsbA(ADP+vanadate), resulting in a scattering difference curve (Fig. 5.7 a). The scattering difference curve possesses a positive difference peak between q of 0.5 and 1.0 nm^{-1} , as well as a small negative scattering peak around q of 1.5 nm^{-1} . These data are in good agreement with a change in the radius of gyration from 40 Å for the apo state to 38.57 Å for the complex with ADP + vanadate, showing as well that the binding of both ADP + vanadate induces conformational changes [60]. A theoretical difference curve was calculated based on the structural models, using the semi-open rigid body model as well as the apo state and the outward-open structure of MsbA [204]. Both the experimental scattering difference as well as the calculated difference curve showed a positive peak in a q -range between 0.5 - 1.0 nm^{-1} indicating that structural re-arrangements are similar in solution to that in the model structures [60]. This is further supported by a χ^2 of 1.48. Moreover these data suggest that small-angle neutron scattering of membrane proteins in stealth nanodiscs is sensitive enough to pick out conformational differences between the different states [60].

Scattering difference curves were calculated for the MsbA-ADP complex in the same

fashion and a consistent difference was observed (Fig. 5.7 b). These differences were of much smaller magnitude, suggesting that the structural changes are of similar nature but less pronounced in the presence of ADP. It is known that ADP is not able to induce the dimerization of the nucleotide binding domains [237], which might explain the less pronounced structural changes [60]. In the recently published cryo-EM structure of MsbA, no conformational changes were observed in the presence of ADP [232], which is contradictory to the presented SANS data. However, crystal structures of the NBD of homologs of MsbA in the presence and absence of ADP (pdb: 5IDV,5DGX) reveal that small structural changes within the domain are visible, showing that ADP is able to interact with the NBDs [238]. Further studies on the nature of conformational changes induced by ADP remain to be investigated. Nevertheless, these data showed that SANS data of MsbA in stealth nanodisc are sensitive enough to observe even subtle structural changes [60].

5.3.3 Structural modelling of MsbA in nucleotide-free state

The SANS data of apo MsbA-sND was used for an *ab initio* reconstruction of the particle using the program DAMMIF [221]. Since, the functional state of MsbA is a dimer, P2 symmetry was used as a structural restraint for *ab initio* modelling. The output model shows a symmetrical shape, as expected for a P2 symmetry, which fits very well with the molecular shape of the closed MsbA structure published by Ward *et al.* [204] (Fig. 5.8 a-b) [60]. The produced models were verified by a cluster analysis. All *ab initio* models showed similar shapes and do not show any shape features of the stealth nanodiscs (Supplementary Fig. A.9). This illustrates, once more, that the stealth nanodisc were invisible from the point of view of neutrons. These data are in good agreement with analysis based on the radius of gyration, which shows that MsbA in stealth nanodisc resembles the closed state in solution. [60]

However, the CRYSON fit of the closed model shows local discrepancies in the mid-q-range and together with a larger experimental R_g value it was speculated that a distinct conformational state is likely to be present in solution. The conformational state of apo MsbA in sNDs was further investigated by using the mixed elastic network modeling (MENM) technique [225]. For this purpose, the open apo V-shaped structure was used as a starting point and a theoretical transition path of MsbA was calculated towards the closed apo state. R_g values of each individual MsbA model along the pathway were calculated using CRYSON [219] and plotted against the individual models (Fig. 5.9 a). The experimentally derived R_g value of MsbA-sND fits in a region of the path where the nucleotide-binding domains (NBD) of MsbA are slightly apart, rather than in contact as seen in the closed structure (indicated by a red star in Fig. 5.9 a). Since changes in the mid-q-region are often due to structural differences in the domain architecture, the differences in the NBD conformation

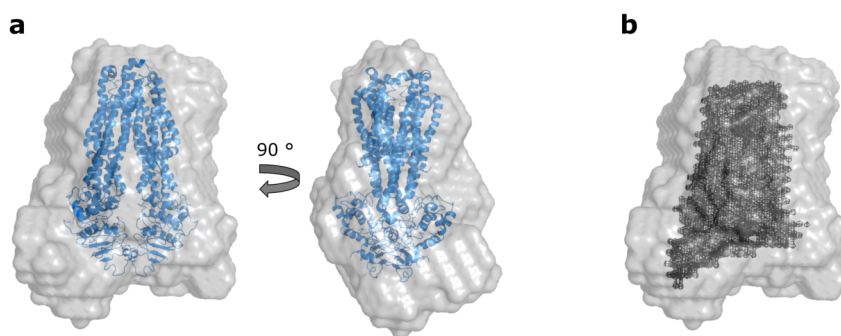


Figure 5.8: Ab initio modelling of apo MSbA. (a) DAMMIF was used for *ab initio* shape reconstruction based on the SANS data of MsbA-sNDs in the nucleotide-free state (grey surface representation). The *ab initio* model was superimposed with the crystal structure of MsbA in the closed apo state (blue cartoon model) [204]. (b) Comparison of the *ab initio* DAMAVER model with the occupancy filtered and most probable model obtained using DAMFILT. Figure reprinted from Josts, Nitsche *et al.* [60]

might explain the discrepancies in the CRYSON fit of the closed structure. [60]

To further probe the conformational state of apo MsbA in solution rigid body modeling was undertaken using the program SASREF [226]. A single MsbA monomer was used and P2 symmetry was applied. Besides, several distance restraints were used; residues in the trans membrane domain of both monomers (residues 51 and 55 of monomer # 1; residues 251 and 255 of monomer # 2) were kept within 7 Å distance from each other. The modelled conformation fits the scattering data well, with a χ^2 of 1.68, and a calculated Rg of 39.4 Å and the discrepancies in the mid-q-range are much less pronounced (Fig. 5.9 d). In this model the NBDs are approximately 20 Å apart from each other (Fig. 5.9 b), as already suggested above. A rather similar conformation was observed for the structure of P-glycoprotein (pdb: 4Q9H) [239] as well as for its homologues ABCB1/ABCB10 (pdb: 4AYX) [240]. The recently published cryo-EM structure of MsbA in POPG nanodisc from Mi *et al.* [232] showed that in a subset of particles the NBDs of MsbA are slightly open, which is consistent with the other structures. This findings are all in good agreement with the measured SANS data of apo MsbA in stealth nanodisc. Whether this conformation is due to the native-like lipid environment of the nanodisc remains to be investigated [60].

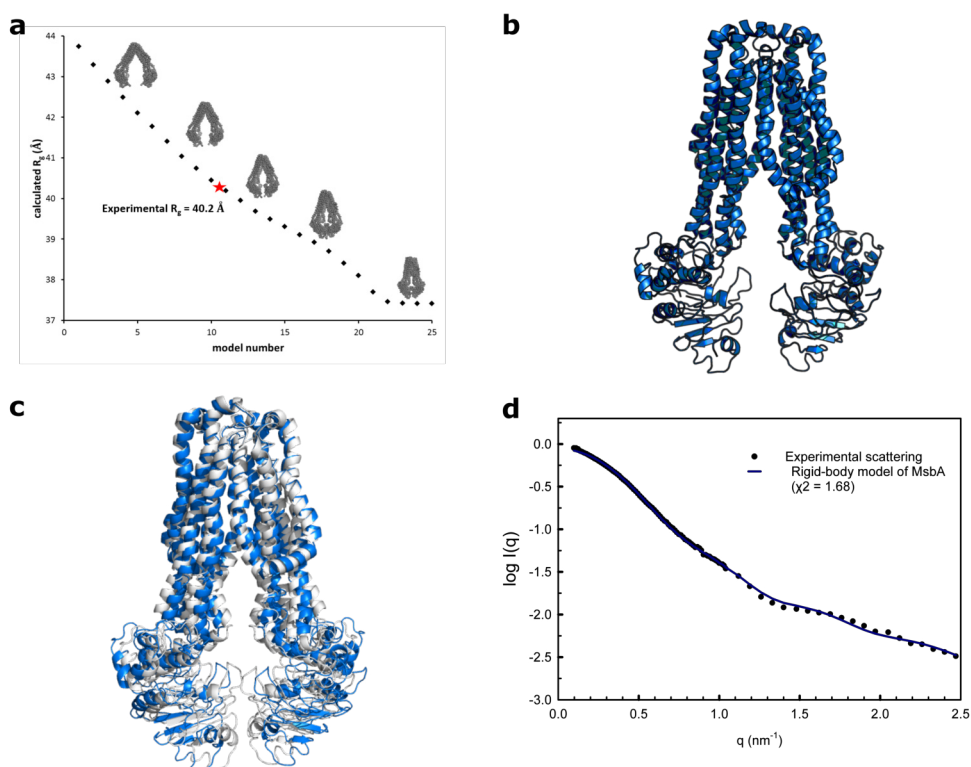


Figure 5.9: Modelling of MsbA in its nucleotide free state. (a) Using the mixed elastic network modeling [225] structures along a theoretical transition path of MsbA from the open apo V-shaped conformation to the closed apo state was computed. The experimental R_g of apo MsbA-sND sample was used to identify the overall conformational state of MsbA in the sND-nanodiscs. (b+d) Rigid-body modelling using SASREF was carried out to model dimeric MsbA from a monomeric template. A P2 symmetry were applied as well as residues in the trans-membrane domain involved in the dimerization were kept within 7 Å distance. The theoretical scattering intensity of the rigid-body model (b) were computed using CRYSON. The model produces a very good fit of the experimental scattering data (d). (c) Rigid-body model of MsbA superimposed with crystal structure of MsbA in the closed apo state. Individual figure reprinted from Josts, Nitsche *et al.* [60].

5.4 Conclusion

Nanodiscs have improved the solution state studies of IMPs. These discoidal protein-lipid complexes keep the IMP soluble in aqueous solution, while being located in a native-like lipid environment [20, 76]. While nanodiscs improved the signal to noise ratio during small-angle scattering (SAS) experiments, due to the lack of empty detergent micelles, the complex scattering contribution of the nanodiscs make structural analysis of incorporated IMP extremely challenging. In contrast to that, the recently developed stealth carrier nanodiscs, which effectively render the bilayer scaffold invisible [61] in 100 % D_2O , enable structural modeling of IMPs without taking the nanodisc into account. This significantly improves the data interpretation of IMPs in SAS experiments [60].

The data presented in this chapter show for the first time a successful analysis of an IMP using the combination stealth-carrier nanodiscs/ SANS technique. Measurements in 100 % D₂O minimized the incoherent scattering from H₂O and enabled the collection of high signal-to-noise neutron scattering data of MsbA. The overall molecular conformation of the ABC transporter MsbA has been described and the SANS data were sensitive enough to characterize a distinct conformational state in solution [60]. ATPase activity assays showed that the deuteration of nanodisc components doesn't affect the functional state of MsbA. Whether the distinct conformational state of the rigid-body model is an effect of the lipid environment in the nanodisc remains to be investigated. In addition, it was possible to study subtle conformational changes in the post-hydrolysis state, adding valuable structural information. The R_g values of MsbA in sND were much higher in the SAXS experiment compared to data of the same sample in SANS, which illustrates the significant scattering contribution of the nanodisc components [60]. Fitting the rigid-body model against the SAXS data, slightly improved the χ^2 but it still shows discrepancies in the mid-q range (Supplementary Fig. A.8). Compared to the fit of the open state model the differences are smaller but still significant. These discrepancies most likely derive from differences in the nanodisc conformation. The conformational heterogeneity of the nanodiscs as well as the complex contrast situation, makes it difficult to precisely differentiate between subtle conformational changes of MsbA in the discs. However, SAXS data provide important control information [60]. Overall, this study demonstrates the suitability of the sND/ SANS technique to analyse conformational states of membrane proteins embedded into a native-like environment [60].

Chapter 6

Small-angle neutron scattering of ACA8 in stealth nanodiscs – modelling of the CaM-activated state

6.1 Introduction

Calmodulin (CaM) is one of the main activator of the tightly regulated plasma-membrane Ca^{2+} ATPases. The binding of two CaM to the regulatory domain (RD) of ACA8, a PMCA from *A. thaliana*, releases the binding of the RD from the core enzyme and significantly increases the overall pump rate (see 4.3.3.2). Fluorescence anisotropy data shown in Chapter 4.3.4.1 suggested that the presence of calcium-loaded CaM is the major driving force of the pump activation, as the RD binds much weaker to the core enzyme compared to the affinity of CaM to the regulator domain. In small-angle X-ray scattering experiments ACA8 incorporated into nanodisc were analysed in different states (apo and CaM-activated state) (see Chapter 4.3.4.2). The data suggested that binding of CaM to the regulatory domain of ACA8 induces large conformational changes. However, in depth analysis of the conformational changes leading to the activation remain to be investigated. Modelling of either the apo state or the activated state based on the SAXS data were not successful, due to the heterogeneity and the complex contrats situation of the nanodiscs. Moreover, the lack of high-resolution structural models of full-length PMCAs made modelling of ACA8 even more challenging. The recently published cryo-EM structure of a human PMCA did not resolve the regulatory domain [116] and modelling of neither the apo state nor the activated state of ACA8 was possible.

In order to probe the structural changes of ACA8 during the activation process the recently developed stealth nanodisc (sND) technology was used [61, 62]. Stealth nanodiscs consists of selectively deuterated phosphatidylcholine lipids and fractionally deuterated MSP1D1. These nanodisc does not contribute to the SANS scattering signal in the appropriate solvent contrast situation (100 % D_2O). The use of stealth nanodiscs allows measuring small-angle neutron scattering (SANS) signals of ACA8 without the contribution of the scaffold scattering signal (see Chapter 5). Using this

stealth nanodisc (sND) / SANS method structural changes involving in the activation of ACA8 are expected to be easier to detect and to model compared to the SAXS data. Therefore, ACA8 incorporated into stealth nanodiscs was analysed in the autoinhibited state (apo) as well as in the activated state, in complex with CaM. The ACA8-CaM complex was analysed with two different CaM variants: (1) deuterated and (2) non-deuterated. Using perdeuteration of CaM with a deuteration level of 73 % the scattering length density (SLD) of d-CaM equals that of 100 % D₂O based buffer, rendering it neutron invisible [241]. This enables analysis and modelling of ACA8 in its activated state without contribution of CaM to the scattering signal.

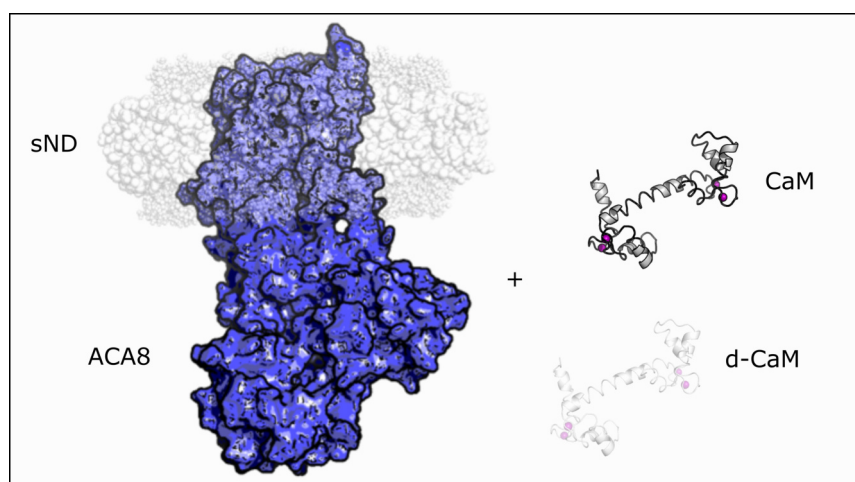


Figure 6.1: Cartoon illustration of used stealth nanodisc technique to study activation process of ACA8. Perdeuterated nanodisc components (shown in semi-transparent grey spheres) are fully matched-out at 100 % D₂O (grey background) and only ACA8 (blue) contributes to the scattering signal. ACA8 in stealth nanodisc in the activated state was measured in complex with deuterated CaM (transparent grey cartoon) or non deuterated (hydrogenated) CaM (grey cartoon).

6.2 Material and methods

6.2.1 Expression and purification of deuterated CaM

Deuteration of CaM7 was performed by the Deuteration Laboratory (D-lab, ILL, Grenoble). A deuteration level of 73% of non-hydrolysable hydrogens was needed to produce deuterated CaM7 (d-CaM7) with the relevant scattering length density. Plasmid pET42a harbouring the *A. thaliana* CaM7 gene was transformed into *E. coli* strain BL21 (DE3) and cells were adapted to growth in deuterated minimal media (see above) [213]. Cells were grown in a 1.8 L (final volume) high-cell-density fed-batch fermenter at 30 °C [126, 212]. At an OD₆₀₀ value of about 5 feeding with glycerol was started. Expression of d-CaM7 was induced at an OD₆₀₀ of about 12 by addition of IPTG (0.5 mM final concentration) and cells were pelleted at an OD₆₀₀ of 19, yielding 100 g wet weight of matchout-labeled cell paste. For purification cells were resuspended in buffer containing 30 mM Tris pH 8.0, 100 mM NaCl, 1 mM CaCl₂, supplemented with 0.5 ml lysozyme (100 mg/ml), DNase (1 mg/ml) and lysed using high-pressure homogenizer (EmulsiFlex-C3, Avestin). The lysate was cleared by centrifugation at 40,000 × g for 45 min and d-CaM7 was bound under low salt condition on a HiTrap Phenyl HP column. d-CaM7 was eluted with 5 mM EDTA and the purity of the sample was judged on a SDS-PAGE. Fractions containing pure d-CaM7 were pooled and concentrated to 10 mg/ml and stored at -80 °C until further use [126].

6.2.2 Reconstitution of ACA8 into stealth carrier nanodisc

Stealth carrier nanodiscs (sND) were reconstituted using the deuterated version of MSP1D1 (see Chapter 5.2.1) together with selectively deuterated PC (see Chapter 5.2.3) through self-assembly based procedure [83]. Reconstitution of ACA8 into sND was carried out as for normal MSP1D1 nanodiscs. Briefly, affinity purified ACA8 (described in Chapter 4.2.5), the deuterated MSP1D1 membrane scaffold protein (described in Chapter 5.2.1) and the deuterated PC lipids (described in Chapter 5.2.3) were mixed in a molar ratio of 1:7:200 in 30 mM Tris pH 8.0, 150 mM NaCl, 1 mM CaCl₂, 1 mM β-mercaptoethanol buffer with 20 mM cholate and incubated for 1 h at 4 °C to ensure a proper distribution of all components. The assembly process was initiated by adding detergent removal beads (Thermo Fischer Scientific) in a 1:1 (v/v) ratio. The assembly mix was incubated over-night at 4 °C under constant agitation. Detergent removal beads were separated and the sample was cleared by centrifugation at 20,000 × g for 10 min before subsequent purification of the ACA8-sND complex on a Superdex200 column (GE Healthcare) (buffer: 20 mM Tris pH 8.0, 150 mM NaCl, 1 mM CaCl₂, 1 mM β-mercaptoethanol).

Prior to SANS measurements, the H₂O-based buffer used for nanodisc preparation

was substituted for a 100% D₂O-based buffer solution by dialysis with a 50 kDa cut-off membrane [126].

6.2.3 Small-angle neutron scattering (SANS)

Small-angle neutron scattering (SANS) with ACA8 incorporated in stealth carrier nanodiscs (sND) was used to characterize the activated state without contribution of the carrier system to the scattering signal. SANS data were acquired for ACA8 in its autoinhibited state (apo) as well as in its activated state (in complex with CaM). The activated state was measured with two different types of CaM7, hydrogenated and matchout-deuterated CaM7 (see Chapter 6.2.1), of which the latter is effectively invisible to neutrons in 100% D₂O. ACA8-CaM complexes were formed by mixing ACA8-sND with excess of either hydrogenated (h-CaM) or deuterated CaM7 (d-CaM7), which were subsequently purified on a Superdex200 (10/300). All SANS data were collected at the SANS-1 beamline at Forschungs-Neutronenquelle Heinz Maier-Leibnitz (FRMII) in Munich [218]. Measurements were performed in 100% D₂O buffer (30 mM Tris pH 7.5, 150 mM NaCl, 1mM MgCl₂, 1 mM CaCl₂) at 10 °C, using a sample concentration of 3.0-3.5 mg/ml [126].

Measurements at FRMII were performed at 5 Å wavelength with a sample-detector distance of 5.5 m ($0.01 < q > 0.23\text{\AA}^{-1}$), while the detector was moved by 404 mm in direction perpendicular to the beam. Water reference sample (H₂O + D₂O), buffers, empty cell, the direct beam and the total absorber boron-cadmium were measured as well to perform data reduction [126]. Radial averaging background subtraction and absolute scale calibration (in cm⁻¹) to convert data into one-dimensional scattering intensities $I(q)$ were carried out using the BerSANS software. The scattering curves of all samples were buffer subtracted using the software PRIMUS [84]. The radii of gyration (R_g) were extracted either by the Guinier approximation $\ln I(q)$ vs q^2) or from the distance distribution function, $p(r)$ using the program GNOM [43]. For SANS data sets at 100% D₂O molecular mass estimates were obtained from the forward scattering ($I(0)$), with the contrast and partial specific volume as determined from the solution components and protein sequence using the MULCH server (<http://smb-research.smb.usyd.edu.au/NCVWeb/>) [126].

6.2.4 Model calculation from SANS Data

SANS data from ACA8-sND in complex with matchout-labeled CaM7 were used to model ACA8 in its activated state. Due to the lack of structural information of full-length ACA8, a homology model of ACA8core (130aa-1074aa) was generated based on the SERCA structure in E2 conformation (pdb:3b9b) using the program Phyre2 [242]. The homology model was combined with the crystal structure of the regulatory domain (RD) (40aa-95aa) (pdb:4aqr) and was used as input domains. Residues at the N-terminus (1aa-39aa) as well as between the regulatory domain and the

core enzyme (69aa-129aa) were modelled as dummy atoms to generate a full-length model of ACA8. A pool of 10,000 ACA8 full-length models with different conformations of the regulatory domain was generated using RANCH [243]. Thereby the conformation of the core enzyme was kept constant and different conformations of the RD with respect to ACA8core were generated. The conformational flexibility of ACA8 in its activated state was probed using the ensemble optimized modelling (EOM) program [244]. Therefore, theoretical scattering intensity of each model was computed with CRYSON [219] and fitted against the experimental scattering data. A modified script from the EOM package was used to create the intensity files (containing theoretical intensities from all 10,000 models) and the size file (list of all R_2 and D_{\max} values) (see Chapter A.3). The genetic algorithm method, GAJOE [243], from the EOM package was subsequently used to select a subset of models, whose weighted average scattering curve showed the best fit to the data of ACA8-dCaM complex. Structural models were displayed using PyMOL [126]. The structural data has been deposited Small Angle Scattering Biological Data Bank (SASBDB) with accession codes SASBDB: SASDES4, SASDET4, SASDEU4.

6.3 Results and discussion

6.3.1 Reconstitution of ACA8 into stealth nanodiscs (sND)

The calcium pump ACA8 was reconstituted into stealth carrier nanodiscs by mixing MsbA with deuterated MSP1D1 (d-MSP1D1) and deuterated phosphatidylcholine lipids (d-PC) in a molar ratio of 1:7:200 (ACA8:d-MSP1D1:d-PC). After detergent removal using cyclodextrin (see Chapter 4.2.8) the assembly was further purified on a size-exclusion chromatography column (Superdex200 10/300). The chromatogram shows three peaks, at 8.5 ml, 11.8 ml and 13.5 ml (Fig. 6.2 a). The peak at the void volume (8.5 ml) shows the highest intensity and mostly ACA8 eluted at this volume. The second peak corresponds to incorporated ACA8 into sND (see Fig. 6.2 d, lane 2) and has a much higher intensity compared to the third peak (empty sND). Compared to previous elution profiles of empty stealth nanodiscs the third peak is shifted to lower elution volumes, indicating that the assembly ratio was sub-optimal. Since the transition temperature of deuterated PC lipids might be different, the optimal assembly ratio might be different as well (see Chapter 5.3.1). Nevertheless, the assembly efficiency was good enough to yield milligram amounts of ACA8-sND sample, which is sufficient for SANS experiments.

The state of inhibition of ACA8 in sND was assessed by the basal ATPase activity. Binding of CaM to the CaM-binding domain of ACA8 in sND leads to an almost two-fold increase in ATPase activity compared to the basal activity in the absence of CaM (Fig. 6.2 b) showing full functionality of ACA8 in deuterated nanodisc [126]. The overall ATPase activity of fully activated ACA8 in sND was two-fold higher compared to detergent solubilized ACA8 (in LMNG) and slightly reduced compared to ACA8 incorporated in non-deuterated POPC-nanodisc. Stealth nanodiscs contain a mixture of deuterated PC lipids with different chain length and this might explain the small differences in the overall activity of ACA8 in sND. Nevertheless, the results show a full functionality of ACA8 in deuterated nanodiscs [126].

In order to investigate whether the deuteration level of d-CaM affects the activation process, the elution profiles of ACA8 in sND with and without d-CaM were compared (Fig. 6.2 c). The SEC-profile of the ACA8+CaM complex in sND reveals a shift of the elution peak (11.0ml for complex vs. 11.8ml for ACA8 alone). This drastic increase in hydrodynamic radius indicates drastic conformational changes as observed for ACA8 in non-deuterated POPC-nanodisc. These results suggest that neither the deuterated disc components nor the deuterated CaM affect the activation process of ACA8 [126].

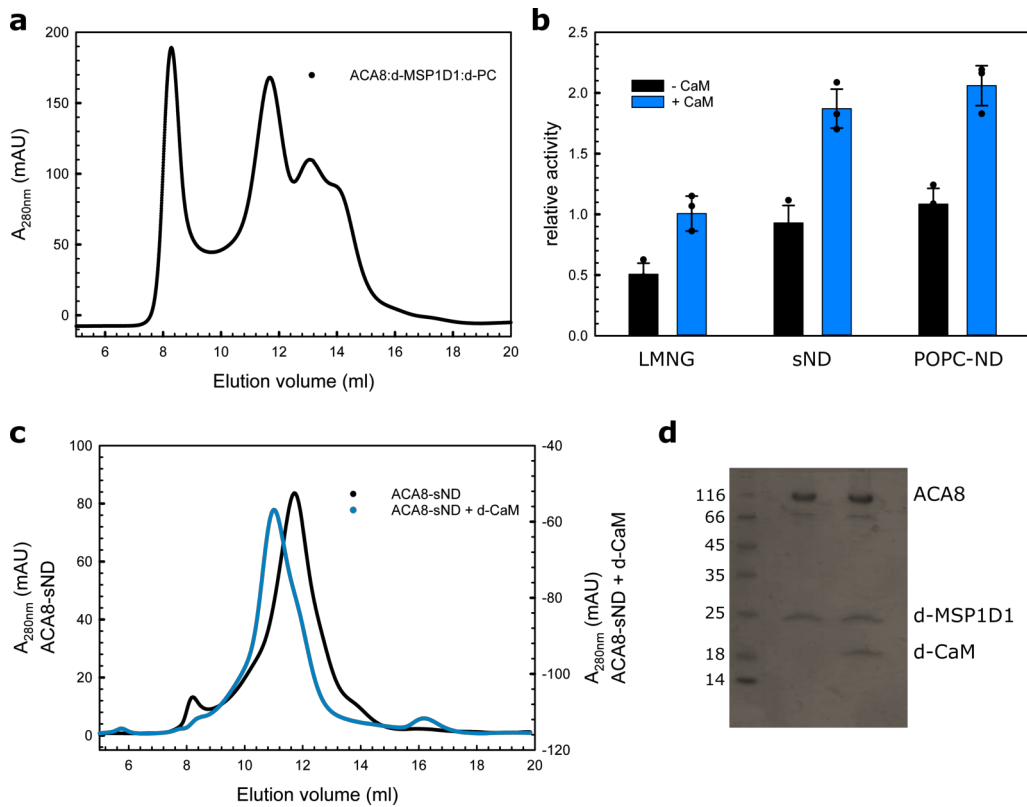


Figure 6.2: Reconstitution of ACA8 in stealth nanodisc. (a) LMNG-purified ACA8 was mixed with d-MSP1D1 and d-PC and assembled by detergent removal using cyclodextrin. Reconstitution was analysed on a size-exclusion chromatography column (Superdex200 10/300). (b) ATPase activity of ACA8 in stealth nanodiscs was analysed using the Baginski assay in the presence (blue) and absence (black) of CaM7. The activity of ACA8-sND was compared to activity in detergent (LMNG) and POPC nanodiscs. (c) Size-exclusion chromatography of ACA8-sND in complex with d-CaM (blue) showing the same increase in hydrodynamic radius. (d) SDS-PAGE of size-exclusion fractions of ACA8 incorporated into sND with and without d-CaM7.

6.3.2 Structural characterization of ACA8 by SANS

Small-angle neutron scattering measurements were carried out with ACA8, reconstituted in stealth nanodisc, in its auto-inhibited state (apo, in absence of CaM) as well as in its activated state (in complex with CaM). Two configurations of the activated state were measured, (1) ACA8 in complex with protonated CaM and (2) ACA8 in complex with perdeuterated CaM (d-CaM) (see Chapter 6.2.1) where the contrast of matched-out CaM is the same like the buffer. Therefore, d-CaM is invisible in the point of view of neutrons and only ACA8 in its activated state contributes to the scattering signal (Fig. 6.3 a). The complexes with either d-CaM or protonated CaM were purified before measurements to separate excess of CaM. Deuterated CaM was measured as control sample as well. All samples were measured in

100 % D₂O to match-out all deuterated nanodisc components. The radius of gyration was calculated from the Guinier approximation and showed a clear expansion upon CaM-binding (Supplementary Table A.4). The experimentally derived radius of gyration for the apo conformation was 4.0 nm and once d-CaM binds to ACA8 the R_g increase significantly to 4.3 nm. The increase in R_g is in line with the SAXS data shown above (see chapter 4.3.4.2). The R_g increases even more to 5.0 nm for the complex of ACA8 with protonated CaM which indicates that the deuterated CaM is effectively matched-out. This is in good agreement with the scattering profile of d-CaM alone, showing a flat line with no increase in scattering intensity (Fig. 6.3 a). The Guinier region of all three ACA8 samples show a linear distribution with enough data points, showing that the detector distance covered a sufficient q-range. Notably, experimentally derived R_g of ACA8 in sND in all conformations are significantly smaller than those obtained by SAXS measurements (Supplementary Table A.3), showing the minimal scattering contribution of all nanodisc components to the SANS data. This is in line with the comparison of scattering profiles of apo ACA8-sND with "empty stealth nanodisc" (Supplementary Fig. A.5) showing much higher scattering intensity of the ACA8-sND sample. [126]

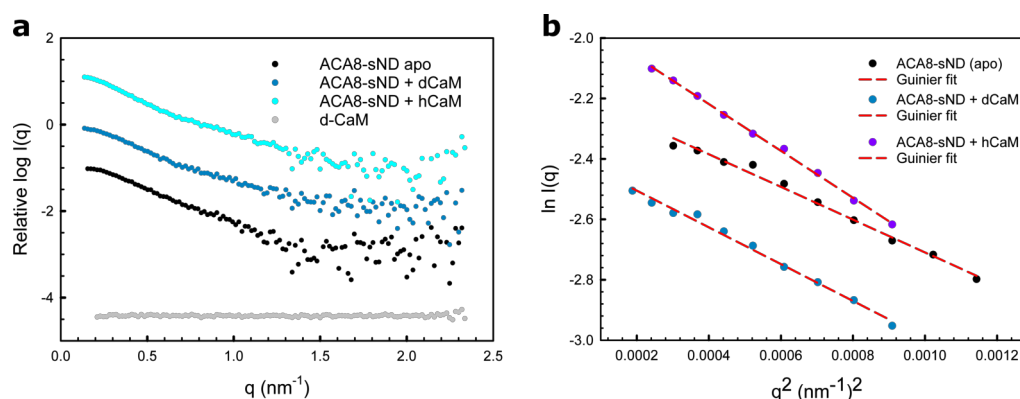


Figure 6.3: Small-angle neutron scattering of ACA8 incorporated into stealth nanodiscs. (a) SANS scattering curves of deuterated CaM7 (d-CaM, 73% deuterated) are shown in grey, show no significant scattering in 100% D₂O and thus do not contribute to the scattering signal. Scattering profiles of ACA8 incorporated into sND in apo conformation (black) were compared with data for the corresponding complex with hydrogenated CaM7 (h-CaM) and selectively deuterated CaM (d-CaM) (light blue and dark blue, respectively). The deuterated nanodisc components do not contribute to the SANS scattering signal in 100 % D₂O (Supplementary Fig. A.5) [60] (b) Guinier region of the SANS data obtained for ACA8 incorporated in stealth nanodiscs in apo form and in complex with deuterated and hydrogenated CaM. First data points were affected by parasitic scattering and removed for data analysis. Individual figures reprinted from Nitsche *et al.* [126].

The pair distance distribution function ($p(r)$) describes all interatomic distances and determines the maximal particle dimension (D_{\max}). This was computed for ACA8-sND samples in all conformations (Fig. 6.4). The $p(r)$ function of ACA8 in its apo

conformation shows a maximal particle dimension of 13 nm and a bi-lobed shape with two distinct peaks at 3.6 nm and 7.0 nm (Fig. 6.4 a). This is consistent with a rather compact, multi-domain particle. Once d-CaM binds to ACA8 the D_{\max} increases to 15 nm and the peak at 7 nm becomes less pronounced and is shifted to larger distances, which indicates a protein expansion. As in the ACA8-(d-CaM) complex only ACA8 contributes to the scattering signal, the obtained particle expansion suggest large conformational changes in the calcium pump during the activation. Combining the SANS data with the fluorescence polarization data (see Chapter 4.3.4.1), the observed expansion is likely due to the release of the regulatory domain from the core enzyme. In the complex of ACA8 with protonated CaM the D_{\max} increases further to 18 nm, showing that CaM contributes to the scattering signal. The $p(r)$ function shows further expansion with an even less pronounced second peak. All these data are consistent with the model that the binding of regulatory domain to the core is released once CaM is bound and the ACA8 structure becomes less compact compared to the apo conformation. The SAXS data, showing an increase in flexibility once CaM binds are in good agreement with the shown SANS data. Since all nanodisc components are effectively matched-out, the effects are more pronounced in the SANS data. [126]

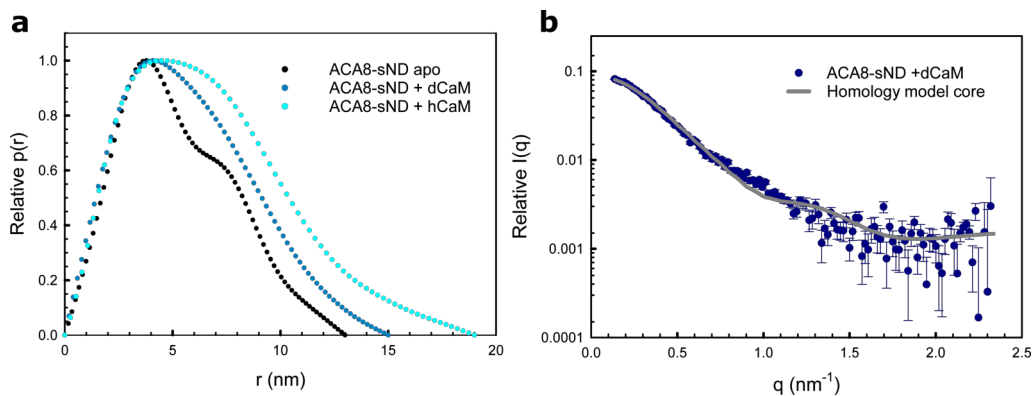


Figure 6.4: Analysis of SANS scattering of ACA8-sND. (a) Distance distribution ($p(r)$)-plot of the SANS data of ACA8 in apo conformation (black) and of data in complex with deuterated CaM (dark blue) and hydrogenated CaM (light blue), indicating that binding of d-CaM to ACA8 leads to an increase of D_{\max} . The D_{\max} value is further increased when hydrogenated CaM is bound, showing that deuterated CaM is matched-out. (b) Scattering intensity of the homology model of ACA8core was computed and fitted against the scattering data of ACA8-(d-CaM) complex.

6.3.3 Structural modelling of ACA8 in its activated state

SANS scattering data allowed modelling of full-length ACA8 without taking the nanodisc components into account. No structural model of the full-length ACA8 was available and even the previously published cryo-EM structure of human PMCA1

didn't resolve the regulatory domain [116]. Therefore, a homology model of ACA8core (130aa - 1074 aa) based on the sarco/endoplasmic reticulum Ca^{2+} - ATPase (SERCA) structure in E2 conformation (pdb: 4aqr) was generated and used for further modelling. Fitting the calculated scattering intensity (using CRYSON) of the homology model shows major discrepancies in the mid-q-range (Fig. 6.4 b) with a χ^2 of 25.2, which is most likely due to the lack of the regulatory domain. To generate a model of full-length ACA8 the previously determined crystal structure of the ACA8 regulatory domain (40aa - 95aa) [67] was used and combined with the ACA8core model. The N-terminal residues (1aa - 39aa) and the linker residues (96aa - 129aa) were placed as dummy atoms. Since no structural informations about the interaction area of the regulatory domain with ACA8core were available, modelling of full-length ACA8 in its auto-inhibited state was extremely challenging. However, the available structural data allowed modelling of ACA8 in its activated state using the SANS data of ACA8-sND in complex with deuterated CaM (d-CaM). In order to model the activated state, 10,000 full-length models of ACA8 were generated with the regulatory domain (1aa - 130aa) in various conformations using the program RANCH [243, 244]. Scattering intensities of each model were calculated using CRYSON [219] and fitted against the experimental SANS data of the ACA8-(d-CaM) complex. The overall size of the full-length models describe the low-q region of the SANS data well, but no single model was found which provide a reasonable fit to the experimental data across the entire q-range. Since, SAXS and SANS data suggested that the regulatory domain becomes more flexible in the activated state, ensemble optimized modelling (EOM) analysis was performed in order to quantitatively assess changes in the ensemble-averaged conformations in the activated state [126].

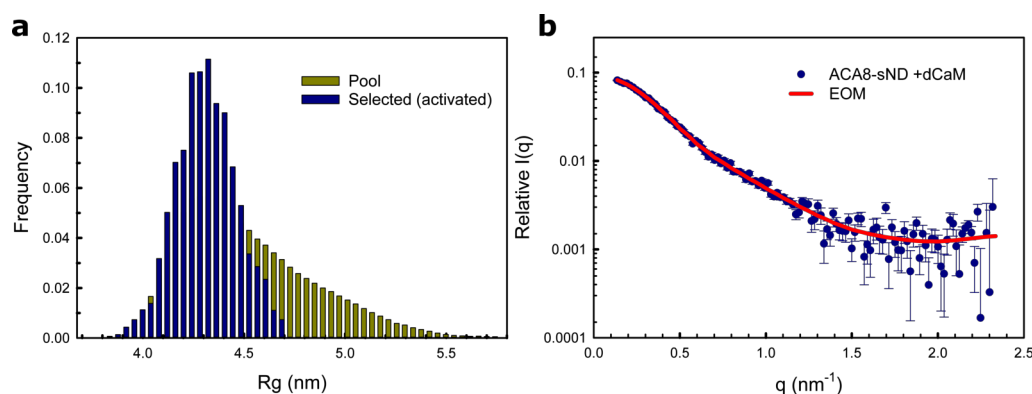


Figure 6.5: Ensemble optimized method to model the activated state of ACA8. The Ensemble Optimization Method (EOM) [244] was used to generate and select a pool of models with different conformations of the regulatory domain (a) that were subsequently used to fit the experimental SANS data (acquired in stealth nanodiscs) (b). Scattering intensity of a selected pool of ACA8 with the RD in different conformation were computed using CRYSON and fitted against the scattering data of ACA8-(d-CaM) complex (b).

The pool of generated ACA8 models with different conformations of the regulatory domain was used for EOM. A genetic algorithm of the program GAJOE was used to select an ensemble of conformers (sub-ensemble) of the regulatory domain. Subsequently, the weighted average theoretical scattering curve is compared with the experimental scattering curve. The sub-ensemble whose theoretical scattering curve best describes the experimental SANS data was selected [243, 244].

In the size distribution plot the R_g values of the generated models were ranging from really compact molecules (R_g of 3.9 nm) to much more extended ones with an R_g of around 5 nm (Fig. 6.5 a, yellow bars). As the conformation of the homology model (ACA8core) was kept constant, the size differences displayed derive from differences in the conformations of the regulatory domain proportional to the ACA8core. The selected sub-ensemble fits the experimental scattering data very well, with an χ^2 of 1.0 (Fig. 6.5 b). The R_g distribution of the selected best fitting sub-ensemble is shifted to smaller R_g values compared to the random pool (Fig. 6.5 a, blue bars), revealing that complex occupies a restricted range of conformations that tend towards the more compact rather than extended conformations, relative to the random pool. This is also reflected in the three representative models (Fig. 6.6) [126]. These models, with R_g values between 4.0 - 4.4 nm, showed different orientations of the regulatory domain and none of the selected conformers contains a fully extended regulatory domain. The R_g distribution plot from EOM analysis against the apo ACA8-sND scattering data shows that selected ensembles are shifted to smaller R_g values compared to analysis of the activated state, indicating more compact molecules (Supplementary Fig. A.6).

The metric R_{flex} provides a quantitative measure for the flexibility of the system. This data shows an R_{flex} of 68.1% for the selected ensemble and 86.1% for the pool, indicating that the regulatory domain possesses some degree of flexibility in the activated state but the whole molecule still shows a more compact arrangement. The fit of the selected sub-ensembles has a perfect χ^2 of 1.0. Nevertheless, the data in the mid- q region are slightly noisy. Conformational changes are expected to produce differences in the scattering profile in the same region. Notably, different conformations of the RD could also produce a similar fit. A more concentrated sample would be able to show more details in the mid- q region and a more precise analysis would be possible. Nevertheless, the Guinier approximation shows a very good fit, indicating a reliable R_g and most likely, the EOM analysis would produce a similar R_g -distribution, with comparable compact conformations of the RD. Moreover, the conformation of the core enzyme was kept constant during the EOM modelling. However studies on human PMCAs using a photoactivatable phosphatidylcholine lipid suggested conformational changes in the transmembrane domain during the activation process [117, 118, 189]. Therefore, for a more in-depth analysis of the conformational changes in the core enzyme, high-resolution structural data of PMCAs

in different conformations are needed.

Taken together, these data supported previous results showing that CaM-binding to ACA8 leads to displacement of the regulatory domain from the ACA8 core enzyme, which releases the autoinhibitor and allows the enzyme to undergo its conformational cycle required for the pumping of Ca^{2+} ions [126].

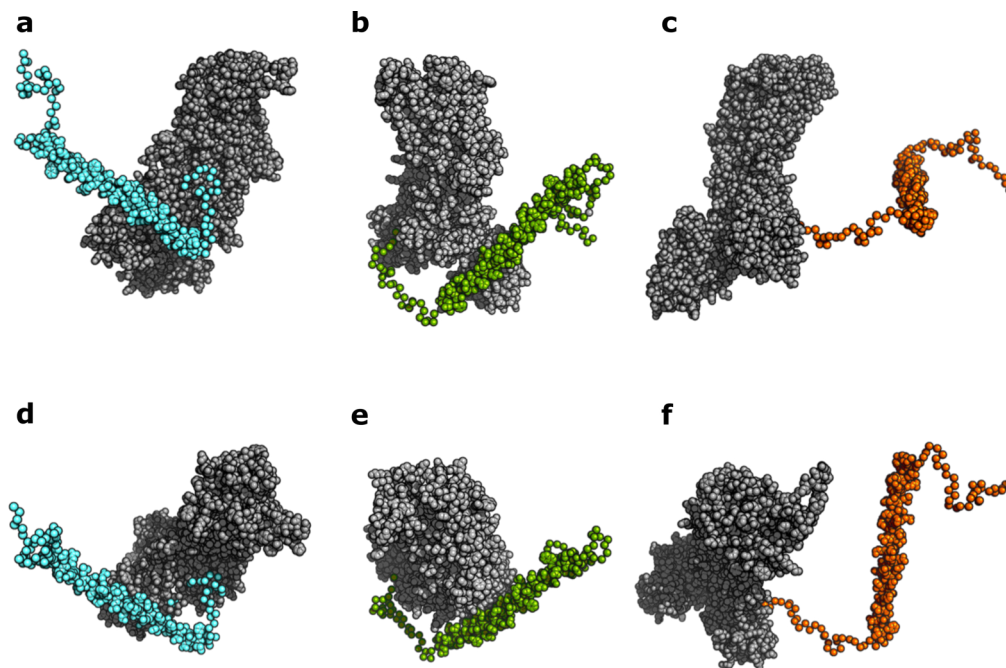


Figure 6.6: Ensemble optimized method to model the activated state of ACA8 – selected models. (a-c) Representative models for the activated ACA8-CaM complex are shown as spheres. Models derived from the best-fitting sub-ensemble. ACA8core is shown in gray and the regulatory domain in different conformations (cyan, green and orange) which are part of the best-fitting sub-ensemble. (d-f) Selected models shown in (a-c) but rotated by 90 degrees.

6.4 Conclusion

In summary, the use of stealth nanodiscs combined with small-angle neutron scattering enabled the modelling of full-length ACA8 in its activated state for the first time. The data showed that all nanodisc components are effectively matched out at 100 % D₂O, where the incoherent scattering of H₂O is minimized. Control experiments showed that the ATPase activity as well as the elution profile of activated ACA8 in sND are comparable to those of ACA8 obtained in non-deuterated nanodiscs, suggesting that stealth nanodiscs do not affect the activation process. Due to the fact, that only ACA8 contributes to the neutron scattering signal the differences between apo state and the activated conformation are more pronounced, although the scattering intensity in SANS is much weaker. By using perdeuteration of CaM to match-out the signal derived from CaM the structural changes during activation within ACA8 could be studied more precisely. These data illustrate that the binding of CaM to ACA8 leads to displacement of the regulatory domain from the core enzyme, which is in good agreement with the data shown above (see Chapter 4). In combination with the biochemical and biophysical studies shown in Chapter 4, the structural model for activated ACA8 sets the structural basis for activation of ACA8 in a native-like lipid environment.

References

1. Palmgren, M. G. & Nissen, P. P-Type ATPases. *Annual Review of Biophysics* **40**, 243–266 (2011).
2. Newstead, S. Recent advances in understanding proton coupled peptide transport via the POT family. *Current Opinion in Structural Biology* **45**, 17–24 (2017).
3. Hilger, D., Masureel, M. & Kobilka, B. K. Structure and dynamics of GPCR signaling complexes. *Nature Structural & Molecular Biology* **25**, 4–12 (2018).
4. Wei, C.-J., Xu, X. & Lo, C. W. Connexins and cell signaling in development and disease. *Annual Review of Cell and Developmental Biology* **20**, 811–838 (2004).
5. Haswell, E., Phillips, R. & Rees, D. Mechanosensitive Channels: What Can They Do and How Do They Do It? *Structure* **19**, 1356–1369 (2011).
6. Kühlbrandt, W. Structure and function of mitochondrial membrane protein complexes. *BMC Biology* **13**, 89 (2015).
7. Wallin, E. & von Heijne, G. Genome-wide analysis of integral membrane proteins from eubacterial, archaean, and eukaryotic organisms. *Protein Science : A Publication of the Protein Society* **7**, 1029 (1998).
8. Overington, J. P., Al-Lazikani, B. & Hopkins, A. L. How many drug targets are there? *Nature Reviews Drug Discovery* **5**, 993–996 (2006).
9. Rask-Andersen, M., Almén, M. S. & Schiöth, H. B. Trends in the exploitation of novel drug targets. *Nature Reviews Drug Discovery* **10**, 579–590 (2011).
10. Seddon, A. M., Curnow, P. & Booth, P. J. Membrane proteins, lipids and detergents: Not just a soap opera. *Biochimica et Biophysica Acta - Biomembranes* **1666**, 105–117 (2004).
11. Sanders, C. R. & Prosser, R. S. Bicelles: A model membrane system for all seasons? *Structure* **6**, 1227–1234 (1998).
12. Czerski, L. & Sanders, C. R. Functionality of a membrane protein in bicelles. *Analytical Biochemistry* **284**, 327–333 (2000).
13. Sanders, C. R., Hare, B. J., Howard, K. P. & Prestegard, J. H. Magnetically-oriented phospholipid micelles as a tool for the study of membrane-associated molecules. *Progress in Nuclear Magnetic Resonance Spectroscopy* **26**, 421–444 (1994).
14. Ujwal, R. & Bowie, J. U. Crystallizing membrane proteins using lipidic bicelles. *Methods* **55**, 337–341 (2011).

15. Faham, S. & Bowie, J. U. Bicelle crystallization: a new method for crystallizing membrane proteins yields a monomeric bacteriorhodopsin structure. *Journal of Molecular Biology* **316**, 1–6 (2002).
16. Johnson, Z. L. & Lee, S.-Y. in *Methods in enzymology* 373–383 (2015).
17. Chan, Y.-H. M. & Boxer, S. G. Model membrane systems and their applications. *Current Opinion in Chemical Biology* **11**, 581–587 (2007).
18. Geertsma, E. R., Nik Mahmood, N. A., Schuurman-Wolters, G. K. & Poolman, B. Membrane reconstitution of ABC transporters and assays of translocator function. *Nature Protocols* **3**, 256–266 (2008).
19. Frauenfeld, J., Löving, R., Armache, J.-P., Sonnen, A. F.-P., Guettou, F., Moberg, P., Zhu, L., Jegerschöld, C., Flayhan, A., Briggs, J. A. G., Garoff, H., Löw, C., Cheng, Y. & Nordlund, P. A saposin-lipoprotein nanoparticle system for membrane proteins. *Nature Methods* **13**, 345–351 (2016).
20. Denisov, I. G. & Sligar, S. G. Nanodiscs for structural and functional studies of membrane proteins. *Nature Structural & Molecular Biology* **23**, 481–486 (2016).
21. Yokoyama, S. Apolipoprotein-mediated cellular cholesterol efflux. *Biochimica et biophysica acta* **1392**, 1–15 (1998).
22. Georgila, K., Vyrta, D. & Drakos, E. Apolipoprotein A-I (ApoA-I), Immunity, Inflammation and Cancer. *Cancers* **11**, 1097 (2019).
23. Bayburt, T. H. & Sligar, S. G. Self-assembly of single integral membrane proteins into soluble nanoscale phospholipid bilayers. *Protein science : a publication of the Protein Society* **12**, 2476–81 (2003).
24. Denisov, I. G., Grinkova, Y. V., Lazarides, A. A. & Sligar, S. G. Directed Self-Assembly of Monodisperse Phospholipid Bilayer Nanodiscs with Controlled Size. *Journal of the American Chemical Society* **126**, 3477–3487. arXiv: 1502.06479 (2004).
25. Borch, J. & Hamann, T. The nanodisc: a novel tool for membrane protein studies. *Biological Chemistry* **390**, 805–14 (2009).
26. Bayburt, T. H., Leitz, A. J., Xie, G., Oprian, D. D. & Sligar, S. G. Transducin Activation by Nanoscale Lipid Bilayers Containing One and Two Rhodopsins. *Journal of Biological Chemistry* **282**, 14875–14881 (2007).
27. Shaw, A. W., Pureza, V. S., Sligar, S. G. & Morrissey, J. H. The Local Phospholipid Environment Modulates the Activation of Blood Clotting. *Journal of Biological Chemistry* **282**, 6556–6563 (2007).
28. Raschle, T., Hiller, S., Yu, T.-Y., Rice, A. J., Walz, T. & Wagner, G. Structural and Functional Characterization of the Integral Membrane Protein VDAC-1 in Lipid Bilayer Nanodiscs. *Journal of the American Chemical Society* **131**, 17777–17779 (2009).

29. Bayburt, T. H., Grinkova, Y. V. & Sligar, S. G. Assembly of single bacteriorhodopsin trimers in bilayer nanodiscs. *Archives of Biochemistry and Biophysics* **450**, 215–222 (2006).
30. Shih, A. Y., Freddolino, P. L., Sligar, S. G. & Schulten, K. Disassembly of Nanodiscs with Cholate. *Nano Letters* **7**, 1692–1696 (2007).
31. Olmeda, B., García-Álvarez, B. & Pérez-Gil, J. Structure–function correlations of pulmonary surfactant protein SP-B and the saposin-like family of proteins. *European Biophysics Journal* **42**, 209–222 (2013).
32. Flayhan, A., Mertens, H. D., Ural-Blimke, Y., Martinez Molledo, M., Svergun, D. I. & Löw, C. Saposin Lipid Nanoparticles: A Highly Versatile and Modular Tool for Membrane Protein Research. *Structure* **26**, 345–355.e5 (2018).
33. Graewert, M. A. & Svergun, D. I. Impact and progress in small and wide angle X-ray scattering (SAXS and WAXS). *Current Opinion in Structural Biology* **23**, 748–754 (2013).
34. Skou, S., Gillilan, R. E. & Ando, N. Synchrotron-based small-angle X-ray scattering of proteins in solution. *Nature Protocols* **9**, 1727–1739 (2014).
35. Wall, M. E., Gallagher, S. C. & Trewthella, J. Large-scale shape changes in proteins and macromolecular complexes. *Annual Review of Physical Chemistry* **51**, 355–380 (2000).
36. Hura, G. L., Menon, A. L., Hammel, M., Rambo, R. P., Poole II, F. L., Tsutakawa, S. E., Jenney Jr, F. E., Classen, S., Frankel, K. A., Hopkins, R. C., Yang, S.-j., Scott, J. W., Dillard, B. D., Adams, M. W. W. & Tainer, J. A. Robust, high-throughput solution structural analyses by small angle X-ray scattering (SAXS). *Nature Methods* **6**, 606–612 (2009).
37. Blanchet, C. E., Spilotros, A., Schwemmer, F., Graewert, M. A., Kikhney, A., Jeffries, C. M., Franke, D., Mark, D., Zengerle, R., Cipriani, F., Fiedler, S., Roessel, M. & Svergun, D. I. Versatile sample environments and automation for biological solution X-ray scattering experiments at the P12 beamline (PETRA III, DESY). *Journal of Applied Crystallography* **48**, 431–443 (2015).
38. Toft, K. N., Vestergaard, B., Nielsen, S. S., Snakenborg, D., Jeppesen, M. G., Jacobsen, J. K., Arleth, L. & Kutter, J. P. High-Throughput Small Angle X-ray Scattering from Proteins in Solution Using a Microfluidic Front-End. *Analytical Chemistry* **80**, 3648–3654 (2008).
39. Mertens, H. D. & Svergun, D. I. Structural characterization of proteins and complexes using small-angle X-ray solution scattering. *Journal of Structural Biology* **172**, 128–141 (2010).

40. Franke, D., Kikhney, A. G. & Svergun, D. I. Automated acquisition and analysis of small angle X-ray scattering data. *Nuclear Instruments and Methods in Physics Research Section A: Accelerators, Spectrometers, Detectors and Associated Equipment* **689**, 52–59 (2012).
41. Jacrot, B. The study of biological structures by neutron scattering from solution. *Reports on Progress in Physics* **39**, 911–953 (1976).
42. Svergun, D. I. & Koch, M. H. J. Small-angle scattering studies of biological macromolecules in solution. *Reports on Progress in Physics* **66**, 1735–1782 (2003).
43. Svergun, D. I. & IUCr. Determination of the regularization parameter in indirect-transform methods using perceptual criteria. *Journal of Applied Crystallography* **25**, 495–503 (1992).
44. Guinier, A., Walker, C. B., York, N. & Wiley, J. *Small-angle scattering of X-rays* tech. rep. (1955).
45. Jacques, D. A. & Trewthella, J. Small-angle scattering for structural biology—Expanding the frontier while avoiding the pitfalls. *Protein Science* **19**, 642–657 (2010).
46. Guinier, A. The diffusion of x-rays under the extremely weak angles applied to the study of fine particles and colloidal suspension. *Cr Hebd Acad Sci* **206**, 1374–1376 (1938).
47. Engelman, D. M. & Moore, P. B. Determination of Quaternary Structure by Small Angle Neutron Scattering. *Annual Review of Biophysics and Bioengineering* **4**, 219–241 (1975).
48. Sears, V. F. Neutron scattering lengths and cross sections. *Neutron News* **3**, 26–37 (1992).
49. Jacrot, B. & Zaccai, G. Determination of molecular weight by neutron scattering. *Biopolymers* **20**, 2413–2426 (1981).
50. Jeffries, C. M., Graewert, M. A., Blanchet, C. E., Langley, D. B., Whitten, A. E. & Svergun, D. I. Preparing monodisperse macromolecular samples for successful biological small-angle X-ray and neutron-scattering experiments. *Nature Protocols* **11**, 2122–2153 (2016).
51. Svergun, D. *Small angle x-ray and neutron scattering from biomacromolecular solutions* 358 (Oxford University Press, 2013).
52. Schroer, M. A., Blanchet, C. E., Gruzinov, A. Y., Gräwert, M. A., Brennich, M. E., Hajizadeh, N. R., Jeffries, C. M. & Svergun, D. I. Smaller capillaries improve the small-angle X-ray scattering signal and sample consumption for biomacromolecular solutions. *Journal of Synchrotron Radiation* **25**, 1113–1122 (2018).

53. Midgett, C. R. & Madden, D. R. Breaking the bottleneck: Eukaryotic membrane protein expression for high-resolution structural studies. *Journal of Structural Biology* **160**, 265–274 (2007).
54. Pandey, A., Shin, K., Patterson, R. E., Liu, X.-Q. & Rainey, J. K. Current strategies for protein production and purification enabling membrane protein structural biology. *Biochemistry and Cell Biology* **94**, 507–527 (2016).
55. Privé, G. G. Detergents for the stabilization and crystallization of membrane proteins. *Methods* **41**, 388–397 (2007).
56. Champeil, P., Menguy, T., Tribet, C., Popot, J.-L. & Le Maire, M. Interaction of Amphipols with Sarcoplasmic Reticulum Ca²⁺-ATPase (2000).
57. Gohon, Y., Dahmane, T., Ruigrok, R. W., Schuck, P., Charvolin, D., Rappaport, F., Timmins, P., Engelman, D. M., Tribet, C., Popot, J.-L. & Ebel, C. Bacteriorhodopsin/Amphipol Complexes: Structural and Functional Properties. *Biophysical Journal* **94**, 3523–3537 (2008).
58. Arana, M. R., Fiori, M. C. & Altenberg, G. A. Functional and structural comparison of the ABC exporter MsbA studied in detergent and reconstituted in nanodiscs. *Biochemical and Biophysical Research Communications* **512**, 448–452 (2019).
59. Chen, Q., She, J., Zeng, W., Guo, J., Xu, H., Bai, X.-c. & Jiang, Y. Structure of mammalian endolysosomal TRPML1 channel in nanodiscs. *Nature* **550**, 415–418 (2017).
60. Josts, I., Nitsche, J., Maric, S., Mertens, H. D., Moulin, M., Haertlein, M., Prevost, S., Svergun, D. I., Busch, S., Forsyth, V. T. & Tidow, H. Conformational States of ABC Transporter MsbA in a Lipid Environment Investigated by Small-Angle Scattering Using Stealth Carrier Nanodiscs. *Structure (London, England : 1993)* **26**, 1072–1079.e4 (2018).
61. Maric, S., Skar-Gislinge, N., Midtgaard, S., Thygesen, M. B., Schiller, J., Frielinghaus, H., Moulin, M., Haertlein, M., Forsyth, V. T., Pomorski, T. G. & Arleth, L. Stealth carriers for low-resolution structure determination of membrane proteins in solution. *Acta Crystallographica Section D Biological Crystallography* **70**, 317–328 (2014).
62. Maric, S., Thygesen, M. B., Schiller, J., Marek, M., Moulin, M., Haertlein, M., Forsyth, V. T., Bogdanov, M., Dowhan, W., Arleth, L. & Pomorski, T. G. Biosynthetic preparation of selectively deuterated phosphatidylcholine in genetically modified *Escherichia coli*. *Applied Microbiology and Biotechnology* **99**, 241–254 (2015).

63. Kawai, T., Caaveiro, J. M., Abe, R., Katagiri, T. & Tsumoto, K. Catalytic activity of MsbA reconstituted in nanodisc particles is modulated by remote interactions with the bilayer. *FEBS Letters* **585**, 3533–3537 (2011).
64. Graziano, V., Miller, L. & Yang, L. Interpretation of solution scattering data from lipid nanodiscs. *J. Appl. Cryst* **51**, 157–166 (2018).
65. Lyons, J. A., Bøggild, A., Nissen, P. & Frauenfeld, J. *Saposin-Lipoprotein Scaffolds for Structure Determination of Membrane Transporters* 1st ed., 85–99 (Elsevier Inc., 2017).
66. Popovic, K., Holyoake, J., Pomès, R. & Privé, G. G. Structure of saposin A lipoprotein discs. *Proceedings of the National Academy of Sciences of the United States of America* **109**, 2908–12 (2012).
67. Tidow, H., Poulsen, L. R., Andreeva, A., Knudsen, M., Hein, K. L., Wiuf, C., Palmgren, M. G. & Nissen, P. A bimodular mechanism of calcium control in eukaryotes. *Nature* **491**, 468–472 (2012).
68. Duquesne, K. & Sturgis, J. N. in *Methods in molecular biology (Clifton, N.J.)* 205–217 (2010).
69. Le Maire, M., Champeil, P & Moller, J. V. Interaction of membrane proteins and lipids with solubilizing detergents. *Biochimica et biophysica acta* **1508**, 86–111 (2000).
70. Garavito, R. M. & Ferguson-Miller, S. Detergents as Tools in Membrane Biochemistry. *Journal of Biological Chemistry* **276**, 32403–32406 (2001).
71. Gohon, Y. & Popot, J.-L. Membrane protein–surfactant complexes. *Current Opinion in Colloid & Interface Science* **8**, 15–22 (2003).
72. Lund, S, Orłowski, S, de Foresta, B, Champeil, P, le Maire, M & Møller, J. V. Detergent structure and associated lipid as determinants in the stabilization of solubilized Ca²⁺-ATPase from sarcoplasmic reticulum. *The Journal of biological chemistry* **264**, 4907–15 (1989).
73. Reinsberg, D., Booth, P. J., Jegerschöld, C., Khoo, B. J. & Paulsen, H. Folding, Assembly, and Stability of the Major Light-Harvesting Complex of Higher Plants, LHCII, in the Presence of Native Lipids† (2000).
74. Champeil, P, Orłowski, S, Babin, S, Lund, S, le Maire, M, Møller, J, Lenoir, G. & Montigny, C. A robust method to screen detergents for membrane protein stabilization, revisited. *Analytical Biochemistry* **511**, 31–35 (2016).
75. Von. Jagow, G. & Schagger, H. *Membrane protein purification and crystallization : a practical guide* 316 (Academic Press, 2003).
76. Bayburt, T. H. & Sligar, S. G. Membrane protein assembly into Nanodiscs. *FEBS letters* **584**, 1721–7 (2010).

77. Autzen, H. E., Myasnikov, A. G., Campbell, M. G., Asarnow, D., Julius, D. & Cheng, Y. Structure of the human TRPM4 ion channel in a lipid nanodisc. *Science* **359**, 228–232 (2018).
78. Hagn, F., Etzkorn, M., Raschle, T. & Wagner, G. Optimized phospholipid bilayer nanodiscs facilitate high-resolution structure determination of membrane proteins. *Journal of the American Chemical Society* **135**, 1919–25 (2013).
79. Skar-Gislinge, N., Kynde, S. A. R., Denisov, I. G., Ye, X., Lenov, I., Sligar, S. G. & Arleth, L. Small-angle scattering determination of the shape and localization of human cytochrome P450 embedded in a phospholipid nanodisc environment. *Acta crystallographica. Section D, Biological crystallography* **71**, 2412–21 (2015).
80. Kynde, S. A. R., Skar-Gislinge, N., Pedersen, M. C., Midtgaard, S. R., Simonsen, J. B., Schweins, R., Mortensen, K. & Arleth, L. Small-angle scattering gives direct structural information about a membrane protein inside a lipid environment. *Acta Crystallographica Section D Biological Crystallography* **70**, 371–383 (2014).
81. Lyons, J. A., Bøggild, A., Nissen, P. & Frauenfeld, J. in *Methods in enzymology* 85–99 (2017).
82. Flayhan, A., Mertens, H. D., Ural-Blimke, Y., Martinez Molledo, M., Svergun, D. I. & Löw, C. Saposin Lipid Nanoparticles: A Highly Versatile and Modular Tool for Membrane Protein Research. *Structure* **26**, 345–355.e5 (2018).
83. Ritchie, T. K., Grinkova, Y. V., Bayburt, T. H., Denisov, I. G., Zolnerciks, J. K., Atkins, W. M. & Sligar, S. G. *Chapter 11 Reconstitution of Membrane Proteins in Phospholipid Bilayer Nanodiscs C*, 211–231 (Elsevier Masson SAS, 2009).
84. Konarev, P. V., Volkov, V. V., Sokolova, A. V., Koch, M. H. & Svergun, D. I. PRIMUS: A Windows PC-based system for small-angle scattering data analysis. *Journal of Applied Crystallography* **36**, 1277–1282 (2003).
85. Hagn, F., Etzkorn, M., Raschle, T. & Wagner, G. Optimized Phospholipid Bilayer Nanodiscs Facilitate High-Resolution Structure Determination of Membrane Proteins. *Journal of the American Chemical Society* **135**, 1919–1925 (2013).
86. Kehlenbeck, D.-M., Josts, I., Nitsche, J., Busch, S., Forsyth, T. & Tidow, H. Comparison of lipidic carrier systems for integral membrane proteins – MsbA as case study. *Biological Chemistry* **0** (2019).
87. Veith, K., MartinezMolledo, M., AlmeidaHernandez, Y., Josts, I., Nitsche, J., Löw, C. & Tidow, H. Lipid-like Peptides can Stabilize Integral Membrane Proteins for Biophysical and Structural Studies. *ChemBioChem* **18**, 1735–1742 (2017).

88. Pedersen, M. C., Arleth, L. & Mortensen, K. WillItFit : a framework for fitting of constrained models to small-angle scattering data. *Journal of Applied Crystallography* **46**, 1894–1898 (2013).
89. Clapham, D. E. Calcium signaling. *Calcium Signaling, Second Edition*, 1–540 (2005).
90. Berridge, M. J., Lipp, P. & Bootman, M. D. The versatility and universality of calcium signalling. *Nature Reviews Molecular Cell Biology* **1**, 11–21 (2000).
91. Clapham, D. E. Calcium signaling. *Cell* **80**, 259–268 (1995).
92. Miyawaki, A., Llopis, J., Heim, R., McCaffery, J. M., Adams, J. A., Ikura, M. & Tsien, R. Y. Fluorescent indicators for Ca²⁺-based on green fluorescent proteins and calmodulin. *Nature* **388**, 882–887 (1997).
93. Pinton, P., Pozzan, T & Rizzuto, R. The Golgi apparatus is an inositol 1,4,5-trisphosphate-sensitive Ca²⁺ store, with functional properties distinct from those of the endoplasmic reticulum. *The EMBO journal* **17**, 5298–308 (1998).
94. Bootman, M. D., Rietdorf, K., Hardy, H., Dautova, Y., Corps, E., Pierro, C., Stapleton, E., Kang, E. & Proudfoot, D. in *eLS* (John Wiley & Sons, Ltd, Chichester, UK, 2012).
95. Berridge, M. J., Bootman, M. D. & Roderick, H. L. Calcium signalling: dynamics, homeostasis and remodelling. *Nature Reviews Molecular Cell Biology* **4**, 517–529 (2003).
96. Axelsen, K. B. & Palmgren, M. G. Evolution of substrate specificities in the P-type ATPase superfamily. *Journal of molecular evolution* **46**, 84–101 (1998).
97. Auland, M. E., Roufogalis, B. D., Devaux, P. F. & Zachowski, A. Reconstitution of ATP-dependent aminophospholipid translocation in proteoliposomes. *Proceedings of the National Academy of Sciences* **91**, 10938–10942 (1994).
98. Tang, X., Halleck, M. S., Schlegel, R. A. & Williamson, P. A Subfamily of P-Type ATPases with Aminophospholipid Transporting Activity. *Science* **272**, 1495–1497 (1996).
99. Wuytack, F, Raeymaekers, L & Missiaen, L. Molecular physiology of the SERCA and SPCA pumps. *Cell calcium* **32**, 279–305 (2002).
100. Inesi, G., Prasad, A. M. & Pilankatta, R. The Ca²⁺ ATPase of cardiac sarcoplasmic reticulum: Physiological role and relevance to diseases. *Biochemical and Biophysical Research Communications* **369**, 182–187 (2008).
101. FLOYD, R & WRAY, S. Calcium transporters and signalling in smooth muscles. *Cell Calcium* **42**, 467–476 (2007).

102. Olesen, C., Picard, M., Winther, A. M. L., Gyrop, C., Morth, J. P., Oxvig, C., Møller, J. V. & Nissen, P. The structural basis of calcium transport by the calcium pump. *Nature* **450**, 1036–1042 (2007).
103. Bublitz, M., Poulsen, H., Morth, J. P. & Nissen, P. In and out of the cation pumps: P-Type ATPase structure revisited. *Current Opinion in Structural Biology* **20**, 431–439 (2010).
104. Apell, H.-J. How do P-Type ATPases transport ions? *Bioelectrochemistry* **63**, 149–156 (2004).
105. Laursen, M., Bublitz, M., Moncoq, K., Olesen, C., Møller, J. V., Young, H. S., Nissen, P. & Morth, J. P. Cyclopiazonic acid is complexed to a divalent metal ion when bound to the sarcoplasmic reticulum Ca²⁺-ATPase. *The Journal of biological chemistry* **284**, 13513–8 (2009).
106. Menguy, T., Corre, F., Juul, B., Bouneau, L., Lafitte, D., Derrick, P. J., Sharma, P. S., Falson, P., Levine, B. A., Møller, J. V. & le Maire, M. Involvement of the Cytoplasmic Loop L6–7 in the Entry Mechanism for Transport of Ca²⁺ through the Sarcoplasmic Reticulum Ca²⁺ -ATPase. *Journal of Biological Chemistry* **277**, 13016–13028 (2002).
107. Strehler, E. E., Filoteo, A. G., Penniston, J. T. & Caride, A. J. Plasma-membrane Ca(2+) pumps: structural diversity as the basis for functional versatility. *Biochemical Society transactions* **35**, 919–22 (2007).
108. Di Leva, F., Domi, T., Fedrizzi, L., Lim, D. & Carafoli, E. The plasma membrane Ca²⁺ ATPase of animal cells: Structure, function and regulation. *Archives of Biochemistry and Biophysics* **476**, 65–74 (2008).
109. Brini, M. & Carafoli, E. Calcium Pumps in Health and Disease. *Physiological Reviews* **89**, 1341–1378 (2009).
110. Malmström, S., Askerlund, P & Palmgren, M. G. A calmodulin-stimulated Ca²⁺-ATPase from plant vacuolar membranes with a putative regulatory domain at its N-terminus. *FEBS letters* **400**, 324–8 (1997).
111. Bonza, M. C. & Luoni, L. Plant and animal type 2B Ca²⁺-ATPases: Evidence for a common auto-inhibitory mechanism. *FEBS Letters* **584**, 4783–4788 (2010).
112. Carafoli, E. Biogenesis: plasma membrane calcium ATPase: 15 years of work on the purified enzyme. *FASEB journal : official publication of the Federation of American Societies for Experimental Biology* **8**, 993–1002 (1994).
113. Carafoli, E. The signaling function of calcium and its regulation. *Journal of hypertension. Supplement : official journal of the International Society of Hypertension* **12**, S47–56 (1994).
114. Penniston, J. T. & Enyedi, A. Modulation of the plasma membrane Ca²⁺ pump. *The Journal of membrane biology* **165**, 101–9 (1998).

115. Brini, M. Plasma membrane Ca²⁺-ATPase: from a housekeeping function to a versatile signaling role. *Pflügers Archiv - European Journal of Physiology* **457**, 657–664 (2009).
116. Gong, D., Chi, X., Ren, K., Huang, G., Zhou, G., Yan, N., Lei, J. & Zhou, Q. Structure of the human plasma membrane Ca²⁺-ATPase 1 in complex with its obligatory subunit neuroplastin. *Nature Communications* **9**, 3623 (2018).
117. Mangialavori, I., Villamil-Giraldo, A. M., Pignataro, M. F., Ferreira-Gomes, M., Caride, A. J. & Rossi, J. P. F. Plasma Membrane Calcium Pump (PMCA) differential exposure of hydrophobic domains after calmodulin and phosphatidic acid activation. *Journal of Biological Chemistry* **286**, 18397–18404 (2011).
118. Mangialavori, I., Giraldo, A. M. V., Buslje, C. M., Gomes, M. F., Caride, A. J. & Rossi, J. P. F. A new conformation in sarcoplasmic reticulum calcium pump and plasma membrane Ca²⁺ pumps revealed by a photoactivatable phospholipidic probe. *Journal of Biological Chemistry* **284**, 4823–4828 (2009).
119. Mangialavori, I., Corradi, G., Rinaldi, D., de la Fuente, M., Adamo, H. & Rossi, J. Autoinhibition mechanism of the plasma membrane calcium pump isoforms 2 and 4 studied through lipid–protein interaction. *Biochemical Journal* **443**, 125–131 (2012).
120. Parker, J. L. & Newstead, S. Method to increase the yield of eukaryotic membrane protein expression in *Saccharomyces cerevisiae* for structural and functional studies. *Protein Science* **23**, 1309–1314 (2014).
121. Drew, D., Newstead, S., Sonoda, Y., Kim, H., von Heijne, G. & Iwata, S. GFP-based optimization scheme for the overexpression and purification of eukaryotic membrane proteins in *Saccharomyces cerevisiae*. *Nature Protocols* **3**, 784–798 (2008).
122. Cormack, B. P., Bertram, G., Egerton, M., Gow, N. A. R., Falkow, S. & Brown, A. J. P. Yeast-enhanced green fluorescent protein (yEGFP): a reporter of gene expression in *Candida albicans*. *Microbiology* **143**, 303–311 (1997).
123. Tidow, H., Veprintsev, D. B., Freund, S. M. V. & Fersht, A. R. Effects of oncogenic mutations and DNA response elements on the binding of p53 to p53-binding protein 2 (53BP2). *Journal of Biological Chemistry* **281**, 32526–32533 (2006).
124. Jones, E. W. [31] Tackling the protease problem in *Saccharomyces cerevisiae*. *Methods in Enzymology* **194**, 428–453 (1991).
125. Miroux, B. & Walker, J. E. Over-production of proteins in *Escherichia coli*: Mutant hosts that allow synthesis of some membrane proteins and globular proteins at high levels. *Journal of Molecular Biology* **260**, 289–298 (1996).

126. Nitsche, J., Josts, I., Heidemann, J., Mertens, H. D., Maric, S., Moulin, M., Haertlein, M., Busch, S., Forsyth, V. T., Svergun, D. I., Uetrecht, C. & Tidow, H. Structural basis for activation of plasma-membrane Ca²⁺-ATPase by calmodulin. *Communications Biology* **1**, 206 (2018).
127. Heidemann, J. *Native Mass Spectrometry for the Structural Characterization of Membrane-Related Protein Complexes* PhD thesis (2018).
128. Van Den Heuvel, R. H., Van Duijn, E., Mazon, H., Synowsky, S. A., Lorenzen, K., Versluis, C., Brouns, S. J., Langridge, D., Van Der Oost, J., Hoyes, J. & Heck, A. J. Improving the performance of a quadrupole time-of-flight instrument for macromolecular mass spectrometry. *Analytical Chemistry* **78**, 7473–7483 (2006).
129. Morgner, N. & Robinson, C. V. *Mass* ign: An Assignment Strategy for Maximizing Information from the Mass Spectra of Heterogeneous Protein Assemblies. *Analytical Chemistry* **84**, 2939–2948 (2012).
130. Chifflet, S., Torriglia, A., Chiesa, R. & Tolosa, S. A method for the determination of inorganic phosphate in the presence of labile organic phosphate and high concentrations of protein: Application to lens ATPases. *Analytical Biochemistry* **168**, 1–4 (1988).
131. Baginski, E. S., Epstein, E & Zak, B. Review of phosphate methodologies. *Annals of clinical and laboratory science* **5**, 399–416 (1975).
132. Lakowicz, J. R. *Principles of fluorescence spectroscopy* 1–954 (Springer, 2006).
133. Blanchet, C. E., Spilotros, A., Schwemmer, F., Graewert, M. A., Kikhney, A., Jeffries, C. M., Franke, D., Mark, D., Zengerle, R., Cipriani, F., Fiedler, S., Roessle, M. & Svergun, D. I. Versatile sample environments and automation for biological solution X-ray scattering experiments at the P12 beamline (PETRA III, DESY). *Journal of applied crystallography* **48**, 431–443 (2015).
134. Wagner, S., Bader, M. L., Drew, D. & de Gier, J.-W. Rationalizing membrane protein overexpression. *Trends in Biotechnology* **24**, 364–371 (2006).
135. Grisshammer, R. Understanding recombinant expression of membrane proteins. *Current Opinion in Biotechnology* **17**, 337–340 (2006).
136. Sahdev, S., Khattar, S. K. & Saini, K. S. Production of active eukaryotic proteins through bacterial expression systems: a review of the existing biotechnology strategies. *Molecular and Cellular Biochemistry* **307**, 249–264 (2007).
137. Wagner, S., Klepsch, M. M., Schlegel, S., Appel, A., Draheim, R., Tarry, M., Högbom, M., van Wijk, K. J., Slotboom, D. J., Persson, J. O. & de Gier, J.-W. Tuning *Escherichia coli* for membrane protein overexpression. *Proceedings of the National Academy of Sciences of the United States of America* **105**, 14371–6 (2008).

138. Arechaga, I., Miroux, B., Karrasch, S., Huijbregts, R., de Kruijff, B., Runswick, M. J. & Walker, J. E. Characterisation of new intracellular membranes in *Escherichia coli* accompanying large scale over-production of the b subunit of F1 Fo ATP synthase. *FEBS Letters* **482**, 215–219 (2000).
139. Kong, B. & Guo, G. L. Soluble Expression of Disulfide Bond Containing Proteins FGF15 and FGF19 in the Cytoplasm of *Escherichia coli*. *PLoS ONE* **9** (ed Riggs, P. D.) e85890 (2014).
140. Van Meer, G., Voelker, D. R. & Feigenson, G. W. Membrane lipids: where they are and how they behave. *Nature Reviews Molecular Cell Biology* **9**, 112–124 (2008).
141. He, Y., Wang, K. & Yan, N. The recombinant expression systems for structure determination of eukaryotic membrane proteins. *Protein & cell* **5**, 658–72 (2014).
142. Parker, J. L. & Newstead, S. Method to increase the yield of eukaryotic membrane protein expression in *Saccharomyces cerevisiae* for structural and functional studies. *Protein Science* **23**, 1309–1314 (2014).
143. Cunningham, K. W. Calcineurin-dependent growth control in *Saccharomyces cerevisiae* mutants lacking PMC1, a homolog of plasma membrane Ca²⁺ ATPases. *The Journal of Cell Biology* **124**, 351–363 (2004).
144. Drew, D. E., von Heijne, G., Nordlund, P. & de Gier, J.-W. L. Green fluorescent protein as an indicator to monitor membrane protein overexpression in *Escherichia coli*. *FEBS Letters* **507**, 220–224 (2001).
145. Drew, D., Lerch, M., Kunji, E., Slotboom, D.-J. & de Gier, J.-W. Optimization of membrane protein overexpression and purification using GFP fusions. *Nature Methods* **3**, 303–313 (2006).
146. Drew, D., Slotboom, D.-J., Friso, G., Reda, T., Genevaux, P., Rapp, M., Meindl-Beinker, N. M., Lambert, W., Lerch, M., Daley, D. O., Van Wijk, K.-J., Hirst, J., Kunji, E. & De Gier, J.-W. A scalable, GFP-based pipeline for membrane protein overexpression screening and purification. *Protein Science* **14**, 2011–2017 (2005).
147. Ricker, R. & Sandoval, L. Fast, reproducible size-exclusion chromatography of biological macromolecules. *Journal of Chromatography A* **743**, 43–50 (1996).
148. Barth, H. G., Boyes, B. E. & Jackson, C. Size Exclusion Chromatography and Related Separation Techniques. *Analytical Chemistry* **70**, 251–278 (1998).
149. Kawate, T. & Gouaux, E. Fluorescence-Detection Size-Exclusion Chromatography for Precrystallization Screening of Integral Membrane Proteins. *Structure* **14**, 673–681 (2006).

150. Lacapère, J.-J., Pebay-Peyroula, E., Neumann, J.-M. & Etchebest, C. Determining membrane protein structures: still a challenge! *Trends in Biochemical Sciences* **32**, 259–270 (2007).
151. Bill, R. M., Henderson, P. J., Iwata, S., Kunji, E. R., Michel, H., Neutze, R., Newstead, S., Poolman, B., Tate, C. G. & Vogel, H. Overcoming barriers to membrane protein structure determination. *Nature Biotechnology* **29**, 335–340 (2011).
152. Loll, P. J. Membrane proteins, detergents and crystals: what is the state of the art? *Acta Crystallographica Section F Structural Biology Communications* **70**, 1576–1583 (2014).
153. Kang, H. J., Lee, C. & Drew, D. Breaking the barriers in membrane protein crystallography. *International Journal of Biochemistry and Cell Biology* **45**, 636–644 (2013).
154. Sonoda, Y., Cameron, A., Newstead, S., Omote, H., Moriyama, Y., Kasahara, M., Iwata, S. & Drew, D. Tricks of the trade used to accelerate high-resolution structure determination of membrane proteins. *FEBS Letters* **584**, 2539–2547 (2010).
155. Sonoda, Y., Newstead, S., Hu, N. J., Alguet, Y., Nji, E., Beis, K., Yashiro, S., Lee, C., Leung, J., Cameron, A. D., Byrne, B., Iwata, S. & Drew, D. Benchmarking membrane protein detergent stability for improving throughput of high-resolution x-ray structures. *Structure* **19**, 17–25 (2011).
156. Pantoliano, M. W., Petrella, E. C., Kwasnoski, J. D., Lobanov, V. S., Myslik, J., Graf, E., Carver, T., Asel, E., Springer, B. A., Lane, P & Salemme, F. R. High-density miniaturized thermal shift assays as a general strategy for drug discovery. *Journal of biomolecular screening* **6**, 429–440 (2001).
157. Ericsson, U. B., Hallberg, B. M., DeTitta, G. T., Dekker, N. & Nordlund, P. Thermofluor-based high-throughput stability optimization of proteins for structural studies. *Analytical Biochemistry* **357**, 289–298 (2006).
158. Alexandrov, A. I., Mileni, M., Chien, E. Y., Hanson, M. A. & Stevens, R. C. Microscale Fluorescent Thermal Stability Assay for Membrane Proteins. *Structure* **16**, 351–359 (2008).
159. Kohlstaedt, M., von der Hocht, I., Hilbers, F., Thielmann, Y., Michel, H. & IUCr. Development of a Thermofluor assay for stability determination of membrane proteins using the Na⁺/H⁺ antiporter NhaA and cytochrome c oxidase. *Acta Crystallographica Section D Biological Crystallography* **71**, 1112–1122 (2015).
160. Kotov, V., Vesper, O., Garcia Alai, M., Loew, C. & Marlovits, T. C. Moltenprot: A High-Throughput Analysis Platform to Assess Thermodynamic Stability of Membrane Proteins and Complexes. *Biophysical Journal* **116**, 191a (2019).

161. Temel, D. B., Landsman, P. & Brader, M. L. Orthogonal Methods for Characterizing the Unfolding of Therapeutic Monoclonal Antibodies: Differential Scanning Calorimetry, Isothermal Chemical Denaturation, and Intrinsic Fluorescence with Concomitant Static Light Scattering. *Methods in Enzymology* **567**, 359–389 (2016).
162. Chae, P. S., Rasmussen, S. G., Rana, R. R., Gotfryd, K., Chandra, R., Goren, M. A., Kruse, A. C., Nurva, S., Loland, C. J., Pierre, Y., Drew, D., Popot, J. L., Picot, D., Fox, B. G., Guan, L., Gether, U., Byrne, B., Kobilka, B. & Gellman, S. H. Maltose-neopentyl glycol (MNG) amphiphiles for solubilization, stabilization and crystallization of membrane proteins. *Nature Methods* **7**, 1003–1008 (2010).
163. Chae, P. S., Rasmussen, S. G. F., Rana, R. R., Gotfryd, K., Kruse, A. C., Manglik, A., Cho, K. H., Nurva, S., Gether, U., Guan, L., Loland, C. J., Byrne, B., Kobilka, B. K. & Gellman, S. H. A new class of amphiphiles bearing rigid hydrophobic groups for solubilization and stabilization of membrane proteins. *Chemistry (Weinheim an der Bergstrasse, Germany)* **18**, 9485–90 (2012).
164. Magnani, F., Serrano-Vega, M. J., Shibata, Y., Abdul-Hussein, S., Lebon, G., Miller-Gallacher, J., Singhal, A., Strege, A., Thomas, J. A. & Tate, C. G. A mutagenesis and screening strategy to generate optimally thermostabilized membrane proteins for structural studies. *Nature protocols* **11**, 1554–71 (2016).
165. Boivin, S., Kozak, S. & Meijers, R. Optimization of protein purification and characterization using Thermofluor screens. *Protein Expression and Purification* **91**, 192–206 (2013).
166. Gohon, Y. & Popot, J.-L. Membrane protein–surfactant complexes. *Current Opinion in Colloid & Interface Science* **8**, 15–22 (2003).
167. Von. Jagow, G. & Schagger, H. *Membrane protein purification and crystallization : a practical guide* 316 (Academic Press, 2003).
168. Champeil, P., Orłowski, S., Babin, S., Lund, S., le Maire, M., Møller, J., Lenoir, G. & Montigny, C. A robust method to screen detergents for membrane protein stabilization, revisited. *Analytical Biochemistry* **511**, 31–35 (2016).
169. Levi, V., Rossi, J., Echarte, M., Castello, P. & González Flecha, F. Thermal Stability of the Plasma Membrane Calcium Pump. Quantitative Analysis of Its Dependence on Lipid-Protein Interactions. *Journal of Membrane Biology* **173**, 215–225 (2000).
170. Pignataro, M. F., Dodes-Traian, M. M., González-Flecha, F. L., Sica, M., Mangialavori, I. C. & Rossi, J. P. F. C. Modulation of Plasma Membrane Ca²⁺-ATPase by Neutral Phospholipids. *Journal of Biological Chemistry* **290**, 6179–6190 (2015).

171. Pomorski, T. G., Nylander, T. & Cárdenas, M. Model cell membranes: Discerning lipid and protein contributions in shaping the cell. *Advances in Colloid and Interface Science* **205**, 207–220 (2014).
172. Bayburt, T. H. & Sligar, S. G. Single-molecule height measurements on microsomal cytochrome P450 in nanometer-scale phospholipid bilayer disks. *Proceedings of the National Academy of Sciences of the United States of America* **99**, 6725–30 (2002).
173. Levi, V., Rossi, J. P., Castello, P. R. & González Flecha, F. Oligomerization of the plasma membrane calcium pump involves two regions with different thermal stability. *FEBS Letters* **483**, 99–103 (2000).
174. DeGrip, W. J. Preparation of Proteoliposomes. *Ratio* **674**, 667–674 (1998).
175. Laganowsky, A., Reading, E., Hopper, J. T. S. & Robinson, C. V. Mass spectrometry of intact membrane protein complexes. *Nature Protocols* **8**, 639–651 (2013).
176. Jurchen, J. C. & Williams*, E. R. Origin of Asymmetric Charge Partitioning in the Dissociation of Gas-Phase Protein Homodimers. *J. Am. Chem. Soc.* **125**, 2817–2826 (2003).
177. Filomatori, C. V. & Rega, A. F. On the mechanism of activation of the plasma membrane Ca²⁺-ATPase by ATP and acidic phospholipids. *The Journal of biological chemistry* **278**, 22265–71 (2003).
178. Ronner, P., Gazzotti, P. & Carafoli, E. A lipid requirement for the (Ca²⁺ + Mg²⁺)-activated ATPase of erythrocyte membranes. *Archives of Biochemistry and Biophysics* **179**, 578–583 (1977).
179. Niggli, V., Adunyahs, E. S. & Carafoli, E. *Acidic Phospholipids, Unsaturated Fatty Acids, and Limited Proteolysis Mimic the Effect of Calmodulin on the Purified Erythrocyte ea²⁺-ATPase** tech. rep. 16 (1981), 8588–8592.
180. Baekgaard, L., Luoni, L., De Michelis, M. I. & Palmgren, M. G. The plant plasma membrane Ca²⁺ pump ACA8 contains overlapping as well as physically separated autoinhibitory and calmodulin-binding domains. *Journal of Biological Chemistry* **281**, 1058–1065 (2006).
181. Fusca, T., Bonza, M. C., Luoni, L., Meneghelli, S., Marrano, C. A. & De Michelis, M. I. Single point mutations in the small cytoplasmic loop of ACA8, a plasma membrane Ca²⁺ -ATPase of *Arabidopsis thaliana*, generate partially deregulated pumps. *Journal of Biological Chemistry* **284**, 30881–30888 (2009).
182. Giacometti, S., Marrano, C. A., Bonza, M. C., Luoni, L., Limonta, M. & De Michelis, M. I. Phosphorylation of serine residues in the N-terminus modulates the activity of ACA8, a plasma membrane Ca²⁺-ATPase of *Arabidopsis thaliana*. *Journal of Experimental Botany* **63**, 1215–1224 (2012).

183. Dalton, K. A., East, J. M., Mall, S, Oliver, S, Starling, A. P. & Lee, A. G. Interaction of phosphatidic acid and phosphatidylserine with the Ca²⁺-ATPase of sarcoplasmic reticulum and the mechanism of inhibition. *The Biochemical journal* **329** (Pt 3, 637–46 (1998).
184. Perrin, F. The polarisation of fluorescence light. Average life of molecules in their excited state. *J. Phys. Radium* **7** (1926).
185. Heyduk, T., Ma, Y., Tang, H. & Ebright, R. H. Fluorescence anisotropy: Rapid, quantitative assay for protein-DNA and protein-protein interaction. *Methods in Enzymology* **274**, 492–503 (1996).
186. Jameson, D. M. & Sawyer, W. H. [12] Fluorescence anisotropy applied to biomolecular interactions. *Methods in Enzymology* **246**, 283–300 (1995).
187. Enyedi, A, Vorherr, T, James, P, McCormick, D. J., Filoteo, A. G., Carafoli, E & Penniston, J. T. The calmodulin binding domain of the plasma membrane Ca²⁺ pump interacts both with calmodulin and with another part of the pump. *The Journal of biological chemistry* **264**, 12313–21 (1989).
188. Luoni, L., Meneghelli, S., Bonza, M. C. & DeMichelis, M. I. Auto-inhibition of *Arabidopsis thaliana* plasma membrane Ca²⁺-ATPase involves an interaction of the N-terminus with the small cytoplasmic loop. *FEBS Letters* **574**, 20–24 (2004).
189. Mangialavori, I. C., Ferreira-Gomes, M. S., Saffioti, N. A., González-Lebrero, R. M., Rossi, R. C. & Rossi, J. P. F. Conformational changes produced by ATP binding to the plasma membrane calcium pump. *Journal of Biological Chemistry* **288**, 31030–31041 (2013).
190. Corradi, G. R. & Adamo, H. P. Intramolecular fluorescence resonance energy transfer between fused autofluorescent proteins reveals rearrangements of the N- and C-terminal segments of the plasma membrane Ca²⁺ pump involved in the activation. *Journal of Biological Chemistry* **282**, 35440–35448 (2007).
191. Pignataro, M. F., Dodes-Traian, M. M., González-Flecha, F. L., Sica, M., Mangialavori, I. C. & Rossi, J. P. F. C. Modulation of Plasma Membrane Ca²⁺-ATPase by Neutral Phospholipids. *Journal of Biological Chemistry* **290**, 6179–6190 (2015).
192. Jo, S., Kim, T., Iyer, V. G. & Im, W. CHARMM-GUI: A web-based graphical user interface for CHARMM. *Journal of Computational Chemistry* **29**, 1859–1865 (2008).
193. Hammel, M. Validation of macromolecular flexibility in solution by small-angle X-ray scattering (SAXS). *European Biophysics Journal* **41**, 789–799 (2012).

194. Rambo, R. P. & Tainer, J. A. Characterizing flexible and intrinsically unstructured biological macromolecules by SAS using the Porod-Debye law. *Biopolymers* **95**, 559–571 (2011).
195. Strehler, E. E. & Zacharias, D. A. Role of Alternative Splicing in Generating Isoform Diversity Among Plasma Membrane Calcium Pumps. *Physiological Reviews* **81**, 21–50 (2017).
196. Holland, I., Cole, S., Kuchler, K. & Higgins, C. *ABC proteins: from bacteria to man* (2003).
197. Higgins, C. F. & Linton, K. J. The ATP switch model for ABC transporters. *Nature Structural & Molecular Biology* **11**, 918–926 (2004).
198. Rees, D. C., Johnson, E. & Lewinson, O. ABC transporters: the power to change. *Nature Reviews Molecular Cell Biology* **10**, 218–227 (2009).
199. Biemans-Oldehinkel, E., Doeven, M. K. & Poolman, B. ABC transporter architecture and regulatory roles of accessory domains. *FEBS Letters* **580**, 1023–1035 (2006).
200. Sebastian, T. T., Baldrige, R. D., Xu, P. & Graham, T. R. Phospholipid flippases: Building asymmetric membranes and transport vesicles. *Biochimica et Biophysica Acta (BBA) - Molecular and Cell Biology of Lipids* **1821**, 1068–1077 (2012).
201. Andersen, J. P., Vestergaard, A. L., Mikkelsen, S. A., Mogensen, L. S., Chalal, M. & Molday, R. S. P4-ATPases as Phospholipid Flippases—Structure, Function, and Enigmas. *Frontiers in Physiology* **7**, 275 (2016).
202. Montigny, C., Lyons, J., Champeil, P., Nissen, P. & Lenoir, G. On the molecular mechanism of flippase- and scramblase-mediated phospholipid transport. *Biochimica et Biophysica Acta (BBA) - Molecular and Cell Biology of Lipids* **1861**, 767–783 (2016).
203. Raetz, C. R., Reynolds, C. M., Trent, M. S. & Bishop, R. E. Lipid A Modification Systems in Gram-Negative Bacteria. *Annual Review of Biochemistry* **76**, 295–329 (2007).
204. Ward, A., Reyes, C. L., Yu, J., Roth, C. B. & Chang, G. Flexibility in the ABC transporter MsbA: Alternating access with a twist. *Proceedings of the National Academy of Sciences of the United States of America* **104**, 19005–10 (2007).
205. Dong, J., Yang, G. & McHaourab, H. S. Structural basis of energy transduction in the transport cycle of MsbA. *Science (New York, N.Y.)* **308**, 1023–8 (2005).
206. Zou, P. & Mchaourab, H. S. Alternating Access of the Putative Substrate-Binding Chamber in the ABC Transporter MsbA. *Journal of Molecular Biology* **393**, 574–585 (2009).

207. Geourjon, C, Orelle, C, Steinfels, E, Blanchet, C, Deléage, G, Di Pietro, A & Jault, J. M. A common mechanism for ATP hydrolysis in ABC transporter and helicase superfamilies. *Trends in biochemical sciences* **26**, 539–44 (2001).
208. Seeger, M. A. & van Veen, H. W. Molecular basis of multidrug transport by ABC transporters. *Biochimica et Biophysica Acta (BBA) - Proteins and Proteomics* **1794**, 725–737 (2009).
209. Dawson, R. J. P. & Locher, K. P. Structure of a bacterial multidrug ABC transporter. *Nature* **443**, 180–185 (2006).
210. Borbat, P. P., Surendhran, K., Bortolus, M., Zou, P., Freed, J. H. & Mchaourab, H. S. Conformational Motion of the ABC Transporter MsbA Induced by ATP Hydrolysis. *PLoS Biology* **5** (ed Petsko, G. A.) e271 (2007).
211. Skar-Gislinge, N., Johansen, N. T., Høiberg-Nielsen, R. & Arleth, L. Comprehensive Study of the Self-Assembly of Phospholipid Nanodiscs: What Determines Their Shape and Stoichiometry? *Langmuir* **34**, 12569–12582 (2018).
212. Dunne, O., Weidenhaupt, M., Callow, P., Martel, A., Moulin, M., Perkins, S. J., Haertlein, M. & Forsyth, V. T. Matchout deuterium labelling of proteins for small-angle neutron scattering studies using prokaryotic and eukaryotic expression systems and high cell-density cultures. *European Biophysics Journal* **46**, 425–432 (2017).
213. Haertlein, M., Moulin, M., Devos, J. M., Laux, V., Dunne, O. & Trevor Forsyth, V. Biomolecular Deuteration for Neutron Structural Biology and Dynamics. *Methods in Enzymology* **566**, 113–157 (2016).
214. Artero, J.-B., Härtlein, M., McSweeney, S., Timmins, P. & IUCr. A comparison of refined X-ray structures of hydrogenated and perdeuterated rat γ E-crystallin in H₂O and D₂O. *Acta Crystallographica Section D Biological Crystallography* **61**, 1541–1549 (2005).
215. Rochel, N., Ciesielski, F., Godet, J., Moman, E., Roessle, M., Peluso-Iltis, C., Moulin, M., Haertlein, M., Callow, P., Mély, Y., Svergun, D. I. & Moras, D. Common architecture of nuclear receptor heterodimers on DNA direct repeat elements with different spacings. *Nature Structural & Molecular Biology* **18**, 564–570 (2011).
216. Bogdanov, M., Heacock, P., Guan, Z. & Dowhan, W. Plasticity of lipid-protein interactions in the function and topogenesis of the membrane protein lactose permease from *Escherichia coli*. *Proceedings of the National Academy of Sciences of the United States of America* **107**, 15057–62 (2010).
217. Bligh, E. G. & Dyer, W. J. A rapid method of total lipid extraction and purification. *Canadian Journal of Biochemistry and Physiology* **37** (1959).

-
218. Heinemann, A. & Mühlbauer, S. SANS-1: Small angle neutron scattering. *Journal of large-scale research facilities JLSRF* **1**, A10 (2015).
219. Svergun, D. I., Richard, S., Koch, M. H., Sayers, Z., Kuprin, S & Zaccai, G. Protein hydration in solution: experimental observation by x-ray and neutron scattering. *Proceedings of the National Academy of Sciences of the United States of America* **95**, 2267–72 (1998).
220. Trewhella, J., Duff, A. P., Durand, D., Gabel, F., Guss, J. M., Hendrickson, W. A., Hura, G. L., Jacques, D. A., Kirby, N. M., Kwan, A. H., Pérez, J., Pollack, L., Ryan, T. M., Sali, A., Schneidman-Duhovny, D., Schwede, T., Svergun, D. I., Sugiyama, M., Tainer, J. A., Vachette, P., Westbrook, J., Whitten, A. E. & IUCr. 2017 publication guidelines for structural modelling of small-angle scattering data from biomolecules in solution: an update. *Acta Crystallographica Section D Structural Biology* **73**, 710–728 (2017).
221. Franke, D. & Svergun, D. I. DAMMIF, a program for rapid ab-initio shape determination in small-angle scattering. *Journal of applied crystallography* **42**, 342–346 (2009).
222. Petoukhov, M. V., Svergun, D. I. & IUCr. Ambiguity assessment of small-angle scattering curves from monodisperse systems. *Acta Crystallographica Section D Biological Crystallography* **71**, 1051–1058 (2015).
223. Kozin, M. B. & Svergun, D. I. Automated matching of high- and low-resolution structural models. *Journal of Applied Crystallography* **34**, 33–41 (2001).
224. Petoukhov, M. V., Franke, D., Shkumatov, A. V., Tria, G., Kikhney, A. G., Gajda, M., Gorba, C., Mertens, H. D. T., Konarev, P. V. & Svergun, D. I. New developments in the ATSAS program package for small-angle scattering data analysis. *Journal of Applied Crystallography* **45**, 342 (2012).
225. Zheng, W., Brooks, B. R. & Hummer, G. Protein conformational transitions explored by mixed elastic network models. *Proteins: Structure, Function, and Bioinformatics* **69**, 43–57 (2007).
226. Petoukhov, M. V. & Svergun, D. I. Global Rigid Body Modeling of Macromolecular Complexes against Small-Angle Scattering Data. *Biophysical Journal* **89**, 1237–1250 (2005).
227. Guard-Friar, D., Chen, C.-H. & Engle, A. S. Deuterium Isotope Effect on the Stability of Molecules: Phospholipids. *J. Phys. Chem* **89**, 1810–1813 (1985).
228. Bryant, G., Taylor, M. B., Darwish, T. A., Krause-Heuer, A. M., Kent, B. & Garvey, C. J. Effect of deuteration on the phase behaviour and structure of lamellar phases of phosphatidylcholines – Deuterated lipids as proxies for the physical properties of native bilayers. *Colloids and Surfaces B: Biointerfaces* **177**, 196–203 (2019).

229. Luchini, A., Delhom, R., Demé, B., Laux, V., Moulin, M., Haertlein, M., Pichler, H., Strohmeier, G. A., Wacklin, H. & Fragneto, G. The impact of deuteration on natural and synthetic lipids: A neutron diffraction study. *Colloids and Surfaces B: Biointerfaces* **168**, 126–133 (2018).
230. Waldie, S., Moulin, M., Porcar, L., Pichler, H., Strohmeier, G. A., Skoda, M., Forsyth, V. T., Haertlein, M., Maric, S. & Cárdenas, M. The Production of Matchout-Deuterated Cholesterol and the Study of Bilayer-Cholesterol Interactions. *Scientific Reports* **9**, 5118 (2019).
231. Franke, D., Petoukhov, M. V., Konarev, P. V., Panjkovich, A., Tuukkanen, A., Mertens, H. D. T., Kikhney, A. G., Hajizadeh, N. R., Franklin, J. M., Jeffries, C. M. & Svergun, D. I. ATSAS 2.8: a comprehensive data analysis suite for small-angle scattering from macromolecular solutions. *Journal of applied crystallography* **50**, 1212–1225 (2017).
232. Mi, W., Li, Y., Yoon, S. H., Ernst, R. K., Walz, T. & Liao, M. Structural basis of MsbA-mediated lipopolysaccharide transport. *Nature* **549**, 233–237 (2017).
233. Moeller, A., Lee, S. C., Tao, H., Speir, J. A., Chang, G., Urbatsch, I. L., Potter, C. S., Carragher, B. & Zhang, Q. Distinct conformational spectrum of homologous multidrug ABC transporters. *Structure (London, England : 1993)* **23**, 450–460 (2015).
234. Mehmood, S., Domene, C., Forest, E., Jault, J.-M. & Kaback, H. R. Dynamics of a bacterial multidrug ABC transporter in the inward-and outward-facing conformations. *Proceedings of the National Academy of Sciences* **109**, 10832–10836 (2012).
235. Mishra, S., Verhalen, B., Stein, R. A., Wen, P.-C., Tajkhorshid, E. & Mchaourab, H. S. Conformational dynamics of the nucleotide binding domains and the power stroke of a heterodimeric ABC transporter. *eLife* **3** (2014).
236. Dawson, R. J. P. & Locher, K. P. Structure of a bacterial multidrug ABC transporter. *Nature* **443**, 180–185 (2006).
237. Eckford, P. D. W. & Sharom, F. J. Functional characterization of Escherichia coli MsbA: interaction with nucleotides and substrates. *The Journal of biological chemistry* **283**, 12840–50 (2008).
238. Doshi, R., Ali, A., Shi, W., Freeman, E. V., Fagg, L. A. & van Veen, H. W. Molecular disruption of the power stroke in the ATP-binding cassette transport protein MsbA. *The Journal of biological chemistry* **288**, 6801–13 (2013).
239. Szewczyk, P., Tao, H., McGrath, A. P., Villaluz, M., Rees, S. D., Lee, S. C., Doshi, R., Urbatsch, I. L., Zhang, Q., Chang, G. & IUCr. Snapshots of ligand entry, malleable binding and induced helical movement in P-glycoprotein. *Acta Crystallographica Section D Biological Crystallography* **71**, 732–741 (2015).

-
240. Shintre, C. A., Pike, A. C. W., Li, Q., Kim, J.-I., Barr, A. J., Goubin, S., Shrestha, L., Yang, J., Berridge, G., Ross, J., Stansfeld, P. J., Sansom, M. S. P., Edwards, A. M., Bountra, C., Marsden, B. D., von Delft, F., Bullock, A. N., Gileadi, O., Burgess-Brown, N. A. & Carpenter, E. P. Structures of ABCB10, a human ATP-binding cassette transporter in apo- and nucleotide-bound states. *Proceedings of the National Academy of Sciences of the United States of America* **110**, 9710–5 (2013).
241. Taylor, J. E., Chow, J. Y. H., Jeffries, C. M., Kwan, A. H., Duff, A. P., Hamilton, W. A. & Trewheella, J. Calmodulin binds a highly extended HIV-1 MA protein that refolds upon its release. *Biophysical journal* **103**, 541–9 (2012).
242. Kelley, L. A., Mezulis, S., Yates, C. M., Wass, M. N. & Sternberg, M. J. E. The Phyre2 web portal for protein modeling, prediction and analysis. *Nature Protocols* **10**, 845–858 (2015).
243. Bernado, P., Mylonas, E., Petoukhov, M. V., Blackledge, M. & Svergun, D. I. Structural Characterization of Flexible Proteins Using Small-Angle X-ray Scattering. *Journal of the American Chemical Society* **129**, 5656–5664 (2007).
244. Tria, G., Mertens, H. D. T., Kachala, M. & Svergun, D. I. Advanced ensemble modelling of flexible macromolecules using X-ray solution scattering. *IUCrJ* **2**, 207–217 (2015).
245. Gietz, D., St Jean, A., Woods, R. A. & Schiestl, R. H. Improved method for high efficiency transformation of intact yeast cells. *Nucleic acids research* **20**, 1425 (1992).

Part IV

Appendix

Appendix A

Supplementary Data

A.1 Supplementary Figures

A.1.1 Native mass spectrometry of CaM7

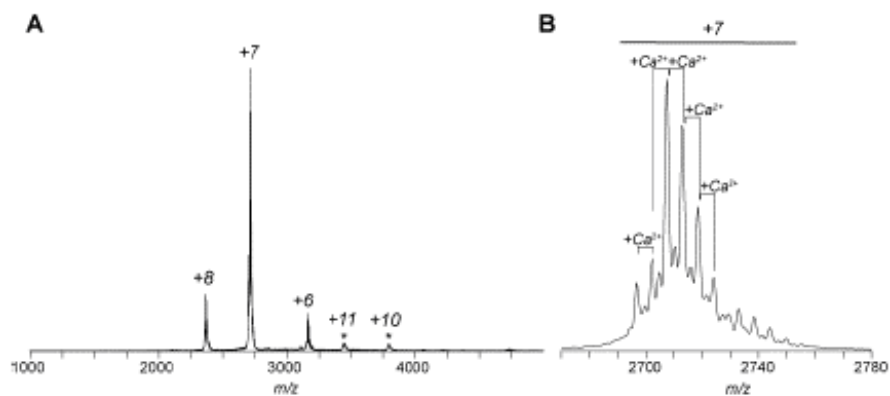


Figure A.1: Native mass spectrometry of CaM7. a + b M/z ratio of monomeric state of CaM7 showing mainly +6 to +8 charges. Reprinted from Heidemann, 2018 [127].

A.1.2 Incorporation of flACA8 into nanodisc composed of various lipids

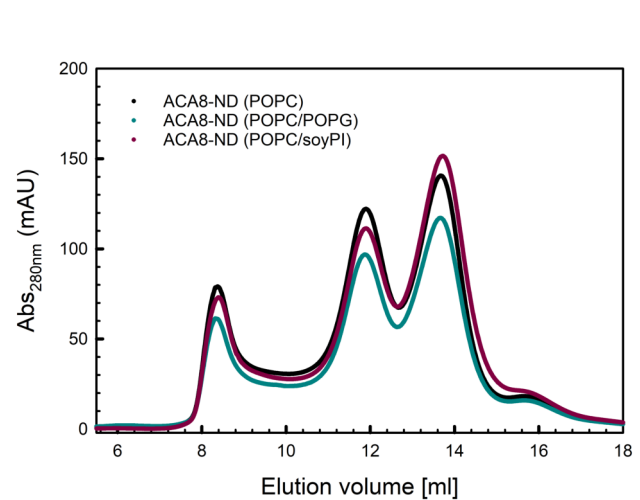


Figure A.2: *ACA8 incorporated into MSP1D1 nanodisc composed of different lipids. a* Size-exclusion profile of purified ACA8 in nanodiscs formed with MSP1D1 and different lipids (POPC, POPC/POPG, POPC/soyPI).

A.1.3 SAXS analysis of ACA8 and its complex with CaM

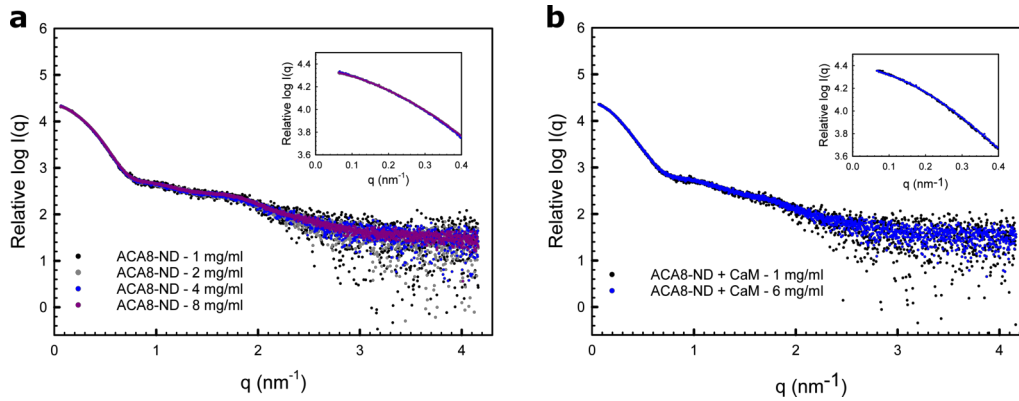


Figure A.3: Small-angle scattering analysis of ACA8-ND at different concentrations. (a + b) Overlay of SAXS profiles obtained for ACA8-ND (a) and ACA8-ND+CaM (b) in concentrations ranging from 1-8 mg/ml (a) or 1-6 mg/ml (b). The curves superimpose very well, indicating there is no for concentration dependence interparticle interaction. [126]

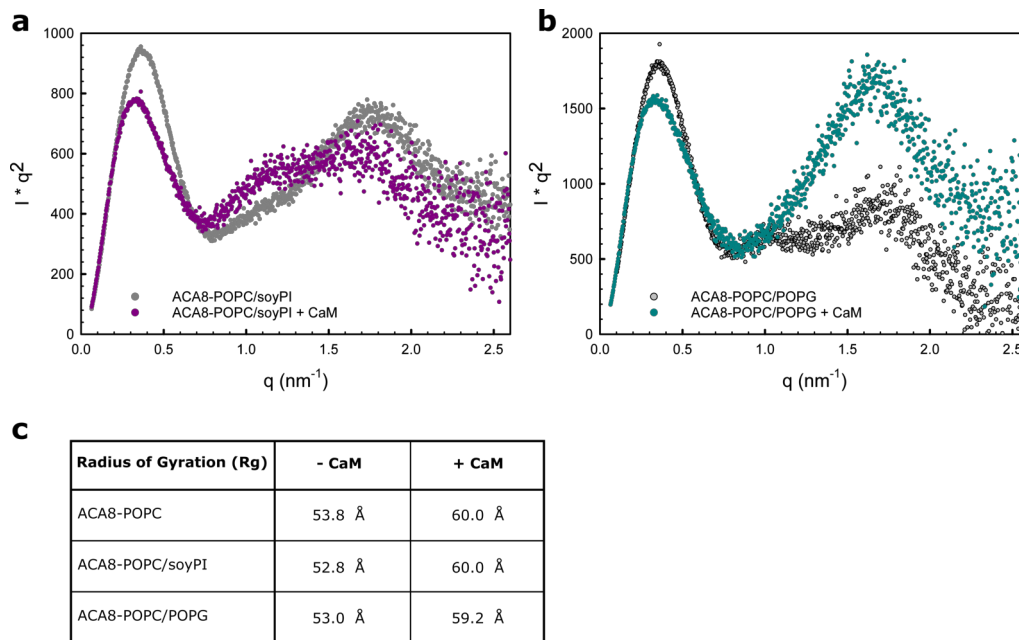


Figure A.4: Small-angle scattering analysis of ACA8 in nanodisc with anionic lipids. Kratky plots of ACA8 incorporated in nanodiscs containing soy-PI (a) or POPG (b) showing changes in the mid-q range upon CaM binding to ACA8. (c) Comparison of radii of gyration for various ACA8-nanodisc samples illustrating that the presence of anionic lipids does not lead to expansion in the absence of CaM. R_g values are comparable to those of ACA8 in POPC-nanodiscs. [126]

A.1.4 SANS analysis of ACA8 in stealth carrier nanodisc

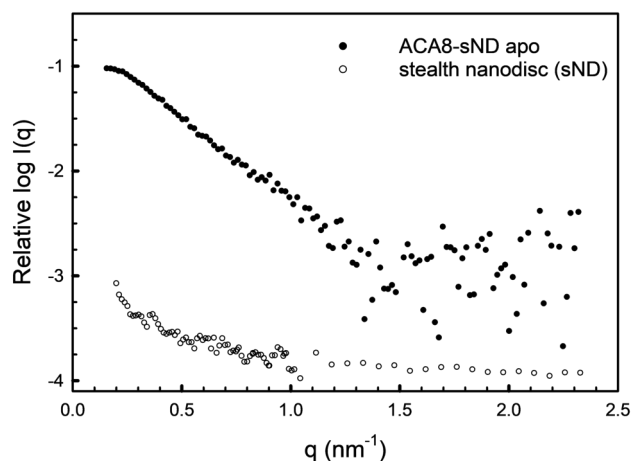


Figure A.5: Comparison of SANS curves of empty sND with ACA8-sND. Semi-log plot of SANS scattering of apo ACA8 in stealth nanodiscs compared to scattering profil of "empty" stealth nanodisc.

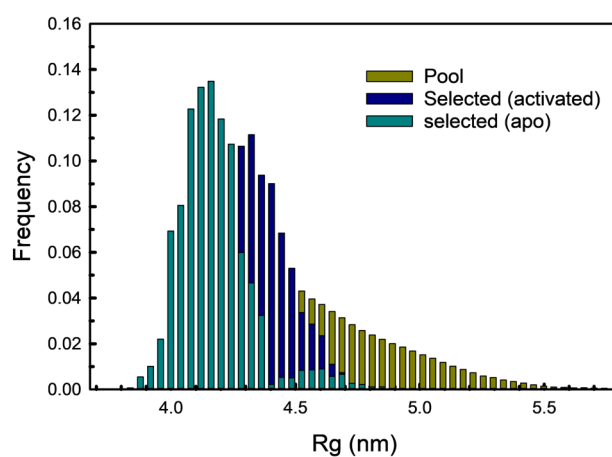


Figure A.6: Rg distribution of ACA8-sND in apo conformation. EOM analysis illustrating the R_{g} distribution plot of ACA8 in apo conformation in comparison with the data of ACA8 in complex with CaM, showing that the selected sub-ensemble is significantly smaller and thus the R_{g} -distribution is shifted to smaller radii for ACA8 in the autoinhibited state.

A.1.5 SANS analysis of MsbA in stealth carrier nanodisc

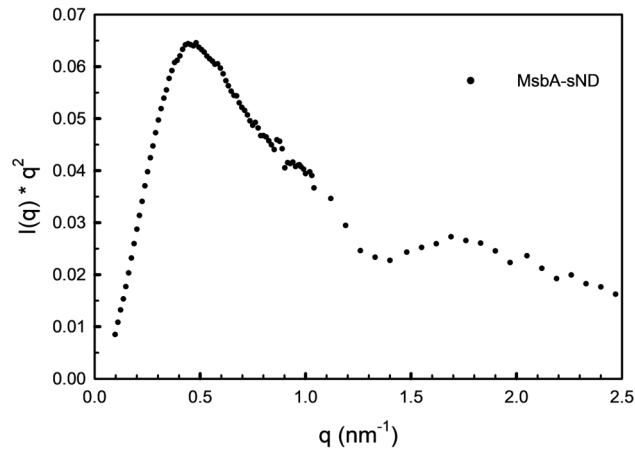


Figure A.7: Kratky analysis of MsbA in stealth carrier nanodisc. Kratky plot of MsbA incorporated in stealth carrier nanodisc analysed by small-angle neutron scattering (SANS) reveals that MsbA forms a compact multi-domain particle in solution.

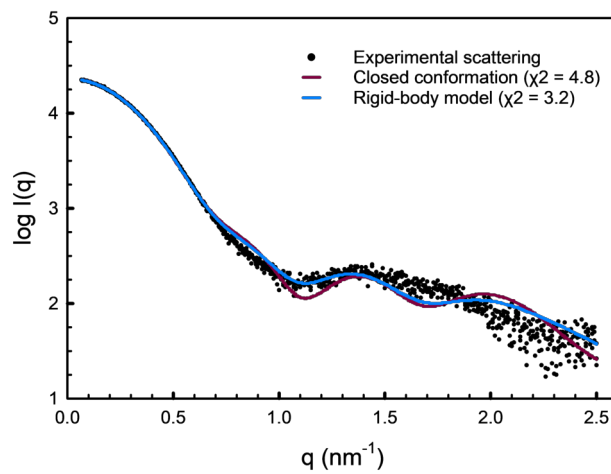


Figure A.8: Cryson fits of MsbA in different conformation. CRYSON analysis illustrating the fit of the closed as well as the rigid-body model for MsbA nanodisc complexes.

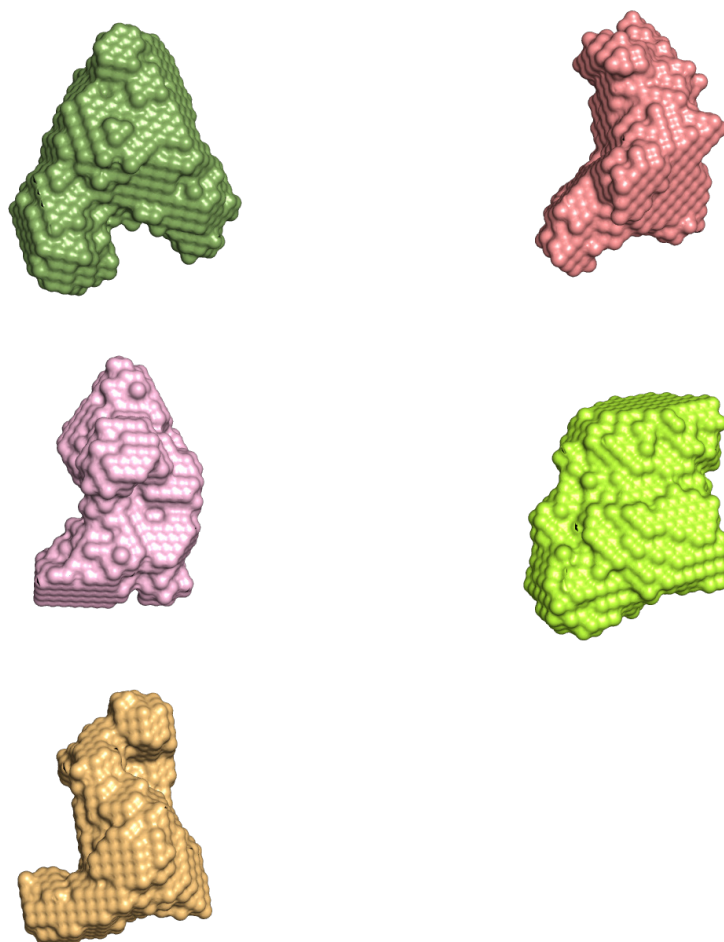


Figure A.9: Cluster analysis of *ab initio* models derived from sND/SANS experiments. Five potential cluster with similar shapes could be observed from 20 models. All shapes are consistent with MsbA and do not show any contribution of stealth nanodiscs. Analysis has been performed using DAMCLUST [224].

A.1.6 Incorporation of MsbA in lipid carrier with different lipids

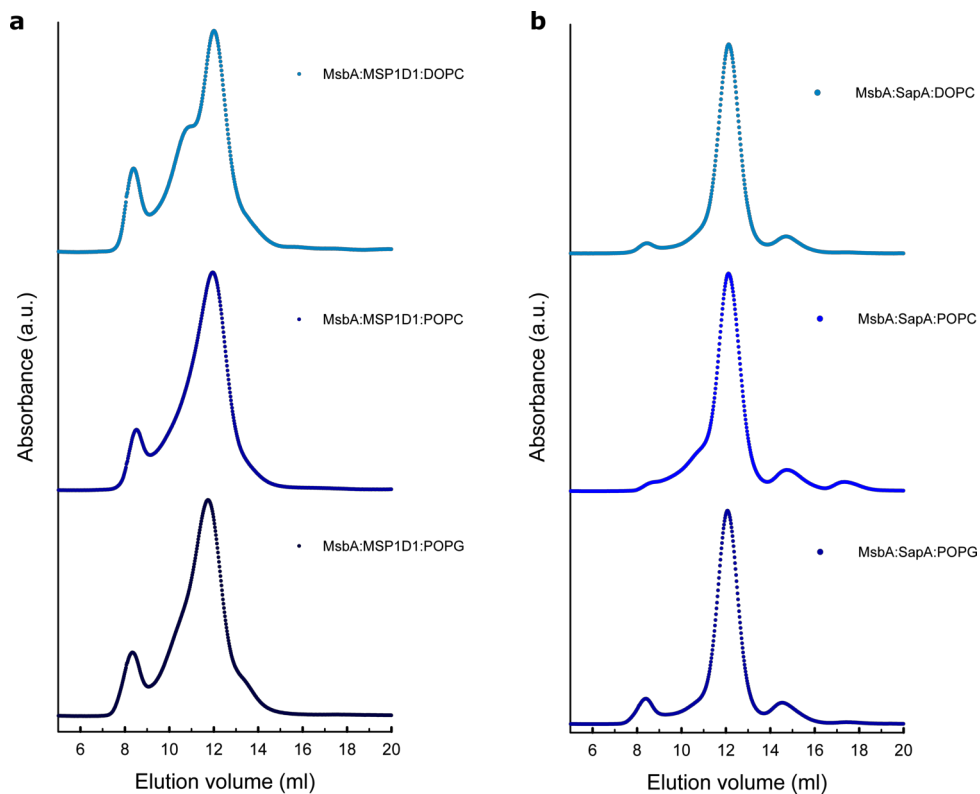


Figure A.10: SEC profiles of MsbA incorporated into MSP1D1 nanodiscs and SapNP composed of different lipids. Size-exclusion chromatography profiles of (a) MsbA-nanodisc samples and (b) MsbA-SapNP samples. Figure reprinted from Kehlenbeck *et al.* [86].

A.2 Supplementary Tables

A.2.1 Sequences of Proteins used in this Study

Table A.1: Aminoacid sequences of proteins used in this study.

Protein	Organism	Sequence
ACA8	<i>A. thaliana</i>	MHHHHHHHHHHHENLYFQGATSLKSSPGRRRG GDVESGKSEHADSDSDTFYIPSKNASIERLQQWRK AALVLNASRRFRYTLDLKKEQETREMRQKIRSHA HALLAANRFMDMGRESGVEKTTGPATPAGDFGIT PEQLVIMSKDHNSGALEQYGGTQGLANLLKTNPE KGISGDDDDLLKRKTIYGSNTYPRKKGKGFRLFLW DACHDLTLIILMVA AVASLALGIKTEGIKEGWYDG GSIAFAVILVIVVTAVSDYKQSLQFQNLNDEKRNI HLEVLRRGRRVEISYDIVVGDVIPLNIGNQVPADG VLISGHSLALDESSMTGESKIVNKDANKDPFLMSG CKVADGNGSMLVTGVGVNTEWGLLMASISEDNG EETPLQVRLNGVATFIGSIGLAVAAAVLVILLTRYF TGHTKDNNGGPQFVKGKTKVGHVIDDVVKVLTV AVTIVVVAVPEGLPLAVTLTLAYS MRKMMADKA LVRRLSACETMGSA TTICSDKTGTLTLNQMTVVES YAGGKKT DTEQLPATITSLVVEGISQNTTGSIFVPE GGDLEYS GSPTEKAILGWGVKLG MNFETARSQS SILHAFPFNSEKKRGGVAVKTADGEVHVHWKGA SEIVLASCRSYIDEDGNVAPMTDDKASFFKNGIND MAGRTLRCVALAFRTYEA EKVPTGEELSKWVLP DDLILLAIVGIK DPCRPGVKDSV VLCQNAGVKVR MVTGDNVQTARAIALECGILSSDADLSEPTLIEGKS FREM TDAERDKISDKISVMGRSSPNDKLLL VQSLR RQGHVVAVTGDGTNDAPALHEADIGLAMGIAGT EVAKESDIILDDNFASVVKVVRWGRSVYANIQK FIQFQLTVNVAALVINVVA AISSGDVPLTAVQLLW VNLIMDTL GALALATEPPTDHL MGRPPVGRKEPLI TNIMWRNLLIQAIYQVSVLLTLNFRGISILGLEHEV HEHATRVKNTIIFNAFVLCQAFNEFNARKPDEKNI FKGVIKNRLFMGIIVITLVLQVIIVEFLGKFASTTKL NWKQWLICVGIGVISWPLALV GK FIPVPAAPISNK LKVLKFWGKKKNSSGEGSL
CaM7	<i>A. thaliana</i>	MHHHHHHHENLYFQGAADQLTDDQISEFKEAFSL FDKDGDCITTKELGTVMRSLGQNPTAEALQDMI NEVDADGNGTIDFPEFLNLMARKMKD TDSEELK EAFRVFDKDQNGFISAAELRHVMTNLGEKLTDEE VDEMIREADV DGDGQINYE EFVKVMMAK

Continued on next page

Protein	Organism	Sequence
MsbA	<i>E. coli</i>	MHNDKDLSTWQTFRRLWPTIAPFKAGLIVAGVAL ILNAASDTFMLSLLKPLDDGFGKTDRSVLVWMP LVVIGLMILRGITSYVSSYICISWVSGKVVMTRRRL FGHMMGMPVSFFDKQSTGTLLSRITYDSEQVASS SGALITVREGASIIIGLFIMMFYYSWQLSIIILVLA VSAIRVVSKRFRNISKNMQNTMGQVTTSAEQML KGGHKEVLIFGGQEVETKRFDKVSNRMRLQGMKM VSASSISDPIIQLIASLALAFVLYAASFPSVMDSLTA GTITVVFSSMIALMRPLKSLTNVNAQFQRGMAAC QTLFTILDSEKDEGKRVIERATGDVEFRNVFTFY PGRDVPALRNINLKIPAGKTVALVGRSGSGKSTIAS LITRFYDIDEGEILMDGHDREYTLASLRNQVALVS QNVHLFNDTVANNIAYARTEQYSREQIEEAARM AYAMDFINKMDNGLDVTIGENGVLLSGGQRQRI AIARALLRDSPIILDEATSALDTESERAIQAALDEL QKNRTSLVIAHRLSTIEKADEIVVVEDGVIVERGTH NDLLEHRGVYAQLHKMQFGQ
MSP1D1	<i>H. sapiens</i>	GHHHHHHHDYDIPTTENLYFQGSTFSKLREQLGP VTQEFWDNLEKETEGLRQEMSKDLEEVKAKVQPY LDDFQKKWQEEMELYRQKVEPLRAELQEGARQK LHELQEKLSPLGEEMRDRARAHVDALRTHLAPYS DELRQRLAARLEALKENGGARLAEYHAKATEHLS TLSEKAKPALEDLRQGLLPVLESFKVSFLSALEEYT KKLNTQ
MSP1E3	<i>H. sapiens</i>	MGHHHHHHHDYDIPTTENLYFQGSTFSKLREQL GPVVTQEFWDNLEKETEGLRQEMSKDLEEVKAKV QPYLDDFQKKWQEEMELYRQKVEPLRAELQEGA RQKLHELQEKLSPLGEEMRDRARAHVDALRTHL APYLDDFQKKWQEEMELYRQKVEPLRAELQEGA RQKLHELQEKLSPLGEEMRDRARAHVDALRTHL APYSDELRQRLAARLEALKENGGARLAEYHAKAT EHLSTLSEKAKPALEDLRQGLLPVLESFKVSFLSAL EYTKKLNTQ
SapA	<i>H. sapiens</i>	SEQUENCEMGSGLPCDICKDVVTAAGDMLKDNAT EEEILVYLEKTCDWLPKPNMSASCKEIVDSYLPVIL DIIKGEMSRPGEVCSALNLCES

A.2.2 Masses of ACA8-CaM complexes measured by NMS

Table A.2: Comparison of theoretical and experimental M_r of ACA8 CaM7. Experimentally derived masses (M_{exp}) as well as theoretical masses (M_{theo}) are listed together with standard deviations and average full width half maximum (FWHM), all values in Da. [126]

Protein/-complex	M_{theo}	M_{exp}	SD [Da, $N_a \geq b3$]	Avg. FWHM
CaM	18,593.5	18,869.9	0.8	11
ACA8	118,194.2	118,520	60	804
ACA8 + CaM	136,787.7	137,500	110	700
ACA8 + 2 CaM	155,381.2	156,600	200	730

A.2.3 SAXS/SANS parameters

Table A.3: SAXS parameters – ACA8-ND.

	ACA8-ND (apo)	ACA8-ND + CaM
Data collection parameters		
Instrument	EMBL P12 (PETRA-III, Desy, Hamburg)	
Beam geometry	0.2 x 0.12 mm ²	
Wavelength (Å)	1.24	
q range (nm ⁻¹)	0.05-4.6	
Exposure time (s)	1 (20 x 0.05 s)	
Concentration range (mg/ml)	1-8	1-6
Temperature (K)	283	283
Structural parameters		
$I(0)$ (cm ⁻¹) [from $p(r)$]	0.093	0.129
$R(g)$ (Å) [from $p(r)$]	53.8	60.0
$I(0)$ (cm ⁻¹) [from Guinier]	0.094	0.128
$R(g)$ (Å) [from Guinier]	53.0 ± 0.9	58.8 ± 1.9
D_{max} (Å)	200	220
Porod volume estimate (Å ³)	626450	805590
Molecular-mass determination		
Partial specific volume (cm ³ g ⁻¹)	0.816 ^a	0.810 ^a
Contrast ($\Delta\rho \times 10^{10} \text{cm}^{-2}$)	1.808	1.876
Molecular mass M_r (Da) [from $I(0)$]	259000	334000
Molecular mass M_r (Da) [from Porod volume ($V_p/1.6$)]	391531	503493
Calculated M_r from sequence (Da)	256240 ^a	288240 ^a
Software employed		
Primary data reduction	RADAVER	
Data processing	PRIMUS/Qt	
Computation of model intensities	CRY SOL	

^a Calculated for a complex composed of 1xACA8 + 2xMSP1D1 + 124xPOPC molecules. This assumption is based on the homology model of ACA8 incorporated into MSP1D1-POPC nanodisc.

Table A.4: SANS parameters – ACA8-sND.

	ACA8-sND (apo)	ACA8-sND + d-CaM	ACA8-sND + CaM
Data collection parameters			
Instrument	SANS-1 (MLZ, Munich)		
Wavelength (Å)	5.0		
q range (nm ⁻¹)	0.12-2.4		
Exposure time (s)	7200		
Concentration range (mg/ml)	3.5	3.2	3.0
Temperature (K)	283	283	283
Structural parameters			
$I(0)$ (cm ⁻¹) [from $p(r)$]	0.11	00.1	0.15
$R(g)$ (Å) [from $p(r)$]	42.5	45.8	52.9
$I(0)$ (cm ⁻¹) [from Guinier]	0.11	0.092	0.1
$R(g)$ (Å) [from Guinier]	40	42.8	50
D_{max} (Å)	130	150	180
Porod volume estimate (Å ³)	202000	217000	297000
Molecular-mass determination			
Partial specific volume (cm ³ g ⁻¹)	0.744	0.744	0.739
Contrast ($\Delta\rho \times 10^{10}$ cm ⁻²)	-3.320	-3.320	-3.320
Molecular mass M_r (Da) [from Porod volume ($V_p/1.6$)]	126250	135625	185625
Calculated M_r from sequence (Da)	118000	118000	150000
Software employed			
Primary data reduction	BerSANS	BerSANS	BerSANS
Data processing	PRIMUS/Qt	PRIMUS/Qt	PRIMUS/Qt
Ab initio analysis		EOM	
Computation of model intensities	CRYSON	CRYSON	CRYSON
3D graphics representation	PyMOL	PyMOL	PyMOL

A.3 Scripts

Skript to combine theoretical intensities of generated models in one file

```
#!/usr/bin/python
# modInt.py, HDTM 12-01-2017
# GENERATES EOM intensities file based on precomputed *.int files from CRY SOL
# TODO: use dictionaries to make this better

import sys, re, os, glob

def modInt(path):
    """Generate EOM jun file from many *.int files"""
    # Dif/Atom/Shape/Bord 10000ks5eh.p Dro: 0.030 Ra: 1.2914 Rg: 52.68 Vtot: 633690.
    # 0.000000E+00 0.135150E+10 0.336283E+11 0.224324E+11 0.996598E+07
    # 0.100000E-01 0.123210E+10 0.309074E+11 0.206368E+11 0.869969E+07

    outfile = open('juneom.eom','w')

    # READ in list of intensity files
    fnames = glob.glob(os.path.join(path, '*.int'))

    # HEADER for s-axis
    head = 'S values 51'

    # Extract S values from first file
    for line in open(fnames[0]):
        list = line.split()
        s = list[0]
        i = list[1]
        if s[0].isalpha():
            print » outfile, ':%>18'.format(head)
        else:
            print » outfile, ':%>14'.format(s)

    # Extract intensities from each file
    for infile in fnames:
        try:
            count = infile[2:7]
            count = count.lstrip('0')
        except IndexError:
```

```
print 'empty'

for line in open(infile):
    list = line.split()
    s = list[0]
    i = list[1]
    if s[0].isalpha():
        i = count
    print » outfile, ':%>10 :>5'.format('Curve no.', i)
    else:
        print » outfile, ':%>14'.format(i)

def main():
    if len(sys.argv) != 2:
        print 'usage: ./modInt.py <path>',
        sys.exit(1)

    path = sys.argv[1]
    modInt(path)
```

```
if __name__ == '__main__':
    main()
```

Skript to combine size parameter of generated models in one file

```
#!/usr/bin/python
# modSize.py, HDTM 01-11-2017
# GENERATES EOM SizeiistXXX.txt file based on precomputed *.log files from CRY SOL / CRY SON
# TODO : use dictionary to make this better

sys, re, os, glob

def modInt(path) :
    """Generate EOM Sizeiist from many *.log files"""
    #147.42159.800.00629100.00#254.74188.700.00633500.00#348.38155.300.00643400.00
    outfile = open('SizeiistXXX.txt', 'w')

    #READ in list of intensity files
    fnames = glob.glob(os.path.join(path, '*.log'))

    #Extract filename, Rg, Dmax and Volume from log files
```

```

for infile in fnames :
    try :
        count = infile[2 : 7]
        count = count.lstrip('0')
    except IndexError :
        print 'empty'

for line in open(infile) :
    i = count
    if line.startswith('Shellwidth') :
        Dmax = line[-10 :]
        Dmax = Dmax.strip()
    elif line.startswith('ExcludedVolume') :
        Vol = line[-11 :]
        Vol = Vol.strip()
    elif line.startswith('Rg from') :
        Rg = line[-7 :]
        Rg = Rg.strip()
    print >> outfile,':> 6:> 7:> 7:> 8:> 9.2f'.format(i, Rg, Dmax,'0.00', float(Vol)),
    #print >> outfile,':> 6:> 8'.format(i, Dmax),
    #print >> outfile, line[-7 :],
    #else :
    #print 'Line' + line,

def main() :
    if len(sys.argv) != 2 :
        print 'usage : ./modSize.py < path >',
        sys.exit(1)

    path = sys.argv[1]
    modInt(path)

if name == '__main__':
    main()

```

Table A.5: SAXS/SANS parameters – MsbA-sND.

	MsbA-sND (apo) SAXS	MsbA-sND (apo) SANS	MsbA-sND (ADP) SANS
Data collection parameters			
Instrument	EMBL P12 (PETRA-III, Hamburg)	ILL D11 (Grenoble, France)	
Beam geometry	0.2 x 0.12 mm ²		
Wavelength (Å)	1.24	4.6	
q range (Å ⁻¹)	0.005-0.46	0.01-0.3	
Exposure time (s)	1 (20 x 0.05 s)	3600	
Concentration range (mg/ml)	2.7	6.0	
Temperature (K)	283	283	283
Structural parameters			
$I(0)$ (cm ⁻¹) [from $p(r)$]	230.20	0.8931 ± 0.003	1.166 ± 0.003
$R(g)$ (Å) [from $p(r)$]	47.5 ± 1	40.11 ± 1	38.7 ± 1
$I(0)$ (cm ⁻¹) [from Guinier]	231.45 ± 0.001	0.89 ± 0.003	1.15 ± 0.003
$R(g)$ (Å) [from Guinier]	47.7 ± 0.2	40.04 ± 1	38.57 ± 3.3
D_{max} (Å)	160	130	125
Porod volume estimate (Å ³)	607200	189000	173000
Molecular-mass determination			
Partial specific volume (cm ³ g ⁻¹)	0.745	0.745	0.745
Contrast ($\Delta\rho \times 10^{10} \text{cm}^{-2}$)	2.724	-3.13	-3.13
Molecular mass M_r (Da) [from $I(0)$]	n.d.	145000	144980
Molecular mass M_r (Da) [from Porod volume ($V_p/1.6$)]	379500	118125	109000
Calculated M_r from sequence (Da)	130000	130000	130000
Software employed			
Primary data reduction	RADDAVER	GRASP	GRASP
Data processing		PRIMUS/Qt	
Ab initio analysis		DAMMIF	
Rigid-body modeling		SASREF	
Computation of model intensities	CRY SOL	CRYSON	CRYSON
3D graphics representation	PyMOL	PyMOL	PyMOL

Appendix B

General Sample Preparation Techniques

Buffer and solution preparation

Buffers and solutions were prepared in de-ionized water from a Milli-Q ultrapure lab water system (Merck Millipore, Germany). The pH of the buffer was adjusted using a peqMeter 1.14 (peqLab via VWR, United Kingdom). All buffers for protein purifications were filtered through a 0.22 µm Millex-GP filter (Merck Millipore, Germany) and degassed prior to usage. Solutions for expression were either autoclaved (20 min, 121 °C) or filtered through 0.45 µm Millex-GP filter (Merck Millipore, Germany).

Maintenance and growth of yeast

Wild-type yeast cells (without a plasmid transformed) were grown on YPD (Yeast Peptone Dextrose) media, whereas cells harbouring a expression plasmid were grown in synthetic complete (SC) media with 2 % glucose with drop-out media either depleted of uracil or leucine (all recipes are provided in Table B.1). For overexpression culture 900 ml of SC media with 0.1 % glucose were grown and expression were induced by adding 2 % galactose. All cells were grown at 30 °C unless otherwise stated.

Table B.1: Yeast growth media.

Media	composition
YPD	20 g/l tryptone 10 g/l yeast extract 20 g/l glucose
SC	6.7 g/l yeast nitrogen base (w/o amino acid) 20 g/l glucose (2%)

Maintenance and growth of bacteria

Bacterial cells without a plasmid were grown in lysogenic broth (LB) media (for recipe see Table B.2). Overexpression were carried out in different media (Table B.2)

and starter culture were grown in LB media at 37 °C unless otherwise stated. Expression culture were grown at 37 °C until the desired OD₆₀₀ was reached. After induction using IPTG cells were grown either at 20 °C or 37 °C. Different antibiotics were used to select for the presence of the expression-plasmid. Ampicilin was used at concentration of 100 µg/ml, kanamycin at 25 µg/ml and chloramphenicol at 34 µg/ml.

Table B.2: *E. coli* growth media.

Media	composition
LB media	10 g/l tryptone 5 g/l yeast extract 0.17 M NaCl
TB media	12 g/l tryptone 24 g/l yeast extract 0.5 % glycerol 0.017 M KH ₂ PO ₄ 0.072 M K ₂ HPO ₄
2x YT media	16 g/l tryptone 10 g/l yeast extract 5 g/l NaCl
Minimal media	6.86 g/l (NH ₄) ₂ SO ₄ 1.56 g/l KH ₂ PO ₄ 6.48 g/l Na ₂ HPO ₄ 0.49 g/l (NH ₄) ₂ -H-citrate 0.25 g/l MgSO ₄ 5 g/l Glycerol 1 ml/l 1000x trace elements

Preparation of electrocompetent *E. coli* cells

For preparation of elektro competent cells, desired *E. coli* strains were inoculated LB media and grown at 37 °C until an OD₆₀₀ of 0.4-0.6. Subsequently, culture was cooled on ice for 20-60 min. Cold cells were pelleted by centrifugation at 4000 x g and 4 °C for 15 min and the pellet was washed with ice-cold ddH₂O and pelleted again by centrifugation at 4000 x g for 15 min. The washing step was repeated 2 times and after the last centrifugation step the pellet was resuspended in 20 ml 10 % glycerol. The 20 ml cellsuspension were pelleted by centrifugation at 3800 x g for 15 min at 4 °C. Cellspaste was resuspended in 2-4 ml 10 % glycerol and aliquoted into 50 µl fractions, which were frozen in liquid nitrogen and stored in -80 °C until further use.

Protein sample concentration

The concentration of protein samples were increased by reducing the volume. This were achieved using Amicon centrifugal filters with a appropriate molecular weight cut-off (MWCO). All filters were used according to the operation instructions.

Protein concentration were determined by UV- spectroscopy on a Thermo Fischer Nanodrop 2000 device. The absorption at 280 nm were used to calculate the concentration with following equation:

$$c = \frac{A_{280} M_w}{\epsilon d} \quad (\text{B.1})$$

where M_w is the theoretical molecular weight and ϵ as the extinction coefficient. The ϵ is protein specific and was calculated based on the sequence using the ProtParam tool. A list of calculated ϵ values for all individual proteins can be found in Table B.3

Table B.3: Properties of proteins used in this study.

Protein	Molecular weight [kDa]	Extinction coefficient ϵ [$M^{-1}cm^{-1}$]
ACA8	118.468	102330
CaM7	18.593	2980
MsbA	64.460	46870
MSP1D1	24.661	21430
MSPE3D1	32.730	29910
SapA	10.024	8480

Sodium Dodecyl Sulphate Polyacrylamide Gel Electrophoresis

Sodium dodecyl sulphate polyacrylamide gel electrophoresis was used to separate protein samples according to their size. Samples were mixed with sample buffer (50 mM Tris-HCl pH 6.8, 10% (v/v) SDS, 0.1% (v/v) bromphenol blue, 50% glycerol, 125mM DTT) in a 1:1 ratio and incubated for several minutes before loaded on a 15 % SDS-gel. Gels were run in Tris-glycine running buffer (190 mM glycine, 24.8 mM Tris-HCL, 0.1% (w/v) SDS) for 45-60 min at 200 V (constant). Subsequently, the gel was stained using Coomassie stain (PhastGel Blue R tablets in 40% (v/v) ethanol, 25% (v/v) 2-propanol, 10% (v/v) acetic acid), incubated for 15-60 min and destained with destain solution (10% (v/v) acetic acid, 24% (v/v) 2-propanol).

Polymerase chain reaction (PCR)

Polymerase chain reaction was used to amplify DNA fragments or perform quick change mutagenesis. A 50 μ l reaction contained 1 μ l Phu DNA polymerase (Thermo Fisher, USA), 10 μ l 5x Phu buffer, 100 pmol of forward and reverse primer, respectively, 0.05 μ g (Quickchange mutagenesis) or 0.1 μ g template DNA and 0.2 mmol

of each nucleotide (dATP, dGTP, dCTP, dTTP, NEB). The reaction was carried out in a peqlab peqSTAR 2x gradient thermocycler. For amplification 30 cycles and for mutagenesis 25 cycles were carried out. Each cycle consists of denaturation (95 °C, 30s), annealing (58 °C, 30s) and elongation (72 °C, time varying with the length of the construct) and a final extension step at 72 °C for 10 min. The amplified products were separated agarose gel electrophoresis. For mutagenesis reactions, 0.5 µl of the restriction enzyme DpnI was added and incubated for 1 h at 37 °C. Afterwards, digested product were transformed into *E. coli* cells.

Bacterial and Yeast strains

Table B.4: Bacterial and yeast strains.

Strain	Genotype	Description
<i>E. coli</i> XL1blue	EndA-endA1 gyrA96(nalR) thi-1 recA1 relA1 lac glnV44 F' [::Tn10 proAB+ lacIq Δ(lacZ)M15]hsdR17(rK – mK+)	Optimized for plasmid amplification
<i>E. coli</i> BL21 (DE3)	EndA-, F-ompT gal dcm lon hsdSB(rB- mB-) (DE3 [lacI lacUV5-T7 gene 1 ind1 sam7 nin5])	Used for protein overexpression of MSP1D1 and CaM7
<i>E. coli</i> Rosetta-gami2	Δ(ara-leu)7697 ΔlacX74 ΔphoA PvuII phoR araD139 ahpC galE galK rpsL (DE3) F[lac+ lacIq pro] gor522::Tn10 trxB pRARE2 (Cam ^R , Str ^R , Tet ^R)	Used for protein overexpression of SapA
<i>E. coli</i> C41	F- ompT gal dcm hsdSB(rB- mB-)(DE3)	Used for overexpression of ACA8RD
<i>S. cerevisiae</i> BJ5460	MATa ura352 trp1 lys2801 leu2delta1 his3delta200 pep4::HIS3 prb1delta1.6R can1 GAL	Used for overexpression of ACA8 and ACA8core constructs
<i>S. cerevisiae</i> InvSc1	MATa his3D1 leu2 trp1-289 ura3-52 MAT his3D1 leu2 trp1-289 ura3-52	Used for overexpression of ACA8 and ACA8core constructs

Transformation of electrocompetent *E. coli* cells

For transformation into *E. coli* cells, aliquots with 50 μ l of elektrocompetent cells were used. The plasmid (about 100 ng/ μ l) were mixed with cells and the mix were electro-shocked using a Bio-Rad MicroPulser (BioRad, USA). Subsequently, 300 μ l of autoclaved LB media (without antibiotics) was added and the suspension were incubated at 37 °C for 45 min and plated out on LB agar plates containing the appropriate antibiotics. Agar-plate were incubated over night (approx. 16 h) at 37 °C.

Transformation of *S. cerevisiae* cells

Transformation into Yeast cells (*S. cerevisiae*) were carried out using the LiAc method [245]. 10 ml YPD media was inoculated with a single colony of Yeast cells (from YPD agar-plate) and incubated at 30 °C for approx. 16 h. Subsequently, 50 ml YPD media were inoculated with an OD₆₀₀ of 0.1 using the 10 ml pre-culture. At an OD₆₀₀ of 0.6 cells were spun down at 3,000 x g for 5 min. Cell pellet were washed twice with 50 ml dH₂O (autoclaved) and pelleted. Cells were resuspended in 500 μ l 100 mM LiAc solution and 50 μ l cell suspension were used for one transformation reaction. 240 μ l 50 % (w/v) PEG 3350, 36 μ l 1 M LiAc, 25 μ l single stranded DNA (2 mg/ml), 5 μ l plasmid DNA (10 ng/ μ l) were added to the cells, vortexed for 1 min and incubated at 42 °C for 20 min. Afterwards, the cells were spun down on a table top centrifuge and resuspended in 100 μ l dH₂O before plated out on SC agar-plates (leucin- or uracil-depleted). Agar-plates were incubated for 72 h at 30°C.

Appendix C

Instrumentation and Chemicals

C.1 Instrumentation

Table C.1: *Instrumentation (listed alphabetically).*

Instruments	Manufacturer
Äkta™ <i>pure</i>	GE Healthcare, USA
Äkta™ <i>start</i>	GE Healthcare, USA
Analogue tube rollers: SRT6	Stuart Equipment, United Kingdom
Analytical balance: ABJ	Kern, Germany
Autoclave: VX-120	Systec, Germany
Beamlines	P12, EMBL, PETRA III, DESY, Hamburg BM29 BioSAXS, ESRF, Grenoble D11, ILL, Grenoble SANS-1, MLZ, München
Centrifuge: 5415 R	Eppendorf, Germany
Centrifuge: 5810 R	Eppendorf, Germany
Centrifuge: Avanti J-26SXP	Beckman & Coulter, USA
Centrifuge rotor: 70 Ti UZ	Beckman & Coulter, USA
Centrifuge rotor: JA 25.50	Beckman & Coulter, USA
Centrifuge rotor: JLA-8.1	Beckman & Coulter, USA
CD-Spectrometer: J-815	Jasco, UK
DLS instrumentation: Spectrolight300	XtalConcepts, Germany
Electrophoresis system: Mini Protetra Cell	Bio-Rad, USA
Electroporation system: MicroPulser	Bio-Rad, USA

Continued on next page

Appendix C. Instrumentation and Chemicals

Instruments	Manufacturer
Fluorescence Spectrophotometer: Cary Eclipse	Agilent echnologies, Inc., USA
Gel documentation: Gel Doc 200	ChemiDoc MP & Bio-Rad, USA
Gel tray for SDS-PAGE	Precision mechanics, University Hamburg, Germany
Heat block: MKR13	HLC, Germany
High-pressure homogeniser: Emulsiflex-C3	Avestin, Canada
Homogenizer: BeadBeater	BioSpec Products, USA
Incubator: Ecotron	Infors HT, Germany
Incubator: Multitron Standard	Infors HT, Germany
ITC: MicroCal iTC200	Malvern, United Kingdom
Laminar airflow cabinet: BDK	Weiss Technik, Germany
Magnetic stirrer: Hei-Mix L	Heidolph Instruments, Germany
Mass spectrometer: QToF2 modified for high mass experiments	Waters, USA MS Vision, Germany
Micropipette puller: P-1000 equipped with a squared box filament (2.5 x 2.5 mm)	Sutter Instruments, USA
Microplate reader: Infinite [®] 200 Pro	Tecan, Switzerland
Microscope: SZX12 with camera DP10	Olympus, Japan
Microwave nanoDSF: Prometheus NT.48	Bosch (via Carl Roth), Germany NanoTemper Technologies, Germany
PCR instrument: Thermocycler peqSTAR2x Gradient	Peqlab (via VWR International), USA
pH-Meter: peqMeter 1,14	Peqlab (via VWR International), USA
Pipetting aid: accu-jet pro	Brand, Germany
Platform shaker: Polymax 1040	Heidolph Instruments, Germany
Power supply unit: peqPower	Peqlab (via VWR International), USA
Precision balance: EG	Kern & Sohn, Germany
Scanner: LiDE 110	Canon, Japan

Continued on next page

Instruments	Manufacturer
Spectrophotometer: Nanodrop 2000	Thermo Fisher Scientific, USA
Spectrophotometer: SmartSpec Plus	Bio-Rad, USA
Spectrophotometer: QE Pro spectrometer and a DH-2000 light source	Ocean Optics, United Kingdom
Ultracentrifuge: Optima XE-90	Beckman & Coulter, USA
Ultrasonic cell disruptor: Sonopuls	Bandelin, Germany
UV hand lamp: H466.1	Carl Roth, Germany
Vacuum pump: BVC control	Vacuubrand, Germany
Vortexer: Vortex-Genie 2	Scientific Industries, USA

C.2 Chemicals used (GHS Classification)

Table C.2: Chemicals (listed alphabetically).

Compound	CAS-No.	Supplier	GHS hazard	Hazard Statements	Precautionary Statements
4-Benzoyl-L-phenylalanine	104504-45-2	Bachem	-	-	-
5,5'-Dithiobis(2-nitrobenzoic acid)	69-78-3	Sigma-Aldrich	GHS07	H315, H319, H335	P261, P305+P351+P338
Acetic acid, 96%	64-19-7	Carl Roth	GHS02, GHS05	H226, H314	P280, P305+351+338, P310
Acetone	67-64-1	Carl Roth	GHS02, GHS07	H225, H319, H336	P210, P280, P304+P340+P312, P305+P351+P338, P337+P313, P403+P235
Active carbon	7440-44-0	Carl Roth	-	-	-
Acrylamide 37%	79-06-1	Carl Roth	GHS06, GHS08	H301, H312, H315, H317, H319, H332, H340, H350, H361f, H372	P201, P280, P301+310, P305+351+338, P308+313
Adenin	73-24-5	Carl Roth	GHS06	H301	P270, P301+P310
Agar-Agar	9002-18-0	Sigma-Aldrich	-	-	-
Agarose	9012-36-6	Sigma-Aldrich	-	-	-

Continued on next page

C.2. Chemicals used (GHS Classification)

Compound	CAS-No.	Supplier	GHS hazard	Hazard Statements	Precautionary Statements
Albumin	90604-	Carl	-	-	-
Fraktion V (BSA)	29-8	Roth			
Alexa Fluor™488 C ₅ -maleimide	500004-82-0	Thermo Fischer Scientific	GHS05	H302, H314, H317	P260, P264, P270, P272, P280, P301+P312, P301+P330+P331, P303+P361+P353, P304+P340, P305+P351+P338
Ammonium acetate	631-61-8	Carl Roth	-	-	-
Ammonium formate	540-69-2	Sigma Aldrich	GH202	H315, H319, H335	P261, P305+351+338
Ammonium heptamolybdate tetrahydrate	12054-85-2	Sigma-Aldrich	GHS07	H315, H319, H335	P261, P304+P340, P305+P351+P338, P405
Ampicillin	69-52-3	Carl Roth	GHS08	H334, H317	P280, P261, P302+352, P342+P311
AMPPCP	7414-56-4	Jena Bioscience	GHS06	H301, H311, H315, H319, H331, H335	P261, P280, P311, P301+P310, P305+P351+P338
APS	7727-54-0	Carl Roth	GHS03 GHS07 GHS08	H272, H302, H315, H317, H319, H334, H335	P280, P305+P351+P338, P302+P352, P304+P341, P342+P311
Arabinose	5328-37-0	Carl Roth	-	-	-
ATP	34369-07-8	Sigma-Aldrich	-	-	-

Continued on next page

Appendix C. Instrumentation and Chemicals

Compound	CAS- No.	Supplier	GHS hazard	Hazard Statements	Precautionary Statements
beta-Mercapto-ethanol	60-24-2	Sigma- Aldrich	GHS05, GHS06, GHS08, GHS09	H301+H331, H310, H315, H317, H318, H373, H410	P260, P262, P273, P280, P301+P310+P330, P302+P352+P310, P305+P351+P338 +P310, P391, P403+P233
Brilliant blue G 250	6104-58-1	Carl Roth	-	-	-
Bromphenol blue	115-39-9	Sigma- Aldrich	-	-	-
CaCl ₂	10043-52-4	Sigma- Aldrich	GHS07	H319	P305+P351+P338
Chlor-amphenicol	56-75-7	Sigma- Aldrich	GHS08	H351	P280
Citric acid	77-92-9	Carl Roth	GHS05	H318	P305+P351+P338, P311
Coomassie Brilliant Blue R250	6104-59-2	Sigma- Aldrich	-	-	-
Copper (II) sulphate	7758-98-7	Sigma- Aldrich	GHS05, GHS09	H302, H315, H319, H410	P264, P273, P280, P337+P313, P391, P501
Cymal-5	250692-65-0	Anatrace	-	-	-
D ₂ O	7789-20-0	Sigma- Aldrich	-	-	-
D(+)-Glucose	50-99-7	Carl Roth	-	-	-
D(+)-Galctose	59-23-4	Carl Roth	-	-	-
DDM	69227-93-6	Anatrace	-	-	-

Continued on next page

C.2. Chemicals used (GHS Classification)

Compound	CAS-No.	Supplier	GHS hazard	Hazard Statements	Precautionary Statements
Di-Potassium hydrogen phosphate	16788-57-1	Carl Roth	-	-	-
Dimethyl-formamid	68-12-2	Carl Roth	GHS02, GHS07, GHS08	H226, H312+H332, H319, H360D	P201, P210, P261, P280, P308+P313, P370+P378
DM	82494-09-5	Anatrace	-	-	-
DMNG	1257852-99-5	Anatrace	-	-	-
Dnase I	-	Sigma-Aldrich	-	-	-
DTT	578517	Carl Roth	GHS07	H302, H315, H319, H335	P302+352, P305+351+338
EDTA	60-00-4	Carl Roth	GHS07	H319	P305+351+338
EGTA	67-42-5	Carl Roth	GHS07	H315, H319, H355	P261, P264, P271, P280, P302+P352, P04+P340, P305+P351+P338, P312, P321
Ethanol	64-17-5	Carl Roth	GHS02	H225	P210
Glycerol	56-81-5	Carl Roth	-	-	-
Hydrochloric acid, 6 N	7647-01-0	Carl Roth	GHS05, GHS07	H290, H314, H335	P260, P280, P303+P361+P353, P304+P340+P310, P305+P351+P338
HEPES	7365-45-9	Carl Roth	-	-	-

Continued on next page

Appendix C. Instrumentation and Chemicals

Compound	CAS- No.	Supplier	GHS hazard	Hazard Statements	Precautionary Statements
Imidazole	288-32-4	Carl Roth	GHS05, GHS06, GHS08	H301, H314, H361	P260, P281, P303+361+353, P301+P330+P331, P305+P351+P338, P308+313
IPTG	367-93-1	Carl Roth	-	-	-
Isopropanol	67-63-0	Carl Roth	GHS02, GHS07	H225, H319, H336	P210, P233, P305+P351+P338
KCl	7447-40- 7	Carl Roth	-	-	-
Kanamycin sulfate	25389- 94-0	Carl Roth	GHS08	H360	P201, P308+P313
LB-medium Lennox	-	Carl Roth	-	-	-
L-Alanine	56-41-7	Carl Roth	-	-	-
L-Arginine	74-79-3	Carl Roth	GHS07	H319	-
L(+)- Ascorbic acid	50-81-7	Sigma- Aldrich	-	-	-
L- Asparagine	5794-13- 8	Carl Roth	-	-	-
L-Aspartic acid	56-84-8	Carl Roth	-	-	-
L-Cysteine	52-90-4	Carl Roth	GHS07	H302	-
L-Glutamic acid	56-86-0	Carl Roth	-	-	-
L-Glutamine	56-85-9	Carl Roth	-	-	-
L-Glycine	56-40-6	Carl Roth	-	-	-
L-Histidine	71-00-1	Carl Roth	-	-	-

Continued on next page

C.2. Chemicals used (GHS Classification)

Compound	CAS-No.	Supplier	GHS hazard	Hazard Statements	Precautionary Statements
L-Isoleucine	73-32-5	Carl Roth	-	-	-
L-Leucine	61-90-5	Carl Roth	-	-	-
L-Lysine	39665-12-8	Carl Roth	-	-	-
L-Methionine	63-68-3	Carl Roth	-	-	-
L-Phenylalanine	63-91-2	Carl Roth	-	-	-
L-Proline	147-85-3	Carl Roth	-	-	-
L-Serine	56-45-1	Carl Roth	-	-	-
L-Threonine	72-19-5	Carl Roth	-	-	-
L-Tryptophan	73-22-3	Carl Roth	-	-	-
L-Tyrosine	60-18-4	Carl Roth	-	-	-
L-Valine	72-18-4	Carl Roth	-	-	-
Lithium Acetate	546-89-4	Carl Roth	-	-	-
LMNG	1257852-96-2	Anatrace	-	-	-
Lysozyme (Gallus gallus)	12650-88-3	Sigma-Aldrich	-	-	-
MES	4432-3-9	Carl Roth	-	-	-
Methanol	67-56-1	Sigma-Aldrich	GHS02, GHS06, GHS08	H225, H301+H311 + H331, H370	P210, P280, P302+P352+P312, P304+P340+P312, P370+P378, P403+P235

Continued on next page

Appendix C. Instrumentation and Chemicals

Compound	CAS- No.	Supplier	GHS hazard	Hazard Statements	Precautionary Statements
MgCl ₂	7786-30-3	Carl Roth	-	-	-
Milk powder	68514-61-4	Carl Roth	-	-	-
Myo-inositol	87-89-8	Sigma- Aldrich	-	-	-
NaOAc	127-09-3	Sigma- Aldrich	GHS07	H319	P305+P351+P338
NaCl	7647-14-5	Carl Roth	-	-	-
Na-meta-arsenite	7784-46-5	Sigma- Aldrich	GHS06, GHS08, GHS09	H300, H310, H331, H350, H400, H410	P301+P310, P280, P361, P322, P321, P403+P233, P201, P281, P308+P313
NaOH	1310-73-2	Carl Roth	GHS05	H314	P280, P310, P305+P351+P338
Ni-NTA-Agarose		Sigma- Aldrich	GHS02, GHS07, GHS08	H226, H317, H350i, H360D, H373, H412	P201, P273, P280, P308+P313, P333+P313, P370+P378
Ni(II)SO ₄	10101-97-0	Carl Roth	GHS07, GHS08, GHS09	H302+H332, H315, H317, H334, H341, H350i, H360d, H372 H410	-
OG	29836-26-8	Anatrace	-	-	-
p-Aminobenzoic acid		University Ham- burg	GHS05	H318	P280, P305+P351+P338, P313

Continued on next page

C.2. Chemicals used (GHS Classification)

Compound	CAS-No.	Supplier	GHS hazard	Hazard Statements	Precautionary Statements
PEG 3350	25322-68-3	Sigma-Aldrich	-	-	-
Penicillin-Streptomycin	-	Gibco	GHS07, GHS07	H315, H317, H334, H335	P280, P261, P264, P284, P271, P302+P352, P333+P313, P304+P340, P342+P311, P312, P403+P233, P501
PMSF	329-98-6	Applichen	GHS06, GHS05	H301, H314	P280, P305+P351+P338, P310
POPC / POPG / DOPC / DMPC / soyPI	26853-31-6 / 268550-95-4 / 4235-95-4 / 18194-24-6 / 383907-36-6	Avanti Polar Lipids	GHS06, GHS07, GHS08	H302, H315, H319, H331, H336, H351, H361d, H372, H402	P201, P202, P260, P264, P270, P271, P273, P280, P301+P312+P330, P302+P352, P304 + P340 + P311, P305 + P351 + P338 , P308 + P313, P332 + P313, P337 + P313, P362, P403 + P233, P405, P501
Potassium Carbonate	584-08-7	Sigma-Aldrich	GHS07	H315, H319, H335	P302+P352, P305+P351+P338
Potassium di-hydrogen phosphate	7778-77-0	Carl Roth	-	-	-
Roti-GelStain	-	Carl Roth	-	-	-

Continued on next page

Appendix C. Instrumentation and Chemicals

Compound	CAS- No.	Supplier	GHS hazard	Hazard Statements	Precautionary Statements
SDS	151-21-3	Carl Roth	GHS02 GHS06	H228, H302, H311, H315, H319, H335	P210, P261, P280, P312, P305+P351+P338
Sodium citrate	1545832	Sigma- Aldrich	-	-	-
Sodium- meta- arsenite	7784-46- 5	Sigma- Aldrich	GHS06, GHS08, GHS09	H300, H310, H331, H350, H400, H410	P301+P310, P280, P361, P322, P321, P403+P233, P201, P281, P308+P313
Sodium vanadate	13721- 39-6	Carl Roth	GHS07	H302 + H312, H332, H402	P280
Succinic acid	110-15-6	Carl Roth	GHS05	H318, H319	P280, P305+P351+P338, P310
TCEP	51805- 45-9	Sigma- Aldrich	GHS05	H314	P280, P305+P351+P338, P310
TEMED	1185-53- 1	Carl Roth	GHS07	H315, H319, H335	P261, P305+P351+P338
Tris base	77-86-1	Carl Roth	GHS07	H315, H319, H335	P261, P264, P280, P304+P340, P305+P351+P338, P337+P313, P405
Tris hy- drochloride	1185-53- 1	Carl Roth	-	-	-
Triton X 100	9002-93- 1	Carl Roth	GHS05 GHS07 GHS09	H302, H315, H318, H410	P280, P301+P312+P330, P305+P351+P338+ P310

Continued on next page

C.2. Chemicals used (GHS Classification)

Compound	CAS-No.	Supplier	GHS hazard	Hazard Statements	Precautionary Statements
Tryptone/ Peptone	8952.4	Carl Roth	-	-	-
Trypsin	9002-07- 7	Carl Roth	GHS07 GHS08	H315, H319, H334, H335	P261, P280, P284, P304+P340, P337+P313, P342+P311
UDM	253678- 67-0	Anatrace	-	-	-
Yeast Extract	8013-01- 2	Carl Roth	-	-	-
Yeast- Nitrogen- Base (without Amino Acids)	-	Carl Roth	-	-	-

C.3 GHS Hazard Statements

H225	Highly flammable liquid and vapour
H226	Flammable liquid and vapour
H228	Flammable solid
H272	May intensify fire; oxidizer
H290	May be corrosive to metals
H301	Toxic if swallowed
H302	Harmful if swallowed
H303	May be harmful if swallowed
H311	Toxic in contact with skin
H312	Harmful in contact with skin
H313	May be harmful in contact with skin
H314	Causes severe skin burns and eye damage
H315	Causes skin irritation
H316	Causes mild skin irritation
H317	May cause an allergic skin reaction
H318	Causes serious eye damage
H319	Causes serious eye irritation
H330	Fatal if inhaled
H331	Toxic if inhaled
H332	Harmful if inhaled
H333	May be harmful if inhaled
H334	May cause allergy or asthma symptoms or breathing difficulties if inhaled
H335	May cause respiratory irritation
H336	May cause drowsiness or dizziness
H340	May cause genetic defects
H341	Suspected of causing genetic defects
H350	May cause cancer
H350i	May cause cancer by inhalation
H360	May damage fertility or the unborn child
H360D	May damage the unborn child
H360F	May damage fertility
H360Fd	May damage fertility. Suspected of damaging the unborn child
H360FD	May damage fertility. May damage the unborn child
H361	Suspected of damaging fertility or the unborn child
H361d	Suspected of damaging the unborn child
H361f	Suspected of damaging fertility

H370	Cause damage to organs
H372	Causes damage to organs through prolonged or repeated exposure
H373	May cause damage to organs through prolonged or repeated exposure
H400	Very toxic to aquatic life with long-lasting effects
H410	Very toxic to aquatic life with long lasting effects
H411	Toxic to aquatic life with long lasting effects
H412	Harmful to aquatic life with long lasting effects
EUH032	Contact with acids liberates very toxic gas
EUH066	Repeated exposure may cause skin dryness or cracking

C.4 GHS Precautionary Statements

P101	If medical advice is needed, have product container or label at hand
P201	Obtain special instructions before use
P210	Keep away from heat/sparks/open flames/hot surfaces – No smoking
P233	Keep container tightly closed
P260	Do not breathe dust/fume/gas/mist/vapours/spray
P261	Avoid breathing dust/fume/gas/mist/vapours/spray
P264	Wash thoroughly after handling
P270	Do not eat, drink or smoke when using this product
P273	Avoid release to the environment
P280	Wear protective gloves/protective clothing/eye protection/face protection
P281	Use personal protective equipment as required
P284	Wear respiratory protection
P309	If exposed or you feel unwell
P310	Immediately call a POISON CENTER or doctor/physician
P311	Call a POISON CENTER or doctor/physician
P312	Call a POISON CENTER or doctor/physician if you feel unwell
P321	Specific treatment (see respective MSDS)
P330	Rinse mouth
P362	Take off contaminated clothing and wash before reuse

Appendix C. Instrumentation and Chemicals

P391	Collect spillage
P405	Store locked up
P501	Dispose of contents/container in accordance with local/regional/national/international regulations
P301+P310	IF SWALLOWED: Immediately call a POISON CENTER or doctor/physician
P301+P312	IF SWALLOWED: Call a POISON CENTER or doctor/physician if you feel unwell
P301+P330+P331	IF SWALLOWED: Rinse mouth. Do NOT induce vomiting
P302+P352	IF ON SKIN: Wash with soap and water
P303+P361+P353	IF ON SKIN (or hair): Remove/Take off immediately all contaminated clothing. Rinse skin with water/shower
P304+P341	IF INHALED: If breathing is difficult, remove victim to fresh air and keep at rest in a position comfortable for breathing
P305+P351+P338	IF IN EYES: Rinse cautiously with water for several minutes. Remove contact lenses if present and easy to do - continue rinsing
P308+P313	IF exposed or concerned: Get medical advice/attention
P309+P311	IF exposed or you feel unwell: Call a POISON CENTER or doctor/physician
P332+P313	If skin irritation occurs: Get medical advice/attention
P333+P313	If skin irritation or rash occurs: Get medical advice/attention
P337+P313	If eye irritation persists: Get medical advice/attention
P342+P311	Call a POISON CENTER or doctor/physician
P370+P378	In case of fire: Use for extinction: Alcohol resistant foam
P370+P378	In case of fire: Use for extinction: Fire-extinguishing powder
P370+P378	In case of fire: Use for extinction: Carbon dioxide
P403+P233	Store in a well-ventilated place. Keep container tightly closed
P403+P235	Store in a well-ventilated place. Keep cool

C.5 Disposal

All chemicals used during the experimental phase were handled and disposed according to their H- and P-Sentences. Solvents and contaminated waste was stored in the specific boxes and disposed according to the safety instructions. Genetically modified organisms and related waste were autoclaved according to the "Gentechnikgesetz" before disposal for 20 min at 121C and 2 bar.

Acknowledgements

Many people has contributed to this thesis and it is difficult to acknowledge all of them. First and foremost, I would like to thank my supervisor Prof. Dr. Henning Tidow for not only giving me the opportunity to join this exciting project but for your constant support throughout this project. Thank you for the freedom to try even challenging and sometimes crazy ideas. It was a truely exciting time and I learned a lot from you.

My sincere thank also goes to to Prof. Dr. Christian Betzel for the preparation of the second opinion as well as to the examiners of my disputation, Prof. Dr. Arwen Pearson and Dr. Maria Riedner.

The daily work is heavily dependent on your colleagues. Therefore, I am very grateful to my whole working group, Dr. Inoketjts Josts, Dr. Katharina Jungnickel, Anne Creon, Ellen Gattkowski, Yasser Almeida Hernandez, Dr. Stephanie Kesgin-Schr, Tina Bohstedt and Katharina Veith. Thank you for all the nice coffee breaks as well as for your support and the help in the lab.

In the course of this thesis some collaborations were created. In this regard, I would like to thank Dr. Haydyn Mertens who was always around during the beamtimes at P12, even late in the night. Moreover, he showed us all the important things in a SANS experiments and joined us in Munich as well as in Grenoble. I really enjoyed all the scientific beer sessions in Garching. In addition I would like to thank Dr. Johannes Heidemann for a great collaboration. Moreover, I would like to thank Prof. Dr. Franz Hagn for the opportunity to learn all important aspects of the exciting nanodisc system and the really nice time I had in your lab.

I would like to thank my two Master students Timm Koller and Dominique Kehlenbeck for all your work in the lab. Due to your constant hard work you pushed this thesis a big step forward. Moreover, I would like to thank Dr. Thomas Seine and Dr. Robin Schubert not only for the nice scientific discussions during our great gin tastings but as well for all of your motivating words in the last years. Thanks a lot! Concerning my private life I am also really thankful for the infinite support of my family, especially for the constant faith of my father.

Finally, I want to thank the most important person in my live. Anna, you supported me throughout this whole time. You motivated me whenever I was struggling and worked as hard as I did in the last five years to complete this project. I am really grateful to have you in my life.

Eidesstattliche Erklärung

Hiermit versichere ich an Eides statt, die vorliegende Dissertation selbst verfasst und keine anderen als die angegebenen Hilfsmittel benutzt zu haben. Ich versichere, dass diese Dissertation nicht in einem früheren Promotionsverfahren eingereicht wurde. Ferner versichere ich, dass ich noch keine Promotionsversuche an anderen Universitäten unternommen habe.

Unterschrift:

Datum:
